Numéro d'ordre: 2016LYSEC28 Année: 2016

THÈSE

présentée pour obtenir le titre de

DOCTEUR DE L'ÉCOLE CENTRALE DE LYON

Spécialité : Acoustique

dans le cadre de l'École Doctorale

Mécanique, Énergétique, Génie civil, Acoustique

par

Jean-Loup CHRISTEN

Acoustic transmission through composite shells with noise treatment: Modelling and sensitivity

-

Transmission acoustique de coques composites avec traitement antibruit: Modélisation et sensibilité

Soutenance prévue en septembre 2016 à l'École Centrale de Lyon, devant le jury composé de :

N. ATALLA	Université de Sherbrooke	Rapporteur
M. BEN TAHAR	Université de Technologie de Compiègne	Rapporteur
D. JUVÉ	École Centrale de Lyon	
M. OUISSE	FEMTO-ST	
M. ICHCHOU	École Centrale de Lyon	
B. TROCLET	Airbus Defence and Space	
O. BAREILLE	École Centrale de Lyon	
A. M. ZINE	École Centrale de Lyon	

Remerciements

Je souhaite en premier lieu remercier mes directeurs de thèse, Mohamed Ichchou et Bernard Troclet, qui m'ont fait confiance tout au long de ce doctorat et m'ont permis de le réaliser. Mes remerciements vont également aux deux rapporteurs de ce travail, Noureddine Atalla et Mabrouk Ben Tahar, ainsi qu'à Daniel Juvé, Morvan Ouisse et Abdelmalek Zine pour avoir accepté de faire partie de mon jury.

Si une thèse est officiellement le travail d'un seul homme, chacune de ses parties doit énormément à d'autres personnes qui y ont contribué plus ou moins directement. Je tiens donc à tous les remercier, sans forcément d'ordre:

- Olivier Bareille pour son aide pratique tout au long de la thèse
- Christophe, Yu, Changwei, Diane, Régis, Wenqi, Zakaria, Omar, pour les longues discussions scientifiques et l'aide pour les manips encombrantes,
- L'équipe du GAUS, et tout particulièrement Raef Chérif qui m'a accueilli à Sherbrooke et dont la contribution au chapitre 8 est plus qu'essentielle,
- Isabelle et Hélène pour leur aide dans les méandres des tâches administratives
- Lionel, Stéphane et Sébastien pour leur aide à la conception et à la réalisation des essais.

Résumé

La transmission acoustique de plaques et de coques est un problème présent dans de nombreuses industries, de l'automobile à l'aéronautique en passant par le génie civil. Il s'agit alors, en présence d'une source externe, de limiter le niveau de bruit à l'intérieur d'une cavité enclose par une structure vibrante, qu'il s'agisse d'une voiture, d'un avion ou d'un immeuble.

Les matériaux composites sont de plus en plus largement utilisés par toutes les industries du transport, du fait de leur faible masse rapportée à leur grande rigidité. Ces caractéristiques, utiles pour réduire la consommation énergétique des véhicules, sont cependant un handicap lorsqu'il s'agit de limiter le niveau de bruit intérieur. Il est alors nécessaire d'ajouter des protections acoustiques. On s'intéresse dans ce travail à la transmission d'un bruit produit à l'extérieur de la cavité, et à des solutions antibruit passives, utilisant des matériaux poreux absorbants. Ceux-ci, mousses ou laines minérales, présentent en général de bonnes performances acoustiques pour des fréquences élevées, mais nettement mois intéressantes en basses fréquences.

Ce travail s'inscrit dans le cadre d'un projet international ayant pour objectif d'étudier la réduction de bruit à travers des structures composites incluant des protections acoustiques passives. Deux axes y sont privilégiés, la modélisation et l'analyse de sensibilité. En effet, les matériaux poreux et composites présentent souvent de grandes incertitudes, dues au procédé de fabrication, à la difficulté de mesure, ou encore simplement à des choix de conception à faire. On cherche donc à s'assurer de la robustesse des solutions étudiées.

Cette thèse est organisée en trois parties. La première traite de la modélisation des structures composites et des traitements poroélastiques. On s'intéresse surtout à deux types de structures, les plaques et les cylindres, pouvant dans les deux cas inclure un grand nombre de couches et de matériaux différents. La deuxième partie traite des méthodes d'analyse de sensibilité, et d'applications dans le cas de la transmission acoustique à travers des structures composites. On s'intéressera enfin dans la troisième partie à l'effet du traitement poroélastique, à travers des études numériques et expérimentales.

Partie I : Modélisation en vibroacoustique

La première partie est consacrée à la modélisation vibroacoustique des structures. Le chapitre 1 présente une revue des principales méthodes existantes pour le calcul de la transmission acoustique de plaques et de coques munies de traitements poroélastiques. On s'intéresse particulièrement à l'indice d'affaiblissement acoustique (TL) de plaques infinies et de cylindres, l'effet de la taille finie pouvant être traité par l'ajout de coefficients correctifs. La méthode TMM, la plus pratique pour ce cas, s'appuie sur une résolution analytique des équations de comportement des matériaux. Une méthode alternative de calcul du TL d'une plaque infinie multicouche excitée par une onde plane, partant de la méthode des éléments finis ondulatoires (WFE) est proposée dans le chapitre 2. Cette formulation est enfin étendue dans le chapitre 3 au calcul de TL d'un cylindre multicouche infini. Dans les deux cas, les formulations proposées sont validées par rapport à des résultats issus de la littérature.

Partie II : Analyse de sensibilité pour la transmission acoustique de composites

L'objectif du projet étant l'atténuation d'un bruit large bande, il est nécessaire d'étudier les problèmes vibroacoustiques à la fois pour les hautes, moyennes et basses fréquences. Cependant, les résultats peuvent être fortement affectés par des incertitudes, dues au modèle ou aux paramètres d'entrée. Les méthodes d'analyse de sensibilité ont pour objectif de quantifier l'influence des paramètres sur la sortie d'un modèle. On se place dans cette partie dans le cadre d'un modèle de transmission acoustique, permettant le calcul du TL à travers une plaque complexe (composite, et éventuellement multicouche). Les paramètres d'entrée sont incertains, le modèle lui-même étant déterministe.

Un état de l'art en matière de méthodes d'analyse de sensibilité est présenté au chapitre 4. On y insiste particulièrement sur la classe de méthode dite ANOVA, pour analyse de la variance, dont font partie les méthodes les plus utilisées. La méthode FAST (Fourier amplitude sensitivity test) est retenue pour la suite de la thèse, car elle permet un calcul rapide et fiable des indices de sensibilité. Le chapitre 5 présente une application de la méthode FAST à des modèles de TL de plaques composites infinies. Enfin, dans le chapitre 6, la méthode FAST est utilisée pour étudier les incertitudes dans un modèle SEA, permettant le calcul de l'indice de réduction de bruit (NR) à travers des structures finies.

Partie III : Effet d'un traitement poroélastique sur l'affaiblissement acoustique

La troisième et dernière partie de cette thèse a pour but d'étudier l'effet d'un traitement poroélastique sur la transmission du son. Une première brève étude numérique présentée dans le chapitre 7 compare l'effet d'une méconnaissance de paramètres de la plaque composite par rapport à celui d'incertitudes dans le traitement antibruit. Le modèle retenu est celui des matrices de transfert simplifiées (sTMM, présentée dans le chapitre 1).

Le chapitre 8 effectue une comparaison entre une étude paramétrique expérimentale et une analyse de sensibilité numérique utilisant la méthode FAST. L'étude porte sur une plaque en matériau composite sandwich sur laquelle sont fixés divers matériaux poreux, installée entre une chambre réverbérante et une chambre semi-anéchoïque. Enfin, une étude expérimentale de la transmission à travers une coque cylindrique en présence d'un matériau poroélastique (mousse de polyuréthane) est réalisée dans le chapitre 9.

Abstract and outline

Acoustic transmission through plates and shells is a problem that appear in many applications, for example in the automotive or aerospace industries, or in civil engineering. The idea is to reduce the noise level inside a caivty enclosed by a vibrating structure, which may be a car, a plane or a building.

Composite materials are widely used in the transportation industries due to their light weight and high mechanic resistance, but these features tend to increase the acoustic transparency of the structures, thus making it necessary to add acoustic protections for reducing noise in the enclosed cavity. The most frequently used acoustic protections take the form of layers of poroelastic materials, which are very efficient noise absorbers in high frequencies, but perform less efficiently in lower frequency ranges.

This thesis is part of an international project aimed at improving the noise reduction performance of composite structures through passive sound packages. This implies the development of reduced models of acoustic transmission through such structures, and optimization studies on these models. Besides, the robustness of a solution with respect to uncertainties in the model have to be ensured. This thesis is organised in three parts, dealing with numerical modelling, sensitivity analysis for acoustic transmission and the effect of a porous treatment on sound transmission. For the first two parts, the first chapter is a literature review of existing techniques, and the other chapters are scientific contributions.

Part I: Vibroacoustic modelling

Vibroacoustic modelling is still an open problem in many applications. After a review of existing techniques in chapter 1, considering transmission loss through planar structures and shells lined with poroelastic noise treatment, an new framework is proposed in chapter 2 in order to address the acoustic transmission of such structures with the WFE method, combining a finite element model of the structure, the periodic structure theory and an analytic model of acoustic waves in the emitting and receiving spaces. The same formulation is extended to cylindrical shells in chapter 3.

Part II: Sensitivity analysis of sound transmission models

As space structures are impacted by broadband noise, it is necessary to set up vibroacoustic problems for low, mid and high frequencies. However, the results may be significantly affected by uncertainties both in the model equations and in the input parameters. Sensitivity analysis methods are aimed at finding indicators of relative influence of parameters on the output of a given model. A review of such methods is made in chapter 4, with emphasis on one of the most popular methods, the ANOVA framework, including the FAST method (standing for Fourier Amplitude Sensitivity Test). Chapter 5 presents an application of the FAST method to analytic models of transmission loss through planar structures, such as isotropic, orthotropic and sandwich plates. Finally, the FAST method is used in chapter 6 to study the uncertainties arising in SEA models of coupled fluid-structure systems.

Part III: Effect of poroelastic treatment on transmission loss

This last part is devoted to analysing the effect of poroelastic treatment on the transmission loss of composite structure. The method of chapter 5 is first used to assess the sensibility of a poroelastic noise treatment modelled with a simple transfer matrix model in chapter 7. In chapter 8, a comparison between experimental parametric analysis and numerical sensitivity analysis of the transmission loss of a plate with noise treatment is presented, with a structure close to that of chapter 7. Finally, chapter 9 presents an experimental verification of the diffuse field noise reduction through a cylindrical composite shell lined with polyurethane foam.

Contents

Nomenclature

Latin notations[1]

Name	Usual unit	Definition
c_0	$\mathrm{m.s^{-1}}$	Sound speed in air
D	N.m	Bending stiffness
E	GPa	Young modulus
f	Hz	Frequency
G	GPa	Shear modulus
h	m	Plate or shell thickness
$\mathbf{I}$	-	Identity matrix
i	-	Imaginary unit $\mathrm{i}^2 = -1$
$\mathbf{k}$	$\mathrm{m^{-1}}$	Wavenumber (vector)
m	$\mathrm{kg.m^{-2}}$	Surface density
V	-	Variance
x, y, z	m	Cartesian coordinates

Greek notations

α	-	Absorption coefficient
α_∞	-	Tortuosity
η	-	Hysteretic damping
η_i	-	Damping loss factor of subsystem i (SEA)
η_{ij}	-	Coupling loss factor (SEA)
θ	rad	Incidence angle
λ, λ_x, λ_y	-	Propagation constant (WFE)
Λ_{visc}	m	Viscous characteristic length
Λ_{therm}	m	Thermal characteristic length
ν	-	Poisson ratio
ρ	$\mathrm{kg.m^{-3}}$	Density
ρ_0	$\mathrm{kg.m^{-3}}$	Density of air
σ	$\mathrm{N.s.m^{-4}}$	Flow resistivity
φ	rad	Azimuthal (direction) angle
ϕ_0	-	Porosity
ω	$\mathrm{rad.s^{-1}}$	Circular frequency
ω_i	-	Integer frequency relative to parameter i (FAST)

[1]Scalar quantities are denoted by Latin or Greek letters in italics (a, α). Vectors are represented by bold lower-case Latin letters ($\mathbf{a}$). Matrices are represented by bold upper-case Latin letters ($\mathbf{A}$). The transposed of a vector or matrix is denoted by $\mathbf{a}^\mathrm{T}$, $\mathbf{A}^\mathrm{T}$

Part I

Vibroacoustic modelling of complex structures

Chapter 1

Literature review on vibroacoustic models

Contents

1 Introduction

Two kinds of approaches can be used for the computation of the structural response of a composite structure to acoustic loads, namely wave and modal approaches. The modal approaches lead to very accurate results in low frequency, but require a good knowledge of the structure's boundary conditions, as they can modify greatly the way modes are calculated. Besides, as modal overlap tends to increase with frequency, the structural response using a modal basis becomes increasingly costly and inaccurate in proportion, unless the modes are well known with an analytical formulation. Wave bases on the other hand do not take boundary conditions into account, which means they are less suitable for low frequencies, but they are a good candidate for mid-and high-frequency modelling.

The present chapter is structured as follows. The first section is concerned with the relevant vibroacoustic indicators for the noise reduction inside cavities, namely transmission loss and noise reduction index. Section 3 presents a survey of methods used for the computation of wave propagation characteristics in plates and shells. Analytical and numerical models are addressed. Modelling of noise control solutions made of poroelastic materials is addressed in section 4. Finally, vibroacoustic models for the whole assembly of a structure and sound package are presented in section 5

2 Vibroacoustic indicators

The efficiency of a noise-reducing treatment can be assessed by a variety of indicators. Two of them will be discussed in this thesis, namely the transmission loss (TL), and the noise reduction index (NR). The transmission loss is a characteristic of the structure, with no account of source and receiving media, whereas the NR characterizes the coupling between the structure and the acoustic cavities. Both are expressed in decibels. A canonical transmission problem will be considered here, as depicted in Figure 1.1 where a plate-like structure separates two cavities, one of which containing a noise source (emission room), the other one being the receiving room.

2.1 Transmission loss

The transmission loss factor is one of the most general available indicator. It is also sometimes called sound transmission loss with the acronym STL. The TL is defined as the ratio between

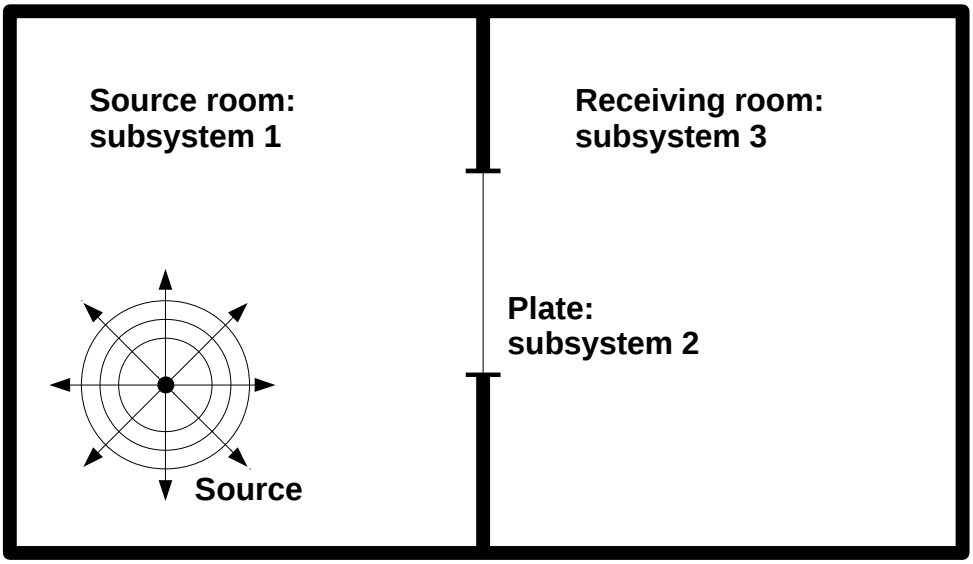

Figure 1.1 – Layout of a canonical transmission problem

the power of the incident (W_i) and transmitted (W_t) sound fields, expressed in decibels.

$$\mathrm{TL} = -10 \log_{10} \frac{W_t}{W_i} \tag{1.1}$$

For an infinite plate, it is defined with the power transmitted per unit surface.

2.2 Noise reduction index

The noise reduction factor is the most used quantity in the space industry. It is defined as the difference between average sound levels in the exterior and interior cavities.

$$\mathrm{NR} = Lp_{ext} - Lp_{int} \tag{1.2}$$

The main difference with the transmission loss is the fact that the NR takes into account absorption effects inside the cavity. For the canonical transmission problem, assuming the receiving cavity walls have an absorption coefficientα over a surface S_3 and the area of the plate is A_2, the relationship between NR and TL is as follows:

$$\mathrm{NR} = \mathrm{TL} + 10 \log_{10} \frac{\alpha S_3}{A_2}. \tag{1.3}$$

3 Wave approaches for 2D structures

3.1 Analytical models

3.1.1 Plates

The prediction of the vibratory response of thick layered panels has been a popular field of research. The classical laminate plate theory (CLPT) is based on the Kirchhoff-Love theory, neglecting the transverse shear deformation and the transverse normal effects of the structure. This hypothesis usually leads to poor results for thick laminates, for which the ratio of the shear modulus to the in-plane elastic moduli is sometimes very low. The shear deformation effect must therefore be taken into account in the analysis. This was firstly attempted by [82] who introduced the panels shear effect in the kinematic assumptions. The work in [116] presented an extension of Mindlin's theory, the First order shear deformation theory (FSDT) for a single layer. Higher-order theories (HSDT) have also been developed, introducing refined kinematic assumptions which render more accurate predictions, at the cost of increased complexity and computation time. However, they require the computation of the parameters for a single layer equivalent to the initial multilayered composite.

More accurate predictions for a multilayered structure can be provided by a Layer-Wise modelling, which considers the individual displacement field of each lamina separately allowing for a discontinuous strain field and a continuous transverse stress field at the interfaces of different materials [91]. Layer-wise modelling usually results in very accurate predictions, however it also implies significant computational effort, as each lamina is modelled through a separate mathematical layer. A good compromise between accuracy and computational effort is achieved through the so called zig-zag or partially layer-wise theories [16], in which an expansion of the displacement field is conducted using a zig-zag variation through the thickness.

The authors in [57] were the first to develop an asymptotic set of equations to model the wave propagation into symmetric flat thick sandwich structures. The authors in [41, 40] used a multi-layer analytical model based on Mindlin's theory to compute the dispersion characteristics of layered structures.

3.1.2 Curved shells and cylinders

The propagation of waves along cylindrical structures has been studied especially for acoustic transmission. Several authors [54, 65, 62] have proposed analytic models of the acoustic transmission through infinite isotropic thin cylindrical shells. A generalization for laminated

shells using the Donnell-Mushtari theory for thin shells is proposed in [31]. Another theory has been proposed in [40, 41], that is more suitable for thick sandwich panels, using the Flügge theory for thicker shells, taking into account shear effects through the thickness direction.

All these theories involve writing a linear differential operator L applied to the displacements of the shell in the three directions u, v and w. The characteristics of the multilayered shell are homogenized through the thickness, and the free wave propagation problem takes the form

$$L \begin{pmatrix} u \\ v \\ w \end{pmatrix} - m_s \omega^2 \begin{pmatrix} \ddot{u} \\ \ddot{v} \\ \ddot{w} \end{pmatrix} = 0 \tag{1.4}$$

where m_s is the surface density of the shell. This can be rewritten as a quadratic eigenvalue problem with the wavenumber k as the eigenvalue, of which the exact formulation depends on the shell theory used.

3.2 Trefftz methods

Vibroacoustics problems ultimately reduce to solving partial differential equations in a volume of space, be it 2D or 3D, under some boundary conditions. The usual finite element approach is to find approximate solutions on a basis of functions which satisfy the boundary conditions, but not the equation inside the domain. Trefftz approaches [111] on the contrary try to find solutions which approximate the boundary conditions and satisfy exactly the interior problem. In mechanical terms, the solution is searched over a basis of solutions to the wave equation in the medium. Several variants of this methods have been developed in the recent years under various names. One can cite for example the Wave Based Method (WBM)[32], the Wave Boundary Element Method (WBEM) [90], or the Variational Theory of Complex Rays [58]. All these theories have in common the advantage of needing a much smaller discretisation than finite element models, however with poor conditioning of the matrix systems to be solved. All these methods are under active development to extend their validity ranges towards mid-frequencies.

3.3 Semi-analytical finite element

The Semi-Analytical Finite Element (SAFE) method is based on the formulation of a variational problem, considering that propagating waves have a sinusoidal shape along their direction of propagation. Depending on the waveguide's features, the numerical model can be established in Cartesian or cylindrical coordinate systems; the axis along which waves propagate may be straight or circular. The wave motion in the propagation direction is de-

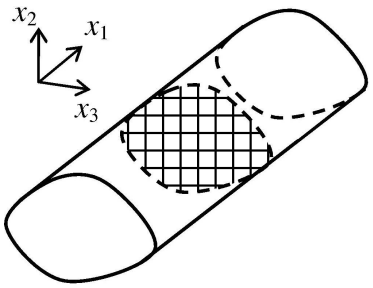

Figure 1.2 – Structural waveguide with arbitrary cross-section discretised by finite elements.

scribed analytically by the harmonic function $\exp(\mathrm{i}(\omega t - kx))$, where k is the wavenumber in wave propagation axis x, and ω is the circular frequency. The cross-sectional wave motion in the $y-z$ plane is approximated by standard FE discretisation, as shown in Figure 1.2 an example for a waveguide with its 2D cross-section discretised in Cartesian coordinate systems. A governing equation of the wave motion can be derived through either virtual work principle or Hamilton's principle [30, 8]. Written in the frequency domain, this equation leads to a quadratic eigenvalue problem of which the wavenumbers k are solutions.

3.3.1 SAFE for plate-like structures

Even if this approach has been initially considered in the sight of building reduced model for beam-like components, its extension to bi-dimensional problems has been also addressed. As an illustration, let us consider a plate-like structural component whose normal direction correspond to the z-axis. If we refer to a volume of material taken out of it, the boundaries in the normal z-direction correspond to the faces of the plates whereas the others are the artificial limits fixed by the sampling of this volume.

Considering waves that propagate along one direction in the plane, say x, the displacement field in the element domain can be expressed in a discrete basis of shape functions $N_k(y,z)$, and the nodal unknown displacements, (U_{xk}, U_{yk}, U_{zk}), in the x_1, x_2 and x_3 directions write:

$$\mathbf{u}(x,y,z,t) = \begin{pmatrix} \sum_{k=1}^{n} N_k(y,z) U_{xk} \\ \sum_{k=1}^{n} N_k(y,z) U_{yk} \\ \sum_{k=1}^{n} N_k(y,z) U_{zk} \end{pmatrix} \exp(\mathrm{i}(\omega t - kx))$$

This specific displacement formulation states that the physics of wave propagation is used to support the solution in the x-direction, while the form of the displacement in the other in-plane direction is postulated by the chosen shape functions. Within the volume of material, the displacement functions can be further detailed in order to account for inner specific

constitutive-materials arrangement.

The propagative assumption can also be applied to the second in-plane direction. However, the convergence and the completeness of the solution can then be questioned, since it has to be assumed that a plane-wave basis is sufficient to describe the vibrational behaviour.

3.3.2 SAFE for cylindrical shells

The SAFE technique has also been applied to a cylindrical pipe [84, 78]. If the cylinder's axis is parallel to the z-axis, the variation of the harmonic modes are represented theoretically in both the circumferential (θ) and the axial directions (z); the displacement field for the harmonic wave modes can be written as $\mathbf{q}(r,\theta,z,t) = \mathbf{q}(r)\exp(\mathrm{i}(\omega t - kz - n\theta))$, where ($n \in \mathbb{Z}$). Only the radial dimension (r) of the pipe needs to be discretised in that case.

3.4 Wave-finite element

The wave finite element method (WFE) couples the finite elements method to the periodic structure theory to compute the free propagating waves in a given waveguide. The typical results include the wavenumber, attenuation coefficient and deformation shape of the wave. It was introduced with Mead's work [80] and Houillon's PhD thesis [48], who first proposed an implementation of the method using matrices assembled with standard FE software.

The base principle of WFE is to model a single unit cell of the periodic structure, and assume a linear relationship between the displacements of opposite sides in the considered propagation direction. We consider here only homogeneous waveguides, meaning that any periodicity can be used. The choice of the unit cell's size must find a compromise between numerical accuracy (the higher the frequency, the smaller the wavelength, hence the smaller the unit cell's size) and matrix conditioning (the mass matrix's coefficients are proportional to the size, while stiffness is constant, leading to poor conditioning in calculation the dynamic stiffness matrix $\mathbf{D} = \mathbf{K} - \omega^2\mathbf{M}$ in the low frequency range)

3.4.1 Wave finite elements for 1D waveguides

For a 1D waveguide, the unit cell is a slice of the waveguide, with a thickness d. We write the displacement and force vectors applied to the faces of the unit cell as $\mathbf{u} = (\mathbf{u_L}\mathbf{u_r})^{\mathrm{T}}$ and $\mathbf{F} = (\mathbf{F_L}\mathbf{F_r})^{\mathrm{T}}$ respectively, so that the equation of dynamics reads:

$$\begin{pmatrix} \mathbf{D_{LL}} & \mathbf{D_{LR}} \\ \mathbf{D_{RL}} & \mathbf{D_{RR}} \end{pmatrix} \begin{pmatrix} \mathbf{u_L} \\ \mathbf{u_R} \end{pmatrix} = \begin{pmatrix} \mathbf{F_L} \\ \mathbf{F_R} \end{pmatrix} \tag{1.5}$$

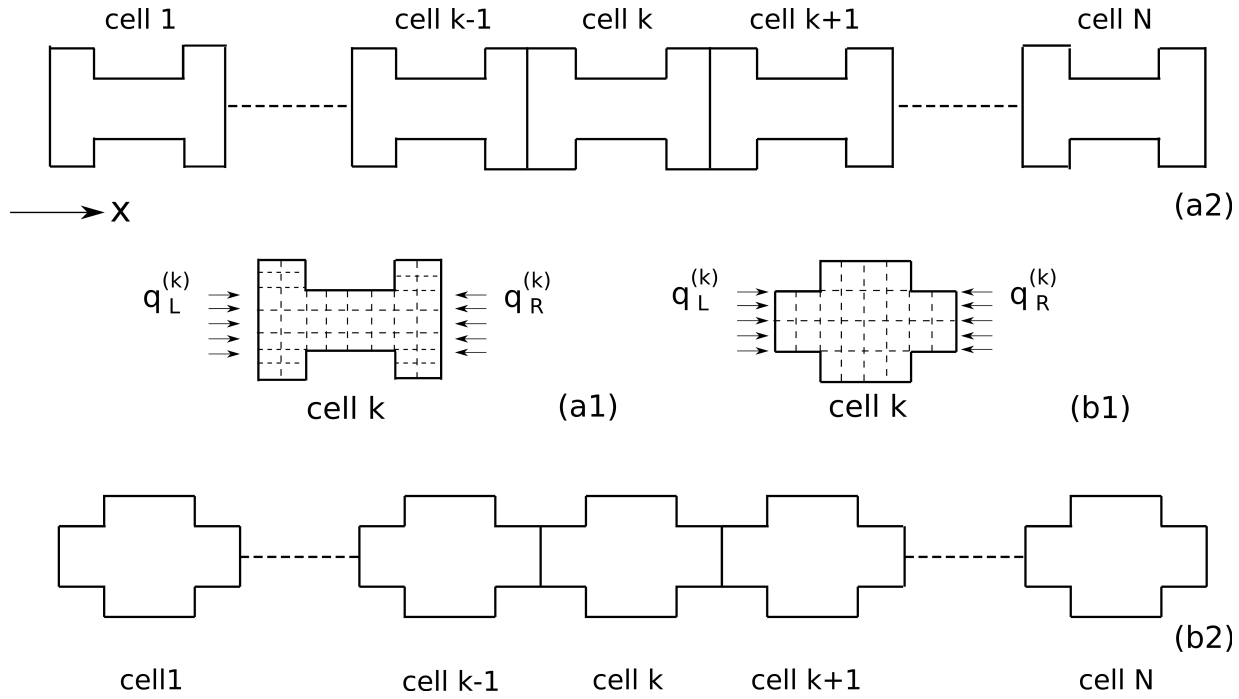

Figure 1.3 – Example of a periodic monodimensional waveguide [120].

where $\mathbf{D}$ is the dynamic stiffness matrix:

$$\mathbf{D} = \mathbf{K}(1 + \mathrm{i}\eta) - \omega^2\mathbf{M} \tag{1.6}$$

The Floquet-Bloch theorem states that the displacement on the right face is proportional to the displacement on the left one, with a complex factor λ, called the propagation constant, hence:

$$\begin{pmatrix} \mathbf{u_R} \\ \mathbf{F_R} \end{pmatrix} = \lambda \begin{pmatrix} \mathbf{I} & 0 \\ 0 & -\mathbf{I} \end{pmatrix} \begin{pmatrix} \mathbf{u_L} \\ \mathbf{F_L} \end{pmatrix}. \tag{1.7}$$

Injecting this in equation 1.5 leads to the quadratic eigenvalue problem

$$(\lambda^2\mathbf{D_{RL}} + \lambda(\mathbf{D_{RR}} + \mathbf{D_{LL}}) + \mathbf{D_{LR}})\mathbf{u_L} = 0, \tag{1.8}$$

which can be solved numerically. The eigenvalues λ are related to the wavenumber through

$$\lambda = \exp(\mathrm{i}kd), \tag{1.9}$$

hence the complex wavenumber k can be computed with a complex logarithm. The real part of k is related to the wavelength, and the imaginary part to the attenuation of the wave as it propagates through the structure. Due to the discretisation of the problem, there are as

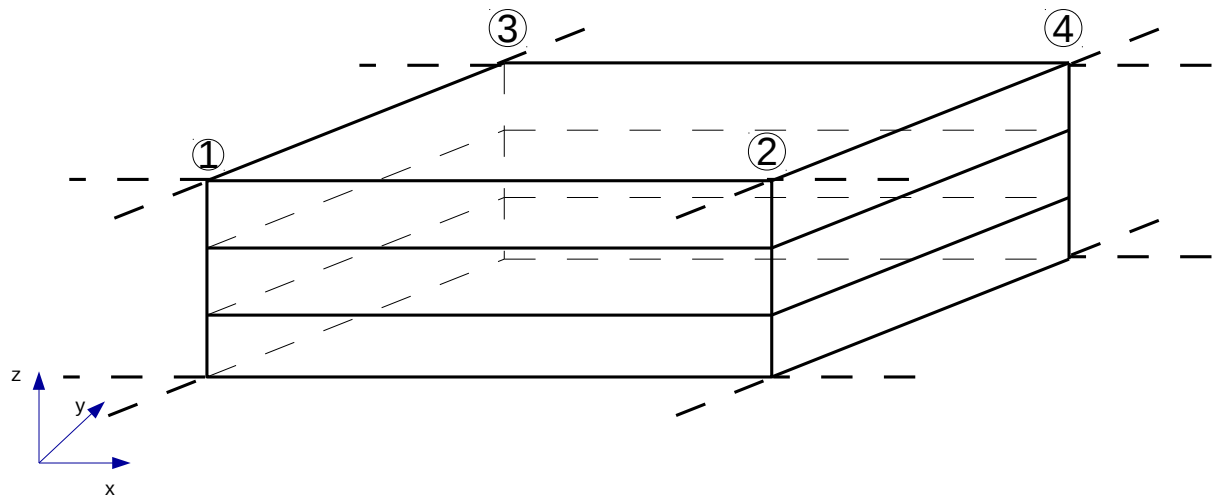

Figure 1.4 – Finite element discretisation of a 2D unit cell.

many solutions to the eigenproblem of equation 1.8 as there are degrees of freedom in one section. However, most of the solutions are purely numerical and do not propagate. A filter must be applied to select only the physical solutions. This is usually done with a criterion on the ratio between the real and imaginary parts of k :

$$\mathrm{Im}k < \varepsilon \mathrm{Re}k. \tag{1.10}$$

The criterion ε has to be tuned according to the considered structure. For composite or damped structures, it is usually taken around unity.

3.4.2 Wave finite elements for 2D waveguides

In the case of a 2D waveguide (ie. a plate or shell) the structure is decomposed in rectangular cells in both directions.

Displacement and force vectors are written so that DOFs relative to the same segment are consecutive. We then have $\mathbf{u} = (\mathbf{u_1}\ \mathbf{u_2}\ \mathbf{u_3}\ \mathbf{u_4})^{\mathrm{T}}$ and the same for $\mathbf{F}$. Dynamics equation in frequency domain writes:

$$\begin{pmatrix} \mathbf{D_{11}} & \mathbf{D_{12}} & \mathbf{D_{13}} & \mathbf{D_{14}} \\ \mathbf{D_{21}} & \mathbf{D_{22}} & \mathbf{D_{23}} & \mathbf{D_{24}} \\ \mathbf{D_{31}} & \mathbf{D_{32}} & \mathbf{D_{33}} & \mathbf{D_{34}} \\ \mathbf{D_{41}} & \mathbf{D_{42}} & \mathbf{D_{43}} & \mathbf{D_{44}} \end{pmatrix} \begin{pmatrix} \mathbf{u_1} \\ \mathbf{u_2} \\ \mathbf{u_3} \\ \mathbf{u_4} \end{pmatrix} = \begin{pmatrix} \mathbf{f_1} \\ \mathbf{f_2} \\ \mathbf{f_3} \\ \mathbf{f_4} \end{pmatrix} \tag{1.11}$$

The next step is to postulate a periodic behaviour of the cell, that is, there exist complex constants Λ_x and Λ_y so that the three following relations hold:

$$\mathbf{u_2} = \Lambda_x \mathbf{u_1} \tag{1.12}$$

$$\mathbf{u_3} = \Lambda_y \mathbf{u_1} \tag{1.13}$$

$$\mathbf{u_4} = \Lambda_x \Lambda_y \mathbf{u_1} \tag{1.14}$$

Constants Λ_x and Λ_y are called *propagation constants* and are related to the wavenumber components along x and y axis by

$$\Lambda_x = \exp(\mathrm{i}k_x L_x) \qquad \text{and} \qquad \Lambda_y = \exp(\mathrm{i}k_y L_y). \tag{1.15}$$

The system in equation 1.14 can be rewritten in a matrix form:

$$\mathbf{u} = \begin{pmatrix} \mathbf{I} & \Lambda_x \mathbf{I} & \Lambda_y \mathbf{I} & \Lambda_x \Lambda_y \mathbf{I} \end{pmatrix}^{\mathrm{T}} \mathbf{u_1}. \tag{1.16}$$

Without external loads, the force equilibrium in the cell can be written as:

$$\begin{pmatrix} \mathbf{I} & \Lambda_x^{-1} \mathbf{I} & \Lambda_y^{-1} \mathbf{I} & \Lambda_x^{-1} \Lambda_y^{-1} \mathbf{I} \end{pmatrix} \mathbf{f} = 0, \tag{1.17}$$

which leads the system in equation 1.11 to be written:

$$\begin{pmatrix} \mathbf{I} & \Lambda_x^{-1} \mathbf{I} & \Lambda_y^{-1} \mathbf{I} & \Lambda_x^{-1} \Lambda_y^{-1} \mathbf{I} \end{pmatrix} \mathbf{D} \begin{pmatrix} \mathbf{I} & \Lambda_x \mathbf{I} & \Lambda_y \mathbf{I} & \Lambda_x \Lambda_y \mathbf{I} \end{pmatrix}^{\mathrm{T}} \mathbf{u_1} = 0. \tag{1.18}$$

This equation can be factored in terms of products of Λ_x, Λ_y, 1 and their inverse, leading after multiplication by $\Lambda_x \Lambda_y$ to a quadratic eigenvalue problem with unknowns Λ_x and Λ_y, which can be solved in the case where one of them is fixed. If we assign a fixed value to Λ_y, the matrix equation writes:

$$\left(\mathbf{A_2} \Lambda_x^2 + \mathbf{A_1} \Lambda_x + \mathbf{A_0} \right) \mathbf{u_1} = 0, \tag{1.19}$$

where:

$$\mathbf{A_2} = \mathbf{D_{14}} \Lambda_y^2 + (\mathbf{D_{12}} + \mathbf{D_{34}}) \Lambda_y + \mathbf{D_{32}}, \tag{1.20}$$

$$\mathbf{A_1} = (\mathbf{D_{13}} + \mathbf{D_{24}}) \Lambda_y^2 + (\mathbf{D_{11}} + \mathbf{D_{22}} + \mathbf{D_{33}} + \mathbf{D_{44}}) \Lambda_y + \mathbf{D_{31}} + \mathbf{D_{42}}, \tag{1.21}$$

$$\mathbf{A_0} = \mathbf{D_{23}} \Lambda_y^2 + (\mathbf{D_{21}} + \mathbf{D_{43}}) \Lambda_y + \mathbf{D_{41}}. \tag{1.22}$$

Solutions to equation 1.19 can be found with the help of a polynomial eigenvalue solver

(for example the Matlab function `polyeig`). The basic idea for solving this kind of polynomial problem is to introduce the auxiliary variable $\mathbf{z} = \Lambda_x \mathbf{u_1}$ and write the problem in companion form, which can be solved as a $2n \times 2n$ linear eigenproblem:

$$\Lambda_x \begin{pmatrix} \mathbf{A_1} & \mathbf{A_2} \\ \mathbf{I} & \mathbf{0} \end{pmatrix} \begin{pmatrix} \mathbf{u_1} \\ \mathbf{z} \end{pmatrix} = \begin{pmatrix} \mathbf{A_0} & \mathbf{0} \\ \mathbf{0} & \mathbf{I} \end{pmatrix} \begin{pmatrix} \mathbf{u_1} \\ \mathbf{z} \end{pmatrix}. \tag{1.23}$$

Solutions to this eigenproblem give the existing wavenumbers for a given frequency. These wavenumbers are complex, and the imaginary part represents the attenuation coefficient. There are $2n$ solutions of the eigenproblem, where n is the number of DOFs of one segment. For a given frequency, only a few of these solutions are propagating waves, and therefore contribute significantly to the response of the waveguide to local excitation. Non-propagating waves are sorted out with the same criterion as in equation 1.10. The propagating solutions then have to be matched so as to provide dispersion curves along frequencies, according to a matching algorithm proposed in [50]. This consists in comparing the eigenvectors with a Wave assurance criterion (WAC), similar to the Modal assurance criterion (MAC), and matching the ones that have the highest WAC together. The WAC criterion is defined for two vectors $\mathbf{u}$ and $\mathbf{v}$ as

$$\mathrm{WAC}(\mathbf{u}, \mathbf{v}) = \frac{(\mathbf{u}^{\mathrm{T}}\mathbf{v})^2}{\mathbf{u}^2\mathbf{v}^2}. \tag{1.24}$$

The interest of the WFE method is that it is rather computationally cheap compared to a full FEM model, and that it allows to compute more complicated waves than the first-order flexural wave, like Lamb waves for single-layer plates, core and skin waves for sandwich-type structures, or more complicated wave-types for multilayered structures.

3.4.3 Extension of the 2D case for curved shells

An extension to curved shells has been proposed by Manconi et al. [76] for shell finite elements. Chronopoulos et al. [20] proposed an extension with solid finite elements, which will be presented here.

The principle is to compute the mass and stiffness matrices of the unit cell, and apply a matrix transform to account for the fact that the structure is curved. Provided the degrees of freedom of the displacement vector are grouped per node, the transformation matrix will

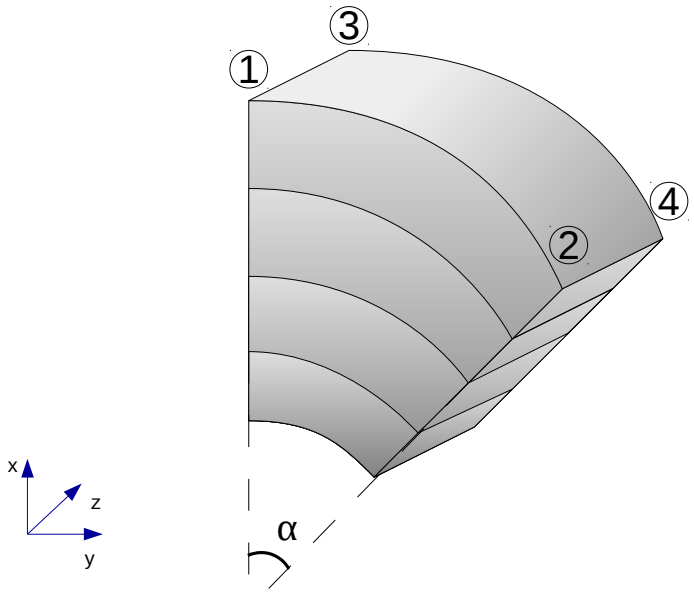

Figure 1.5 – A thick composite cylindrical shell

be as follows for a curvature around the z-axis.

$$\mathbf{C} = \begin{pmatrix} \mathbf{I} & & & \\ & \mathbf{R} & & \\ & & \mathbf{I} & \\ & & & \mathbf{R} \end{pmatrix}, \tag{1.25}$$

where $\mathbf{I}$ is the identity matrix and $\mathbf{R}$ is a block diagonal matrix, where all blocks are identical and equal to

$$\begin{pmatrix} \cos(\alpha) & \sin(\alpha) & 0 \\ -\sin(\alpha) & \cos(\alpha) & 0 \\ 0 & 0 & 1 \end{pmatrix}.$$

The angle $\alpha = 2\arcsin(\frac{L_y}{2R})$ is the angle between the sections of the curved unit cell.

For a cylinder of axis x, the orthoradial wavenumber k_y can only take discrete values, namely $k_y = \frac{n}{R}$, where n is a non-negative integer. The case $n = 0$ corresponds to breathing modes, where the cylinder's section remains circular and keeps the same axis as the undeformed shape. When $n = 1$ the section remains also circular, but with an axis parallel to the x-axis, and when $n \geqslant 2$, the axis is unchanged, but the shape is deformed. The dispersion curves must be calculated with a loop on the integer parameter n.

4 Poroelastic material modelling

Poroelastic materials are composed of a solid matrix, called the skeleton, containing interconnected pores filled with a fluid. For our applications, we will only consider air as the saturating fluid. As a diphasic system, poroelastic are characterized by the parameters of the solid and fluid phases and parameters describing the coupling of the two. These materials have been studied since the 1950's and Biot's article [13].

Wave propagation in porous materials is described by Biot and Allard's theory [3]. A poroelastic material is considered as the superposition of continuous solid and fluid phases occupying the same space. These two phases are coupled through viscous and thermal effects.

Besides classical elastic parameters like Young modulus E, Poisson ratio ν, density ρ and hysteretic damping factor η, poroelastic materials are characterized by 5 additional parameters in Johnson-Champoux-Allard model [3]:

- Porosity, denoted ϕ_0, is the volume fraction of fluid within the material. For typical polymer foams used for acoustic applications, it ranges between 0.9 and 0.98.

- Tortuosity, denoted α_∞ is the average ratio of the distance between two points along the pores network to the euclidean distance between these points. It is therefore always greater than 1.

- Flow resistivity, denoted σ, has units of N.s.m^{-4}. It corresponds to the ratio of pressure difference per unit length to flow speed: $\sigma = \frac{p_1 - p_2}{lv}$

- The viscous characteristic length Λ_{visc} characterizes the viscous energy exchanges between the fluid and solid phases. It corresponds to the smallest size of a pore in the medium.

- The thermal characteristic length Λ_{therm} characterizes the thermal energy exchanges. it corresponds to the largest size of a pore. The thermal length is always greater than the viscous length, usually by a factor of about 2.

The homogenized model has degrees of freedom for the fluid and solid phases at each point of the poroelastic domain. Several formulations have been proposed for the constitutive equations, taking into account displacement of the solid phase and either the pressure in the fluid phase [5], the fluid displacement [6], or the total displacement [3].

The first formulation leads to 4 degrees of freedom per node (3 displacements and 1 pressure), while the other two need 6 (3 displacements for the solid, and 3 for the fluid).

4.1 U-u formulation

The equilibrium equations in terms of displacements writes in absence of volume forces:

$$\begin{cases} \text{Div}\left(\boldsymbol{\sigma}^s(\mathbf{u}^s,\mathbf{u}^f)\right)+\omega^2\left(\widetilde{\rho}_{11}\mathbf{u}^s+\widetilde{\rho}_{12}\mathbf{u}^f\right)=0 \\ \text{Div}\left(\boldsymbol{\sigma}^f(\mathbf{u}^s,\mathbf{u}^f)\right)+\omega^2\left(\widetilde{\rho}_{12}\mathbf{u}^s+\widetilde{\rho}_{22}\mathbf{u}^f\right)=0, \end{cases} \tag{1.26}$$

where $\mathbf{u}^s$ is the solid displacement, $\mathbf{u}^f$ the fluid displacement, $\boldsymbol{\sigma}^s$ and $\boldsymbol{\sigma}^f$ the stress tensors of the solid and fluid phases respectively. Equivalent densities $\widetilde{\rho}_{11}$, $\widetilde{\rho}_{12}$, and $\widetilde{\rho}_{22}$, are complex and frequency-dependent functions of material parameters.

The equivalent densities are expressed with the Johnson-Champoux-Allard model as

$$\widetilde{\rho}_{11}=\phi_0\rho_0(\alpha_\infty-1)-\mathrm{i}\sigma\phi_0^2\frac{G(\omega)}{\omega} \tag{1.27}$$

$$\widetilde{\rho}_{12}=-\phi_0\rho_0(\alpha_\infty-1)+\mathrm{i}\sigma\phi_0^2\frac{G(\omega)}{\omega} \tag{1.28}$$

$$\widetilde{\rho}_{22}=\phi_0\rho_0\alpha_\infty-\mathrm{i}\sigma\phi_0^2\frac{G(\omega)}{\omega} \tag{1.29}$$

where

$$G(\omega)=\sqrt{1+\frac{4\mathrm{i}\omega\alpha_\infty^2\rho_0\mathrm{Pr}}{\sigma\Lambda_{visc}\phi_0^2}}. \tag{1.30}$$

In the latter equation, Pr is the Prandtl number of the interstitial fluid.

4.2 U-p formulation

The displacement-pressure formulation is introduced in a paper by Atalla et al. [5]. The idea is to describe the fluid phase's behaviour with pressure variation as the only variable. The stress tensor in the fluid is written as

$$\boldsymbol{\sigma}_f=-\phi_0\nabla p \tag{1.31}$$

which allows to express the fluid displacement as a function of pressure and solid displacement with the second equation of 1.26. The dependence of the solid phase stress tensor on the fluid displacement is removed by introducing the *in vacuo* stress tensor $\hat{\sigma}_s$, corresponding to the stress tensor in the skeleton in the absence of fluid. This latter tensor is defined as

$$\hat{\boldsymbol{\sigma}}_s=\boldsymbol{\sigma}_s+\phi_0\frac{\widetilde{Q}}{\widetilde{R}}p\mathbf{I}, \tag{1.32}$$

where $\mathbf{I}$ is the identity matrix, $\widetilde{Q}$ and $\widetilde{R}$ are coefficients related to the porosity and the bulk moduli of the skeleton material K_s, the homogenized skeleton *in vacuo* K_b, and the fluid phase K_f:

$$\widetilde{Q} = \frac{(1-\phi_0-K_b/Ks)\,\phi_0 K_s}{1-\phi_0-K_b/Ks+\phi_0 Ks/\widetilde{K}_f}, \tag{1.33}$$

$$\widetilde{R} = \frac{\phi_0^2 K_s}{1-\phi_0-K_b/Ks+\phi_0 Ks/\widetilde{K}_f}. \tag{1.34}$$

For high-porosity materials commonly used for acoustic treatments, the bulk modulus of the skeleton material is very high compared to that of the skeleton, $K_s \gg K_b$, hence:

$$\frac{Q}{R} = \frac{1-\phi_0}{\phi_0}. \tag{1.35}$$

The constitutive equations then write:

$$\begin{cases} \mathrm{Div}\left(\hat{\boldsymbol{\sigma}}^s(\mathbf{u}_s)\right) + \widetilde{\rho}\omega^2\mathbf{u}_s + \widetilde{\gamma}\nabla p = 0 \\ \Delta p + \dfrac{\widetilde{\rho}_{22}}{\widetilde{R}}\omega^2 p + \dfrac{\widetilde{\rho}_{22}}{\phi_0^2}\widetilde{\gamma}\,\mathrm{div}(\mathbf{u}_s) = 0 \end{cases}, \tag{1.36}$$

where the coupling term is

$$\widetilde{\gamma} = \phi_0\left(\frac{\widetilde{\rho}_{12}}{\widetilde{\rho}_{22}} - \frac{\widetilde{Q}}{\widetilde{R}}\right), \tag{1.37}$$

and the equivalent complex density is

$$\widetilde{\rho} = \widetilde{\rho}_{11} - \frac{\widetilde{\rho}_{12}^2}{\widetilde{\rho}_{22}} \tag{1.38}$$

A variational problem can be derived from equations 1.26 and 1.36, which can be implemented in a finite element code [3]. WFE formulations have been proposed by Q. Serra [105] in order to compute wave propagation in structures comprising passive noise treatment.

5 Vibroacoustic models

5.1 The transfer matrix method

This method has first been proposed by Brouard et al.[14] and is extensively described in chapter 11 of [3] in the case where all layers are isotropic. It allows to model multilayer

systems comprising thick elastic solids and full Biot-Allard poroelastic materials, in which the mechanical properties of the foam plays a non-negligible role. The principle is to write a transfer matrix relationship between the state variables of each layer on each side of the layer, then couple these equations using boundary conditions that are characteristic of each interface between layers.

5.1.1 The simplified transfer matrix method

A simplified version of the TMM, which will be called sTMM in the following, was presented by Hu [49] for multilayer structures alternating plates and acoustic fluid layers. Poroelastic materials can be modelled with equivalent fluids. The acoustic behaviour of the structure can be represented with only the fluid pressure p and normal velocity v as state variables. These two variables are defined in each point in the fluid layers, and on each side of the solid layers. Each layer can be represented by a 2×2 matrix linking the state variables on one side to those on the other side, and a global transfer matrix can be obtained by multiplying all these matrices together. The transfer equation then reads:

$$\begin{pmatrix} p_L \\ v_L \end{pmatrix} = \begin{pmatrix} T_{11} & T_{12} \\ T_{21} & T_{22} \end{pmatrix} \begin{pmatrix} p_R \\ v_R \end{pmatrix}, \tag{1.39}$$

where indices R and L stand for right and left sides of the structure. Waves on each side can be decomposed in positive- and negative-going waves, which can be written :

$$p_R = p_R^+ + p_R^- \qquad \text{and} \qquad p_L = p_L^+ + p_l^-. \tag{1.40}$$

According to the pressure-displacement relation in the fluid, the normal velocities are:

$$v_R = Y_0(p_R^+ - p_R^-) \qquad \text{and} \qquad v_L = Y_0(p_L^+ - p_l^-), \tag{1.41}$$

where $Y_0 = \cos\theta/\rho_0 c_0$ is the characteristic admittance of the surrounding fluid.

This leads to rewriting equation 1.39 as

$$\begin{cases} p_L^+ + p_L^- = T_{11}(p_R^+ + p_R^-) + Y_0 T_{12}(p_R^+ - p_R^-) \\ p_L^+ - p_L^- = \dfrac{T_{21}}{Y_0}(p_R^+ + p_R^-) + T_{22}(p_R^+ - p_R^-) \end{cases}. \tag{1.42}$$

We will be studying transmission of a plane wave incident from the left side, whose interaction with the structure creates a reflected wave into the left side, and a transmitted wave into the right side. In that case, no negative-going wave will propagate in the right

side. The acoustic transparency is defined as the ratio of transmitted to incident acoustic intensities, which reduces to

$$\tau = \left| \frac{p_R^+}{p_L^+} \right|^2 \tag{1.43}$$

in the case of identical fluids on each side of the structure. Solving the system in equation 1.42, we get

$$\tau(\omega, \theta) = \frac{1}{4} \left| T_{11} + T_{12} Y_0 + \frac{T_{21}}{Y_0} + T_{22} \right|^2 . \tag{1.44}$$

The transmission loss for a plane wave is then defined as

$$\mathrm{TL} = -10 \log_{10} \tau. \tag{1.45}$$

The diffuse field transmission loss can be obtained by performing a weighted average of the transparency over an angular range $[\theta_{\min}, \theta_{\max}]$. This writes

$$\tau_d(\omega) = \frac{\int_{\theta_{\min}}^{\theta_{\max}} \tau(\omega, \theta) \sin\theta \cos\theta \mathrm{d}\theta}{\int_{\theta_{\min}}^{\theta_{\max}} \sin\theta \cos\theta \mathrm{d}\theta}. \tag{1.46}$$

In the case where the full range [0;π/2] is retained, we obtain:

$$\tau_d(\omega) = 2 \int_0^{\pi/2} \tau(\omega, \theta) \sin\theta \cos\theta \mathrm{d}\theta. \tag{1.47}$$

The diffuse field transmission loss is then defined as

$$\mathrm{TL}_d = -10 \log_{10} \tau_d. \tag{1.48}$$

The transfer matrices for plates and a limp poroelastic material are derived in the following subsections. Due to the forced nature of the excitation, the transverse wavenumber $k_t = \frac{\omega}{c_0} \sin\theta$ and the pulsation of the incident wave ω are conserved across the whole system.

5.1.2 Transfer matrix of plate-like structures

The transfer matrix of a general plate can be obtained from its constitutive equation in presence of forced loads. When excited by a plane wave with frequency ω, the plate will vibrate and radiate one acoustic wave on each side, respectively reflected and transmitted. The constitutive equation can be put under the general form

$$Zv = p, \tag{1.49}$$

where Z is the impedance of the plate. It is a linear operator linking the normal speed v and the imposed pressure on the plate p. The sound field on the left side of the plate is p_L and on the right side it is p_R, hence $p = p_L - p_R$

The continuity of normal velocity between the surrounding fluids and the plate imposes $v_L = v_R$, hence

$$\begin{pmatrix} p_L \\ v_L \end{pmatrix} = \begin{pmatrix} 1 & Z \\ 0 & 1 \end{pmatrix} \begin{pmatrix} p_R \\ v_R \end{pmatrix} \tag{1.50}$$

Isotropic plate Infinite isotropic plates can be defined by a single geometrical parameter, their thickness h, and four material parameters, namely the Young modulus E, the Poisson ratio ν, density ρ and hysteretic damping η. The governing equation for thin isotropic plate, in the frequency domain is:

$$D\nabla^4 w - \omega^2 m w = p, \tag{1.51}$$

where $D = \dfrac{Eh^3}{12(1-\nu^2)}(1+\mathrm{i}\eta)$ is the bending stiffness of the plate and $m = \rho h$ is the surface density. As all directions in the plane are equivalent, there is no dependency on the direction φ, so $\nabla = \frac{\partial}{\partial x} = -\mathrm{i}k = -\mathrm{i}\frac{\omega}{c_0}\sin\theta$. The equation reduces to :

$$\left(D\left(\frac{\omega}{c_0}\right)^4 \sin^4\theta - \omega^2 m \right) w = p, \tag{1.52}$$

and the structural impedance is then:

$$Z(\omega,\theta) = \mathrm{i}\omega m \left(1 - \omega^2 \frac{D}{c_0^4 m}\sin^4\theta\right). \tag{1.53}$$

Orthotropic plate An orthotropic plate is characterised by different properties in the x and y directions. The forced wave equation then becomes

$$D_x \frac{\partial^4 w}{\partial x^4} + 2D_{xy}\frac{\partial^4 w}{\partial x^2 \partial y^2} + D_y \frac{\partial^4 w}{\partial y^4} - m\omega^2 w = p, \tag{1.54}$$

where the bending stiffness along each axis is

$$\begin{aligned} D_x =& \frac{E_x h^3}{12(1-\frac{E_y}{E_x}\nu_{xy}^2)}(1+\mathrm{i}\eta) \\ D_y =& \frac{E_y h^3}{12(1-\frac{E_y}{E_x}\nu_{xy}^2)}(1+i\eta) \\ D_{xy} =& \frac{h^3}{12(1-\frac{E_y}{E_x}\nu_{xy}^2)}\left(E_y\nu_{xy}+2G_{xy}\right)(1+\mathrm{i}\eta). \end{aligned}$$

Writing $\frac{\partial}{\partial x} = -\mathrm{i}k_x = -\mathrm{i}k\cos\varphi$ and $\frac{\partial}{\partial y} = -\mathrm{i}k_y = -\mathrm{i}k\sin\varphi$, the system reduces to the same form as in the isotropic case, with a heading-dependent impedance. The heading dependent bending stiffness is

$$D(\varphi) = D_x\cos^4\varphi + 2D_{xy}\sin^2\varphi\cos^2\varphi + D_y\sin^4\varphi, \tag{1.55}$$

and the structure's impedance is consequently:

$$Z(\omega,\theta,\varphi) = -\omega^2 m\left(1-\omega^2\frac{D(\varphi)}{c_0^4 m}\sin^4\theta\right). \tag{1.56}$$

Isotropic sandwich plate The constitutive equation for the bending of a sandwich beam is given by Mead [81], with five main parameters, namely skin bending stiffness D_t, overall bending stiffness B, damping η, surface mass m and a shear parameter g. An adaptation for a sandwich plate has been proposed by [83], which reads:

$$D_t(1+\mathrm{i}\eta)\nabla^6 w + g(D_t+B)(1+\mathrm{i}\eta)\nabla^4 w - m\omega^2\nabla^2 w - mg(1-\nu^2)\omega^2 w = (\nabla^2+g)p, \tag{1.57}$$

where $w = v/\mathrm{i}\omega$ is the normal displacement of the plate. In the considered frame where a forced wave is imposed on the plate with a wavenumber $k_t = \frac{\omega}{c}\sin\theta$, the spatial derivative operator ∇ can be replaced by $-\mathrm{i}k_t$. This leads to the following expression of the impedance

$$Z(\omega,\theta) = \frac{D_t k^6 + g(D_t+B)k^4 - m\omega^2 k^2 - mg\omega^2(1-\nu^2)}{\mathrm{i}\omega(k^2+g)}. \tag{1.58}$$

For sandwiches made of isotropic materials and identical skins, the skin bending stiffness is $D_t = \frac{Eh_s^3}{6(1-\nu^2)}$ and the overall bending stiffness is $B = Eh_c^2 h_s(1+\frac{h_s}{h_c})^2/2$. The shear parameter is given by $g = \frac{2G}{Eh_s h_c}$, where G is the shear modulus of the core. This expression is equivalent to that of a thin plate if the shear modulus is infinite.

5.1.3 Limp poroelastic model

Poroelastic materials can be modelled with the Biot-Allard model, taking into account wave propagation in the fluid and solid phases. However, if the material is especially limp, like fibreglass, it can be possible to neglect the solid part and model it as an equivalent fluid with complex and frequency dependent parameters. The wave propagation equation in the porous layer reduces to one scalar equation [3]

$$\Delta p + \frac{\widetilde{\rho}_{limp}}{\widetilde{K}_{eq}}\omega^2 p = 0, \tag{1.59}$$

where $\widetilde{\rho}_{limp}$ is the equivalent density and $\widetilde{K}_{eq}$ the equivalent bulk modulus of the fluid representing the porous material. These two quantities are complex and frequency dependent. Their expression is given in chapter 5 of reference [3]:

$$\widetilde{K}_{eq} = \frac{\gamma P_0}{\varphi\left(\gamma - \frac{\gamma-1}{K}\right)} \tag{1.60}$$

$$\tag{1.61}$$

$$\widetilde{\rho}_{limp} = -\frac{\rho_0^2 - \frac{1}{\varphi^2}(\rho_1 + \varphi\rho_0)(\frac{\mathrm{i}B}{\omega} + \alpha_\infty\varphi\rho_0)}{\rho_1 - 2\rho_0 + \varphi\rho_0 + \frac{1}{\varphi^2}(\frac{\mathrm{i}B}{\omega} + \alpha_\infty\varphi\rho_0)} \tag{1.62}$$

where the coefficients K and B can be expressed as

$$K = 1 + \frac{8\mu_0}{\mathrm{i}\omega\mathrm{Pr}\Lambda_{therm}^2\rho_0}\sqrt{1 + \mathrm{i}\omega\frac{\mathrm{Pr}\Lambda_{therm}^2\rho_0}{16\mu_0}} \tag{1.63}$$

$$\tag{1.64}$$

$$B = \sigma\varphi^2\sqrt{1 + 4\mathrm{i}\omega\frac{\alpha_\infty^2\mu_0\rho_0}{(\sigma\Lambda_{visc}\varphi)^2}}. \tag{1.65}$$

The parameters Pr, μ_0, P_0 and ρ_0 are respectively the Prandtl number, the dynamic viscosity, the bulk modulus and the density of air, whose reference values at 20°C are given in Table 1.1.

The porous material is described by six characteristic parameters, namely the porosity φ, the flow resistivity σ, the static tortuosity α_∞, the viscous and thermal dissipation characteristic lengths Λ_{visc} and Λ_{therm}, and the *in vacuo* skeleton density ρ_1.

The complex wavenumber of the wave propagating in the equivalent fluid is, according to

Parameter	description	unit	value
Pr	Prandtl number	-	0.71
μ_0	dynamic viscosity	Pa.s	$1.845 \cdot 10^{-5}$
ρ_0	density	kg.m^{-3}	1.21
P_0	reference pressure	Pa	101325

Table 1.1 – Reference parameters for air at 20^oC.

equation 1.59:

$$k = \omega \sqrt{\frac{\widetilde{\rho}_{limp}}{\widetilde{K}_{eq}}}, \tag{1.66}$$

and the normal component is $k_n = \sqrt{k^2 - k_t^2}$.

The transfer equation between two points inside the equivalent fluid separated by a distance h then writes:

$$\begin{pmatrix} p_L \\ v_L \end{pmatrix} = \begin{pmatrix} \cos(k_n h) & \mathrm{i}\omega \dfrac{\widetilde{\rho}_{limp}}{k_n} \sin(k_n h) \\ \mathrm{i} \dfrac{k_n}{\omega \widetilde{\rho}_{limp}} \sin(k_n h) & \cos(k_n h) \end{pmatrix} \begin{pmatrix} p_R \\ v_R \end{pmatrix}. \tag{1.67}$$

The previous equation is valid for the wave inside the fluid. When coupled to another medium, the continuity of normal speed should account for the porosity of the material. If the other material is a plate or the surrounding air, this conditions reads

$$\varphi v_{poro} = v_m, \tag{1.68}$$

where v_m is the normal velocity inside the other medium. The complete transfer matrix of the porous layer then writes:

$$\mathbf{T}_{poro} = \begin{pmatrix} 1 & 0 \\ 0 & \varphi \end{pmatrix} \mathbf{T}_p \begin{pmatrix} 1 & 0 \\ 0 & \frac{1}{\varphi} \end{pmatrix}. \tag{1.69}$$

The matrices of each layer are then used to compute the transmission loss as per equations 1.44 to 1.48.

5.1.4 Transfer matrices for elastic and poroelastic layers

In the case where there are thick elastic layers or poroelastic materials which cannot be represented with equivalent fluid models, the sTMM described above is not sufficient, and

one has to resort to the full TMM.

Each system is modelled with a matrix linking the state variables on the left side to those on the right side:

$$\mathbf{v}_L^i = \mathbf{T}_i \mathbf{v}_R^i. \tag{1.70}$$

For a fluid or fluid-like layer, these variables are the normal particle velocity v_z and the acoustic pressure p and the transfer matrix has size 2×2 as in section 5.1.1. For an elastic solid layer, the presence of a shear wave in the layer induces the need to take into account the particle velocity in the transverse direction v_x as well as the normal velocity v_z. The dual quantities are then the shear stress σ_{xz} and the normal stress σ_{zz}. The transfer matrix has then a size 4×4. Finally, for a poroelastic layer, the 2 variables of the fluid and the 4 of the solid component have to be considered, leading to a 6×6 transfer matrix.

The coupling of two layers of the same nature is written simply by multiplying the transfer matrices. For layers of different natures, the coupling conditions write

$$\mathbf{B}_L^i \mathbf{v}_R^i = \mathbf{B}_R^i \mathbf{v}_L^{i+1} = \mathbf{B}_R^i \mathbf{T}_{i+1} \mathbf{v}_R^{i+1}, \tag{1.71}$$

for matrices $\mathbf{B}_L^i$ and $\mathbf{B}_R^i$ with appropriate sizes.

The system is then described by all state vectors at the rightmost points of every layer. For a system with n layers separating two acoustic media, this leads to the singular matrix equation

$$\begin{pmatrix} \mathbf{B}_L^0 & -\mathbf{B}_R^0 \mathbf{T}_1 & \mathbf{0} & & \\ \mathbf{0} & \mathbf{B}_L^2 & -\mathbf{B}_R^2 \mathbf{T}_2 & \mathbf{0} & \\ & \ddots & & & \\ \mathbf{0} & \cdots & \mathbf{B}_L^{n-1} & -\mathbf{B}_R^{n-1} \mathbf{T}_n & \mathbf{0} \\ \mathbf{0} & \cdots & \mathbf{B}_L^n & -\mathbf{B}_R^n & \end{pmatrix} \begin{pmatrix} \mathbf{v}_R^0 \\ \mathbf{v}_R^1 \\ \vdots \\ \mathbf{v}_R^n \\ \mathbf{v}_L^\infty \end{pmatrix} = \mathrm{Dv} = \mathbf{0}, \tag{1.72}$$

where $\mathbf{v}_R^0$ is the state vector of the fluid layer in the incident side and $\mathbf{v}_L^\infty$ the state vector on the transmission side. This matrix system is rectangular and has one equation less than unknowns. One way to compute the vibroacoustic indicators is to start with the impedance condition linking the state vector in the incident fluid layer:

$$\begin{pmatrix} 1 & -Z_s \end{pmatrix} \mathbf{v}_R^0 = 0. \tag{1.73}$$

Completing the matrix system with this equation leads to a square system, whose determinant has to be 0 for non-trivial solutions to exist. The surface impedance Z_s of the structure is therefore given by

$$Z_s = -\frac{\det \mathbf{D}_1}{\det \mathbf{D}_2}, \tag{1.74}$$

where $\det \mathbf{D}_k$ is the matrix of equation 1.72 where the k^{th} column has been removed. The reflection coefficient is then given by:

$$R = \frac{Z_s \cos\theta - Z_0}{Z_s \cos\theta + Z_0}, \tag{1.75}$$

where $Z_0 = \rho_0 c_0$ is the impedance of air. Knowing that, the transmission coefficient can be computed with the equation

$$\frac{p^0}{1+R} - \frac{p^\infty}{T} = 0, \tag{1.76}$$

where p^0 and p^∞ are the pressure components of state vectors $\mathbf{v}_R^0$ and $\mathbf{v}_L^\infty$ respectively. This leads to

$$T = -(1+R)\frac{\det \mathrm{D}_{N-1}}{\det \mathrm{D}_1}, \tag{1.77}$$

if N is the number of columns in matrix D. The transparency is then given by

$$\tau = |T|^2. \tag{1.78}$$

The transmission loss and diffuse field transmission loss are then obtained as in equations 1.45 and 1.48.

5.1.5 Radiation efficiency correction for finite plates correction

A correction for finite size effects in the TMM was first proposed by Villot et al. [114] and later enhanced by Ghinet and Atalla [39] and Rhazi and Atalla [98]. The acoustic transparency τ_∞ of the infinite multilayer is first computed, either with TMM or sTMM, then multiplied by a correction factor σ_R, so that the transparency of the actual structure for a plane wave with incidence θ and direction φ is:

$$\tau(\omega, \theta, \varphi) = \tau_\infty(\omega, \theta)\cos\theta\sigma_R(\omega, \theta, \varphi). \tag{1.79}$$

The correction factor is the radiation efficiency of the plate, and is obtained by evaluating the following integral:

$$\sigma_R = \mathrm{Re}\left[\frac{\mathrm{i}\omega L_y}{4\pi c_0}\int_0^2\int_0^2 (2-u)(2-v)K(u,v)F(u,v)\mathrm{d}u\mathrm{d}v\right], \tag{1.80}$$

where

$$F(u,v) = \exp\left(\frac{-\mathrm{i}k_t L_x}{2}\left(u\cos\varphi + \frac{v}{r}\sin\varphi\right)\right) \tag{1.81}$$

and

$$K(u,v) = \frac{\exp\left(\frac{-\mathrm{i}k_0 L_x}{2}\left(u^2+\frac{v^2}{r^2}\right)^{1/2}\right)}{\left(u^2+\frac{v^2}{r^2}\right)^{1/2}}. \tag{1.82}$$

In these equations, we have $r = L_x/L_y$, $k_0 = \omega/c_0$ is the free wavenumber in the fluid and $k_t = k_0 \sin\theta$ is the wavenumber trace component on the plate's surface.

Since the correction factor depends only on the plate's dimensions, and the numerical computation of the integral is time-consuming, it needs only be computed once for all values of φ,θ and ω that will be used in the analysis, and stored in a file used by every call to the model.

5.2 Statistical energy analysis

The Statistical Energy Analysis (SEA) method [69] has been developed since the 60's in order to model the high-frequency behaviour of vibrating systems. While the low frequency behaviour of elastic structures can be reliably calculated with deterministic models such as Finite Element models, the high frequency domain is characterized by high modal densities in the different parts of the structure, and high modal overlap, thus leading to a high computation cost due to fine discretisation. Even then, as high frequency response is more sensitive to local uncertainties in the model, a deterministic calculation would not be very robust. SEA models arose from these considerations, and aim at calculating a mean response in the sense of an ensemble average over a number of implementations of the studied structure.The basic idea of SEA is a thermal analogy, in which the power flow between two vibrating subsystems is proportional to the difference of internal energy level. These quantities are evaluated in frequency bands, usually octave or third-octave bands. The system to be studied is decomposed into subsystems with similar behaviours, and the coupling factors between each is evaluated.

It is often sought to decompose of the whole system into simple substructures whose mode shapes and eigenfrequencies can be determined analytically, such as rectangular plates, cylindrical shells or parallelepipedic cavities. An important assumption of SEA is that of *weak coupling*, which states that the coupling between the subsystems do not affect their mode shapes and eigenfrequencies.

In a given frequency band, the power balance of subsystem k writes:

$$P^k_{diss} + \sum_{l\neq k} P^k_l = P^k_{inj} \tag{1.83}$$

Injected power P_{inj}^k usually comes from a known excitation, such as an exterior sound field, an earthquake or a shaker. The dissipated power is assumed proportional to the internal energy level of the structure E_k:

$$P_{diss}^k = \omega \eta_k E_k, \tag{1.84}$$

where ω is the central circular frequency of the considered frequency band, and η_k is called the damping loss factor (DLF) of subsystem k.

The power exchanged between two subsystems k and l is slightly more complicated. The power flow between a mode of subsystem n and one of subsystem $k \neq n$ is assumed to write

$$\mathcal{P}_l^k = \Delta\omega c_{kl} \left(\mathcal{E}_k - \mathcal{E}_l \right), \tag{1.85}$$

where $\mathcal{E}_k$ is the energy of a mode of subsystem k, $\Delta\omega$ is the width of the considered band, and c_{kl} is a constant coefficient depending only on frequency and on the subsystems' coupling.

Here comes the important hypothesis of *energy equipartition*, which states that the total energy E_k of subsystem k is equally divided between its modes, hence

$$E_k = N_k \mathcal{E}_k \tag{1.86}$$

where n_k is the number of modes (mode count) in subsystem k. The power flow between the two subsystems k and l is then the sum of the power flows between all modes of both systems, hence

$$P_l^k = \Delta\omega N_k N_l c_{kl} \left(\frac{E_k}{N_k} - \frac{E_l}{N_l} \right), \tag{1.87}$$

which is also equal to

$$P_l^k = n_k n_l \Delta\omega^2 c_{kl} \left(\frac{E_k}{n_k} - \frac{E_l}{n_l} \right), \tag{1.88}$$

where $n_k = \frac{N_k}{\Delta\omega}$ is the modal density in the frequency band of interest.

Finally, introducing the non-dimensional coupling loss factors (CLF) $\eta_{kl} = \Delta\omega^2 c_{kl} n_k / \omega$ and $\eta_{lk} = \Delta\omega^2 c_{kl} n_l / \omega$, we get

$$P_l^k = \omega \left(\eta_{kl} E_k - \eta_{lk} E_l \right). \tag{1.89}$$

It is important to note that the CLFs are not symmetric, but satisfy the reciprocity relation:

$$\eta_{kl} n_l = \eta_{lk} n_k. \tag{1.90}$$

Using these relationships and writing the power balance for all subsystems, one obtains the

SEA matrix equation for n subsystems:

$$\omega \mathbf{A} \begin{pmatrix} E_1 \\ \vdots \\ E_n \end{pmatrix} = \begin{pmatrix} P_{inj}^1 \\ \vdots \\ P_{inj}^n \end{pmatrix}, \tag{1.91}$$

where the coefficients a_{ij} of matrix $\mathbf{A}$ are:

$$\begin{cases} a_{ii} = \eta_i + \sum\limits_{\substack{j=1 \\ j \neq i}}^{n} \eta_{ij} & \text{for the diagonal terms} \\ a_{ij} = -\eta_{ij} & \text{for the other terms.} \end{cases} \tag{1.92}$$

Knowing the input powers P_{inj}^i, the CLFs and the DLFs of all couples of subsystems, it is possible to find back the energy levels in every subsystem. The coupling loss factors are often evaluated through analytical formulas such as those presented in [69]. The assumptions presented above (weak coupling and energy equipartition) can be completed by a third one, stating that the CLF for pairs of non-physically connected subsystems is zero. The latter hypothesis is not always enforced, as it may be necessary to take non-resonant coupling into account. The use of the SEA method to compute vibroacoustic indicators is presented in section 2 of chapter 6.

In another perspective, this framework can also be used to build models from experimental set-ups, by measuring the energy level in each subsystem (which is linked to the mean-square velocity for plates for example). Knowing the input power, the SEA coefficients can be derived. This is known as the power injected method (PIM) [47].

Much work has also been carried out to extend the validity of SEA towards mid-frequencies, especially by relaxing the weak coupling assumption. The SEA-like [38] and quasi-SEA [70] allow indirect energy flows between subsystems which are not physically connected.

The main issue in SEA lies in the derivation of the coupling loss factors. There exist analytical formulations [69] for plates, cylindrical and conical shells and cavities, which depend on simple parameters such as the material parameters, the geometry being reduced to the perimeter, surface and volume of the elements. Porous treatments can be taken into account through their absorption and added mass. For complex geometries, the usual approach is to feed the SEA model with CLFs and DLFs measured experimentally with the PIM or the Energy Influence Coefficient method [45].

Chapter 2

Acoustic transfer matrix within a wave-finite element framework

Abstract

A finite element-based derivation of the transmission loss (TL) of anisotropic layered infinite plates is presented in this chapter. The wave-finite element method (WFE) is used to represent the plate with a finite element model of a single unit cell. The incident acoustic field is a known plane wave, and the reflected and transmitted pressures are supposed to be plane waves with unknown amplitudes and phases. The periodicity conditions on the unit cell allow to find a simple matrix equation linking the amplitudes of the transmitted and reflected fields as a function of the incident one. This approach is validated for several cases against classical analytical models for thin plates and sandwich constructions, where the results agree perfectly for a reasonable mesh size. The method is then used to study the effect of stacking order in a laminated composite plate. The main interest of the method is the relative easy modelling due to the use of finite elements, compared to analytical models, where different formulations have to be implemented for every kind of material.

Contents

1 Introduction

Sound transmission modelling is a very important topic in the industry, yet it is often still difficult to calculate for complex geometries or materials. Several methods have been proposed for the computation of transmission loss through infinite plate-like structures. Analytic models based on the constitutive equations for infinite thin plates [36], sandwich constructions [57, 83, 56], and even double plates with periodical stiffeners [67] have been proposed in the past. The Transfer Matrix Method (TMM) [14, 3] is a general framework used to compute acoustic transmission features of infinite plane isotropic layerings comprising elastic solids, poroelastic materials and air gaps. It relies on an analytical formulation of the problem in each layer, thus making it necessary to derive new equations for every kind of material that can be encountered (isotropic or anisotropic, elastic or poroelastic).

Finite Element (FE) modelling has the practical advantage over analytical models that most constitutive laws and couplings between materials are already implemented in commercial codes. However meshing a large and simple structure such as a plate can lead to high computational times. The Wave-Finite Element (WFE) method is a response to this issue in the case of large periodic structures. It couples finite elements and the periodic structure theory (also called Bloch's theory), that has been successfully used in the past for the analysis of free wave propagation in mono- and bi-dimensional waveguides [35]. The WFE was also used to compute vibroacoustic indicators such as group velocities and modal densities for use in Statistical Energy Analysis (SEA) [23, 20]. Extensions of this method towards the calculation of forced responses of waveguides have also been proposed [95], without considering fluid-structure coupling. An application of 1D WFE formulation was used by Serra et al. [106] for finite multilayers comprising poroelastic materials, but the transfer approach necessitated meshing the whole surface of the plate. An assessment of wave methods can be found in [86], comparing 3 methods, namely TMM, the WFE+SEA approach of [23] and a procedure based on Rayleigh-Ritz modelling of a unit-cell.

Since the periodic structure theory deals primarily with infinite structures, the WFE can be used to compute the transmission loss of infinite plane structures excited by a superposition of plane waves directly, without having to resort to SEA. The derivation of this application is proposed in this paper, making use of the WFE framework for a plate with homogeneous properties in its plane. This enables to model an arbitrary layering with the finite element model of a single unit cell, which is just 1 element wide in each of the plane's dimensions, as in [75] and [71].

This chapter is structured as follows: the WFE model under forced plane wave is presented in section 2, with the derivation of the formulation of the TL and absorption coefficient. The method is validated on several cases in section 3: an isotropic thin plate, an orthotropic plate, a sandwich construction with a soft viscoelastic core and a stiff sandwich plate with honeycomb core. A discussion on the element size closes this section. Finally, section 4 presents an application case in which the proposed method is used to study the effect of the order of the layers in a composite plate.

2 Forced response to an incident plane wave

We consider a multilayered plate with one surface lying in the plane $z = 0$. Each layer is considered homogeneous, while this is of course not the case for the assembly. As a homogeneous structure is periodic for any period, the unit cell is a parallelepiped. It is modelled with standard (8 nodes) brick elements. The FE discretisation has only a single element in each of the x and y directions, and as many as needed in the z direction.

2.1 Equilibrium formulation

Let $\mathbf{D}$ denote the dynamic stiffness matrix of the unit cell. This matrix is computed from the finite element stiffness and mass matrices $\mathbf{K}$, $\mathbf{M}$ with the relationship

$$\mathbf{D} = \mathbf{K} - \omega^2 \mathbf{M}. \tag{2.1}$$

Viscoelastic damping can be taken into account through a complex part of the stiffness matrix $\mathbf{K}$.

The equilibrium equation of the unit cell then writes

$$\mathbf{D}\mathbf{u} = \mathbf{f} + \mathbf{e}, \tag{2.2}$$

where $\mathbf{f}$ represents the forces due to the interaction with the neighbouring cells, and $\mathbf{e}$ the forces imposed on the plate by the acoustic pressure fields on each side. As can be seen in

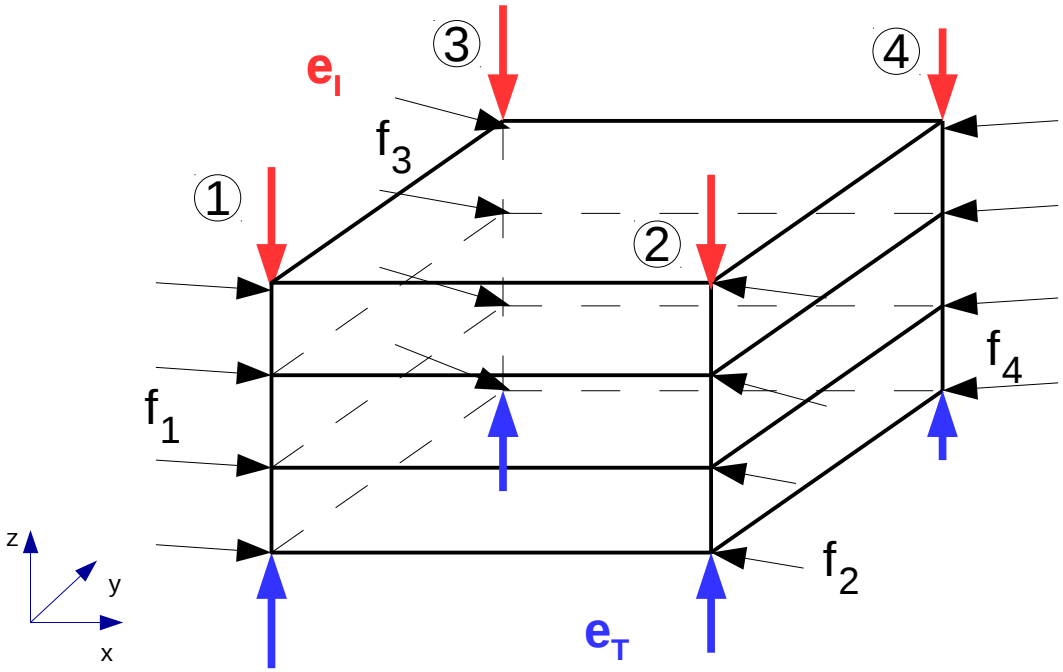

Figure 2.1 – FE model of a unit cell and notation for the applied forces.

Figure 2.1, the displacement vector $\mathbf{u}$ can be partitioned as

$$\mathbf{u} = \begin{pmatrix} \mathbf{u}_1 \\ \mathbf{u}_2 \\ \mathbf{u}_3 \\ \mathbf{u}_4 \end{pmatrix}. \tag{2.3}$$

We now search for solutions as plane waves with the same wave characteristics as the projection of the incident wave on the plate, hence:

$$\begin{aligned} \mathbf{u}_2 &= \lambda_x \mathbf{u}_1 \\ \mathbf{u}_3 &= \lambda_y \mathbf{u}_1 \\ \mathbf{u}_4 &= \lambda_x \lambda_y \mathbf{u}_1, \end{aligned}$$

where $\lambda_x = \exp(\mathrm{i}k_x d_x)$ and $\lambda_y = \exp(\mathrm{i}k_y d_y)$. The reduced variable $\mathbf{u}_1$ can be used with the

transformation

$$\mathbf{u} = \begin{pmatrix} \mathbf{I} \\ \lambda_x \mathbf{I} \\ \lambda_y \mathbf{I} \\ \lambda_x \lambda_y \mathbf{I} \end{pmatrix} \mathbf{u}_1 = \mathbf{T}\mathbf{u}_1, \tag{2.4}$$

where $\mathbf{I}$ is the identity matrix.

The imposed pressure is condensed to forces exerted on the nodes, and can be partitioned in the same way:

$$\mathbf{e} = \mathbf{T}\mathbf{e}_1. \tag{2.5}$$

The internal forces exerted on each vertical segment are derived from the stress field applied to the normal to the two faces related to that segment. The linearity of the stress tensor with respect to displacement field $\mathbf{u}$ and the previous periodicity relations lead to

$$\mathbf{f}_1 + \lambda_x^{-1}\mathbf{f}_2 + \lambda_y^{-1}\mathbf{f}_3 + \lambda_x^{-1}\lambda_y^{-1}\mathbf{f}_4 = 0, \tag{2.6}$$

or $\widetilde{\mathbf{T}}\mathbf{f} = 0$, where $\widetilde{\mathbf{T}} = \begin{pmatrix} \mathbf{I}, & \lambda_x^{-1}\mathbf{I}, & \lambda_y^{-1}\mathbf{I}, & \lambda_x^{-1}\lambda_y^{-1}\mathbf{I} \end{pmatrix}$. Equation 2.2 can then be premultiplied by $\widetilde{\mathbf{T}}$ and rewritten as follows:

$$\widetilde{\mathbf{T}}\mathbf{D}\mathbf{T}\mathbf{u}_1 = \widetilde{\mathbf{T}}\mathbf{T}\mathbf{e}_1 = 4\mathbf{e}_1. \tag{2.7}$$

Let's denote $\mathbf{A} = \frac{1}{4}\widetilde{\mathbf{T}}\mathbf{D}\mathbf{T}$. We finally obtain the reduced equation:

$$\mathbf{A}\mathbf{u}_1 = \mathbf{e}_1, \tag{2.8}$$

linking the forces and the displacements on one single segment instead of the initial four.

2.2 Acoustic coupling

We are concerned with an oblique incident plane wave impinging the plate on one side, with a known amplitude p_I. The interaction between this incident wave and the plate create a reflected wave on the same side, and a transmitted wave on the other one, whose respective amplitudes p_R and p_T we want to calculate. The sound field on the incident side is then the superposition of the incident and reflected waves

$$\begin{aligned} P_I &= p(x,y,z)|_{z>0} \\ &= p_I \exp\left(-\mathrm{i}k_{z,I}z\right) + p_R \exp\left(+\mathrm{i}k_{z,I}z\right), \end{aligned} \tag{2.9}$$

where the common factor $\exp\left(\mathrm{i}(\omega t - k_x x - k_y y)\right)$ has been omitted for legibility. The wavenumber components satisfy the relationship $k_x^2 + k_y^2 + (k_{z,I})^2 = k^2 = \left(\frac{\omega}{c_I}\right)^2$ and c_I is the speed of sound in the fluid on the incident side. In the same way, the sound field on the transmission side contains only the transmitted wave propagating in the same direction as the incident wave

$$P_T = p(x,y,z)|_{z<0} = p_T \exp\left(-\mathrm{i}k_{z,T}z\right), \tag{2.10}$$

with the relationship $k_x^2 + k_y^2 + (k_{z,T})^2 = \left(\frac{\omega}{c_T}\right)^2$ where c_T is the speed of sound in the fluid on the transmission side. Potential phase difference between the pressure fields are accounted for through the fact that the amplitudes p_R and p_T may be complex. The wavenumbers k_x and k_y are conserved across the plate, so only the k_z component may vary with the nature of the fluid. We will consider in the following that the fluid is the same on both sides, thus $\rho_I = \rho_T = \rho_0$ and $c_I = c_T = c_0$.

In this case, the incidence angle θ is the angle between the wave vector and the normal of the plate, while the azimuthal angle φ gives its orientation in the plane. We therefore have $k_x = k\sin\theta\cos\varphi$, $k_y = k\sin\theta\sin\varphi$ and $k_z = k\cos\theta$.

The load imposed on the plate can be written from these two pressure fields lumped on the nodes of the finite element model. As the pressure force is exerted along the normal to the structure, the only non-zero terms in the vector $\mathbf{e}_1$ of forces imposed on segment 1 will be those relative to the DOFs in z-direction on the incident side, e_I, and on the transmission side e_T. For an elastic material, these quantities are scalar. Let $\mathbf{u}_O$ and $\mathbf{e}_O$ denote the displacement and force vectors on all other degrees of freedom in the segment. The force exerted on the nodes of segment 1 is then, as shown in Figure 2.1:

$$\mathbf{e}_1 = \begin{pmatrix} e_I \\ \mathbf{e}_O \\ e_T \end{pmatrix} = \begin{pmatrix} S(p_I + p_R) \\ \mathbf{0} \\ S p_T \end{pmatrix}, \tag{2.11}$$

where S is the free surface of the element, which is identical on both sides. All other vectors and matrices can be written following the same decomposition, allowing to rewrite equa-

tion 2.8 as follows:

$$\begin{pmatrix} a_{II} & \mathbf{A}_{IO} & a_{IT} \\ \mathbf{A}_{OI} & \mathbf{A}_{OO} & \mathbf{A}_{OT} \\ a_{TI} & \mathbf{A}_{TO} & a_{TT} \end{pmatrix} \begin{pmatrix} u_I \\ \mathbf{u}_O \\ u_T \end{pmatrix} = \begin{pmatrix} S(p_I + p_R) \\ \mathbf{0} \\ Sp_T \end{pmatrix}. \tag{2.12}$$

The second line of equation 2.12 leads to

$$\mathbf{u}_O = -\mathbf{A}_{OO}^{-1} \left(\mathbf{A}_{OI}\mathbf{u}_I + \mathbf{A}_{OT}\mathbf{u}_T \right), \tag{2.13}$$

which allows to condense this equation into

$$\begin{pmatrix} b_{II} & b_{IT} \\ b_{TI} & b_{TT} \end{pmatrix} \begin{pmatrix} u_I \\ u_T \end{pmatrix} = \begin{pmatrix} S(p_I + p_R) \\ Sp_T \end{pmatrix}. \tag{2.14}$$

The fluid-structure interaction is characterized by the continuity of normal particle velocity at the interface. This writes for the incident side:

$$\rho_0 \omega^2 u_I = \frac{\partial P_I}{\partial z} = -\mathrm{i}k_z \left(p_I - p_R \right), \tag{2.15}$$

and for the transmission side:

$$\rho_0 \omega^2 u_T = \frac{\partial P_T}{\partial z} = -\mathrm{i}k_z p_T. \tag{2.16}$$

Introducing the acoustic admittance $Y_0 = \cos(\theta)/(\mathrm{i}\omega\rho_0 c_0)$, we obtain

$$\begin{aligned} u_I &= Y_0 \left(p_I - p_R \right) \\ u_T &= Y_0 p_T \end{aligned}$$

These expressions for u_I and u_T can be re-injected into equation 2.14, leading to two scalar equations linking the unknowns p_R and p_T and the incident pressure p_I:

$$\begin{pmatrix} b_{II} + \dfrac{S}{Y_0} & -b_{IT} \\ b_{TI} & -b_{TT} - \dfrac{S}{Y_0} \end{pmatrix} \begin{pmatrix} p_R \\ p_T \end{pmatrix} = p_I \begin{pmatrix} b_{II} - \dfrac{S}{Y_0} \\ b_{TI} \end{pmatrix} \tag{2.17}$$

Solving this equation gives the acoustic transparency $\tau = \left| \dfrac{p_T}{p_I} \right|^2$ and the absorption coef-

ficient $\alpha = 1 - \left|\frac{p^R}{p^I}\right|^2$. The transmission loss for a plane wave is then finally

$$\mathrm{TL} = -10 \log_{10} \tau. \tag{2.18}$$

This leads also to the diffuse field transmission loss by integrating over all possible incidences between minimum and maximum bounds $\theta \in [\theta_{min}, \theta_{max}]$ and directions $\varphi \in [0, 2\pi]$. It is recommended to avoid the full range $[0, \frac{\pi}{2}]$ for θ because numerical errors occur close to grazing incidences $\theta = \pi/2$. However, $\theta_{min} = 0$ causes no issue. The diffuse field transparency is then:

$$\tau_d = \frac{\int_0^{2\pi} \int_0^{\theta_{max}} \tau(\omega\theta, \varphi) \sin\theta \cos\theta \mathrm{d}\theta \mathrm{d}\varphi}{\int_0^{2\pi} \int_0^{\theta_{max}} \sin\theta \cos\theta \mathrm{d}\theta \mathrm{d}\varphi}, \tag{2.19}$$

and the diffuse field transmission loss:

$$\mathrm{TL}_d(\omega) = -10 \log_{10} \tau_d(\omega). \tag{2.20}$$

3 Validation results

In order to assess the validity of the method, a comparison with various analytical models is performed in this section. A discussion on the size of the elements to be used is proposed in paragraph 3.5.

3.1 Isotropic plate

The first case is an isotropic aluminium plate, under two different excitations: a 45^o plane wave and a diffuse field. The material parameters are the Young modulus $E = 70$GPa, the Poisson ratio $\nu = 0.33$, the density $\rho = 2700\mathrm{kg.m}^{-3}$. The loss factor is $\eta = 0.5\%$, which leads to a complex Young's modulus $\widetilde{E} = E(1 + \mathrm{i}\eta)$. The unit cell consists of 10 elements through the thickness, with an overall thickness of 2mm and lengths $d_x = d_y = 0.1$mm.

Two kinds of analytical models are used for comparison. The first one is based on the Kirchhoff-Love plate assumption, while the other is the Transfer Matrix Method (TMM) described in [3]. All three model agree perfectly with each other, with a difference of less than 1dB over most of the frequency range, except in a tiny region around the coincidence frequency, which is slightly underestimated in the thin plate model. Because the TMM and the current model agree in this region, this difference must be due to the fact that the Kirchhoff-Love assumptions neglect shear, while the other two use a 3D elasticity theory.

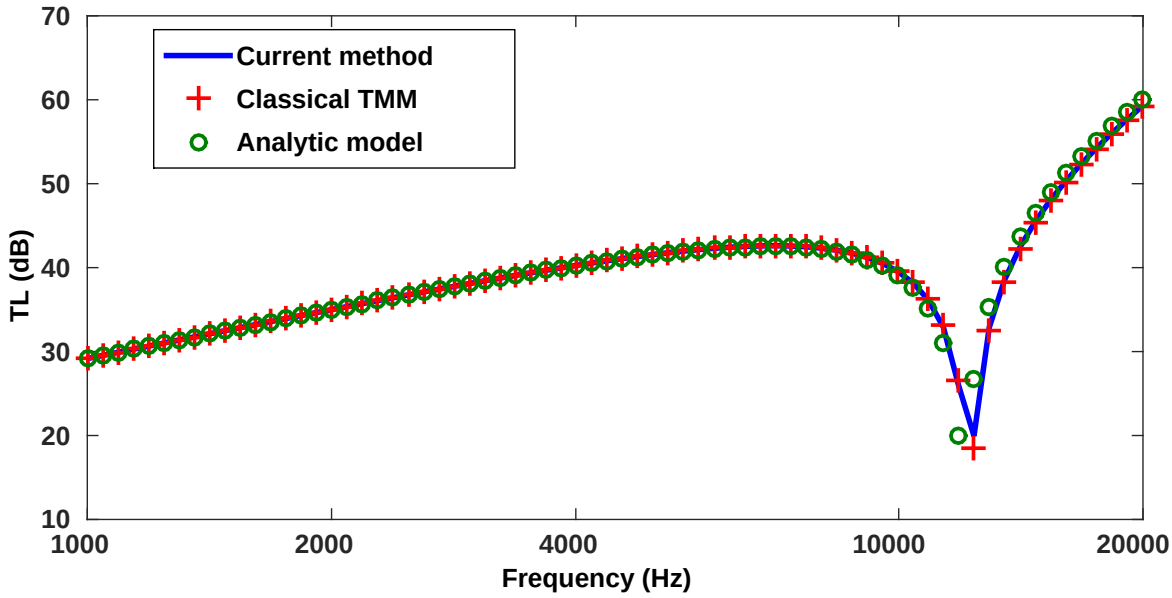

Figure 2.2 – Transmission loss of an infinite steel plate for an oblique plane wave with $\theta = \pi/4$ o: analytic model (plate), +:TMM, —: current method, $d_x = 0.1$mm.

The diffuse field integration has been performed over the range $[0, 0.999\frac{\pi}{2}]$ to avoid numerical issues with grazing incidence. The range was discretised with 1000 points. The three models are found here to agree perfectly, with less than 1dB difference over the whole frequency range. Because of the averaging over 1000 incidence angles, the small difference at coincidence is no longer visible in this case.

3.2 Orthotropic plate

The diffuse field transmission loss of an orthotropic plate is compared against an analytical model [44]. The material parameters are given in Table 2.1, and the TL results presented in Figure 2.4 for frequencies ranging between 100 Hz and 20 kHz The mesh of the unit cell has 10 elements in the z direction and lengths $d_x = d_y = 0.1$mm. Here again, the analytical and current models agree well with each other, with an error smaller than 1.5dB over the whole range. There are two coincidence frequencies due to the very different Young's moduli in the x and y directions.

3.3 Stiff sandwich plate

The 6^{th} order constitutive equation for the bending of a sandwich beam was given by Mead and Markus [81] and later extended to a plate by Narayanan and Shanbhag [83]. The main

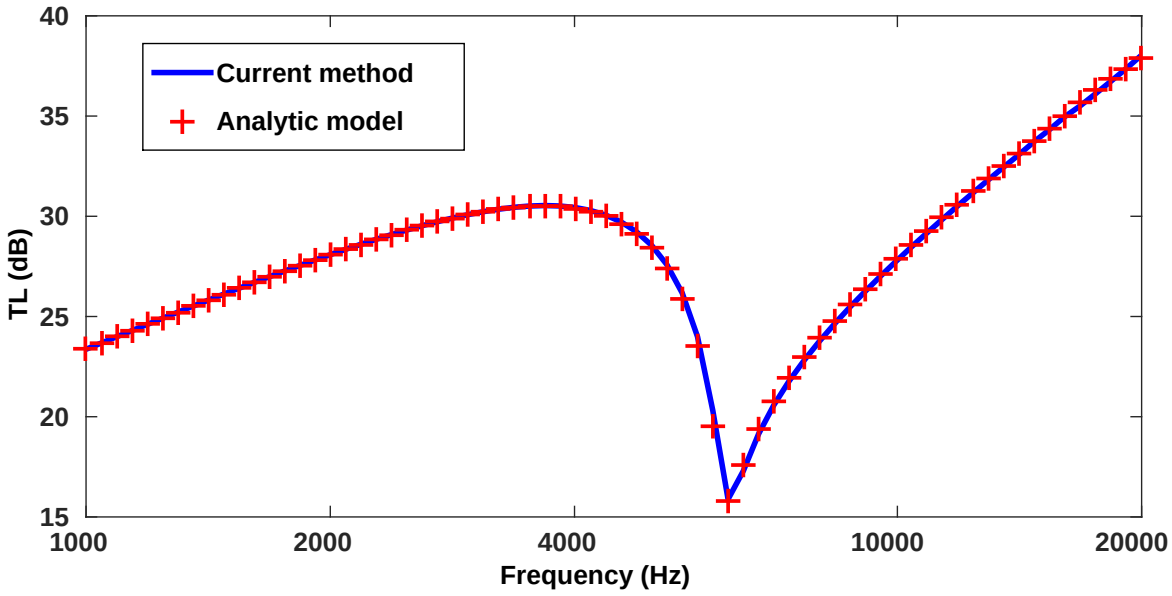

Figure 2.3 – Diffuse field TL of an infinite steel plate +: analytical model (thin plate), —: current method, $d_x = 0.1$mm.

E_x	$E_y = E_z$	$\nu_{xy} = \nu_{xz}$	ν_{yz}	$G_{xy} = G_{xz}$
(GPa)	(GPa)	(–)	(–)	(GPa)
224	6.9	0.25	0.3	56.58
G_{yz}	ρ	η	h	
(GPa)	(kg.m^{-3})	(–)	(mm)	
1.38	1578	0.5%	50	

Table 2.1 – Parameters of the orthotropic plate

assumptions are that the predominant deformation of the core is due to shear, while that of the skins is due to pure bending. This implies that the Young modulus of the core is high compared to the out-of-plane shear modulus. The model has five main parameters, namely skin bending stiffness D_t, overall bending stiffness B, damping η, surface mass m and shear parameter g. The constitutive equation reads:

$$\begin{aligned} D_t(1+\mathrm{i}\eta)\nabla^6 w - g(D_t+B)(1+\mathrm{i}\eta)\nabla^4 w + m\frac{\partial^2 w}{\partial t^2} \\ -\frac{mB}{N}\frac{\partial^2}{\partial t^2}\nabla^2 w = (\nabla^2 - g)(p_L - p_R), \end{aligned} \tag{2.21}$$

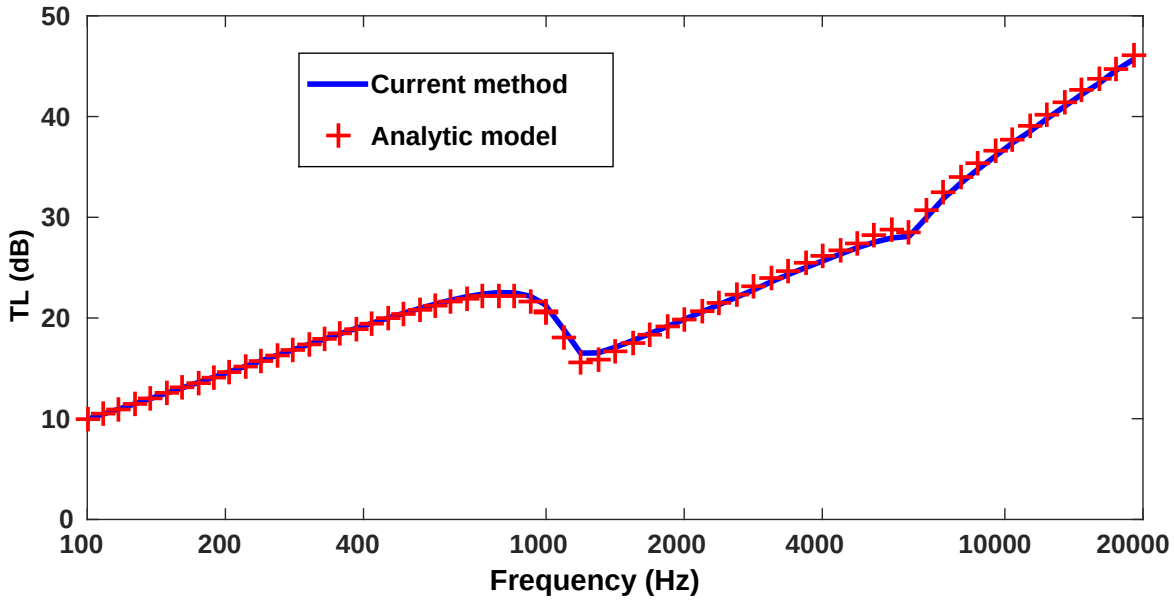

Figure 2.4 – Diffuse field TL of an orthotropic plate + analytic, - current method. The difference is less than 1dB on the whole range (100Hz, 20kHz)

where $w = v/\mathrm{i}\omega$ is the normal displacement of the plate. In the considered frame where a forced wave is imposed on the plate with a wavenumber $k_t = \frac{\omega}{c}\sin\theta$, the spatial derivative operator ∇ can be replaced by $-\mathrm{i}k_t$. This leads to the following expression of the impedance

$$Z(\omega,\theta) = \frac{D_t k^6 + g(D_t + B)k^4 - m\omega^2\left(k^2 + g(1-\nu^2)\right)}{\mathrm{i}\omega(k^2+g)}. \tag{2.22}$$

For sandwiches made of isotropic materials and identical skins, the skin bending stiffness is $D_t = \frac{Eh_s^3}{6(1-\nu^2)}$ the overall bending stiffness is $B = Eh_c^2 h_s(1+\frac{h_s}{h_c})^2/2$ and the shear parameter is $g = \frac{2G}{Eh_s h_c}$, where G is the core shear modulus.

The two models are compared between 1kHz and 20kHz on a sandwich plate with isotropic skins and orthotropic core impinged by a 45^o plane wave. The parameters of the sandwich construction are given in Table 2.2, and the TL results shown in Figure 2.6. With a mesh using 3 elements for each skin and 45 for the core, and again $d_x = d_y = 0.1mm$, the two models differ also by less than 1dB in the whole range. Since the analytical model takes shear into account, the agreement is also excellent at coincidence.

3.4 Sandwich plate with soft core

The same calculation was made with a thick sandwich plate made of a rather soft isotropic core and thick skins. The material properties are described in Table 2.3. The transmission

	E_x (GPa)	E_z (GPa)	ρ (kg.m^{-3})	ν
Skin	70	70	2700	0.33
Core	0.08	8	8	0.1
	G_{xy} (MPa)	G_{xz} (MPa)	G_{yz} (MPa)	h (mm)
Skin	26310	26310	26310	2
Core	0.04	4	4	30

Table 2.2 – Parameters of the stiff sandwich plate.

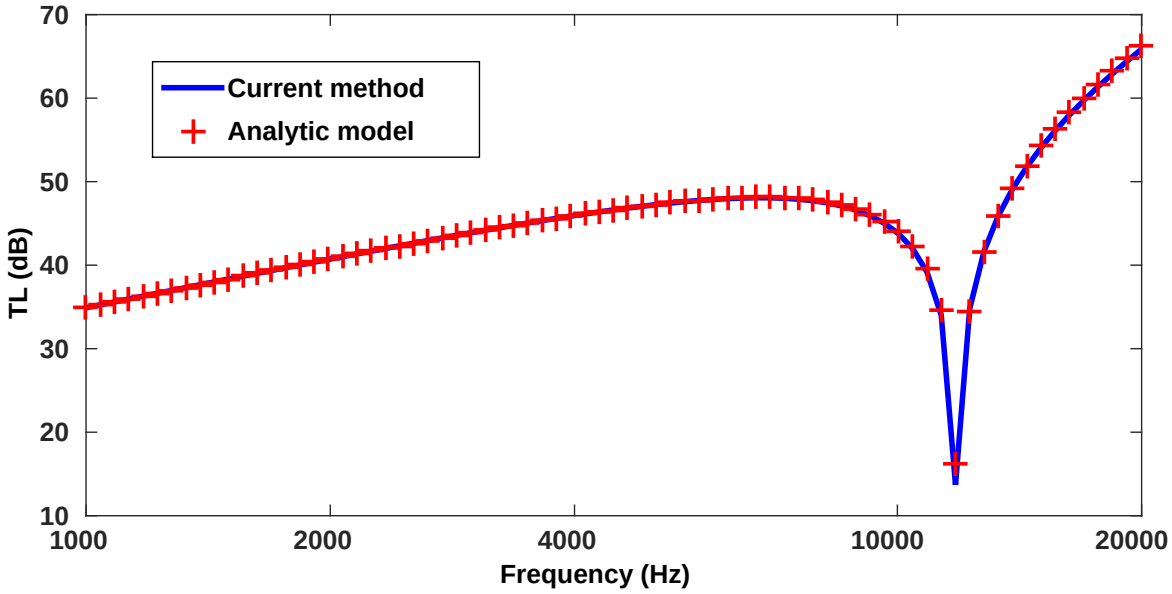

Figure 2.5 – TL of a sandwich plate impinged by a 45^o plane wave. +: Analytical model, — current method

loss curve is shown on Figure 2.6. Again this correlates well with the analytical TMM, with a maximum error of 1dB over the considered range. Three dips in TL can be observed between 1kHz and 6kHz, corresponding to coincidence frequencies. The first two drops around 1730Hz and 5470Hz are due to coincidences with a wave having a symmetric motion of the skin and compression in the core, while the third one around 5620Hz is due to coincidence with the bending wave. The dispersion curves for these two waves are presented in Figure 2.7.

	E (MPa)	ν	ρ (kg.m^{-3})	h (mm)
Skin	8300	0.15	629.9	6.35
Core	8.3	0	16	38.1

Table 2.3 – Parameters of the soft sandwich plate

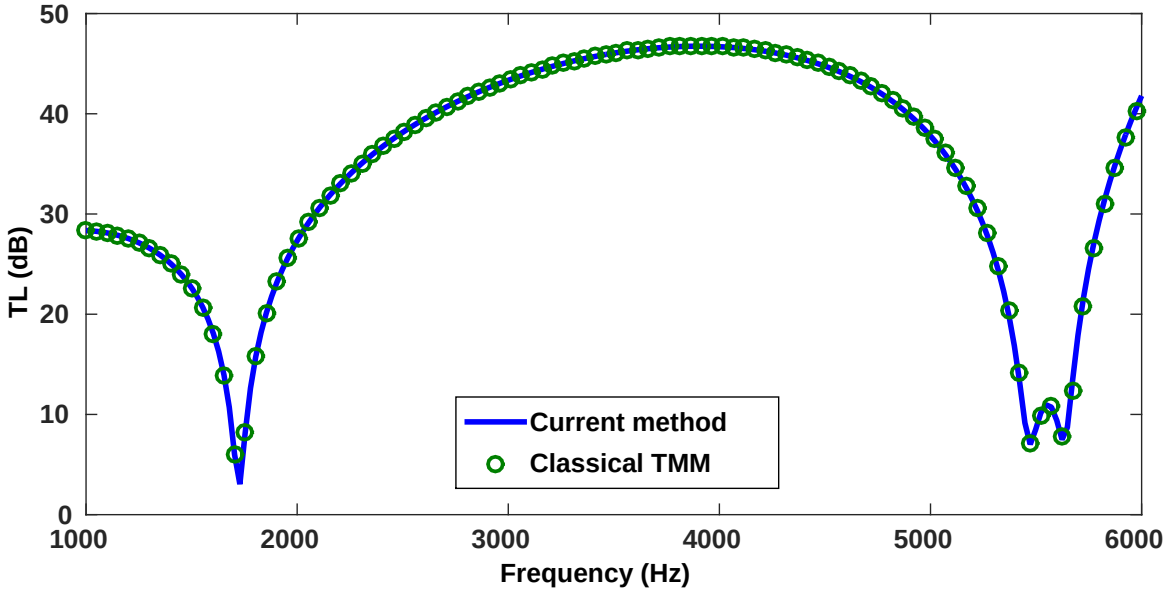

Figure 2.6 – Transmission loss for the sandwich plate impinged by a 45^o plane wave o TMM (analytic) — current method.

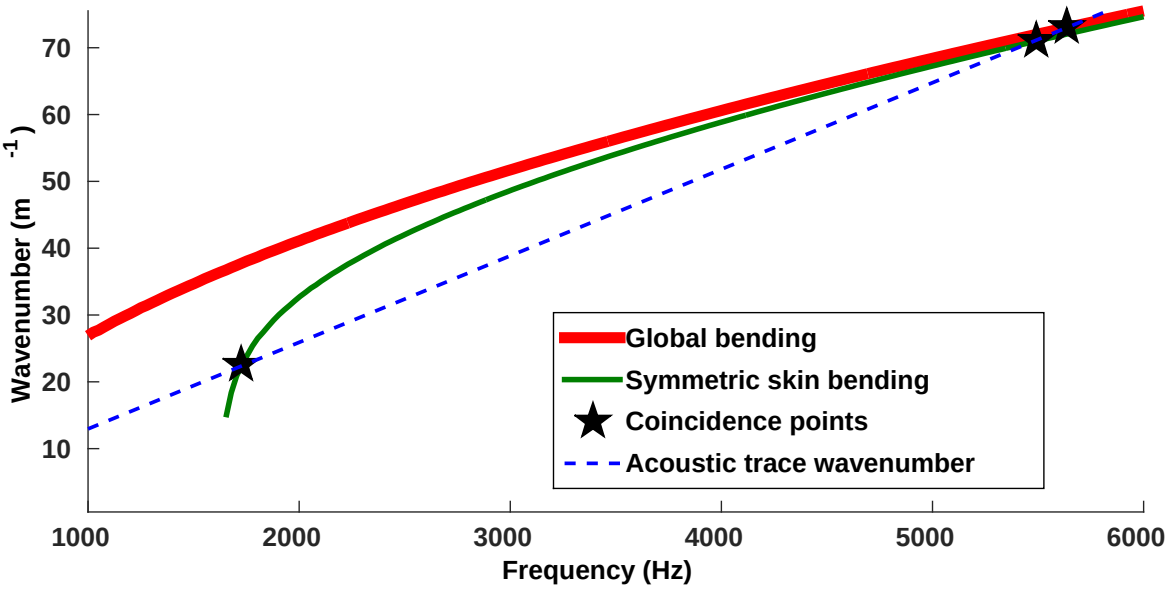

Figure 2.7 – Dispersion curves of the out-of-plane waves of the soft sandwich structure and trace wavenumber of the incident acoustic plane wave at 45^o.

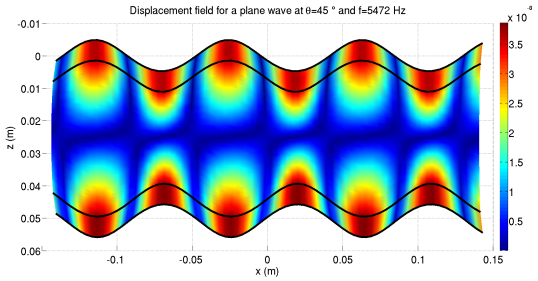

(a) Symmetric coincidence at 5472Hz.

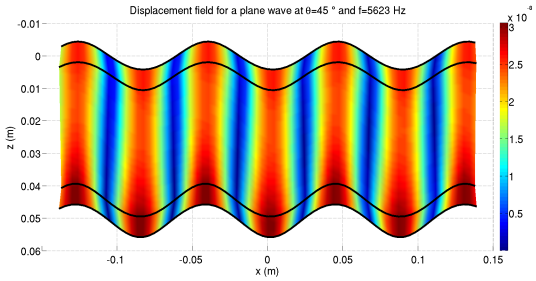

(b) Antisymmetric coincidence at 5623Hz.

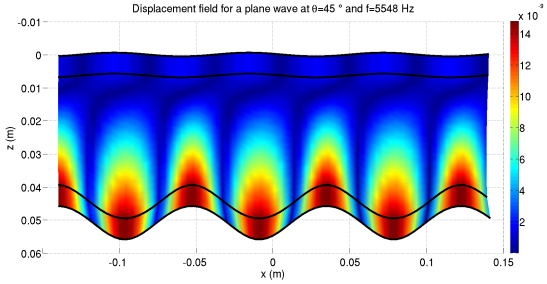

(c) Displacement field at 5548Hz.

Figure 2.8 – Displacement fields at several frequencies. The color indicates the absolute value of the z-displacement, in meters, for an incident amplitude of 1Pa. The incident wave comes from the top.

The displacement field can be calculated back from equation 2.13. They are displayed at several frequencies on Figure 2.8. The first one is related to the symmetric motion of the skins (Figure 2.8a), while the second is related to a global bending motion of the sandwich, or antisymmetric motion of the skins (Figure 2.8b). In both cases, it can be observed that a shearing motion of the skins is involved, due to their rather high thickness. In the antisymmetric case, the cross-section remain straight and vertical, indicating that only shear is at stake, with practically no bending motion.

The field represented on Figure 2.8c is at a frequency between the two coincidences, showing a decoupling of the two skins. On the latter example, it may be noted that the amplitude of the z-displacement is higher on the transmission side than on the incident side, yet the amplitude of the transmitted wave is of course smaller. This is due to the fact that the pressure field on the incident side is result of interference between incident and reflected waves, while the transmitted field consists of a single plane wave.

3.5 Discussion on element size

In the validation cases presented in this section, the mesh parameters are chosen so as to ensure convergence with the TMM model, which is based on 3D isotropic elastic theory and therefore exact in this case. A coarser mesh leads to errors in the coincidence frequency region. Of all the waves considered in acoustic transmission, the acoustic wave in the fluid has the shortest wavelength, at the highest frequency considered in all these cases. The element sizes in x and y directions must therefore satisfy about 100 elements per wavelength, which is much stricter than the usual 10 elements per wavelength used for finite elements. Since there is only one element in the in-plane directions, this has no impact on the number of degrees of freedom in the mesh. However, the results are also found to be quite sensitive to the aspect ratio of the elements, which means that the element size in the z-direction must be about the same as that in the plane, leading to a potentially high number of elements through the thickness.

4 Influence of stacking on the transmission loss

The current approach can be used to study the influence of the stacking sequence of a multilayer plate on the TL. We consider a 1.6mm thick composite plate made of 24 layers of the same transverse isotropic material described in Table 2.4 in order to study the effect of the stacking sequence on the TL. Three different stacking sequences have been studied: a classical symmetric quasi-isotropic stacking, a random permutation of it, and a grouping of the same orientation in ascending order. All of these have the same proportion of layers with fibres oriented towards each direction, at -45, 0, 45 or 90 degrees of the global coordinate system. The sequences are described in Table 2.5.

E_x (GPa)	E_z (GPa)	ν_{xy} (–)	ν_{yz} (–)	G_{xy} (GPa)	G_{yz} (GPa)
175.0	6.90	0.2542	0.4689	4.18	2.35

ρ (kg.m^{-3})	η (%)	h (μm)
1520	0.1	67

Table 2.4 – Material parameters of a single layer. For a transverse isotropic material, we have $E_y = E_z$, $\nu_{xz} = \nu_{xy}$ and $G_{xz} = G_{xy}$

The TL was computed for these three sequences with the method described above, using 2 elements per layer and a mesh size of 0.1mm in the x and y directions. The results are

Initial	$[45_3; -45_3; 0_3; 90_3]_s$
Sorted	$[-45_6; 0_6; 45_6; 90_6]$
Random	$[0; 90; -45; 90; 45; 0_3; -45; 90; -45; 45; 90;$ $-45; 0; 90; -45; 45_2; 90; -45; 45; 0; 45]$

Table 2.5 – The three stacking configurations.

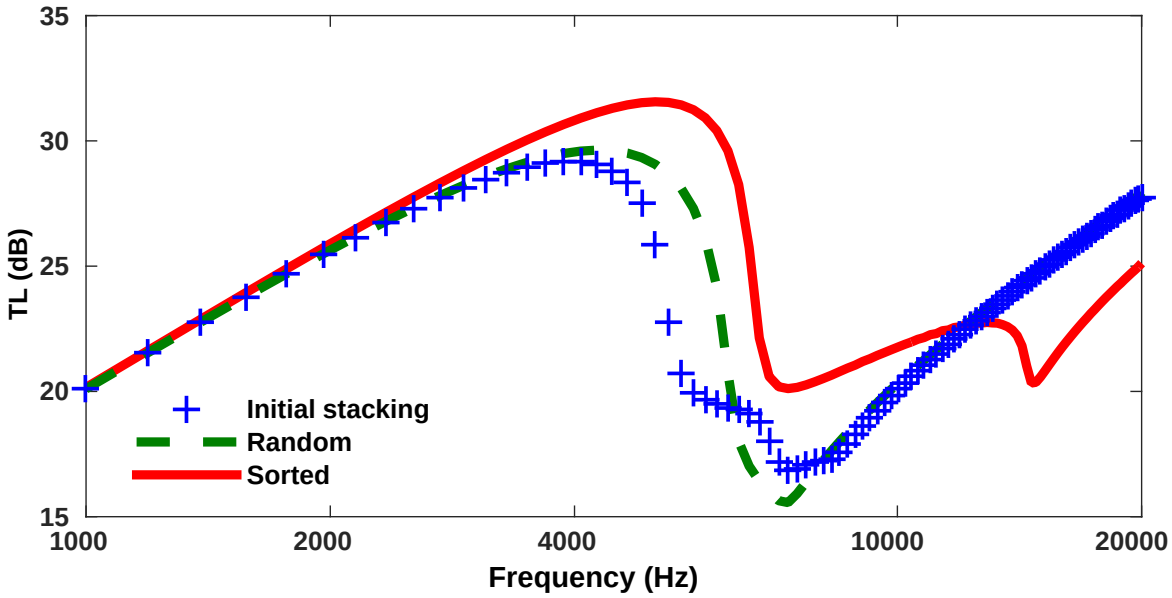

Figure 2.9 – Diffuse field transmission loss for 3 different stacking sequences.

presented in Figure 2.9. Several observations can be made:

- The stacking sequence has practically no influence for frequencies below 2kHz, and little up to 4kHz. This is due to the fact that below this frequency, the plate behaves according to the mass law, and the actual stiffness has no effect on TL.
- The random and initial stacking sequences have the same asymptotic behaviour in high frequencies (above 8kHz). This is also true for the sorted case but at higher frequencies, and due to the dominant effect of damping on the high-frequency TL, above the highest critical frequency. These effects are the same as those studied in chapter 5.
- The sorted stacking exhibits a wide coincidence region with two critical frequencies, a behaviour that is similar to that of an orthotropic plate.
- The coincidence zone is narrowest in the random stacking case, which is closest to an isotropic plate.

5 Conclusion

A new method for computing the transmission loss of infinite plates made of arbitrarily layered materials has been presented in this paper. The originality of the approach is that it couples the periodic structure theory to finite elements as in the WFE method, while taking into account the coupling with an acoustic fluid analytically. The method is validated against classical analytic Transfer Matrix Method computation for isotropic, orthotropic and sandwich constructions. The main interest of the method is that it natively takes into account complex behaviour of the structure, such as symmetric motion of the skins with respect to the neutral plane. Besides, the use of finite elements makes it easy to retrieve the displacement field inside the structure. The computation time is much higher than that of analytical methods, but remains low, typically several seconds or minutes for diffuse field computations. A possible use of this method is the validation of analytical model for multilayers.

An application case is proposed to study the effect of the stacking sequence of a layered composite plate on the diffuse field TL. It is shown that the stacking sequence has an effect on the width of the coincidence range, and little influence outside it, the low frequencies being governed by mass law and the higher by damping effects. The most extreme case of a sorted stacking shows a wide coincidence zone limited by two critical frequencies, while the random permutation exhibits a dip in a narrower zone around the lowest critical frequency (7kHz in this case). In applications where noise control is important at frequencies corresponding to the coincidence range, stacking sequence should therefore be considered for acoustic criteria too.

Chapter 3

Transmission loss of cylindrical shells with the WFE method

Summary

The WFE-based transfer approach presented in chapter 2 for plates is here extended to cylinders of infinite length. The periodic decomposition is made here on plane wave harmonics in the axial direction and cylindrical harmonics in the circumferential direction. The method is validated against literature results for the ring frequency and above. The modal behaviour below the ring frequency follows the correct trends, but numerical errors remain in this range.

Contents

1 Introduction

The sound transmission through cylindrical shells is a problem that has been studied extensively over the last four decades, having applications in aeronautic, marine and space industries. The first models have been proposed by Koval in the 70s for isotropic [53] and orthotropic [54] infinite cylindrical shells, taking into account an external mean flow. A variant of this model was proposed by Lee and Kim [62]. Ghinet et al. [41] came up with an analytical model for wave propagation along curved shells. Renno and Mace [96] used the Wave Finite Element method to compute the forced structural response of a cylindrical shell to an arbitrary load. Recently Alimonti et al. [2] proposed a new method to model radiation and transmission of structures lined with poroelastic sound packages with FE model of the structure and an analytic model of the sound package. A model for the transmission of sound through cylindrical sandwich shells has also been developed using an analytic formulations by Magniez et al. [72] and later extended to poroelastic cores [73].

In this chapter, a calculation method for the TL through a cylindrical shell using periodic finite elements is presented. It is based on an analytical model of the surrounding fluid as in [72], while the cylinder is modelled following the WFE principle, with a finite element discretisation of a single unit cell and periodic boundary conditions.

The derivation of the calculation is presented in section 2. The model is then validated in section 3 against cases found in the literature. Possible extensions are then discussed in the concluding section.

2 Numerical model derivation

We consider an infinite cylinder of axis z, subjected to an oblique progressive harmonic acoustic plane wave, as depicted in figure Figure 3.1. Assuming that the properties of the structure are invariant with respect to the polar angle θ, the coordinate system can be taken so that the wavenumber k_y is zero. The wave vector $\mathbf{k}$ has an angle ψ with the x-axis, so that

$$\mathbf{k} = \begin{pmatrix} k_x \\ 0 \\ kz \end{pmatrix} = \frac{\omega}{c_0} \begin{pmatrix} \cos\psi \\ 0 \\ \sin\psi \end{pmatrix}. \tag{3.1}$$

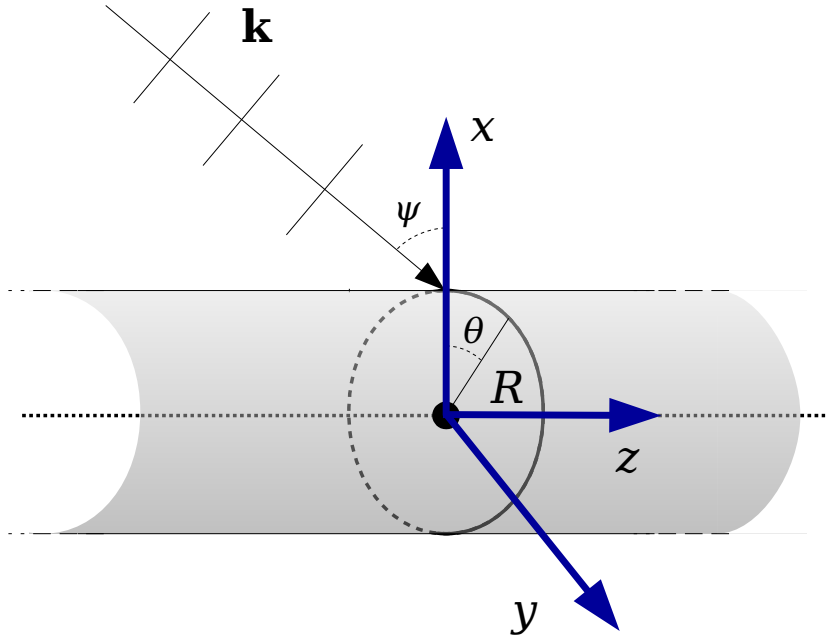

Figure 3.1 – An infinite cylindrical wave subjected to a plane wave excitation.

2.1 Acoustic fields

The incident wave's equation writes in Cartesian coordinates

$$p^I = P_0 \exp\left(\mathrm{i}k_x x + \mathrm{i}k_z z\right) \exp(\mathrm{i}\omega t). \tag{3.2}$$

Writing $x = r\cos\theta$ into the incident pressure definition, one obtains a periodic function of θ

$$p^I = P_0 \exp\left(\mathrm{i}k_x r\cos\theta + \mathrm{i}k_z z\right). \tag{3.3}$$

The Fourier transform of this expression with respect to θ yields:

$$p^I(r,\theta,z)\theta = P_0 \sum_{n\in\mathbb{Z}} \mathrm{i}^n J_n(k_x r) \exp\left(\mathrm{i}n\theta\right) \exp(\mathrm{i}k_z z) \exp(\mathrm{i}\omega t), \tag{3.4}$$

where J_n is the Bessel function of the first kind with order n.

The transmitted and reflected pressure fields can be computed as a sum of cylindrical propagating waves. Inwards and outwards going waves are represented with Hankel functions

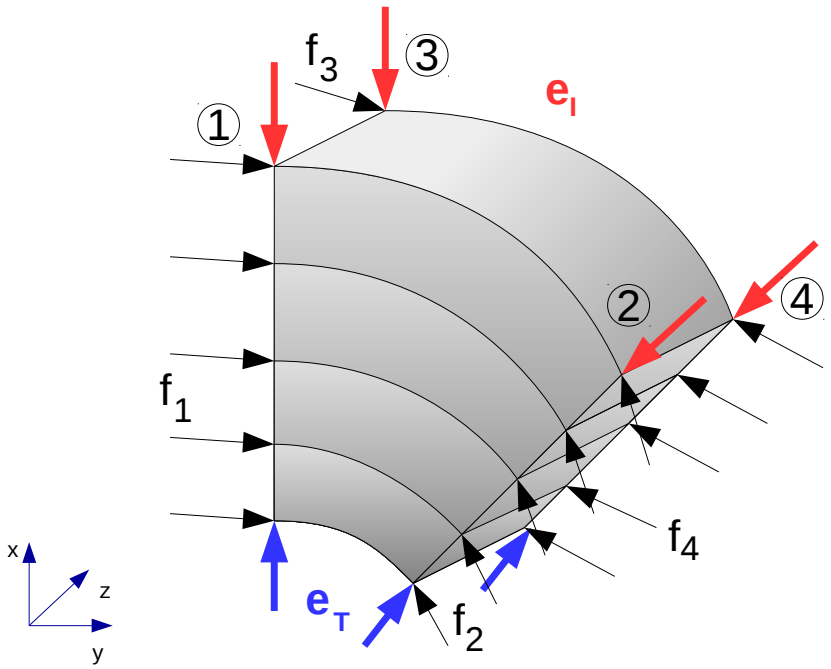

Figure 3.2 – The cylindrical unit cell. The curved edges are approximated by straight lines in the actual model.

of the first (H_n^1) and second (H_n^2) kind respectively. The reflected field writes

$$p^R(r,\theta,z) = \sum_{n\in\mathbb{Z}} p_n^R H_n^2(k_x r)\exp(in\theta)\exp(ik_z z)\exp(i\omega t), \tag{3.5}$$

an the transmitted field:

$$p^T(r,\theta,z) = \sum_{n\in\mathbb{Z}} p_n^T H_n^1(k_x r)\exp(in\theta)\exp(ik_z z)\exp(i\omega t). \tag{3.6}$$

2.2 Complex shell and finite elements

The main idea of the proposed method is to compute the displacement field inside the cylindrical structure with a hybrid finite-element/semi analytical method. A small unit cell is first chosen to represent the whole cylinder, and discretised according to Figure 3.2. This cell is modelled using standard brick (Q8) finite elements.

The dynamic equilibrium of the cell writes

$$\mathbf{D}\mathbf{u} = \mathbf{f} + \mathbf{e}, \tag{3.7}$$

where $\mathbf{D}$ is the dynamic stiffness matrix, $\mathbf{u}$ is the vector of displacements of the cell's nodes, $\mathbf{f}$ is the vector of forces deriving from the stress tensor of the whole structure, and $\mathbf{e}$ is the vector of imposed efforts.

The imposed forces derive from the pressure fields: only the displacements DOFs that are normal to the surface are impacted, that is, for the segment 1 lying on the x-axis, The vector of forces imposed on edge 1 can be decomposed into incident side forces and transmitted side forces:

$$\mathbf{e_1} = \begin{pmatrix} e_I \\ \mathbf{0} \\ e_T \end{pmatrix}, \tag{3.8}$$

where e^I is is the force on the incident side and e^T is the force on the transmission side. According to equations 3.4,3.5 and 3.6, these forces can written as a cylindrical harmonic decomposition:

$$e^I = \sum_{n\in\mathbb{Z}} \left(e_n^I + e_n^R\right) \exp(\mathrm{i}n\theta) \exp(\mathrm{i}k_z z) \tag{3.9}$$

and

$$e^T = \sum_{n\in\mathbb{Z}} e_n^T \exp(\mathrm{i}n\theta) \exp(\mathrm{i}k_z z). \tag{3.10}$$

The force exerted on one segment can be approximated as one quarter of the force exerted on the whole surface, hence for the segment 1,

$$e^{I1} = e^I(\theta = 0, z = 0) = \frac{S_I}{4}(p^I + p^R) \tag{3.11}$$

$$e^{T1} = e^T(\theta = 0, z = 0) = \frac{S_T}{4}p^T. \tag{3.12}$$

Introducing shorthand notations:

$$\begin{aligned} \beta_n^I &= \frac{S_I}{4}\mathrm{i}^n J_n(k_x R_I) \\ \beta_n^T &= \frac{S_T}{4}H_n^1(k_x R_T) \\ \beta_n^R &= \frac{S_I}{4}H_n^2(k_x R_I). \end{aligned} \tag{3.13}$$

we finally obtain:

$$\begin{aligned} e_n^I &= \beta_n^I p_0 + \beta_n^R p_n^R \\ e_n^T &= \beta_n^T p_n^T. \end{aligned} \tag{3.14}$$

The displacement field inside the structure can be searched for in a similar fashion:

$$\mathbf{u}(\theta, z) = \sum_{n\in\mathbb{Z}} \mathbf{u}_n^1 \exp(in\theta) \exp(ik_z z) \exp(i\omega t), \tag{3.15}$$

where $\mathbf{u}(\theta = 0, z = 0)$ is the vector of displacement DOFs of the nodes in segment 1 of the unit cell. Let d_θ be the angle between edges 1 and 2 of the unit cell, and d_z the unit cell's length along axial direction z. For a given order n, the harmonic excitation imposes, in cylindrical coordinates,

$$\begin{aligned} \mathbf{u}_n(d_\theta, 0) &= \exp(ind_\theta)\mathbf{u}_n(r, 0, 0) \\ \mathbf{u}_n(0, d_z) &= \exp(ik_z d_z)\mathbf{u}_n(r, 0, 0) \\ \mathbf{u}_n(d_\theta, d_z) &= \exp(ik_z d_z)\exp(ind_\theta)\mathbf{u}_n(r, 0, 0). \end{aligned} \tag{3.16}$$

Transferring these relations in Cartesian coordinates and using the notation described on Figure 3.2, we obtain:

$$\begin{aligned} \mathbf{u}_n^2 &= \exp(ind_\theta)\mathbf{R}(d_\theta)\ \mathbf{u}_n^1 \\ \mathbf{u}_n^3 &= \exp(ik_z d_z)\ \mathbf{u}_n^1 \\ \mathbf{u}_n^4 &= \exp(ik_z d_z)\exp(ind_\theta)\mathbf{R}(d_\theta)\ \mathbf{u}_n^1 \end{aligned} \tag{3.17}$$

where $\mathbf{R}(d_\theta)$ is a block diagonal matrix in which all the blocks are identical and equal to the rotation matrix around axis z:

$$\mathbf{R}(d_\theta) = \begin{pmatrix} \widetilde{\mathbf{R}} & & & \\ & \widetilde{\mathbf{R}} & & \\ & & \ddots & \\ & & & \widetilde{\mathbf{R}} \end{pmatrix} \text{ and } \widetilde{\mathbf{R}} = \begin{pmatrix} \cos d_\theta & -\sin d_\theta & 0 \\ \sin d_\theta & \cos d_\theta & 0 \\ 0 & 0 & 1 \end{pmatrix}. \tag{3.18}$$

Let's introduce the propagation constants $\lambda_\theta = \exp(id_\theta)$ and $\lambda_z = \exp(ik_z d_z)$, so that equation 3.17 rewrite in a matrix form:

$$\mathbf{u}_n = \begin{pmatrix} \mathbf{u}_1 \\ \mathbf{u}_2 \\ \mathbf{u}_3 \\ \mathbf{u}_4 \end{pmatrix} = \begin{pmatrix} \mathbf{I} \\ \lambda_\theta^n \mathbf{R}(d_\theta) \\ \lambda_z \mathbf{I} \\ \lambda_z \lambda_\theta^n \mathbf{R}(d_\theta) \end{pmatrix} \mathbf{u}_1 = \mathbf{T}_n \mathbf{u}_1. \tag{3.19}$$

Using all these properties, equation 3.7 can be reduced to

$$\mathbf{DTu}_1 = \mathbf{f} + \mathbf{Te}_1. \tag{3.20}$$

Now, as the internal forces applied on each edge derive from the stress tensor, they obey the following relationship:

$$\mathbf{f}_1 + \left(\lambda_\theta^n \mathbf{R}(d_\theta)\right)^{-1} \mathbf{f}_2 + \lambda_z^{-1}\mathbf{f}_3 + \left(\lambda_z \lambda_\theta^n \mathbf{R}(d_\theta)\right)^{-1} \mathbf{f}_4 = 0. \tag{3.21}$$

Since the propagation constants have unit modulus and $\mathbf{R}(d_\theta)^{-1} = \mathbf{R}(-d_\theta) = \mathbf{R}(d_\theta)^H$, this can be written in a more condensed way:

$$\mathbf{T}_n^H \mathbf{f} = 0. \tag{3.22}$$

Finally, using equation 3.22, multiplying equation 3.20 by $\mathbf{T}_n^H$ leads to:

$$\mathbf{T}_n^H \mathbf{D} \mathbf{T}_n \mathbf{u}_1 = 4\mathbf{e}_1, \tag{3.23}$$

since $\mathbf{T}_n^H \mathbf{T}_n = 4\mathbf{I}$. Denoting

$$\mathbf{A}_n = \frac{1}{4} \mathbf{T}_n^H \mathbf{D} \mathbf{T}_n \tag{3.24}$$

and partitioning the equation into incident side DOFs, transmission side DOFs and the rest, we can write this equation as

$$\begin{pmatrix} a_n^{II} & \mathbf{A}_n^{IO} & a_n^{IT} \\ \mathbf{A}_n^{OI} & \mathbf{A}_n^{OO} & \mathbf{A}_n^{OT} \\ a_n^{TT} & \mathbf{A}_n^{TO} & a_n^{TI} \end{pmatrix} \begin{pmatrix} u_n^I \\ \mathbf{u}_n^O \\ u_n^T \end{pmatrix} = \begin{pmatrix} e_n^I \\ \mathbf{0} \\ e_n^T \end{pmatrix}. \tag{3.25}$$

As the matrix A derives from a finite element dynamic stiffness matrix, it is always invertible, except when $\omega = 0$. We can therefore eliminate the second line of the matrix, writing

$$\mathbf{u}_O = -\mathbf{A}_{OO}^{-1} \left(\mathbf{A}_{OI}\mathbf{u}_I + \mathbf{A}_{OT}\mathbf{u}_T\right). \tag{3.26}$$

Using the following notations:

$$\begin{aligned} \mu^{OI} &= -\left(\mathbf{A}^{OO}\right)^{-1} \mathbf{A}^{OI}, & \mu^{OT} &= -\left(\mathbf{A}^{OO}\right)^{-1} \mathbf{A}^{OT}, \\ b^{II} &= a^{II} + \mathbf{A}^{IO}\mu^{OI}, & b^{IT} &= a^{IT} + \mathbf{A}^{IO}\mu^{OT}, \\ b^{TI} &= a^{TI} + \mathbf{A}^{TO}\mu^{OI}, & b^{TT} &= a^{TT} + \mathbf{A}^{TO}\mu^{OT}, \end{aligned}$$

this equation can be condensed into:

$$\begin{pmatrix} b_n^{II} & b_n^{IT} \\ b_n^{TI} & b_n^{TT} \end{pmatrix} \begin{pmatrix} \mathbf{u}_I \\ \mathbf{u}_T \end{pmatrix} = \begin{pmatrix} \mathbf{e}_I \\ \mathbf{e}_T \end{pmatrix}. \tag{3.27}$$

2.3 Impedance conditions

The fluid-structure interface is characterised by the continuity of velocity normal to the surface, hence the radial velocity. This writes

$$\rho_0 \omega^2 u_r = \frac{\partial p}{\partial r} \tag{3.28}$$

on both the inner and outer sides of the cylinder. This leads to the following equations

$$u_n^I = \alpha_n^I p_0 + \alpha_n^R p_n^R \tag{3.29}$$

for the incident side and

$$u_n^T = \alpha_n^T p_n^T \tag{3.30}$$

for the transmission (inner) side. The short notations introduced in equation 3.31 are used, where the $'$ symbol indicates the derivative of the single variable function.

$$\begin{aligned} \alpha_n^I &= \mathrm{i}^n k_x J_n'(k_x R_I) \\ \alpha_n^T &= k_x H_n^{1'}(k_x R_T) \\ \alpha_n^R &= k_x H_n^{2'}(k_x R_I). \end{aligned} \tag{3.31}$$

We can then introduce equations 3.29 and 3.30 in equation 3.27, which leads to the matrix system:

$$\begin{pmatrix} b_n^{II} & b_n^{IT} \\ b_n^{TI} & b_n^{TT} \end{pmatrix} \begin{pmatrix} \alpha_n^I p_0 + \alpha_n^R p_n^R \\ \alpha_n^T p_n^T \end{pmatrix} = \begin{pmatrix} \beta_n^I p_0 + \beta_n^R p_n^R \\ \beta_n^T p_n^T. \end{pmatrix}. \tag{3.32}$$

The latter equation can be reshaped, putting the known terms p_0 on the right hand side and the unknown terms p_n^R and p_n^T on the left hand side:

$$\begin{pmatrix} \alpha_n^R b^{II} - \beta_n^R & \alpha_n^T b_n^{IT} \\ \alpha_n^R b^{TI} & \alpha_n^T b_n^{TT} - \beta_n^T \end{pmatrix} \begin{pmatrix} p_n^R \\ p_n^T \end{pmatrix} = p_0 \begin{pmatrix} -\alpha_n^I b^{II} + \beta_n^I \\ -\alpha_n^I b^{TI} \end{pmatrix}. \tag{3.33}$$

Solving this system yields the amplitudes of the transmitted and reflected pressure fields. In order to compute the transmission loss, we need the time-average power flow of the incident

wave per unit length of the cylinder,which reads [65, 31]:

$$W^I(\psi) = \frac{R}{\rho_0 c_0}\cos\psi, \tag{3.34}$$

and the power flow transmitted to the acoustic medium inside the cylinder for order n:

$$\begin{aligned} W_n^T &= \frac{1}{2}\mathrm{Re}\left(\int_0^{2\pi} p_n^T H_n^1(k_x R)\exp\left(\mathrm{i}n\theta\right)\left(\overline{\mathrm{i}\omega u_n^T \exp\left(\mathrm{i}n\theta\right)}\right)\mathrm{d}\theta\right) \\ W_n^T &= \pi R\omega \mathrm{Im}\left(\overline{u_n^T} p_n^T H_n^1(k_x R))\right). \end{aligned} \tag{3.35}$$

The acoustic transparency of mode n is then given by:

$$\tau_n(\omega,\psi) = \frac{W_n^T}{W^I}, \tag{3.36}$$

and the total acoustic transparency for the plane wave is then:

$$\tau(\omega,\psi) = \sum_{n\in\mathbb{Z}} \tau_n. \tag{3.37}$$

The diffuse field transparency is finally calculated by a weighted average of plane waves with all possible incidences

$$\tau_d(\omega) = \frac{\int_0^{\pi/2}\tau(\omega,\psi)\sin\theta\cos\theta\mathrm{d}\psi}{\int_0^{\pi/2}\cos\theta\sin\theta\mathrm{d}\theta}. \tag{3.38}$$

The former integral can be evaluated with the trapeze rule or a Gaussian scheme on a finite number of incidence angles.

3 Numerical results

3.1 Isotropic shell

The first case is that of an isotropic thin aluminium shell under oblique plane wave excitation. The density and speed of sound in the fluid are respectively $\rho_0 = 1.284\mathrm{kg.m}^{-3}$ and $c_0 = 340\mathrm{m.s}^{-1}$. The shell is 3mm thick, with Young modulus $E = 69\mathrm{GPa}$, Poisson ratio $\nu = 0.3$, density $\rho = 2768\mathrm{kg.m}^{-3}$ and hysteretic damping $\eta = 5\%$. The mesh for the current model consists of 2 elements through the thickness. The length in the axial direction is $L_z = 2\pi\cdot 10^{-5}\mathrm{m}$ and the angle in the orthoradial direction is $d_\theta = 2\pi\cdot 10^{-5}$ radians for a mean radius $R = 2.164\mathrm{m}$. The results are shown in Figure 3.3, and compared with the results in section 4.1 of reference [72] seems to perform well over the whole frequency range,

with a difference with the reference model mostly less than 3dB. However, below the ring frequency, the results do not comply with the reference, despite showing a behaviour that would be expected from a cylindrical shell. The plateau shown in the reference between the low frequency modal behaviour and the ring frequency is absent on the current model, replaced by a dip with roughly the same width. The ring, coincidence and cylinder pseudo-coincidence frequencies are estimated correctly.

3.2 Sandwich shell

The current model is also applied to a sandwich with thick viscoelastic core and compared to reference [72]. The results are shown on Figure 3.4. The cylinder's diameter is $R = 2.164$m, and the other parameters of the model are defined in Table 3.1. Again the characteristic frequencies of the cylinder are estimated correctly, the only difference with the reference being below the ring frequency at 100Hz. It can be noted that for several frequencies below 100Hz, corresponding to modes of the cylinder close to the ring frequency, the TL is negative, which also happens in the reference model, though with smaller values. These localised discrepancies between the two models are still unexplained, but maybe due to an error in the reconstruction of the reference model.

Layer	Skins	Core
Density (kg.m^{-3})	1600	1000
E_z (Pa)	$1.379{\cdot}10^{11}$	$1{\cdot}10^{6}$
E_y (E_θ) (Pa)	$8.96{\cdot}10^{9}$	$1{\cdot}10^{6}$
G_{zy} ($G_{z\theta}$) (Pa)	$7.1{\cdot}10^{9}$	$3.4{\cdot}10^{5}$
G_{zx} (G_{zr})(Pa)	$7.1{\cdot}10^{9}$	$3.4{\cdot}10^{5}$
G_{yx} ($G_{\theta r}$)(Pa)	$6.2{\cdot}10^{9}$	$3.4{\cdot}10^{5}$
Poisson's ratio	0.3	0.49
Damping η (%)	0	5
h (mm)	2	12
Number of elements	4	50

Table 3.1 – Parameters of the cylindrical sandwich shell model.

4 Conclusion and discussion

A new method for the computation of transmission loss through arbitrarily layered cylindrical shells has been presented in this work. Compared to existing models, it is shown to predict the TL correctly above the ring frequency, but the results are less accurate in the mode-governed

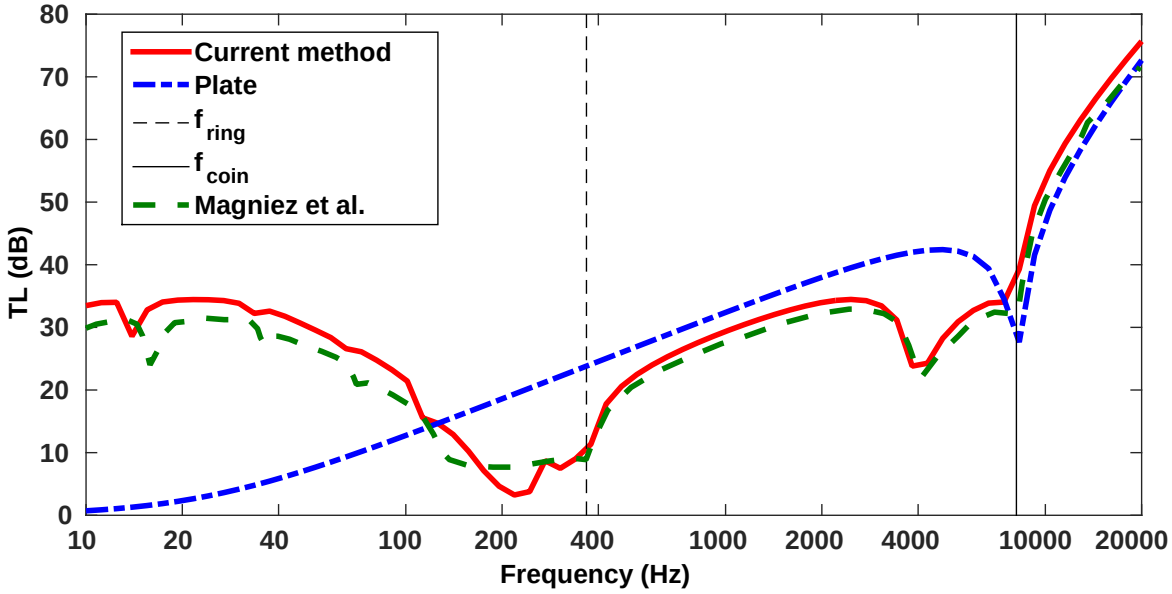

Figure 3.3 – Transmission loss through an aluminium cylindrical shell under 45° plane wave.

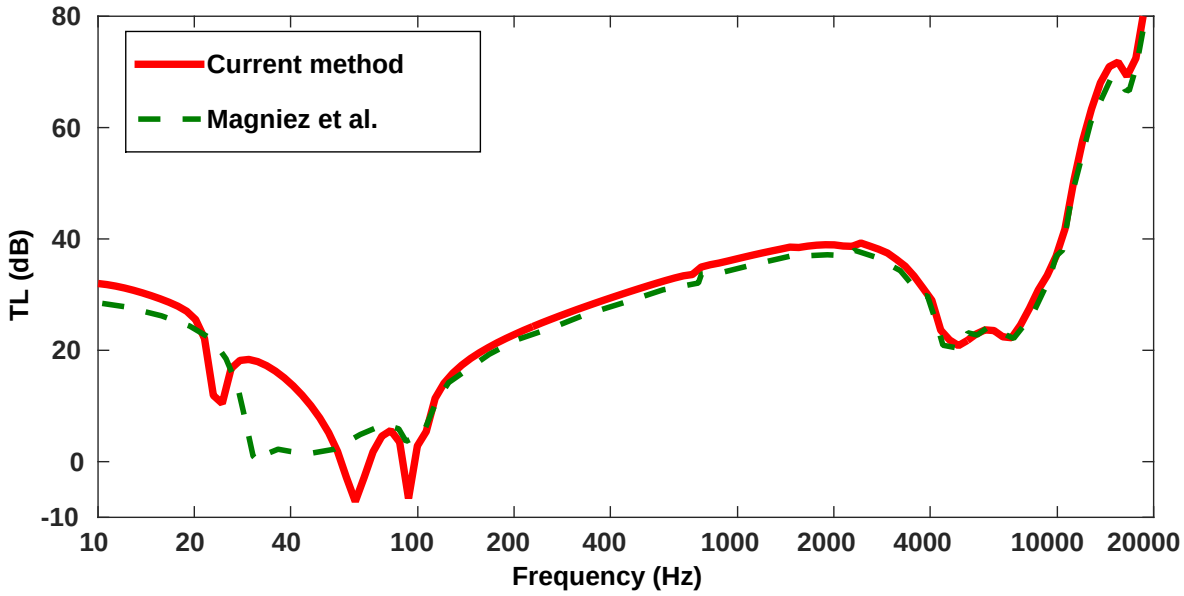

Figure 3.4 – Transmission loss through an sandwich cylinder with thick and soft core under 45° plane wave.

region below it. The method is also very sensitive to numerical errors: the chosen unit cell has to be very close to a square in order to yield correct results. The main advantage of the proposed method is the fact that coupling between layers is naturally taken into account in the finite element model of the unit cell, which avoids having to develop new analytical formulations for each layer added.

This has potential practical interest especially if new physics are to be taken into account, for example acoustics or piezoelectric materials, and especially poroelastic materials. The U-U formulation with 6 DOFs per node can be directly applied with the presented development, provided the layers in contact with the inner and outer fluids are elastic solids, as the coupling conditions with air are slightly more complex to write. The U-p formulation with 4 DOFs per node necessitates in addition changes to the rotation matrix $\mathbf{R}$ in equation 3.17, and again the coupling conditions in case it is in contact with the fluid. In either case, the coupling with the elastic parts is "naturally" taken into account in the FE code. Another possible improvement is in the use of periodic cells, involving more than one element in the surface directions.

Appendix: Useful expressions involving Bessel and Hankel functions

The coefficient of the Fourier series expansion of the plane wave yield integrals with the following form [1]:

$$J_n(z) = \frac{\mathrm{i}^{-n}}{2\pi} \int_{-\pi}^{\pi} \exp(\mathrm{i}n\theta) \exp(\mathrm{i}z\cos\theta)\mathrm{d}\theta \tag{3.39}$$

Hankel functions are defined from the Bessel functions of the first and second kinds as

$$H_n^1(z) = J_n(z) + \mathrm{i}Y_n(z) \tag{3.40}$$

$$H_n^2(z) = J_n(z) - \mathrm{i}Y_n(z) \tag{3.41}$$

The derivatives of the Bessel function that appear in the impedance expressions equation 3.13 can be computed with the following recurrence relations:

$$J_n'(z) = \frac{n}{z} J_n(z) - J_{n+1}(z) \tag{3.42}$$

$$H_n^{1'}(z) = \frac{n}{z} H_n^1(z) - H_{n+1}^1(z) \tag{3.43}$$

$$H_n^{2'}(z) = H_{n-1}^2(x) - H_{n+1}^2(x). \tag{3.44}$$

Part II

Sensitivity analysis of sound transmission models

Chapter 4

Literature review on sensitivity analysis

Contents

1 Introduction

Uncertainties and variability occur very often in vibroacoustic design. In early conception stage, many parameters of the structure may not be known exactly, such as geometric quantities (thicknesses, diameters...) or materials. Other uncertainties may appear later in the development cycle, due for example to manufacturing limitations. It is therefore interesting to get some knowledge on how uncertain parameters influence the result, which parameters are important and which are less. Sensitivity analysis relates to a class of methods aiming at quantifying the relative importance of parameters on the model output. The first question arising is that of the definition of a model.

In the following chapter, a model will be a black-box mathematical function f with n inputs and one output. The inputs $(x_1, ..., x_n)$ are the parameters, such as masses, material properties, or geometric features. The output y is the quantity of interest. In our case, this can be any vibroacoustic indicator, NR, TL or other. This representation is depicted on Figure 4.1.

The model function f usually cannot be represented explicitly and is evaluated through a complex computer code. We are then interested in computing influence measures for all parameters, which is the goal of sensitivity analysis.

Sensitivity analysis methods can be separated in two groups, namely local and global methods. Local methods look for indices in the vicinity of a reference point, such as the nominal value of all parameters, whereas global methods give indications on a larger range. The other difference between local and global methods is their computational cost, as local methods need typically very few calls to the model function, whereas global methods need to cover a broad range, and therefore require many more model evaluations. This can be overcome by the use of a metamodel, which can capture the behaviour of the model function at a reduced computational cost.

This chapter is structured as follows. Section 2 presents some definitions that will be used throughout this report. Section 3 is a review of global sensitivity analysis methods, focused especially on the analysis of variance. Section 5 gives an example of comparison between local and global sensitivity analysis methods. Finally, section 6 is a review of metamodelling technique with emphasis on kriging.

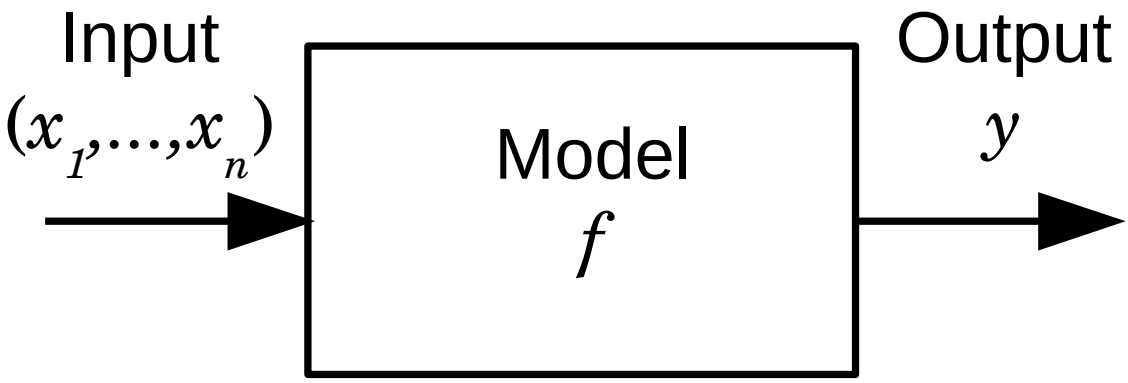

Figure 4.1 – Schematic representation of a model function

2 Definitions

2.1 Model

Throughout this chapter, we will be dealing with a model function f with n input parameters $x_1, ..., x_n$, and one output y. This function is defined over the unit hypercube $K = [0, 1]^n$, and the output is real, which can be summarized in the following equation:

$$\begin{array}{rccc} f: & K & \to & \mathbb{R} \\ & (x_1, ...x_n) & \mapsto & y \end{array}$$

The physical parameters are usually very different in nature, and the type of uncertainty that affects them is not always the same. For example, there can be a Young modulus, with typical order of magnitude of 10^{10}Pa, and a Poisson ratio, which is non-dimensional and for an isotropic material lies strictly between -1 and 0.5. The definition ranges of the physical parameters reflect the uncertainties or design latitudes. In any case, this definition range has to be scaled back to the $[0, 1]$ interval by means of a one-to-one map. This is easy to do when dealing with uniform probability laws, in which case one has to map a bounded interval to another. In case the uncertainty is defined by another kind of probability law, the mapping is the inverse cumulative distribution function (CDF) of the law.

2.2 Notations

In the following development, n will be a positive integer. The notation $\mathfrak{P}(n)$ represents the set of all subsets of the integer interval $[1, n]$. Let $\mathbf{x} \in K = [0, 1]^n$ be a vector of parameters,

and $U \in \mathfrak{P}(n)$ a subset of indices. We can also write $U = (i_1, ..., i_s)$.

3 Global sensitivity analysis

Global sensitivity analysis is a broad category of methods aimed at finding global indices characterising the sensitivity of the model to its parameters. Several classes of sensitivity analysis methods have been proposed, which are reviewed in [46], however the most interesting ones all relate to the ANOVA framework, which will be presented in detail in the following.

3.1 The ANOVA framework

The analysis of variance (ANOVA) class of sensitivity analysis methods is a very interesting tool to study the influence of individual parameters on the output result of a model, as well as possible interactions between input parameters. These techniques are based on Sobol's work [107].

For any model such as defined in section 2, there exists a decomposition, called the Hoeffding decomposition or High Dimensionality Model Representation (HDMR):

$$y = f(x_1, ..., x_n) = f_0 + f_1(x_1) + ... + f_n(x_n) + f_{12}(x_1, x_2) + ... + f_{1...n}(x_1, ..., x_n), \quad (4.1)$$

which also writes in a condensed form as:

$$y = \sum_{U \subset [1,n]} f_U(\mathbf{x}|_U), \quad (4.2)$$

where $f_\emptyset = f_0 = \int_K f(X)\mathrm{d}\mathbf{x}$ is the mean value of f over its range of definition, and $\mathbf{x}|_U$ denotes the restriction of the parameter vector $\mathbf{x} = (x_1, .., x_n)$ to the subset U.

Sobol's theorem states that this decomposition is unique provided that for any subset of parameters U, the mean value of f_U over its range of definition is zero, that is:

$$\int f_U \mathrm{d}\mathbf{x}|_U = 0 \quad (4.3)$$

For $U = \{i_1, \ldots, i_s\} \in \mathfrak{P}(n)$, the function f_U writes :

$$f_U(X|_U) = \int_{K|_{\widetilde{U}}} f(X)\mathrm{d}X|_{\widetilde{U}} - \sum_{\substack{I \in \mathfrak{P}(n) \\ \#(I) < s}} f_V(x|_V) \quad (4.4)$$

where $\widetilde{U}$ stands for the complementary set of U in interval $[1, n]$, and $\mathbf{x}|_U = (x_{i_1}, \ldots, x_{i_s})$.

The notation $\#(I)$ is used for the number of elements in the discrete set I.

The total variance of the system is then

$$V = \int_K f^2(X)\mathrm{d}X - f_0^2. \tag{4.5}$$

The main idea of the ANOVA technique is to use a decomposition of this variance in the same way as the HDMR.

3.2 Sobol's sensitivity indices

For each subset of parameters U, we define a partial variance as the contribution of subset $X|_U$ to the total variance:

$$V_U = \int_{K|_U} f_U^2(\mathbf{x}|_U)\mathrm{d}\mathbf{x}|_U. \tag{4.6}$$

The sensitivity index relative to subset U is then the ratio of the partial variance to the total variance:

$$\mathrm{SI}(U) = \frac{V_U}{V}. \tag{4.7}$$

As all functions in the HDMR decomposition of equation 4.1 have zero mean, the total variance can be decomposed the same way as the function, as $V = \sum_{U\in\mathfrak{P}(n)} D_U$, hence

$$\sum_{U\in\mathfrak{P}(n)} \mathrm{SI}(U) = 1. \tag{4.8}$$

The computation of all the 2^n sensitivity indices is needed to completely represent the model. This may quickly become a very costly task in terms of computational time, as they have to be evaluated by numerical integration. The most common method for this task is the Monte-Carlo integration [107]. However, most information about a parameter's influence can be found in the first-order sensitivity index and the total sensitivity index, which can be computed more efficiently with the FAST method.

For a given parameter $i \in [1, n]$, the main effect (ME) is then the sensitivity index relative to the 1-dimensional function f_i:

$$\mathrm{ME}(i) = \frac{V_{\{i\}}}{V} \tag{4.9}$$

Another interesting sensitivity measure for a given parameter i is the total sensitivity index, defined as the sum of the indices of all sets of parameters U to which i belong.

$$\mathrm{TSI}(i) = \sum_{\substack{U\in\mathfrak{P}(n)\\ i\in U}} \mathrm{SI}(U). \tag{4.10}$$

To quantify the influence of an individual parameter on the output result, it is useful to know both its main effect and total sensitivity index. The first one is a measure of the share of the variance induced by the parameter alone, while the second is a measure of the quantity that would be removed from the total variance if the considered parameter was fixed to a reference value. The difference between the two is a measure of the interactions in which the parameter is involved.

3.3 Interpretation

By definition, the sensitivity indices range between 0 and 1. The sum of main effects is less than or equal to 1. The difference $1 - \sum_{i=1}^{n} \mathrm{ME}(i)$ is a measure of how much interaction there is between parameters to produce the variance, i.e. how much of the variance cannot be explained by variations of each parameter individually. This difference is exactly zero only for functions whose outputs are linear combinations of 1D functions of the input parameters. Those functions are called additive models. For such models, main effect and total sensitivity index are equal. For the other models, the first-order index represents the share of the output variance that is explained by the considered parameter alone. Most important parameters therefore have high ME, but a low ME does not mean the parameter has no influence, as it can be involved in interactions.

The total index is a measure of the share of the variance that is removed from the total variance when the considered parameter is fixed to its reference value. Therefore parameters with low TSI can be considered as non-influential. The difference between TSI and ME is a measure of the interactions in which the parameter is involved.

Both ME and TSI represent shares of the variance of the function, which allows for an interesting graphical representation of the sensitivity indices as a function of another parameter, which we will call list parameter, and which will often be frequency in the following development. Instead of plotting the first-order sensitivity indices, one may indeed plot the related partial variances stacked on top of each other, the difference between their sum and the total variance being a measure of the interactions occurring in the model.

Because its dimension is the same as that of the model output, the standard deviation can be a more readily understandable indicator of the output variability. However, while the HDMR decomposition (equation 4.1) is valid for the variance, it no longer holds for the standard deviation, which means the previous graphical representation in terms of standard deviation only has a qualitative meaning, and by no means quantitative. In other words, the sensitivity index can be said to explain a fraction of variance, but not of the standard deviation, which does not reduce much the interest of such graphs, which are used in chapter 7.

4 The FAST method

The FAST (Fourier Analysis Sensitivity Test) method was introduced in 1973 by Cukier et al. [26] to study chemical reactions, and was later proven equivalent to the computation of Sobol's first-order indices. It was later extended by the work of Saltelli et al. [99] to improve robustness. The same work introduced a method to compute the total sensitivity indices. The idea behind the FAST method is to compute all first-order sensitivity indices at the same time by using a clever sampling of the design space which can be treated with Fourier analysis, instead of computing all integrals in equation 4.6.

4.1 Evaluation of 1st order sensitivity indices

The sampling proposed by Schaibly and Shuler [102] is defined by the following parametric curve

$$x_i(s) = \frac{1}{2} + \frac{1}{\pi} \arcsin(\sin(\omega_i s + \varphi_i)) \tag{4.11}$$

where the frequencies ω_i are integers chosen so as to minimize interference between parameters. An example of such a curve sampling the 2D unit square is shown in Figure 4.2.

The random phase φ_i was proposed by Saltelli et al. [99] to improve the "space-filling" property of the sampling curve. One possibility is to run several analyses with different values of the phases φ_i and take an average to ensure robustness of the result. The evolution of variable $s \in [0, 2\pi]$ is dependent on the probability density function of the actual variables. For a uniform probability density of all parameters in their definition ranges, s will sample interval $[0, 2\pi]$ equally. Due to Shannon's theorem, the number of samples must be greater than twice the highest frequency $\max(\omega_i)$. The frequencies ω_i are said to be free of interference up to order M if the following relation

$$\sum_{i=1}^{n} \alpha_i \omega_i \neq 0 \tag{4.12}$$

holds for all linear combinations with coefficients $\alpha_i \in \mathbb{Z}$ and $\sum_{i=1}^{n} |\alpha_i| < M$.

Value tables for $M = 4$ have been determined empirically and are given for up to 19 parameters in Table 4.1 in [102] and up to 50 parameters in [79]. For less than 20 parameters, the first ones should be used, as the maximum frequency is smaller, thus reducing the number of samples needed.

As all frequencies are integers, the resulting function is 2π-periodic with respect to variable s. The sampling is then done using $N > 2\omega_n + 1$ samples in the $[0, 2\pi]$ interval. Calling

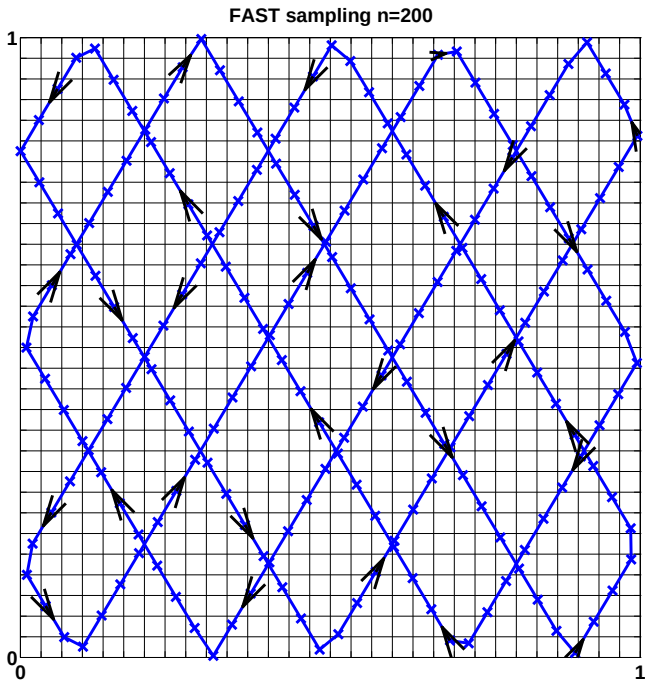

Figure 4.2 – "Space-filling" curve for n=2, $\omega_1 = 5$, $\omega_2 = 3$ and 200 sample points. The arrows indicate the increasing values of s

Number of parameters	Frequencies
5	[11; 21; 27; 35; 39]
6	[1; 21; 31; 37; 45; 49]
7	[17; 39; 59; 69; 75; 83; 87]
8	[23; 55; 77; 97; 107; 113; 121; 125]
9	[19; 59; 91; 113; 133; 143; 149; 157; 161]
10	[25; 63; 103; 135; 157; 177; 187; 193; 201; 205]

Table 4.1 – Integer frequencies for the FAST method free of interference up to order 4 for 5 to 10 parameters. Values for less than 5 parameters can be derived by taking the first values of the first line.

$y_k = f(x_k)$ the model output on each sample, the discrete Fourier transform $\hat{y}_k$ can be computed.

The total variance of the function in the design space is computed with Parseval's theorem as:

$$V = \int_K \left(f^2(x) - f_0^2\right) \mathrm{d}x \approx \sum_{k=1}^{N} y_k^2 = \sum_{k=1}^{N} \hat{y}_k^2 \tag{4.13}$$

The sum of the M first multiples of i

$$V_i = \sum_{k=1}^{M} \hat{y}_{k\omega_i} \tag{4.14}$$

is then the main contribution of parameter i to the variance, excluding interactions with other parameters. The ratio

$$\mathrm{ME}(i) = \frac{V_i}{V} \tag{4.15}$$

is called the *main effect* or first-order sensitivity index of parameter i.

4.2 Evaluation of total sensitivity indices

A method for the computation of the TSIs is proposed in [99]. For this purpose one analysis must be done for each parameter, which is longer than the estimation of main effects, but still faster than the evaluation of all integrals needed to assign a "high" frequency ω_i to parameter i and "low" frequencies to all other parameters. The low frequencies must be integers smaller than ω_i/M. Ultimately, only one frequency could be used for the other parameters, but choosing a group of frequencies increases the space-filling property of the sampling curve.

The same sampling curve as defined in equation 4.11 is used with these frequencies. The total sensitivity index of parameter i is then

$$\mathrm{TSI}(i) = 1 - \frac{V_{\sim i}}{V} \tag{4.16}$$

where $V_{\sim i}$ is the partial variance relative to the group of all parameters except i.

5 Local sensitivity analysis

5.1 Partial derivative analysis

Local sensitivity analysis is generally achieved through the evaluation of the partial derivatives of the model function f with respect to all its variables. In order to enable comparison between these derivative, the parameters should be non-dimensional. The sensitivity index of parameter i is then

$$\mathrm{LSI}(i) = \frac{\partial f}{\partial x_i} \tag{4.17}$$

This index can be normalized by the sum of the absolute values of all indices in order to get a result in the $[-1, 1]$ interval. The advantages of local sensitivity indices are twofold:

- they are easy to compute with a finite difference scheme, and need only $n+1$ evaluations of the model function for a non-centred scheme, and
- their signs give an indication of the direction of the effect of the parameter.

However, local sensitivity indices give only information about the behaviour of the function in a very narrow range around the nominal value, and may not be relevant for non-linear models with broad varition ranges. Besides, interaction between parameters, which usually derive from non-linearities in the model function, are not captured. The following example shows the interest of using global sensitivity over partial derivative sensitivity.

5.2 2D example

The following bivariate function defined over $[0, 1] \times [0, 1]$ will be studied as an example for a comparison between local and global sensitivity methods:

$$f(x_1, x_2) = \mathrm{Re}\left(\frac{1}{1 + 2i\xi(x_1, x_2) + 4\xi(x_1, x_2)^2}\right), \tag{4.18}$$

where

$$\xi = x_1 - \frac{1}{5}\tanh\left(50(x_2 - \frac{1}{2})\right) - 2/5 \tag{4.19}$$

This function is represented on Figure 4.3.

Visually, most of the behaviour is explained by the first variable x_1, while the second only has influence in the central zone of its definition range. If one only looks at the derivative at the center point of the domain (0.5,0.5), then the most important parameter in the sense of the partial derivative sensitivity is x_2. However, a FAST analysis, summarized on the bar chart of Figure 4.4, gives a more intuitive result, namely that the ME of x_1 is greater than that of x_2. The sum of the MEs being far from 1, there is a high level of interaction between the two parameters, as can be observed from the difference between ME and TSI.

6 Metamodelling

As we have seen in the previous sections, global sensitivity analysis rely on a high number of calls to the model function, which can become costly if the function takes a significant amount of time to be evaluated. Several methods can be used to overcome this limitation,

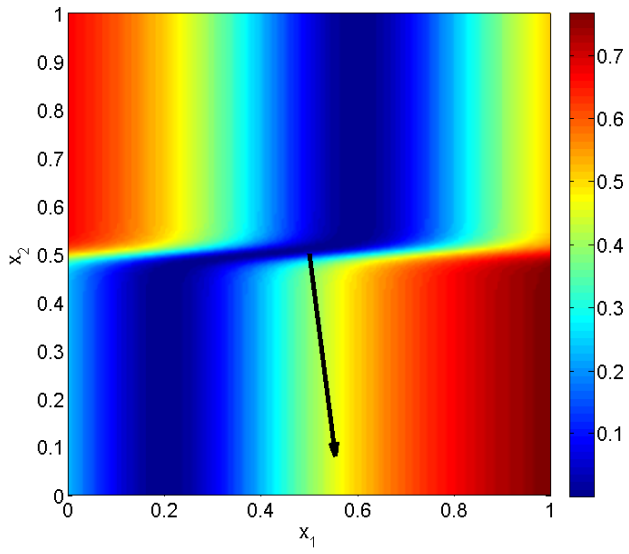

Figure 4.3 – Graph over $[0,1]^2$ of the 2D function defined in equation 4.18. The arrow represents the gradient at the central point (0.5,0.5).

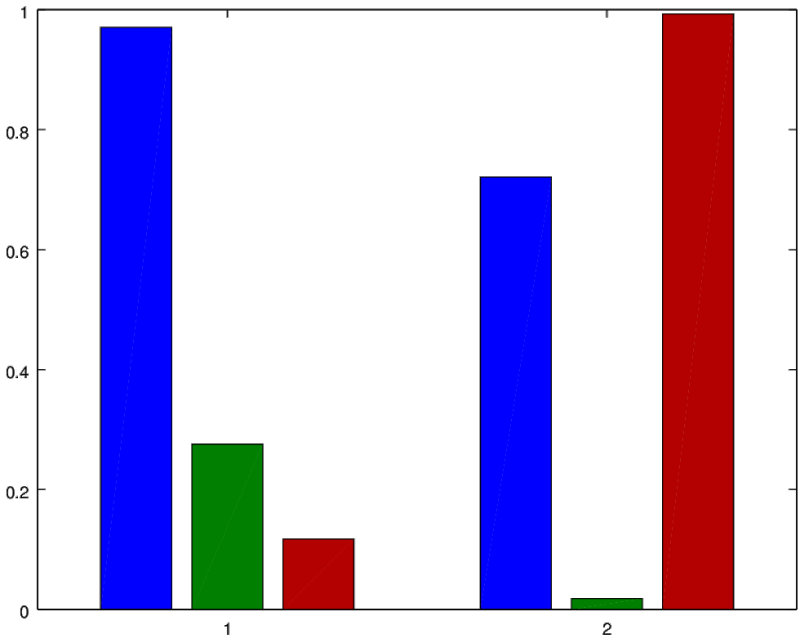

Figure 4.4 – Different sensitivity results on the function 4.18. The first group is for x_1, the second for x_2. In each group, the first bar (blue) is the TSI, the second (green) the ME and the third (red) the normalized partial derivative LSI.

the most frequent ones being the use of reduced models and metamodelling. Whereas a reduced model is built with the aim of diminishing the number of degrees of freedom of the model while respecting the underlying physics of the problem, a metamodel is a much simpler mathematical estimate computed with evaluations of the model at a few control points. This can greatly reduce the time needed for the sensitivity analysis, as the metamodel evaluation is much cheaper than the model itself, and most of the time used for analysis is due to model evaluation.

Given a number of known points of the response function, several methods exist to build an estimate of the real function at every point of its definition space. The simplest is linear regression, trying to fit a linear function through the samples. One can also cite Lagrange interpolation, neural networks, support vector machines [101], and Gaussian process metamodelling (kriging) [52]. Being the only one used in this thesis, only the latter will be explained in detail in the following.

6.1 Latin Hypercube sampling

The Latin hypercube (LH) [113] sampling is a quasi-random sampling technique which allows to sample the design range equally. Let p be the dimension of the design space, that is, the number of parameters of the models. With appropriate scaling, the design space can be reduced to the p-dimensional hypercube $K = [0, 1]^p$. For an LH sampling with N points, the hypercube K is divided in N equal parts along each dimension, hence N^p parts. From these, a subset of N parts is randomly chosen so that exactly one small hypercube in each dimension is in the set. One random sample is the chosen in each of the selected hypercubes. An Optimal Latin hypercube sampling (OLH) is one that maximizes the minimum distance between two samples (*minimax* criterion). Because there exist $N!$ possible Latin hypercubes, it is impractical to find an OLH for reasonable values of N, but the aforementioned process can be repeated several times to approximate an OLH. This technique avoids the "clumps" of points that may occur in purely random sampling, while keeping some randomness in the sampling process. Figure 4.5 presents a comparison between a LH sample and a random sample with the same number of points. The sampling points are better spread over the sampling range in the LH sampling scheme than in the purely random one.

6.2 Kriging

Gaussian process metamodelling, also called kriging after its inventor engineer Daniel Krige, has its origins in geophysics, but has been used for many applications. A more or less standard implementation is the Matlab toolbox DACE [68]. Marrel et al. [77] proposed to

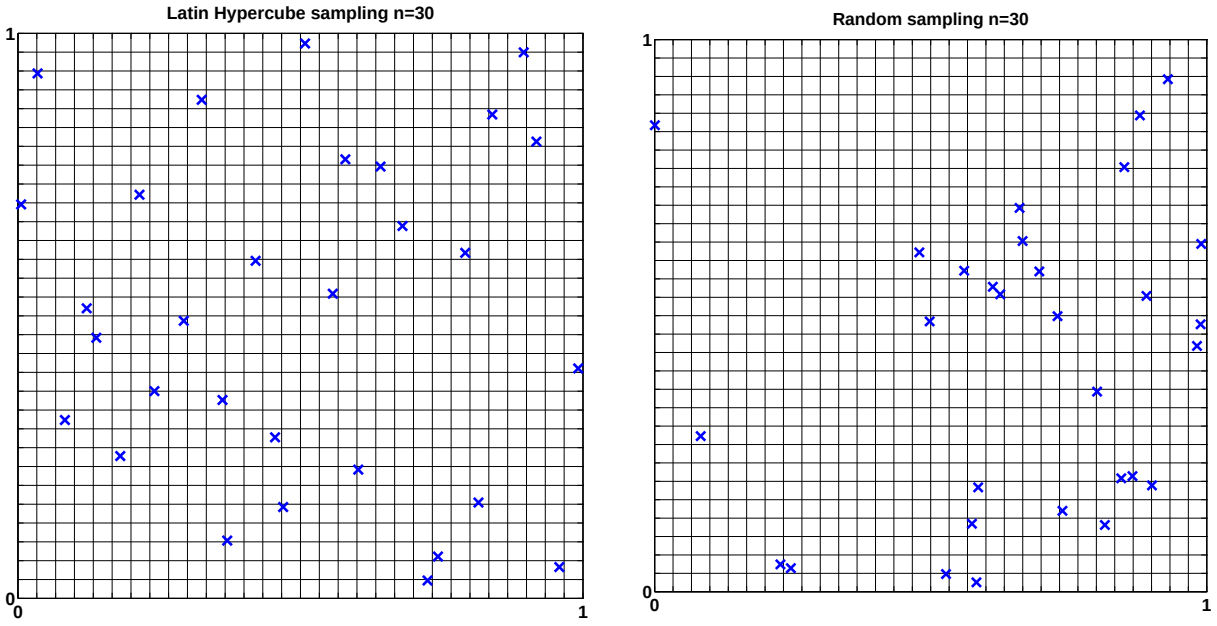

(a) Latin Hypercube Sampling

(b) Random sampling

Figure 4.5 – Comparison of LH and random sampling for 30 points in the 2D unit square

apply Gaussian process metamodelling prior to a process of sensitivity analysis implying a very heavy computer code.

The Gaussian process metamodelling [52] is based on a decomposition of the model function into a regression part and a "stochastic part". Let the unknown model function f be computed over a sample of m points $(\mathbf{x}_1, ..., \mathbf{x}_m)$, and the values at these points be called $y_i = f(\mathbf{x}_i)$. Polynomial regression is usually considered for the former part, so that we can write:

$$f(\mathbf{x}) = P(\mathbf{x}) + Z(\mathbf{x}), \tag{4.20}$$

where $P(\mathbf{x}x)$ is a polynomial in with respect to the components of $\mathbf{x}$. In our case, we assume a zero-order (constant) polynomial regression, so that $P(x) = \sum_{i=1}^{m} y_i/m$ is a constant scalar, taken to the mean value of the function over its definition set.

The stochastic part $Z(\mathbf{x})$ is assumed to be a centred stationary Gaussian process, meaning that the value at point $\mathbf{x}$ depends only on the distance to the known points $\mathbf{x}_i$ (and of course on the known values y_i at these points). It is characterized by its covariance function σ. The word "stationary" here means that the covariance function depends only on the distance

between the considered points. The covariance between two points is then

$$\mathrm{cov}(\mathbf{x}_i, \mathbf{x}_j) = \prod_{k=1}^{n} \sigma\left(\theta \left| x_i^{(k)} - x_j^{(k)} \right|\right), \tag{4.21}$$

where θ is a parameter defining the distance in the parameter space at which two parameters are independent of each other. The DACE toolbox [68] estimates it with a maximum of likelihood estimator (MLE).

The spherical covariance function

$$\sigma(r) = \begin{cases} 1 - 1.5r + 0.5r^3 & \text{if } r \leqslant 1 \\ 0 & \text{if } r > 1 \end{cases} \tag{4.22}$$

is preferred for our case, as it is continuously differentiable, but non-zero only on a compact domain, meaning that the contribution of points far away from the estimate is exactly zero. Thus, the matrix Γ and correlation γ are sparse and the computation is eased when the number of sampling points m is high. Once the covariance function is chosen, the estimated value at the new point $\mathbf{x}$ is calculated by $\hat{y} = \sum_{i=1}^{n} \lambda_i y_i$. The vector of optimal weights $\mathbf{w}(\mathbf{x})$ is again chosen with a MLE [52], so that:

$$\mathbf{w}(\mathbf{x}) = \Gamma^{-1}\left(\gamma(\mathbf{x}) + \mathbf{1}\frac{1 - \mathbf{1}'\Gamma^{-1}\gamma(\mathbf{x})}{\mathbf{1}'\Gamma\mathbf{1}}\right). \tag{4.23}$$

In this equation, Γ is the matrix of covariances between trial points $\Gamma_{ij} = \mathrm{cov}(\mathbf{x}_i, \mathbf{x}_j)$, γ denotes the vector of covariances between the points to be estimated and the known points $\gamma_i = \mathrm{cov}(\mathbf{x}_i, \mathbf{x})$, and $\mathbf{1}$ is a shorthand notation for a column vector of ones of the appropriate size. The desired value y at point $\mathbf{x}$ is finally evaluated with

$$y = \mathbf{w}^T(\mathbf{x})\mathbf{y} = \sum_{i=1}^{n} w_i(\mathbf{x}) y_i. \tag{4.24}$$

The advantage of this method is that most of the computational effort is made evaluating the function at the sampling points $\mathbf{x}_i$ and the inversion of matrix Γ, which has to be performed only once, the rest being simple analytical computations.

Chapter 5

Global sensitivity analysis of acoustic transmission models

This chapter is, with minor changes, based on a paper [19] published in the Journal of Sound and Vibration, with following authors: Jean-Loup Christen (ECL), Mohamed Ichchou (ECL), Bernard Troclet (Airbus Defence and Space), Olivier Bareille (ECL) and Morvan Ouisse (FEMTO-ST).

Abstract

Noise reduction issues arise in many engineering problems. One typical vibroacoustic problem is the transmission loss (TL) optimisation and control. The TL depends mainly on the mechanical parameters of the considered media. At early stages of the design, such parameters are not well known. Decision making tools are therefore needed to tackle this issue. In this paper, we consider the use of the Fourier Amplitude Sensitivity Test (FAST). FAST is implemented with several structural configurations. FAST method is used to estimate the relative influence of the model parameters while assuming some uncertainty or variability on their values. The method offers the way to synthesize the results of a multiparametric analysis with large variability. Results are presented for transmission loss of isotropic, orthotropic and sandwich plates excited by a diffuse field on one side. Qualitative trends found agree with the physical expectation. Design rules can then be set up for vibroacoustic indicators. The case of a sandwich plate is taken as an example of the use of this method inside an optimisation process and for uncertainty quantification.

Contents

1 Introduction

Noise control can be a very important topic in engineering, and noise reduction problems can take many forms. Among these, noise transmission is about the transmission of energy from an incident sound field through a structure into an enclosure. Typical situations include for example the phonic isolation of a building in civil engineering, noise reduction inside a plane's cabin or a car. One of the most used indicators in vibroacoustics is the transmission loss (TL), which is the ratio of incident to transmitted energies, expressed in decibels. Transmission loss through composite structures depends on numerous structural parameters, such as Young's modulus, density, honeycomb geometry or damping ratio of each constituent. Noise transmission through isotropic plates has become a classical vibroacoustic problem, for

which analytical solutions are derived in textbooks [36, 65]. The case of orthotropic plates has been studied by Guyader and Lesueur [44]. Renji et al. proposed models for the transmission loss of sandwich panels [93]. All these models are based on analytical expressions of bending wavenumbers in the considered plate. At early design stages, these parameters are unknown with potentially wide variation ranges, due to either uncertainty or design latitude. In order to efficiently set up an optimisation problem, it can be of first importance to find which parameters contribute most to TL variability. Later on in the design cycle, lack of knowledge will be reduced, but uncertainty may remain on some parameters, due for example to identification issues or industrial tolerances [33]. It is therefore important to find out how parameter variability will affect vibroacoustic indicators. Identifying which parameters contribute most to output variability can help focus on them for optimisation or uncertainty reduction.

A number of methods have been developed to address uncertainties in vibroacoustics. Reynders [97] uses the maximum entropy principle to compute confidence intervals for the TL of walls between two uncertain rooms, where the probability densities and cross-correlations of the considered parameters are known. Batko and Pawlik [9] use a method derived from interval arithmetics to estimate variability intervals for the same kind of constructions. Regarding industrial structures, a stochastic boundary element method (BEM) has been proposed by D'Amico et al. [28, 29] to estimate the variability of noise radiation by structures with geometric uncertainties. Cicirello and Langley [21] combined parametric and non-parametric uncertainty analyses on a hybrid FE-SEA method. In their recent book, Ohayon and Soize [85] review methods of uncertainty assessment in vibroacoustics, including non-parametric uncertainties. All these approaches give interval estimates of the model output given input parameter uncertainty, but do not describe the influence of each parameter on this variability.

Sensitivity analysis aims at identifying the relative influence of parameters. One of the most used methods is to study the partial derivatives of the model output with respect to all variables, which gives local estimates around a reference point. Global sensitivity analysis (GSA) [100] on the other hand aims at deriving indicators of influence for broad variation ranges. The ANOVA class of methods uses the variance decomposition [107] as an estimate for the sensitivity of each parameter. The computation of each term in the variance decomposition requires time-consuming calculation. The Fourier amplitude sensitivity test (FAST) was developed by Cukier et al. [26] to reduce the computation time, with application in the study of complex chemical reactions. This method has later been reused by Iooss et al. [51] for radiologic risk assessment models. Ouisse et al. [87] applied the FAST method to porous material models, regarding acoustic impedance and absorption. This work was later extended to different models of porous materials with focus on microgeometry in [34]. We

propose here an application of the FAST method to the analytical models of the transmission loss of infinite flat plates to illustrate the potential of global sensitivity analysis in this field.

It is important to remark that the ranking of parameters by order of influence on the transmission loss is not absolute, but depends on frequency. As the frequency ranges considered for noise transmission may be quite wide, the system will present very different behaviours in different regions of the excitation spectrum. Transmission of noise through a plate is due to the excitation of travelling waves in the plate by the incident sound, and the radiation on the other side created by these travelling waves. Radiation efficiency [64] varies depending on the relative wavenumbers of the waves propagating in the structure and the velocity of sound in the fluid. The peak of transmission is around the coincidence frequency, where these wavenumbers match. Below this frequency it is well known (see [36] for example) that the mass of the plate will be dominant, while for a plane wave, the bending stiffness will be preponderant in the higher frequency range. For anisotropic constructions, these results are still valid and well established [44], but the coincidence frequency is no longer well defined.

The main claims of the paper are: a study of the sensitivity of transmission loss of isotropic plates under plane wave and diffuse field excitations to parametric uncertainties. The trends provided by the FAST method are compared with common qualitative trends in the vibroacoustic community. The case of an orthotropic thin plate is then studied in the same way. Finer features corresponding to that case are highlighted that could not be obtained as easily with asymptotic expansion. Finally a less common sandwich panel is studied in the same framework, in order to investigate the effect of shear stiffness introduced by this model.

The paper is structured as follows. Section 2 presents an overview of the FAST global sensitivity analysis method used in this work. The mathematical framework and sensitivity indices are defined in this section. The general model of acoustic transmission of plane wave and diffuse field through an infinite plate is presented in section 3, then detailed in sections 4, 5 and 6 for the isotropic, orthotropic and sandwich plates respectively. Results of the FAST method are presented and analysed in these sections The case study of a sandwich panel in section 6 enables us to give hints on how this method could be applied to uncertain design in vibroacoustics.

2 The FAST method

2.1 Analysis of variance

The influence of a single parameter on the model output can be quantified by the impact it has on the variance in the given design range. In the following development, a generic mathematical model is considered. A model is defined as a real valued function f defined over $K = [0,1]^n$. With appropriate variable changes, any function defined over continuous ranges of parameters can be represented that way.

For a given model f mapping a vector of input parameters $\mathbf{x} = (x_1, ...x_n)$ to a scalar output $y = f(\mathbf{x})$, there exists a unique partition of f so that:

$$\begin{aligned} y =& f(x_1, x_2, ...x_n) = \sum_{U \subset [1,n]} f_U(x|_U) \mathrm{d}x|_U \\ =& f_0 + \sum_{i=1}^{n} f_i(x_i) + \sum_{1 \leqslant i < j \leqslant n} f_{ij}(x_i, x_j) + ... + f_{1...n}(x_1, ..., x_n), \end{aligned} \tag{5.1}$$

provided that each function f_U involved in the decomposition has zero mean over its range of variation $K|_U$, which is the subspace of K spanned by the dimensions contained in subset U. This writes:

$$\int_{K|_U} f_U(x_U) \mathrm{d}x_U = 0. \tag{5.2}$$

The decomposition given by Eq. (5.1) is called the Hoeffding decomposition or high order model representation (HDMR) [107].

For a given set of indices $U = \{i_1, \ldots, i_k\}$, the partial variance is therefore the variance of f_U:

$$V_U = \int_{K|_U} f_U(x_U)^2 \mathrm{d}x_U. \tag{5.3}$$

The sensitivity index relative to the set U is expressed as the ratio of the variance of the function f_U to the total variance of the model:

$$\mathrm{SI}(U) = \frac{V_U}{V}. \tag{5.4}$$

The computation of all the 2^n sensitivity indices is needed to fully represent the model, however this quickly becomes a very costly task in terms of computational time, as they have to be evaluated by numerical integration. However, most information about a parameter's influence can be found in the first-order sensitivity index and the total sensitivity index, which can be computed more efficiently with the FAST method.

For a given parameter $i \in [1, n]$, the main effect (ME) is then the sensitivity index relative to the 1-dimensional function f_i:

$$\mathrm{ME}(i) = \mathrm{SI}(\{i\}). \tag{5.5}$$

Another interesting sensitivity measure for a given parameter i is the total sensitivity index, defined as the sum of the indices of all sets of parameters U to which i belongs:

$$\mathrm{TSI}(i) = \sum_{\substack{U \subset [1,n] \\ i \in U}} \mathrm{SI}(U). \tag{5.6}$$

2.2 Main effect computation

The idea of the FAST method is to avoid the evaluation of the multi-dimensional integrals needed for the computation of the f_i functions, and replace them by a single 1-dimensional integral along a *space-filling* curve in the design space. This curve is defined so as to be periodic with different periods relative to each parameter. Saltelli et al. [99] propose the sampling function defined by:

$$x_i = \frac{1}{2} + \frac{1}{\pi} \arcsin\left(\sin\left(\omega_i s + \phi_i\right)\right). \tag{5.7}$$

The frequencies ω_i are integers chosen so as to minimize interferences between parameters [26], and the ϕ_i are random real numbers in the interval $[0, 2\pi]$. The set of integer frequencies $\{\omega_i\}$ is said to be free of interferences up to order M if all linear combinations

$$\sum_{i=1}^{n} \alpha_i \omega_i \neq 0, \tag{5.8}$$

where $\alpha_i \in \mathbb{Z}$ and $\sum_{i=1}^{n} |\alpha_i| < M$.

As all the frequencies are integers, the resulting function is 2π-periodic with respect to variable s. A sampling is then done using $N > 2\omega_n + 1$ samples in the $[0, 2\pi]$ interval. Calling $y_k = f(x_k)$ the model output on each sample, the discrete Fourier transform $\hat{y}_k$ can be easily computed numerically.

The values of the frequencies ω_i for $M = 4$ and less than 19 parameters have been found by Schaibly and Shuler [102] and are recalled up to 6 parameters in Table 5.1

The total variance of the function in the design space is computed with Parseval's theorem

Number of parameters	Set of frequencies
5	{11, 21, 27, 35, 39 }
6	{1, 21, 31, 37, 45, 49 }

Table 5.1 – Sets of integer frequencies ω_i for 5 and 6 parameters and $M = 4$. For $n < 5$, the n smallest values of the set for 5 parameters are used.

as

$$V = \int_K \left(f^2(x) - f_0^2\right) \mathrm{d}x \approx \sum_{k=1}^{N} y_k^2 = \sum_{k=1}^{N} \hat{y}_k^2. \tag{5.9}$$

The contribution of parameter i is then approximated by the sum of the coefficients indexed by the M lowest multiples of ω_i:

$$V_i = \sum_{k=1}^{M} \hat{y}_{k\omega_i}^2, \tag{5.10}$$

and the main effect is calculated as

$$\mathrm{ME}(i) = \frac{V_i}{V}. \tag{5.11}$$

These analysis steps are repeated for several (typically 3) draws of the ϕ_i and the results averaged over these draws. This ensures more robustness in the evaluation of the sensitivity indices.

2.3 Total sensitivity index computation

A method proposed in [99] is to assign one high frequency ω_i to parameter i and a set of low frequencies $\{\omega_{\sim i}\}$ to all other parameters. The same sampling curve as defined in Eq. (5.7) is used with these frequencies. Extracting the low frequency content gives the share of variance due to all parameters but i. The total sensitivity index of parameter i is then:

$$\mathrm{TSI}(i) = 1 - \frac{V_{\sim i}}{D}, \tag{5.12}$$

where $V_{\sim i}$ is the partial variance relative to all parameters but i.

2.4 Interpretation

By definition, the sensitivity indices range between 0 and 1. The sum of main effects (ME) is less than or equal to 1. The difference $1 - \sum_{i=1}^{n} \mathrm{ME}(i)$ is a measure of how much interaction there is between parameters to produce the variance, i.e. how much of the variance cannot

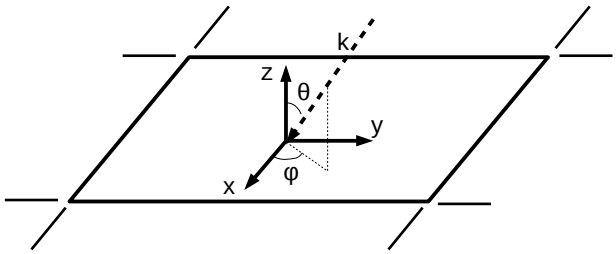

Figure 5.1 – Notations used for geometric parameters.

be explained by variations of each parameter individually. This difference is exactly zero only for functions whose outputs are linear combination of the input parameters, also called additive models. For such models, main effect and total sensitivity index are equal.

The value of the ME represents the share of the output variance that is explained by the considered parameter alone. Most important parameters therefore have high ME, but a low ME does not mean the parameter has no influence, as it can be involved in interactions.

The total sensitivity index (TSI) is a measure of the share of the variance that is removed from the total variance when the considered parameter is fixed to its reference value. Therefore parameters with low TSI can be considered as non-influential.

3 Sound transmission through plane structures

The general set-up that will be studied in the following is made of an infinite plate located in the plane $z = 0$, separating two half-spaces filled with a light fluid with density ρ_0 and characteristic sound speed c_0. A plane pressure wave of pulsation ω travels in the half space $z < 0$ with an angle θ with respect to the $x - y$ plane and a trace direction φ in the $x - y$ plane. The notation is presented in Figure 5.1.

This situation leads to a incident acoustic pressure field in the half-space $z < 0$ that can be written as:

$$p_I = p_0 \exp\left(\mathrm{i}(\omega t - \mathbf{k} \cdot \mathbf{x})\right), \tag{5.13}$$

where $\mathbf{k} = \begin{pmatrix} k_x & k_y & k_z \end{pmatrix}^T = \frac{\omega}{c_0} \begin{pmatrix} \sin\theta\cos\varphi & \sin\theta\sin\varphi & \cos\theta \end{pmatrix}^T$ is the wave number vector, $\mathbf{x} = \begin{pmatrix} x & y & z \end{pmatrix}^T$ is the position vector of the current point in space and $\mathrm{i}^2 = -1$. The sound speed in the fluid is denoted by c_0. From now on, time harmonic dependence of all pressure and displacement quantities will be assumed, and the factor $\exp(\mathrm{i}\omega t)$ will be omitted from the equations in the remaining of the article.

The interaction between the incident wave and the plate creates a forced wave in the

plate, with the same pulsation ω. The wave vector of this wave is:

$$\mathbf{k} = \frac{\omega}{c_0} \sin\theta \begin{pmatrix} \cos\varphi \\ \sin\varphi \end{pmatrix}. \tag{5.14}$$

The plate in turn radiates acoustic plane waves on both sides, a transmitted wave of magnitude p_T and a reflected wave p_R in the $z > 0$ and $z < 0$ half-spaces respectively.

The coupling is characterized by the continuity of normal speed at the interface between the fluid and the plate, hence on either side of the structure we have :

$$\frac{\partial p}{\partial z} = \rho_0 \omega^2 w, \tag{5.15}$$

where w is the displacement of a point in the plate in the z-direction. On the incident side, we get:

$$-\mathrm{i}k_z(p_I - p_R) = \rho_0 \omega^2 w, \tag{5.16}$$

and on the transmission side:

$$-\mathrm{i}k_z p_T = \rho_0 \omega^2 w. \tag{5.17}$$

We then have easily:

$$p_R = p_I - p_T. \tag{5.18}$$

Introducing the characteristic impedance of the fluid $Z_0 = \rho_0 c_0$, we obtain:

$$w = p_T \cos\theta / (\mathrm{i}\omega Z_0). \tag{5.19}$$

The other equation needed to solve the problem is the forced vibration equation in the plate, which depends on the nature of the plate and the direction of the incident wave. It can be written under the general form:

$$L(k_x, k_y, \omega) w = q, \tag{5.20}$$

where L is a linear operator, and the load q is in this case:

$$q = p_I + p_R - p_T = 2(p_I - p_T). \tag{5.21}$$

The structural impedance of the system is the ratio between load and normal speed, which reads:

$$Z = \frac{L}{\mathrm{i}\omega}. \tag{5.22}$$

As we are concerned with the forced response of the plate to an oblique plane wave, the projection of the wavenumber onto the plate's plane is constant, and equal to:

$$k = \frac{\omega}{c_0} \sin\theta. \tag{5.23}$$

For the cases presented in this paper, the impedance Z can be expressed as a complex number in the frequency domain.

Combining equations 5.19 through 5.22, we obtain a relationship between the incident and transmitted pressures:

$$\frac{p_T}{p_I} = \left(\frac{Z\cos\theta}{2Z_0} + 1 \right)^{-1}. \tag{5.24}$$

The intensity of sound on one side is $I = \rho c |p|^2$, and the acoustic transparency of the plate is defined as the ratio of intensities on both sides, so:

$$\tau = \frac{I_T}{I_I} = \left| \frac{p_T}{p_I} \right|^2. \tag{5.25}$$

It is usually more convenient to express the noise reduction capability of a structure as a logarithmic quantity, called the transmission loss:

$$\mathrm{TL} = -10 \log_{10} \tau. \tag{5.26}$$

It is important to note that this expression for the transmission loss is valid for a plane wave characterized by its direction angles θ and φ. Another interesting case in the industry is that of the diffuse field, which is a superposition of plane waves from random incidences. This assumption is valid above a limit frequency [65].

The diffuse field transparency can be calculated from the plane wave one as a weighted average over all possible incidence angles θ and directions φ:

$$\tau_d = \frac{\int_{\theta_{\mathrm{inf}}}^{\theta_{\mathrm{sup}}} \int_0^{2\pi} \tau(\theta,\varphi) \cos\theta \sin\theta \mathrm{d}\varphi \mathrm{d}\theta}{\int_{\theta_{\mathrm{inf}}}^{\theta_{\mathrm{sup}}} \int_0^{2\pi} \cos\theta \sin\theta \mathrm{d}\varphi \mathrm{d}\theta}. \tag{5.27}$$

Several choices can be made concerning the limits of the integration range, we will consider here a full range with $\theta_{\mathrm{inf}} = 0$ (normal incidence) and $\theta_{\mathrm{sup}} = \pi/2$ (grazing incidence). This choice may have a large influence on the value of the TL, but not on the following sensitivity analysis.

4 Isotropic plates

4.1 Model

Infinite isotropic plates can be defined by a single geometrical parameter, their thickness h, and four material parameters, namely Young's modulus E, Poisson's ratio ν, density ρ and hysteretic damping η. The governing equation for thin isotropic plates is:

$$D\nabla^4 w - \omega^2 m w = q, \tag{5.28}$$

where $D = \dfrac{Eh^3}{12(1-\nu^2)}(1+\mathrm{i}\eta)$ is the bending stiffness of the plate and $m = \rho h$ is the surface density. As all directions in the plane are equivalent, there is no dependency on the direction φ, so $\nabla = \frac{\partial}{\partial x} = -\mathrm{i}k = -\mathrm{i}\frac{\omega}{c_0}\sin\theta$. The equation then reduces to:

$$\left(D\left(\frac{\omega}{c_0}\right)^4 \sin^4\theta - \omega^2 m\right) w = q, \tag{5.29}$$

and the structural impedance is:

$$Z(\omega,\theta) = \mathrm{i}\omega m\left(1 - \omega^2 \frac{D}{m c_0^4}\sin^4\theta\right). \tag{5.30}$$

The acoustic transparency can then be computed as per Eq. (5.25) for the oblique plane wave case and Eq. (5.27) for the diffuse field case. In the case of an excitation by a oblique plane wave, the transmission loss exhibits a minimum for the so-called *coincidence* frequency:

$$f_{coin} = \frac{c^2}{2\pi \sin^2\theta}\sqrt{\frac{m}{\mathrm{Re}D}}, \tag{5.31}$$

where the bending wave group velocity in the plate meets the trace speed of the incident sound wave. At this frequency, the plate's impedance reaches a minimum, which is zero if there is no damping. Bending waves below f_{coin} are called subcoincident, and supersonic at frequency above coincidence.

4.2 Results

A FAST analysis was first conducted on the analytical model of an infinite isotropic plate with 6 mm thickness, with parameters uniformly distributed in the ranges defined in Table 5.2, corresponding to typical values for aluminium with ±10% variation. This rather high thickness has been chosen so that the coincidence frequency is low, around 4kHz for

$\theta = 45^o$.

In all the following examples, the computation of the main effects was done using 7,000 samples in the design range and an averaging over 3 repetitions, therefore 21,000 model evaluations, while that of the TSI necessitated 50,000 samples per parameter and repetition. The use of kriging metamodeling could reduce this number to just 1,000 evaluations per frequency range for both analyses without los of accuracy [18].

4.2.1 Oblique plane wave

We first consider the case where the incident sound field is a plane wave with 45^o incidence. The results are presented in Figure 5.2. The first-order sensitivity indices (ME) for all four parameters are shown with respect to frequency. It can be seen that they sum up to 1 in the whole range, except in a narrow band around 4kHz, which corresponds to the coincidence frequency.

The density is shown to have a very high ME in low frequencies, while for higher frequencies, Young's modulus is predominant. This is consistent with the classical result that high frequencies are governed by stiffness effects and the low frequencies by mass effects. As the chosen design range is rather narrow, all coincidence frequencies occur rather close to each other.

A high level of interactions between parameters can be observed in the middle of the considered frequency range, where all parameters have rather low ME, but E and ρ exhibit high TSI as can be seen on Figure 5.3. This high level of interaction can be explained by the fact that the coincidence frequency is characterized by an important drop in the TL, and that the value of this frequency (see Eq. (5.31)) is a function of both density and stiffness. It can also be noticed that neither Poisson ratio nor damping have any significant influence in this range. While this was expected for the Poisson ratio, it is more surprising for the damping factor. It means that the location of the coincidence frequency is more important than the actual drop of the TL there, which is controlled by damping.

Variable	Min. value	Max. value
E_x (GPa)	63	77
ν	0.27	0.33
ρ (kg.m^{-3})	2430	2970
η ($\cdot 10^{-3}$)	2.5	7.5

Table 5.2 – Variation ranges of the 4 parameters of the isotropic plate model with 10% variability.

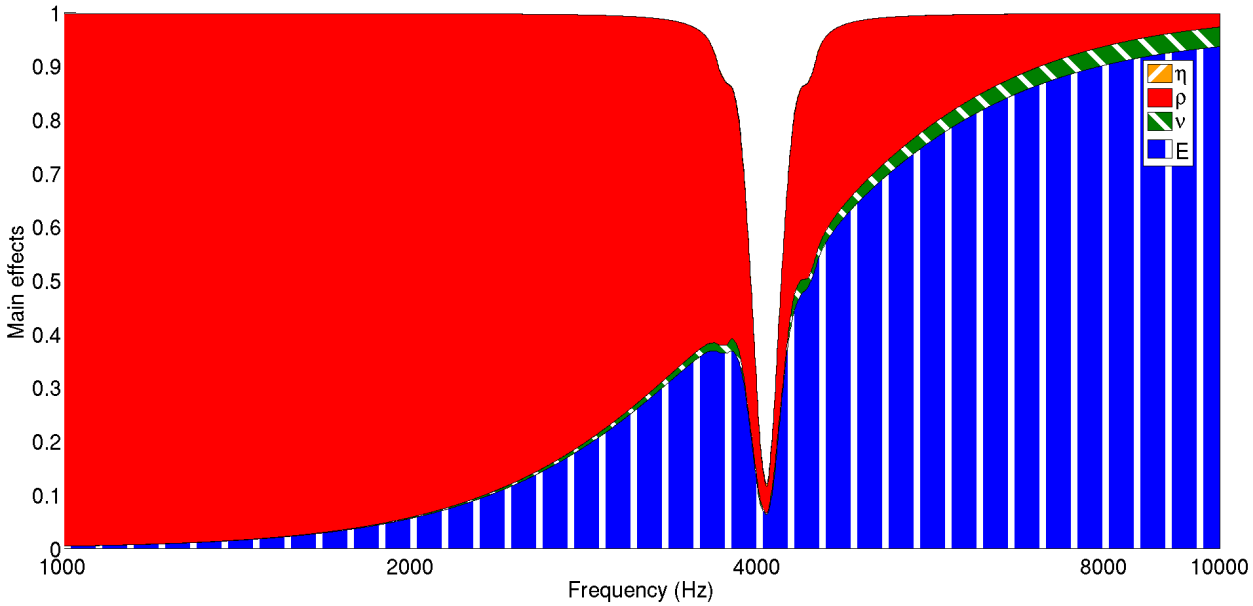

Figure 5.2 – Main effects for the four parameters for an infinite isotropic plate impinged by a 45^o incident plane wave with 10% variability on parameters.The effect of η is too small to be visible on the figure.

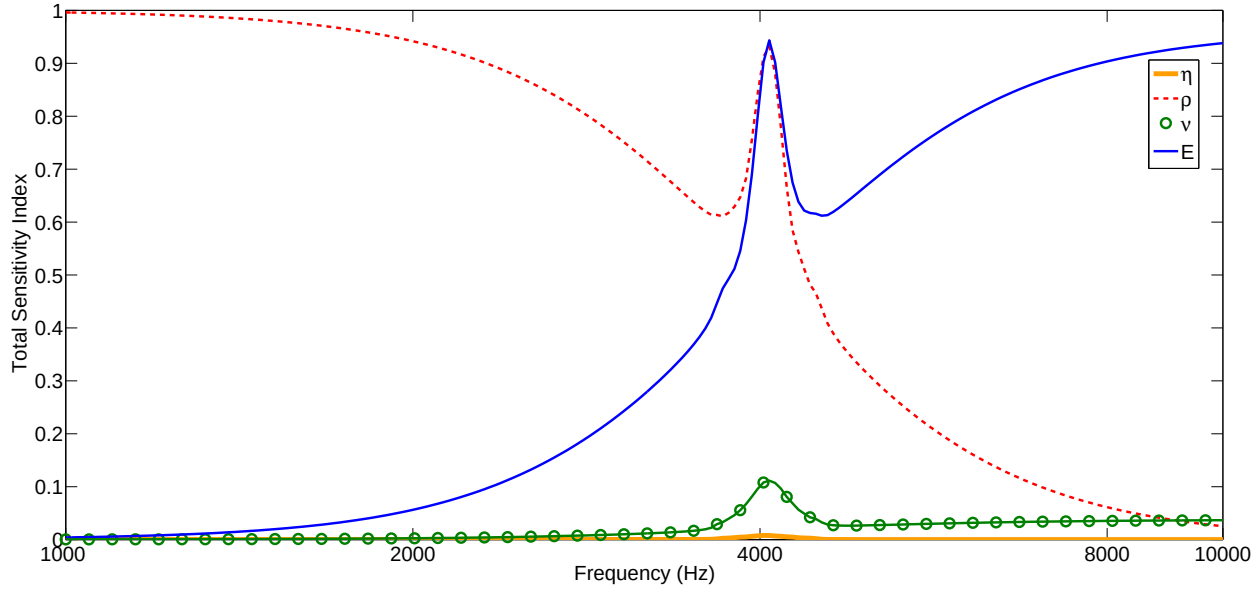

Figure 5.3 – Total sensitivity indices of the 4 parameters of an infinite isotropic plate under 45^o incident plane wave with 10% parameter variability.

4.2.2 Influence of parameter variability range

The influence of parameter variability range has been studied by varying the ranges of the three parameters E, ν and ρ without changing that of damping η, which stays between 0.25% and 0.75%. These ranges are now set at $\pm 0.1\%$ of their reference values, as in Table 5.3.

Variable	Min value	Max. value
E_x (GPa)	69.93	70.07
ν	0.2997	0.3003
ρ (kg.m^{-3})	2697	2703
η ($\cdot 10^{-3}$)	2.5	7.5

Table 5.3 – Variation ranges of the 4 parameters of the isotropic plate model with 0.1% variability

Figure 5.4 presents the results for this case. It can be seen that the discrepancy between ME and TSI no longer exist at coincidence, and the transition between mass-dominated and stiffness dominated is smoother, but the relative influence of parameters stays unchanged compared to the 10% case, except around coincidence. As damping still varies within $\pm 50\%$ of its median value, it becomes much more important in the coincidence range. This is what would be expected from a parametric analysis, as the effect of damping is on the TL drop at coincidence. Because of the very low variability of E and m, the value of f_{coin} is practically fixed, and the value of the drop becomes important.

4.2.3 Diffuse field

Diffuse field computations in the remaining of this paper are averaged over third-octave bands using 7 points, which are logarithmically spaced in each band. For the 10% parameter variation case, the diffuse field integration introduces a different behaviour in the higher frequency range. The critical frequency is now the minimum of all coincidence frequencies $f_{crit} = f_{coin}(\theta = \pi/2)$, and lies this time around 2kHz. Below the f_{crit}, mass is still the most influential parameter. However above the critical frequency the most influential parameter is damping, while stiffness (Young's modulus) only has some influence in the bands where the critical frequency occurs most often. This can be explained by the fact that for all frequency $f > f_{crit}$, there exist one value of angle θ such that $f = f_{coin}(\theta)$. In that case, the main effect governing the TL value is effectively the dip at coincidence, and no longer the coincidence frequency itself, so that damping becomes preponderant, even if it still lies in the same range, as can be seen on Figure 5.5.

It can also be noted that the density of the plate keeps a small influence in high frequency,

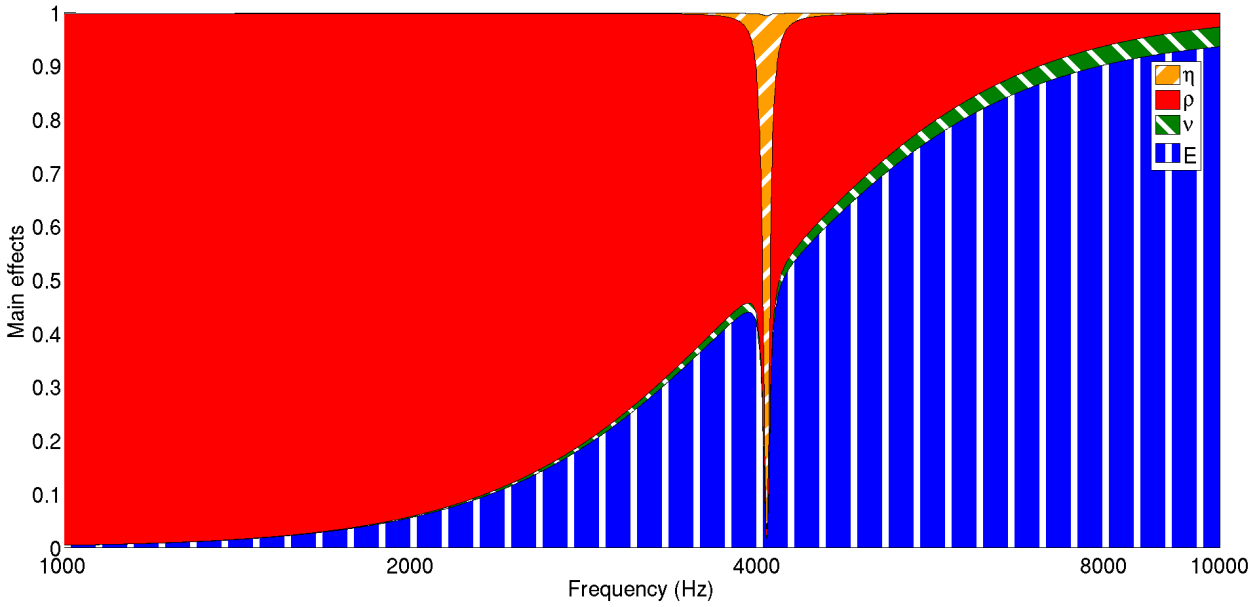

Figure 5.4 – Main effects of the 4 parameters of an infinite isotropic plate under 45^o incident plane wave with 0.1% parameter variability.

due to the fact that grazing incidence, where the mass law is valid up to high frequencies, is always taken into account in the diffuse field calculation.

5 Orthotropic plates

5.1 Model

An orthotropic plate is characterised by different properties in the x and y directions. The forced wave equation then becomes:

$$D_x \frac{\partial^4 w}{\partial x^4} + 2D_{xy} \frac{\partial^4 w}{\partial x^2 \partial y^2} + D_y \frac{\partial^4 w}{\partial y^4} - m\omega^2 w = q, \tag{5.32}$$

where the bending stiffness in each axis is:

$$\begin{aligned} D_x &= \frac{E_x h^3}{12(1 - \frac{E_y}{E_x}\nu_{xy}^2)}(1 + \mathrm{i}\eta) \\ D_y &= \frac{E_y h^3}{12(1 - \frac{E_y}{E_x}\nu_{xy}^2)}(1 + \mathrm{i}\eta) \\ D_{xy} &= \frac{h^3}{12(1 - \frac{E_y}{E_x}\nu_{xy}^2)}\left(E_y\nu_{xy} + 2G_{xy}\right)(1 + \mathrm{i}\eta). \end{aligned}$$

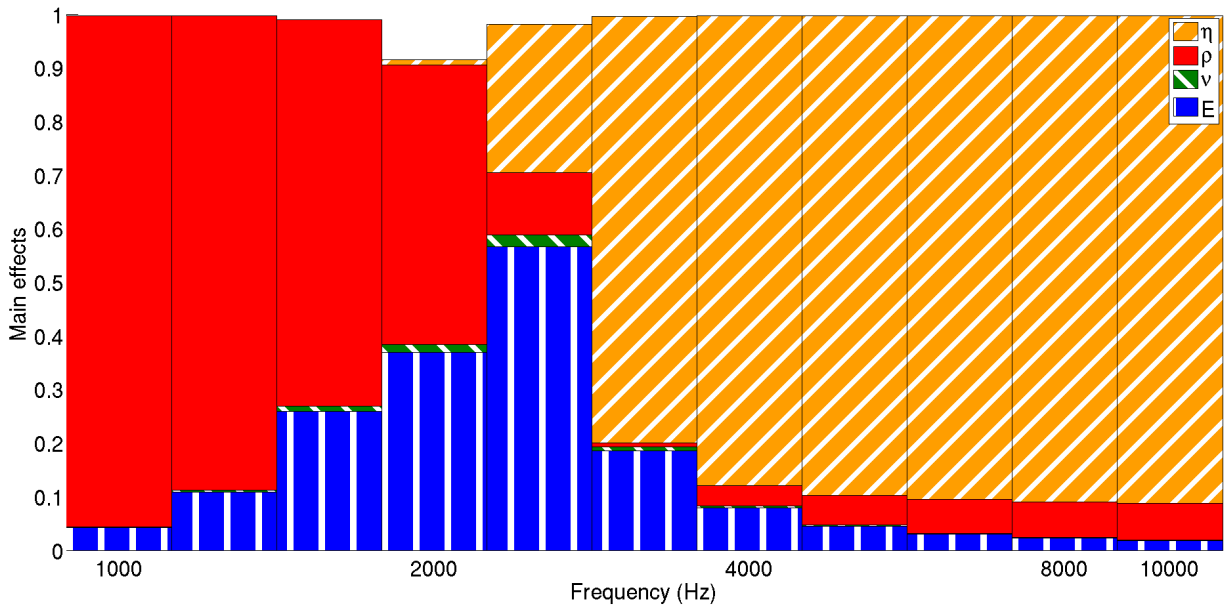

Figure 5.5 – Main effects for the four parameters of an infinite isotropic plate under diffuse field excitation with 10% parameter variability.

Writing $\frac{\partial}{\partial x} = -\mathrm{i}k_x = -\mathrm{i}k\cos\varphi$ and $\frac{\partial}{\partial y} = -\mathrm{i}k_y = -\mathrm{i}k\sin\varphi$, the system reduces to the same form as in the isotropic case, with a heading-dependent impedance. The heading dependent bending stiffness is:

$$D(\varphi) = D_x \cos^4\varphi + 2D_{xy}\sin^2\varphi\cos^2\varphi + D_y\sin^4\varphi, \tag{5.33}$$

and the structure's impedance is then:

$$Z(\omega,\theta,\varphi) = \mathrm{i}\omega m\left(1 - \omega^2\frac{D(\varphi)}{mc_0^4}\sin^4\theta\right). \tag{5.34}$$

The transmission loss is then computed with Eq. (5.27), taking into account the dependence on heading direction.

5.2 Unidirectional composite plate

A unidirectional composite plate is made of very stiff fibres oriented along a given direction, say x, held together by a much softer material called the matrix. This results in very different Young's moduli in the longitudinal (x) and transverse (y) directions. The difference can reach two orders of magnitude for some carbon-reinforced composites such as the one presented in first column of Table 5.4. The chosen variation ranges correspond roughly to ±10% variation

of the reference parameters.

The main effects of all six parameters on the TL in diffuse field excitation are presented in Figure 5.6. The plate is 1cm thick. The diffuse field transmission loss exhibits the same behaviour that was observed in section 4 with the isotropic plate in the low and high frequency ranges: Mass density is dominant in low frequencies, and damping in high frequencies, for the same reasons. However the orthotropic plate exhibits a range of critical frequencies, between the two corresponding to the x and y directions:

$$f_{crit,x} = \frac{c_0^2}{2\pi}\sqrt{\frac{m}{\mathrm{Re}D_x}} \text{ and } f_{crit,y} = \frac{c_0^2}{2\pi}\sqrt{\frac{m}{\mathrm{Re}D_y}}. \tag{5.35}$$

For any direction other than the axes, the critical frequency lies between these two, hence the transmission loss is characterized by a minimum zone between these frequencies. The Young's moduli E_x and E_y are only influential around $f_{crit,x}$ and $f_{crit,y}$ respectively. Between these, both damping and mass density are dominant, as the TL is the result of the sum of both subcoincident (mass-law) and supersonic (damping-controlled) waves. Density again has one peak of influence around the highest coincidence frequency. It can be noted that in the considered ranges, neither the Poisson's ratio ν_{xy} nor the in-plane shear modulus G_{xy} have any practical influence on the transmission loss.

The main effect of all parameters sum up close to 1, which means that there are practically no interactions between parameters. It is therefore not necessary to compute the TSIs as they would be nearly equal to the main effects.

Variable	Min. value	Max. value
E_x (GPa)	201.6	246.4
E_y (GPa)	6.21	7.59
ν_{xy}	0.225	0.275
G_{xy} (GPa)	51.3	62.7
ρ (kg.m^{-3})	1420	1736
η (10^{-3})	2.5	7.5

Table 5.4 – Values for the FAST analysis of a unidirectional orthotropic plate

5.3 Quasi isotropic plate

A quasi isotropic plate is obtained by stacking fibre-matrix composite plates with different fibre orientations. They can be modelled as orthotropic plates with equal Young's moduli in x and y directions, but with an independent in-plane shear modulus G_{xy}, not equal in general

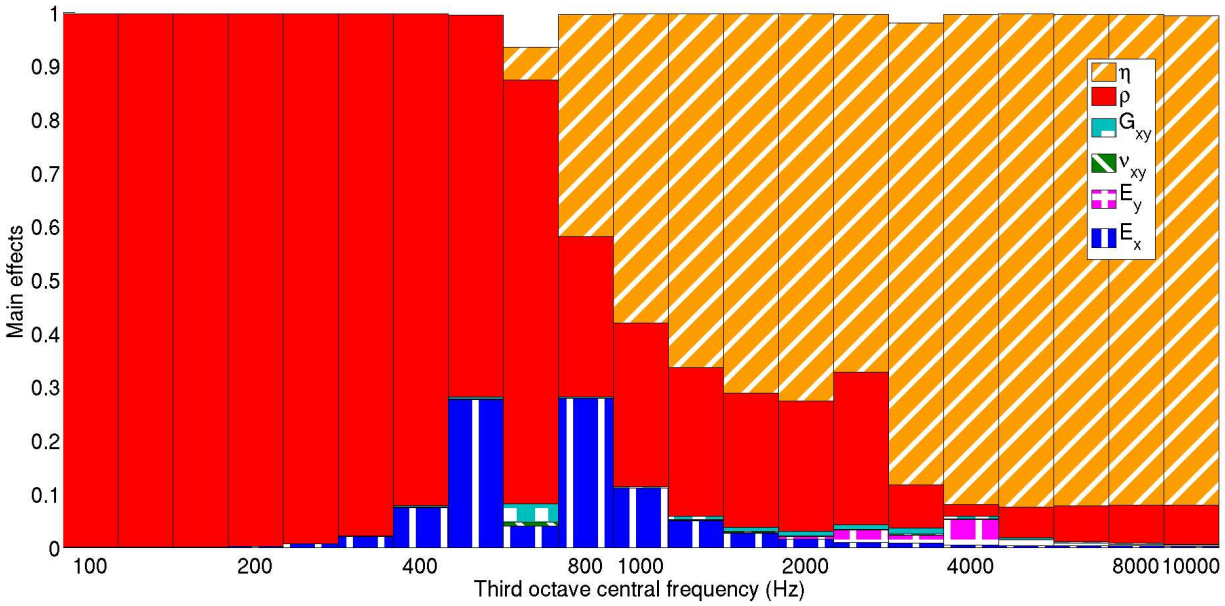

Figure 5.6 – Main effects for the six parameters of the unidirectional orthotropic plate.

to that of an isotropic plate. In that case, only five parameters will be taken into account, with $E_x = E_y = E$ and so $D_x = D_y = D$. The in-plane shear term D_{xy} can be replaced by αD, introducing a dimensionless coefficient α as in [94]. It is exactly 1 for isotropic structures, and less than 1 for most types of laminated composites, but can for some constructions be greater than 1. We chose here arbitrarily to make this parameter vary between 0.4 and 1.2.

Variable	Min. value	Max. value
E_x (GPa)	40	54
ν (-)	0	0.2
α (-)	0.4	1.2
ρ (kg.m^{-3})	1350	1650
η (10^{-3})	2.5	7.5

Table 5.5 – Values for the FAST analysis of a quasi-isotropic plate

Results of the FAST analysis are presented on Figure 5.7 in the same fashion than for the unidirectional plate in previous section. The plate's thickness is again 1cm. The results are close to those of the isotropic plate of section 4 for parameters relevant to both models (damping, density, Poisson's ratio and Young's modulus), and it can be seen that the in-plane shear parameter alpha does not account for much of the TL variance, except in the third octave just above coincidence. This can be explained that, as parameter α is mostly less than 1 on its range of variation, it tends to increase the wavenumber at 45^o of the axes, which

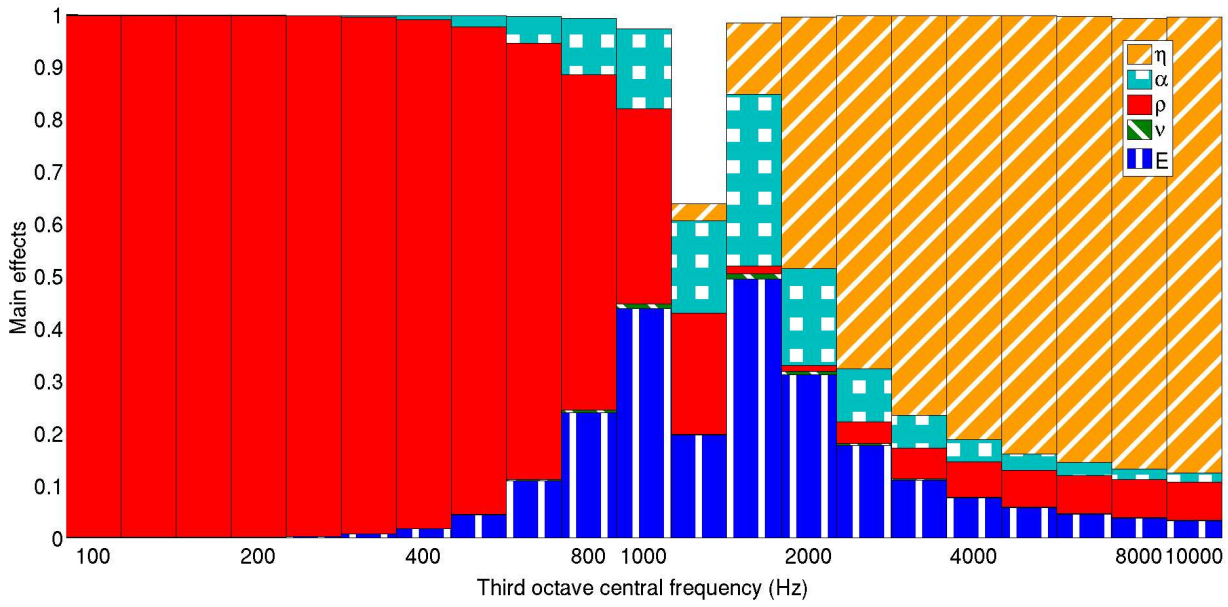

Figure 5.7 – Main effects for the five parameters of the quasi isotropic plate

leads to a slightly higher coincidence frequency for waves propagating in this direction.

6 Uncertain design of a sandwich panel

6.1 Model

A sandwich construction is made of two thin plates, called the skins, glued to a thick core. The core is usually made of very stiff and light material, which ensures a high stiffness-to-mass ratio of the structure, interesting for aerospace applications. However the shear stiffness must be taken into account to accurately model this kind of materials. Out of plane waves propagating in a sandwich plate are no longer purely bending wave, but incorporate some shear deformation form the core. However, other deformations are not considered, which allows to represent the skins with their Young's modulus E and the core by its sole shear modulus G. The equation of motion for an isotropic sandwich plate submitted to an external force is given by Renji [92]. Substituting the viscous damping term in the reference by an hysteretic damping, defined as an imaginary part of the bending stiffness D, this equation becomes

$$Dk^4 - \rho\omega^2 \left(1 + \frac{D}{N}k^2\right) w = q, \tag{5.36}$$

which leads to the following form for the structural impedance:

$$Z(\omega,\theta) = \mathrm{i}m\omega\left[1 + \left(\frac{D}{Nc_0^2}\sin^2\theta - \frac{D}{mc_0^4}(1+\mathrm{i}\eta)\sin^4\theta\right)\omega^2\right]. \tag{5.37}$$

For sandwiches made of isotropic materials, the bending stiffness is $D = Eh_c^2 h_s(1+\frac{h_s}{h_c})^2$ and the shear stiffness is $N = Gh_c\left(1+\frac{h_s}{h_c}\right)^2$. This expression is equivalent to that of a thin plate if the shear stiffness is infinite.

6.2 Results

We consider a sandwich panel with four uncertain parameters, whose variations range are summarised in Table 5.6, namely the sandwich's surface density m, the core's shear stiffness G, the skin's Young's modulus E and the structural damping η. The thicknesses of the skins and core were assumed constant, respectively at h_s = 1mm and h_c = 2cm. These values are in the order of magnitudes attained by sandwich panels made of aluminium skins and honeycomb core. The choice of surface density over material density comes from the fact that the former depends on the properties of the honeycomb core, rather than a homogeneous material, and that this quantity directly arises in the sandwich's constitutive equation (Eq. 5.37).

Variable	Min. value	Max. value
E (GPa)	60.0	80.0
G (GPa)	0.1	0.7
m (kg.m^{-2})	10	14
η (10^{-3})	2.5	7.5

Table 5.6 – Values for the initial FAST analysis of an isotropic sandwich plate

In high frequencies, the sandwich construction under diffuse field excitation has a very different behaviour from that observed previously with thin plates.

Figure 5.8 presents the main effects of each parameter. The main effects plotted do not always sum up to 1, which indicates interactions between parameters, especially around coincidence, as was observed for the isotropic case studied in section 4.

The most interesting result is here that the dominant parameter in high frequencies is no longer damping, but the shear modulus G, whereas the Young's modulus E is not important in the whole frequency range, except around coincidence, through interactions with the mass and shear modulus. This suggests that the variation range set for the shear modulus is very large, and may correspond to a design latitude. If a reduction of the TL in high frequencies

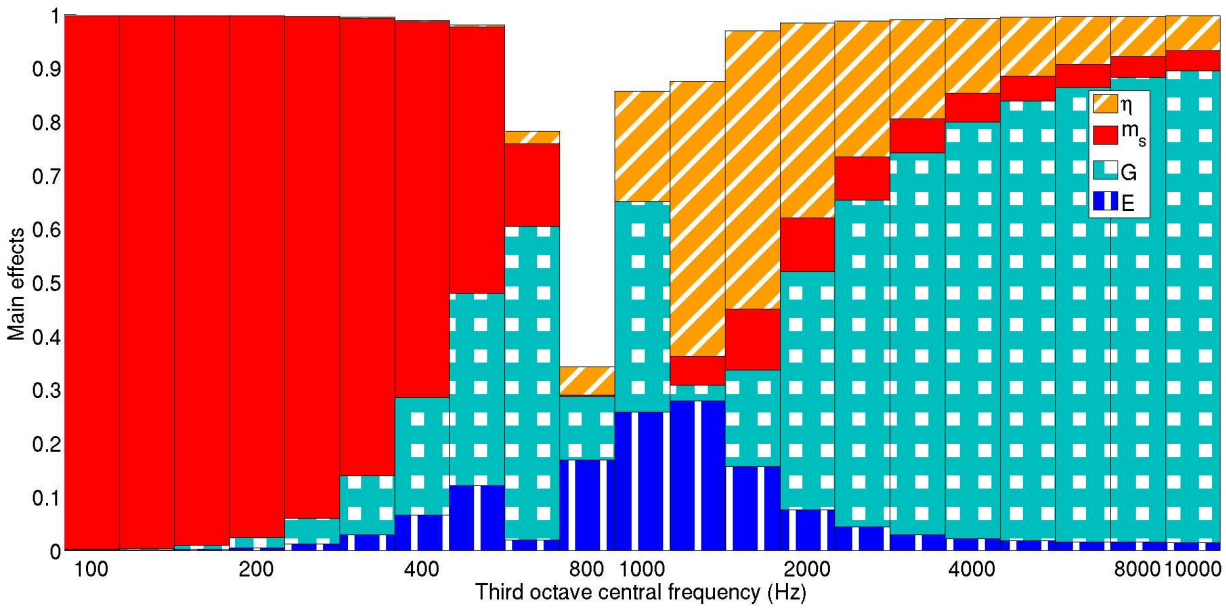

Figure 5.8 – Main effects of the three parameters of the sandwich plate model with high variability of shear modulus

is wanted, it is therefore necessary to work out a better range of variation for G, while the other parameters' ranges can be kept.

We shall consider the same average value of G (400 MPa here), but with a narrower range of $\pm$50MPa on the actual value. This remaining uncertainty may be due to the homogenisation of the honeycomb construction of the core. The main effects for this case are presented in Figure 5.9. It can be seen that with these values, the most influential parameter in high frequency is now damping, as was observed for the cases studied in the above sections. Shear is only moderately influential throughout the whole frequency range. The standard deviation in the highest frequency range is reduced by 1.5 dB, which is lower than the uncertainty due to the model itself.

Figure 5.10 presents the average transmission loss and the standard deviation per octave bands in both cases. The standard deviation is most important around coincidence and in high frequencies. The final case exhibits a reduced standard deviation compared to the initial case, except in the low frequency range where the modified parameter G was not influential. It can be noted that the average TL is slightly lower in the final case.

In this case the FAST method can be used as a tool for both uncertainty quantification and preparation of an optimisation procedure.

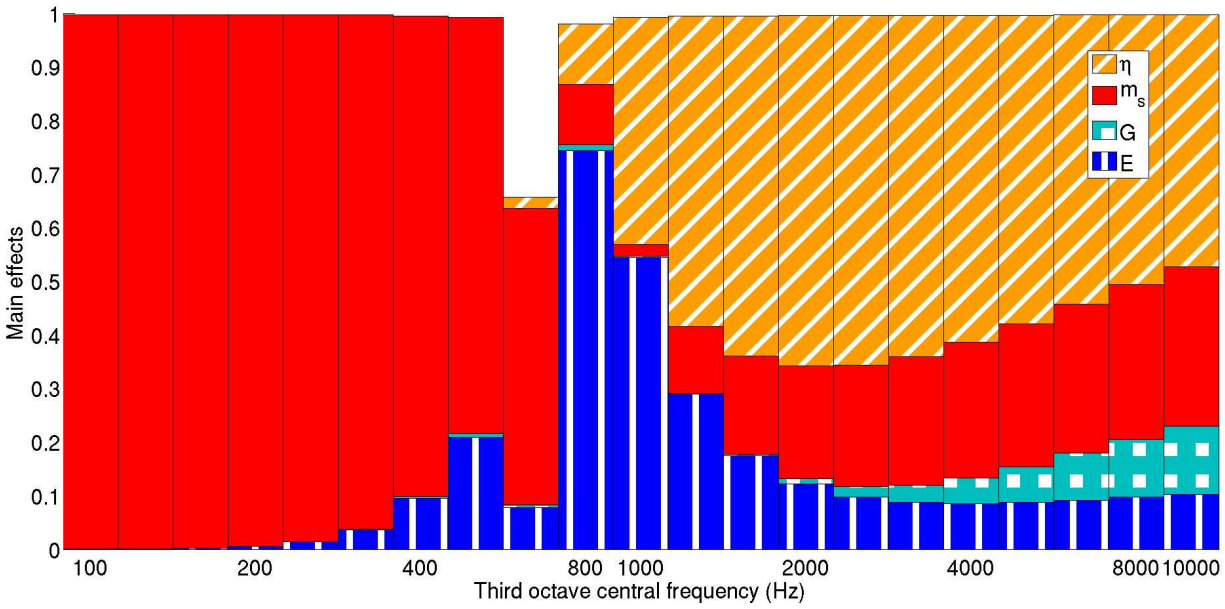

Figure 5.9 – Main effects of the four parameters of the sandwich plate model with low variability of shear modulus

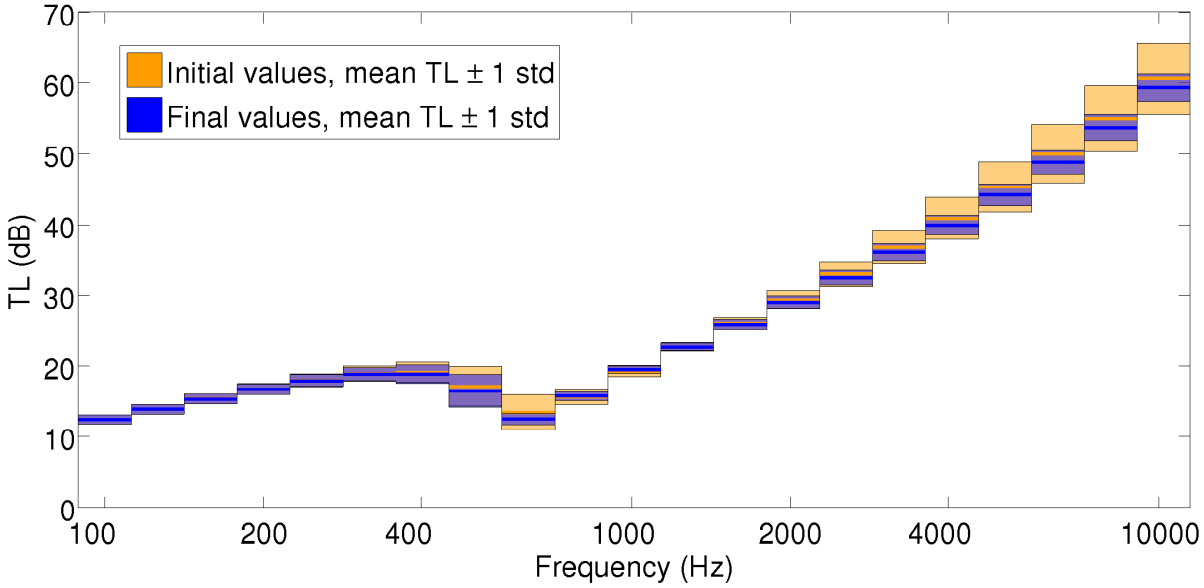

Figure 5.10 – Average value and standard deviations for the two cases of sandwich plates.

7 Conclusion

The FAST method has been applied on several models for sound transmission through infinite plates. It efficiently allows identification of the most influential parameter per frequency range. It is firstly validated with classical results on transmission loss of a plane wave through an isotropic plate: mass is dominant in the lower frequency range as predicted by mass law, while bending stiffness, represented by the Young's modulus, is dominant for high frequencies. Damping only has some influence around coincidence. The case of diffuse field transmission is then studied for isotropic and orthotropic plates. Damping is now found to be dominant in the higher frequency ranges, whereas stiffness is important only around coincidence. Orthotropic plates are characterised by a coincidence zone bounded by two critical frequencies corresponding to the minimum and maximum values of the bending stiffness in the plate's plane.

Finally, the application of the method to an orthotropic sandwich panel illustrates a potential application in vibroacoustic design of structures: used with a rather wide range for the shear modulus of the core, FAST demonstrated a high influence of this parameter in the highest frequency range and around coincidence, where the standard deviation is also maximum, around 3 dB. If a smaller range can be worked out for the variability of this parameter, this influence reduces greatly, and damping becomes preponderant, while the overall standard deviation of the output is significantly reduced.

The FAST sensitivity analysis can therefore be used to identify the most influential parameters, and quantify their effect on the overall variance. In any case, good estimates of parameter variability ranges need to be known a priori, as they may greatly influence the results. That being known, the method can be used for both optimisation and parametric uncertainty quantification. The fact that it is a non-intrusive method makes it readily usable with existing models.

Chapter 6

Use of the FAST method for uncertainty assessment in SEA models

This chapter has been submitted to Mechanical Systems and Signal Processing, with following authors: Jean-Loup Christen (ECL), Mohamed Ichchou (ECL), Bernard Troclet (Airbus Defence and Space), Olivier Bareille (ECL) and Morvan Ouisse (FEMTO-ST).

Abstract

The effect of parametric uncertainties on the dispersion of Statistical Energy Analysis (SEA) models of structural-acoustic coupled systems is studied with the Fourier analysis sensitivity test (FAST) method. The method is firstly applied to an academic example representing a transmission suite, then to a more complex industrial structure from the space industry. Two sets of parameters are considered, namely error on the SEA model's coefficients, or directly the engineering parameters. The first case is an intrusive approach, but enables to identify the dominant phenomena taking place in a given configuration. The second is non-intrusive and appeals more to engineering considerations, by studying the effect of input parameters such as geometry or material characteristics on the SEA outputs. A study of the distribution of results in each frequency band with the same sampling shows some interesting features, such as bimodal repartitions in some ranges.

1 Introduction

Vibroacoustic design is a topic of great importance in many engineering sectors. Especially in the transportation industries, both on the ground or in aeronautics, noise and vibration

have to be addressed in order to achieve competitive products. This has even become more important since a trend towards lightweight design has initiated in order to improve energy efficiency, which has the downside of degrading noise and vibration performance. The wide frequency spectrum which has to be studied leads to different methodologies in handling vibroacoustic problems: some methods deal primarily with low frequencies, and others with high frequencies. Statistical Energy Analysis (SEA) [69] belongs to the second category. It is a widely-used method, which considers average energy quantities through energy balance. SEA modelling is quite simple. The system is divided into simple substructures, and the power balance leads to an algebraic equations giving the total energy stored within each of them. This model requires knowledge of several coefficients, which can be difficult to estimate reliably. For instance, the energy flow balance needs the damping loss factor (DLF) to be provided for each subsystem. The coupling loss factor (CLF) of each couple of subsystems is also needed to close the analytical formulation. CLF and DLF are often provided by a database of materials and interfaces. These quantities can also be estimated experimentally or numerically. The literature about SEA reports a significant amount of publications dealing with SEA inputs estimation in vibroacoustic contexts, either analytically [69] or deriving from finite element models [110, 109]. The impact of the variability of such inputs on the SEA design can be of great interest at the pre-design stage.

Uncertainty and variability are the core of the SEA approach, as it deals with ensemble statistics rather than deterministic quantities. However, the actual averaging lies in the SEA hypotheses rather than in the mathematical formulation itself, and the account of uncertainty is not explicit in classical SEA. Fahy and Mohammed [37] investigated the effect of uncertainties on the output variance of power flows in SEA systems composed of coupled plates and beams. Work has been done by Langley and Brown [59, 60] to estimate the variance of the kinetic energy of an SEA subsystem. This was extended and validated in [22] for systems with only structural components. Uncertainties in SEA models have been studied by several authors as well: Culla et al. [27] used partial derivative analysis and Design of Experiment (DoE) techniques to study the sensitivity of models to the SEA factors. Partial derivative sensitivity was also used for transfer path analysis by Büssow and Petersson [15]. The effect of the variance of SEA couplig loss factors on transfer path analysis is studied by Aragonès and Guasch [4]. Cicirello and Langley [21] also studied the sensitivity of a mixed FE-SEA model to both parametric and non-parametric uncertainties.Xu et al. [118] proposed two methods to estimate the interval of variability of SEA results for structural-acoustics coupled systems.

The objective of this work is to contribute to the quantification of uncertainty due to model inaccuracy, by establishing a ranking of the most influential parameters of a SEA

model. Global sensitivity analysis in general is used to derive indicators of influence for parameters which have broad variation ranges, as opposed to local methods which target variations around a working point. There are several ways of deriving global indicators [100]. Among these, the class of methods grouped under the term ANOVA (acronym of Analysis of Variance) are based on the variance decomposition [107] as an estimate for the sensitivity of each parameter. The Fourier amplitude sensitivity test (FAST) is one of these methods, which was originally developed by Cukier et al. [26] as a computationally efficient method to compute the ANOVA sensitivity indices, with application in the study of complex chemical reactions. This method has later been reused by Iooss et al. [51] for radiologic risk assessment models. Ouisse et al. [87] applied the FAST method to porous material models, regarding acoustic impedance and absorption. This work was later extended to different models of porous materials with focus on microgeometry in [34]. The parametric approach proposed here can be used both for lack of knowledge of parameters, or for model inaccuracies, and so be used in combination with an interval analysis such as the one proposed by Reynders [97].

SEA models are subject to uncertainty in two forms: lack of knowledge of the input parameters, and modelling errors in evaluating the damping and coupling coefficients. The originality of the present work lies in the application of an ANOVA global sensitivity analysis method to an SEA model in order to identify the contribution of every uncertain parameter to the output variance. Both modelling uncertainties and input parameter variability can be handled in the proposed framework.

The method is first presented on the academic case of noise transmission between two reverberant rooms through a composite plate. Variation on the coupling coefficients enable to highlight the dominant phenomena occurring in the model. The effect of engineering parameters is then studied on the same academic set-up and an industrial structure. Because the FAST method is a sampling method, the values at samples can also be recovered and used in a statistical analysis enabling to get more information about the distribution, such as the standard deviation or simplified models of the probability law.

This chapter is structured as follows: section 2 presents the general SEA model that will be used for the academic case. The uncertainty of modelling itself is investigated on the academic transmission suite case in section 3. Finally, the effect of uncertainties on engineering parameters is studied in section 4 with the same transmission suite example and an industrial test case.

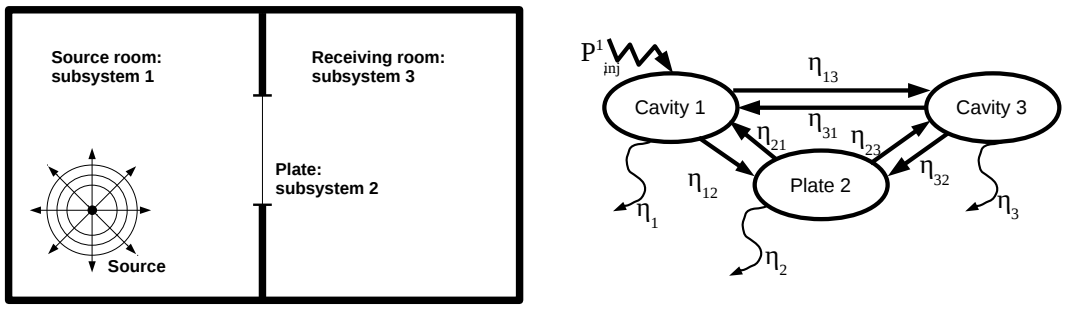

Figure 6.1 – Schematic of a transmission suite and its SEA model

2 SEA modelling

2.1 General SEA equations

SEA modelling is based on the analogy between energy exchanges in vibrating systems and heat transfer between bodies at different temperatures. The mechanical system is decomposed into N elementary subsystems. The power flow between each pair of subsystems is supposed to be proportional to the difference between their total vibrational energies. In addition, each system can dissipate energy, again proportionally to its energy level. The power transferred from subsystem i with total energy E_i to subsystem j with energy E_j in the band centred around frequency f is written

$$P_{ij} = \omega \left(\eta_{ij} E_i - \eta_{ji} E_j \right), \tag{6.1}$$

where $\omega = 2\pi f$, η_{ij} and η_{ij} are called coupling loss factors (CLF), while the power dissipated in system i is

$$P_{i,diss} = \omega \eta_i E_i, \tag{6.2}$$

where η_i is the damping loss factor (DLF). All these coefficients depend on the nature of the subsystems and their coupling, as well as on the width of the frequency band considered. The CLFs obey a reciprocity rule, as $\eta_{ij} n_i = \eta_{ji} n_j$ where n_i and n_j are the modal densities of systems i and j. The SEA system is obtained by writing the power balance of each subsystem, where the injected power equates the power losses due to dissipation and couplings:

$$P_{i,inj} = \sum_{j \neq i} P_{ij} + P_{i,diss}. \tag{6.3}$$

The considered configuration is that of the transmission suite shown on Figure 6.1, com-

prising two rooms separated by the studied plate. The plate is made of a sandwich composite material whose core is honeycomb-shaped. The SEA model used in [121] is considered in this study. It consists of 3 subsystems, numbered 1 for the cavity where the source is radiating, 2 for the plate, and 3 for the receiving cavity. The non-resonant transmission introduces a direct coupling between the two rooms, and is taken into account through the CLF η_{13}. The SEA equations then write as a matrix system:

$$\omega \begin{pmatrix} (\eta_1+\eta_{12}+\eta_{13})n_1 & -\eta_{21}n_2 & -\eta_{31}n_3 \\ -\eta_{12}n_1 & (\eta_2+\eta_{21}+\eta_{23})n_2 & -\eta_{32}n_3 \\ -\eta_{13}n_1 & -\eta_{23}n_2 & (\eta_{31}+\eta_{32}+\eta_3)n_3 \end{pmatrix} \begin{pmatrix} E_1/n_1 \\ E_2/n_2 \\ E_3/n_3 \end{pmatrix} = \begin{pmatrix} P_{inj}^1 \\ 0 \\ 0 \end{pmatrix}, \tag{6.4}$$

where P_{inj}^1 is the power injected in this frequency band in the source cavity 1.

Since the two rooms are identical and the plate radiates identically on both sides, the following equalities between CLFs, DLFs and modal densities hold, respectively: $\eta_{23} = \eta_{21} = \eta_{rad}$, $\eta_1 = \eta_3 = \eta_{cav}$ and $n_1 = n_3 = n_{cav}$. Since the system is symmetrical, we also have $\eta_{13} = \eta_{31}$. With the reciprocity rule, we also have for all $i, j \in \{1, 2, 3\}$. The energy ratio between the two rooms then writes

$$\frac{E_1}{E_3} = 1 + \frac{2\eta_{rad}\eta_1 n_1 + (\eta_1 n_1 + \eta_{rad} n_2)\eta_2}{\eta_{rad}^2 n_2 + \eta_{13}(2\eta_{rad} + \eta_2)n_1}; \tag{6.5}$$

The noise reduction index (NR), which is the difference of sound pressure levels in the two rooms, then writes

$$\mathrm{NR} = 10\log_{10}\left(\frac{E_1}{E_3}\frac{V_3}{V_1}\right), \tag{6.6}$$

where V_1 and V_3 are the volumes of the two rooms, which are equal in the considered case. The sound transmission loss (TL), defined as the logarithmic ratio of sound intensities on each side of the plate, can be computed from this ratio as well, introducing the receiving cavity's absorption α_{cav}, which is part of the definition of the DLF η_{cav}. According to [121], the TL writes:

$$\mathrm{TL} = 10\log_{10}\left(\frac{A_2}{S_{cav}\alpha_{cav}}\left(\frac{E_1}{E_3} - 1\right)\right), \tag{6.7}$$

where A_2 is the area of the plate and S_{cav} the absorbing surface of the receiving room.

2.2 Evaluation of SEA parameters

2.2.1 Damping loss factors

The damping loss factor for the composite plate can be expressed as a function of frequency f. It is calculated with the following formula [112]:

$$\eta_2 = \eta_{plate} = Af^{-B}. \tag{6.8}$$

The parameters A and B are found experimentally. The same reference gives $B = 0.63$ as a good fit for experiments on space structures, and coefficient A may vary between 0.1 and 0.6.

The DLF of a room is given from the reverberation time as

$$\eta_{cav} = \frac{2.2}{fT_{cav}}, \tag{6.9}$$

where $T_{cav} = 0.161\dfrac{V_{cav}}{\alpha_{cav}S_{cav}}$ is the reverberation time and V_{cav} is the volume of the cavity. This equation, known as Sabine's formula, is valid for normal conditions in which the speed of sound in air is $c_0 = 343$ m.s^{-1} and the density of air is $\rho_0 = 1.21$ kg.m^{-3}.

2.2.2 Plate-cavity coupling

The coupling loss factor between the plate and one cavity is linked to the radiation efficiency of the plate, which itself depends on the critical frequency f_c. Maidanik's corrected formulas [74, 24], are used for the radiation resistance of the plate, with following notations: $\tilde{f} = \sqrt{\frac{f}{f_c}}$, $\lambda_c = \frac{c_0}{f_c}$. The plate is rectangular with length l_x and width l_y. The radiation resistance is then

$$R_{rad} = A_2\rho_0 c_0 \begin{cases} \sigma_{corner} + \sigma_{edge} & \text{if } f < f_c \\ \sqrt{l_x/\lambda_c} + \sqrt{l_y/\lambda_c} & \text{if } f = f_c \\ \left(1 - \frac{f_c}{f}\right)^{-\frac{1}{2}} & \text{if } f > f_c, \end{cases} \tag{6.10}$$

where

$$\sigma_{corner} = \begin{cases} 0 & \text{if } f > f_c/2 \\ \dfrac{8c_0^2}{A_2 f_c^2 \pi^4} \dfrac{1 - 2\tilde{f}^2}{\sqrt{\tilde{f}^2\left(1 - \tilde{f}^2\right)}} & \text{otherwise,} \end{cases} \tag{6.11}$$

$$\sigma_{edge} = \frac{P_2 c_0}{4\pi^2 f_c A_2} \frac{\left(1-\tilde{f}^2\right)\left(\ln\frac{1+\tilde{f}}{1-\tilde{f}} + 2\tilde{f}\right)}{\left(1-\tilde{f}^2\right)^{\frac{3}{2}}}, \tag{6.12}$$

and $P_2 = 2(l_x + l_y)$ is the perimeter of the plate. The CLF for the power flow from the plate to the cavity is finally:

$$\eta_{rad} = \frac{R_{rad}}{\omega m A_2}, \tag{6.13}$$

where m is the surface density of the plate and mA_2 is therefore the total mass of the structure.

2.2.3 Non-resonant transmission

The non resonant transmission is due to the contribution of modes located outside the frequency band of interest. This phenomenon is dominant in low frequencies, and can be taken into account with a direct coupling term between the two rooms, which depends on the room's volume and the mass of the plate. Since the two rooms are identical, the expression of the CLF is given by [69]:

$$\eta_{13} = \frac{3\rho_0^2 c_0^3 A_2}{2\omega^3 m^2 V_{cav}}; \tag{6.14}$$

2.2.4 Critical frequency

The critical frequency is the frequency where the wavenumber of free propagating flexural waves k_{bend} is equal to that of a grazing acoustic wave, which reads

$$k_{bend}(f_c) = 2\pi \frac{f_c}{c_0}. \tag{6.15}$$

This corresponds to the minimum of all possible coincidence frequencies. Since this chapter only discusses diffuse fields, by language abuse the terms "coincidence" and "critical frequency" will be used interchangeably. Narayanan and Shanbhag's model [83] for wave propagation in sandwich panels is used, for which the constitutive equation for an isotropic sandwich without damping writes in the frequency domain

$$-D_t k_{bend}^6 - g(D_t + B)k_{bend}^4 - m\omega^2 - \frac{mB}{N}\omega^2 k_{bend}^2 = 0, \tag{6.16}$$

where $g = 2\frac{G}{Eh_s h_c}$, m is the surface mass of the whole plate, $D_t = \dfrac{Eh_s^3}{6(1-\nu^2)}$ is the skins' bending stiffness, $B = Eh_s(h_c+h_s)^2$ is the overall bending stiffness and $N = Gh_c$ is the shear stiffness. In these definitions, E is the Young's modulus of the skins, G the shear modulus of the core, h_c and h_s respectively the thickness of the core and each skin, and ν is the Poisson's ratio of the skins. Combining equation 6.16 with equation 6.15, gives the equation to which the critical frequency is solution

$$D_t \left(2\pi \frac{f_c}{c_0}\right)^4 + \left(\frac{g(D_t+B)}{c_0^2} + \frac{mB}{N}\right)(2\pi f_c)^2 w + mc_0^2 = 0. \tag{6.17}$$

As this equation is a second order polynomial in f_c^2, the positive root is the critical frequency.

2.2.5 Modal densities

The modal density of a rectangular acoustic cavity surrounded by hard walls is classically evaluated with the following formula [121]

$$n_{cav} = \frac{4\pi f^2 V_{cav}}{c_0^3} + \frac{\pi f S_{cav}}{2c_0^2} + \frac{P_{cav}}{8c_0} \tag{6.18}$$

where V_{cav}, S_{cav} and P_{cav} are respectively the volume, surface and perimeter of the cavity. The perimeter P_{cav} is the sum of the lengths of the cavity's edges, and is independent of the plate.

The modal density of a composite plate is obtained from the wave propagation analysis of the plate

$$n_2 = A_2 k_{bend} \frac{\mathrm{d}k_{bend}}{\mathrm{d}\omega}, \tag{6.19}$$

where the expression for k_{bend} with respect to frequency is obtained again from equation 6.16. All the expressions of the SEA coefficients are averaged over third-octave frequency bands when used in equation 6.5.

3 Model uncertainty

The formulas established in the previous sections are approximations, especially in the case of Maidanik's formulas, which were primarily established for a thin plate. As the behaviour of a sandwich structure implies some shear in the core that is not taken into account, it is expected that the SEA parameters calculated above contain some inaccuracy. Other

error-prone parameters include the DLFs, as damping is notoriously difficult to evaluate for complex structures.

The sensitivity of the NR with respect to uncertainties in the following four SEA parameters is studied with the FAST method: the plate-cavity CLF η_{rad}, the cavity absorption α_{cav}, the plate DLF η_{plate}, and the critical frequency f_c. The academic design chosen has following characteristics: the cavities are cubic with an edge length of 5.1m, the size of the plate is 0.8m×1.2m. The plate is made of a composite sandwich with isotropic core (shear modulus G=400MPa, thickness h_c=12.7mm) and isotropic skins (Young modulus E=50GPa, Poisson ratio ν=0.1, thickness h_s=1mm). The overall surface density of the plate is $m = 5\text{kg.m}^{-2}$. The fluid is air with density $\rho_0 = 1.21\text{kg.m}^{-3}$ and sound speed $c_0 = 343\text{m.s}^{-1}$. Under these conditions, the critical frequency is around 640Hz.

In order to study this uncertainty, the reference values of each parameter are evaluated for each frequency band with the formulas described in section 2. The reference value of parameter i is then multiplied by a random error factor $\varepsilon(i)$ with a probability law centred on 1. For example, if the reference DLF in the plate is denoted η_{plate}, then the error factor is denoted $\varepsilon(\eta_{plate})$, which should not be interpreted as a function of η_{plate}, but simply as a writing commodity. The actual DLF in one sample is then $\eta_{plate}\varepsilon(\eta_{plate})$.

Two kinds of probability laws are considered for the error factors, namely a uniform law, in which the possible values are bounded and equiprobable, and a lognormal law, which only restricts the error factor to positive values, with an average value equal to 1.

3.1 FAST results

3.1.1 Uniform law on uncertainty parameters

The uniform laws are chosen to be centred on 1, and with non-negative values. The chosen bounds for each parameter are presented in Table 6.1. The error on the critical frequency is chosen rather low (±10%), while that on the plate's internal damping is very high (±40%).

Name	Description	Uncertainty
f_c	Critical frequency	±10%
η_{rad}	Plate-cavity CLF	±30%
η_{plate}	Plate damping parameter	±40%
α_{cav}	Cavity absorption	±20%

Table 6.1 – Parameters of the uniform laws used for the model uncertainty parameters

Figure 6.2 shows the first-order sensitivity indices (ME) of all the considered parameters for the NR in each third-octave band between 100Hz and 20kHz. It can be seen that the

CLF between the plate and the cavities is dominant over most of the frequency range, except in the bands around 800Hz, where the nominal value of the critical frequency lies, and in which the error on f_c is dominant. This can be expected, as all energy flowing between the emitting and receiving cavities has to go through the plate, no indirect coupling being taken into account in this model. Despite its high uncertainty ($\pm 40\%$), the plate's damping is on the contrary relatively unimportant on the whole range, meaning that whatever its value in the considered range, much less power is dissipated in the plate than transferred to the receiving cavity. The effect of the critical frequency is limited to the third octave bands around coincidence, and negligible for extreme high and low frequencies.

The asymmetry observed between high and low frequencies is partly due to the logarithmic scale used but also mainly to the expression of the radiation efficiency (equation 6.10), which tends to infinity when f approaches f_c as $\left|1 - \frac{f}{f_c}\right|^{-\frac{3}{2}}$ when $f < f_c$, faster than $\left|1 - \frac{f}{f_c}\right|^{-\frac{1}{2}}$ when $f > f_c$. As the NR varies with η_{rad}^{-1}, this means that an error on f_c will have more importance when $f < f_c$ than when $f > f_c$.

It can be noted that the sum of the main effects is always close to 1, meaning that the model is free from interactions between parameters in the case a uniform law is used for all of them.

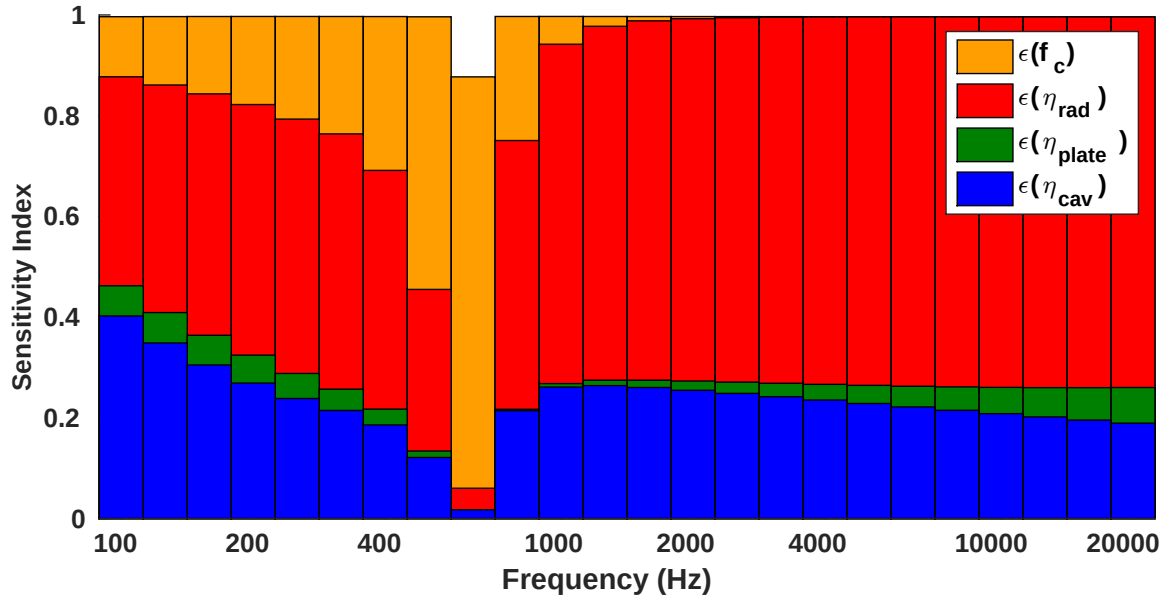

Figure 6.2 – Sensitivity indices of the NR for model error parameters with uniform law (for each bar, from top to bottom: f_c, η_{rad}, η_{plate}, α_{cav})

3.1.2 Lognormal law

A lognormal law is traditionally characterised by the mean μ and the standard deviation σ of the associated Gaussian law, while its actual average is

$$\mu_l = \exp\left(\mu + \frac{\sigma^2}{2}\right), \tag{6.20}$$

and its actual standard deviation is

$$\sigma_l = \left(\exp(\sigma^2) - 1\right)\exp(2\mu + \sigma^2). \tag{6.21}$$

The parameters of the lognormal law presented in Table 6.2 are chosen so that their actual mean is 1, and their actual standard deviations match those of the corresponding uniform laws.

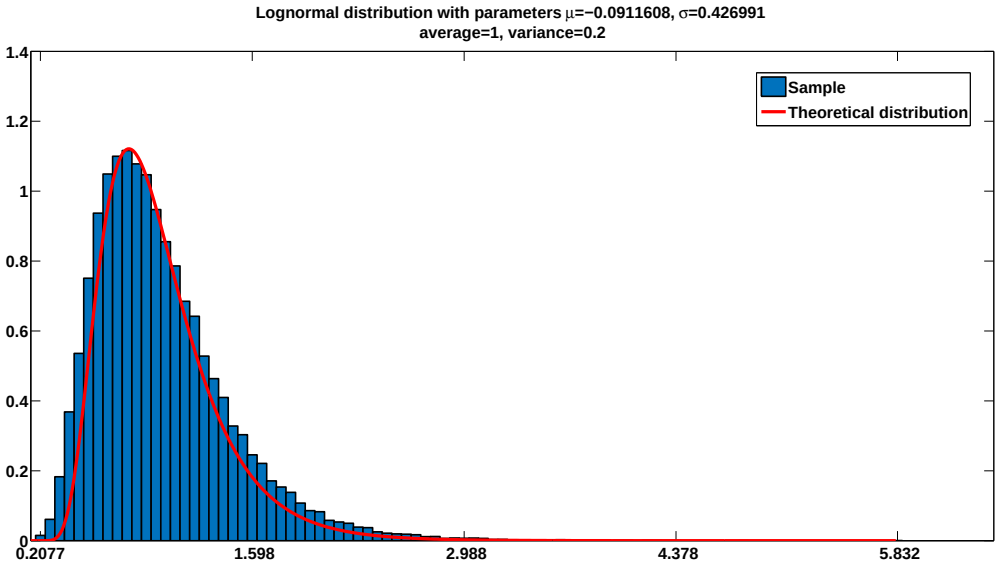

Figure 6.3 – Probability density function of a lognormal law and distribution of a random sample

The main effects from the FAST analysis of the NR in this case are presented on Figure 6.4. They compare well with those computed in the previous section with a uniform law, except the fact that they do not add up to 1, but to a slightly lower value around 0.95, indicating the presence of interactions. As the parameters vary in a broader range, albeit with a low probability, this indicates that the model is not fully additive in this case, and that the use of a non-uniform probability law induces some interaction between parameters.

Name	Description	Standard deviation
f_c	Critical frequency	0.0577
η_{rad}	Core shear modulus	0.1732
η_{plate}	Plate damping parameter	0.2309
α_{cav}	Cavity absorption	0.1155

Table 6.2 – Actual standard deviations σ_l of the lognormal laws used for the model uncertainty parameters. The mean μ_l is always equal to 1.

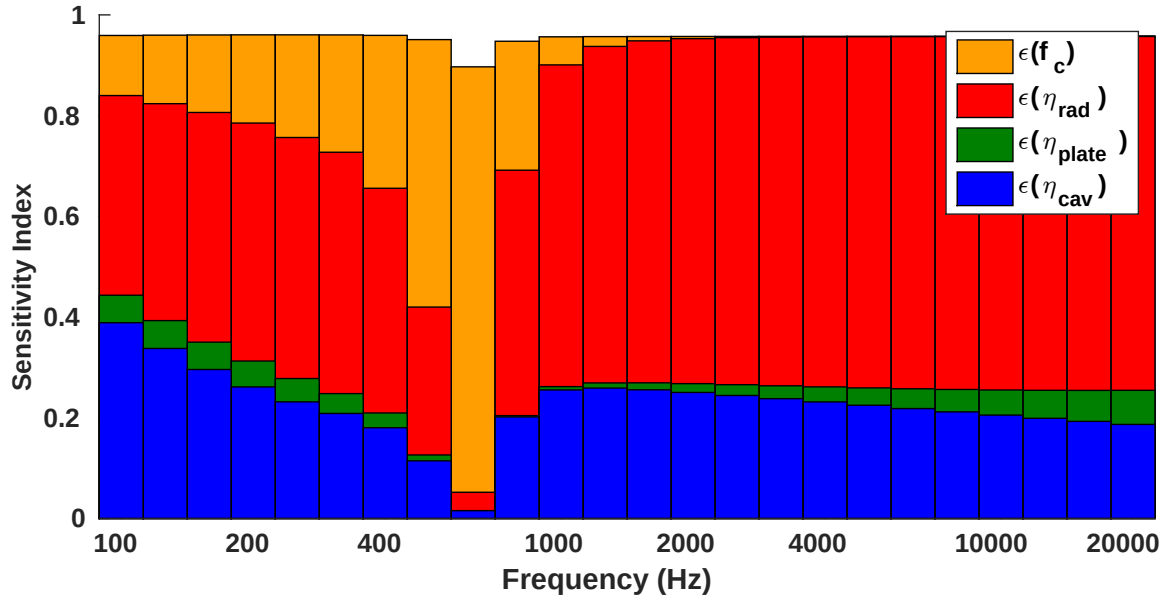

Figure 6.4 – Sensitivity indices for model error parameters with lognormal law (for each bar, from top to bottom: f_c, η_{rad}, η_{plate}, α_{cav})

3.2 Statistical considerations

With the sampling used for the FAST analysis, it is possible to compute some statistical features of the response, which are summarized on Figure 6.5 for the uniform law and Figure 6.6 for the lognormal law. These two figures present the distribution of the response on a coloured scale, the bluer part indicating the least probable values, and the redder the most probable. The mean and the interval width of ± 1 standard deviation around the mean are superimposed as black and dashed black lines respectively, and the nominal response is shown as a dashed purple line.

It can be seen that in both cases, for most of the frequency range the nominal response coincides with the average, but the most probable response may differ by several dB, especially in the coincidence range around 800Hz. The lognormal law show as expected a wider

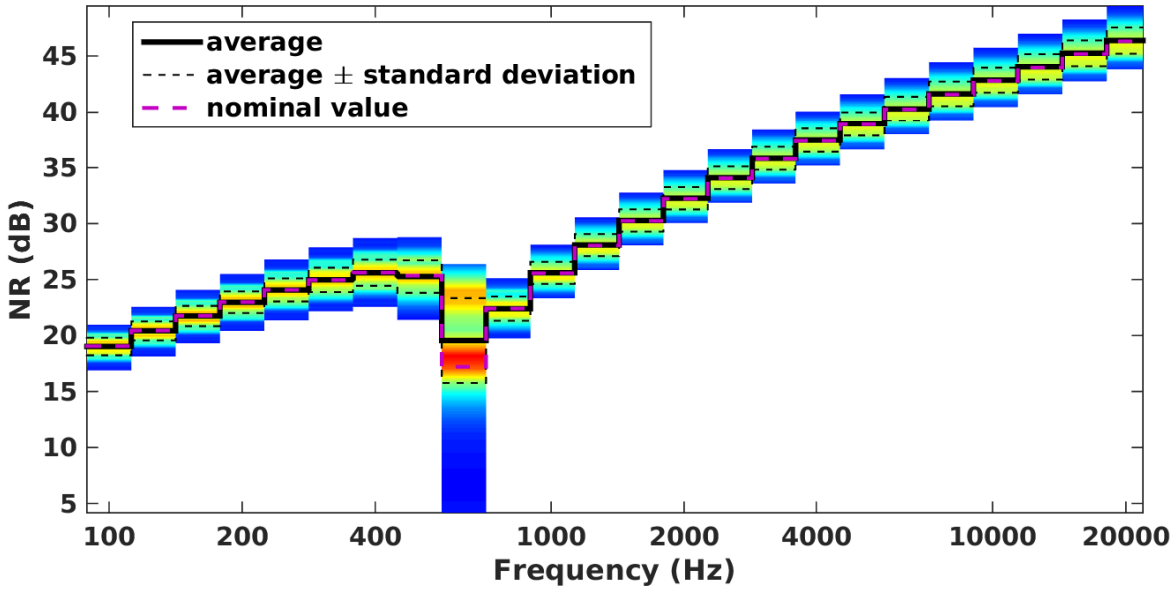

Figure 6.5 – Distribution of the NR around the mean for the "model error" setting and uniform distributions

range: as the parameter values are theoretically unbounded, so is the response. The standard deviation is nearly the same in both cases, and reaches about 2dB, which is acceptable for most industrial applications. The considered errors on modelling parameters are therefore reasonable here.

4 Parametric uncertainty

One of the main aims of sensitivity analysis is to study the effect of input parameters. While the analysis in section 3 was focused on internal parameters of the SEA model, we propose here to apply it to parameters that are more readily manipulable by a designer, namely material parameters. The two cases considered are first the same academic transmission suite, and second a test structure shaped like a mock-up of a space structure.

4.1 Transmission suite

The plate between the two rooms of the transmission suite being made of sandwich composite material, the most relevant parameters from an engineering point of view are the Young's modulus of the skins E, the equivalent transverse shear modulus of the core G, the overall surface mass m, the plate's damping η_{plate} and the cavity's absorption coefficient α_{cav}. The

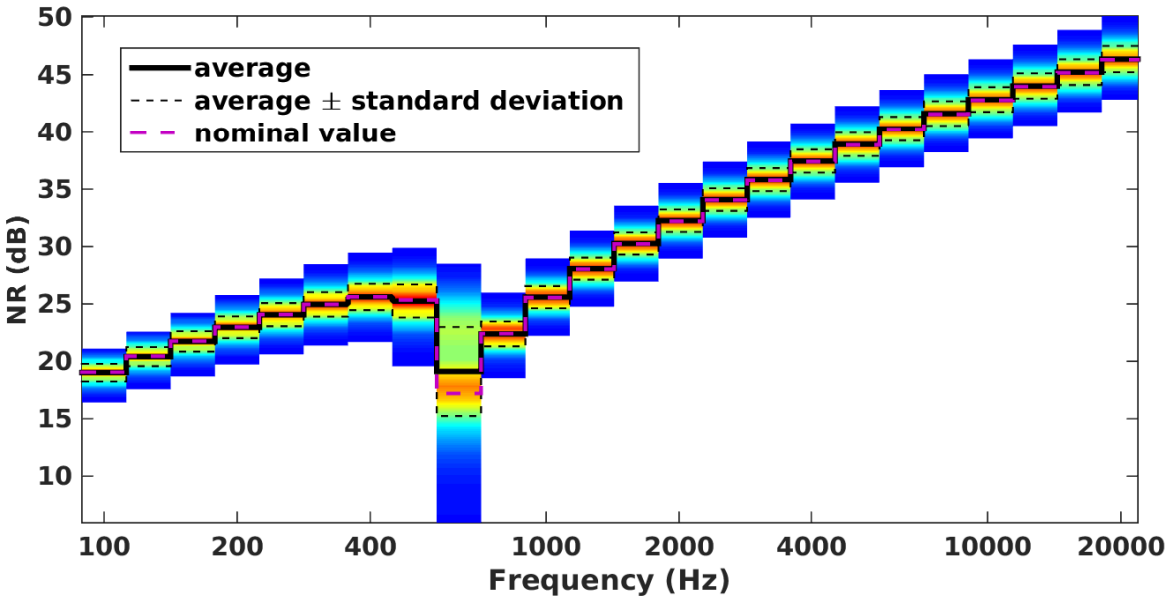

Figure 6.6 – Distribution of the NR around the mean for the "model error" setting and lognormal distributions

Name	Description	Unit	Reference value	Uncertainty
E	Skin Young modulus	GPa	50	±15 %
m	Surface density	kg.m^{-2}	5.0	±10%
G	Core shear modulus	GPa	0.24	v30%
η	Plate damping	–	0.6	±30%
α_{cav}	Cavity absorption	–	0.1	±30%

Table 6.3 – Parameters of the uniform laws used for the engineering parameters

damping loss factor is calculated with the formula defined in equation 6.8. The uncertainty is applied on the coefficient A, while the exponent B is constant and taken equal to 0.63, which is thus equivalent to the uncertainty studied previously.

The main effects on the NR are presented in Figure 6.7. It is noticeable that the absorption of the cavity has a high impact, accounting for between 50 and 60% of the variance everywhere, except around coincidence. The second most important parameter is mass below coincidence, and the shear modulus above it.

The same analysis on the transmission loss (TL) defined in equation 6.7, which should neutralise the effect of absorption in the rooms exhibits a similar ranking of parameters, except that absorption does no longer play a role, as shown in Figure 6.8. These results are consistent with a previous study made on an analytical model of the same configuration [19]:

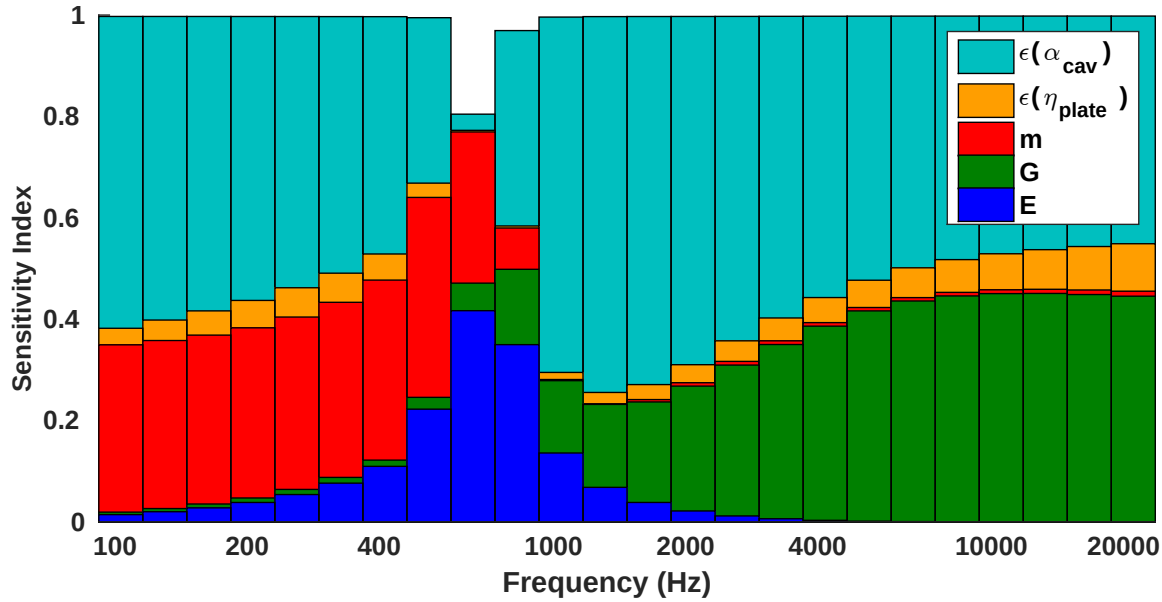

Figure 6.7 – Sensitivity indices of engineering parameters for the NR of the transmission suite. For each bar, from top to bottom: α_{cav}, η_{plate}, m, G, E.

mass is dominant in low frequencies, while the influence of stiffness peaks around coincidence, and the effects of shear and damping are predominant in high frequencies. Both for NR and TL, the model is additive for all frequency ranges, except the coincidence range, where a high level of interaction is observed. This is due to the expression of the critical frequency as a function of mass and stiffness of the plate: the value of the critical frequency has more effect on the overall variability than the drop in TL that occurs at this frequency.

4.2 Industrial structure

The same kind of analysis was finally applied to a structure composed of two cones and a cylinder, as shown in Figure 6.9a. It will be referred to as SYLDA-like, because its configuration is loosely inspired from the Ariane 5 SYLDA double launch system. The holes on the top and bottom sides are supposed to be hermetically sealed. An SEA model has been implemented in the industrial code SEALASCAR, based on modal formulations for the CLFs. Five subsystems are considered, one cavity representing the exterior diffuse sound field, the inner cavity, and three structural parts: the top and bottom conical shells and the cylindrical shell in the middle, as shown in Figure 6.9b. All shells are made in the same sandwich material, and feature the same engineering parameters as the plate in the previous subsection (Table 6.3). The outer cavity is open, and the sound field is supposed to be uni-

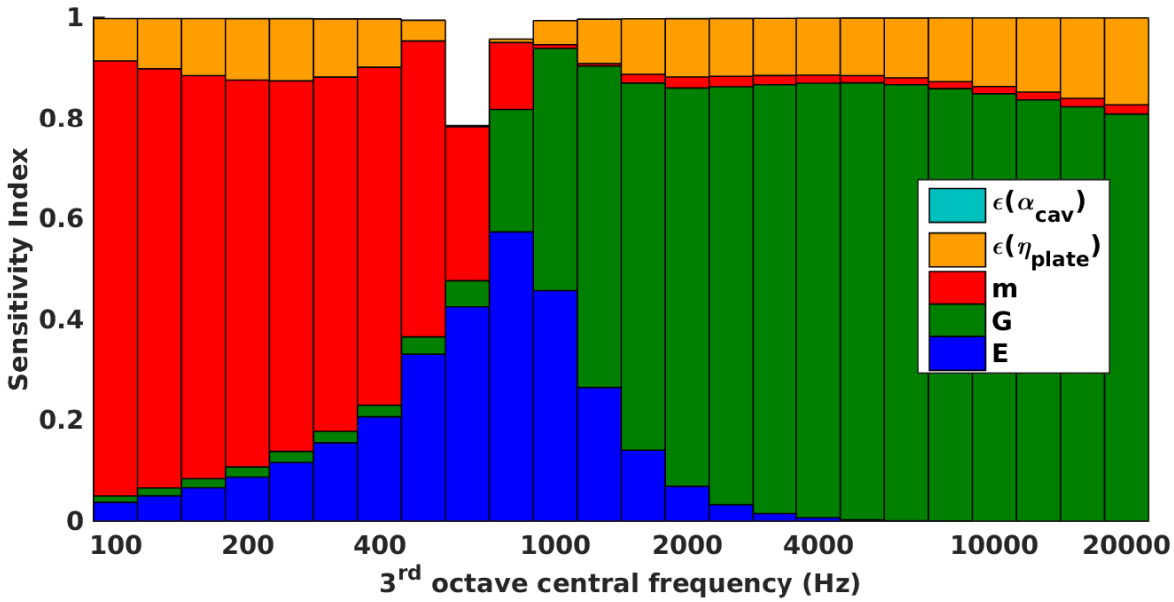

Figure 6.8 – Sensitivity indices of engineering parameters for TL of the transmission suite. For each bar, from top to bottom: α_{cav} (too small to be visible), η_{plate}, m, G, E.

form and diffuse in the vicinity of the shell. The model output is the noise reduction (NR) factor, which is the difference in sound pressure levels between the outer and inner cavities.

Figure 6.10 shows the results of the FAST analysis by third-octave bands between 400Hz and 16 kHz. The lowest frequency band is chosen because there are no structural modes in the lower (320Hz) third-octave band, making the mode-based model used unable to compute CLFs in this range. The main effects (ME) presented in 6.10a indicate an additive model except again in the coincidence range. This time, as the transmission occurs through the whole surface of the structure, the cavity absorption is again predominant in most of the frequency range, while the effect of mass is sensible only in low frequencies, and the effect of shear increases with frequency. The total sensitivity indices (TSI) presented in 6.10b are, as expected from the previous figure, identical to the ME except in the band where most critical frequencies appear, where the highest TSIs are those of the mass and Young's modulus, indicating again that the variance of the NR in this band is largely due to an interaction between these two factors, which determine the value of the critical frequency.

The FAST sampling here leads to interesting considerations concerning the distribution of the response (Figure 6.11): in this case, the average response is globally centred in the distribution for all third-octave-bands, except the one centred on 630Hz, which contains the reference critical frequency. In this octave the probability density function is not centred, but exhibits two local maxima, one being a real maximum around 4dB, 2dB lower than the

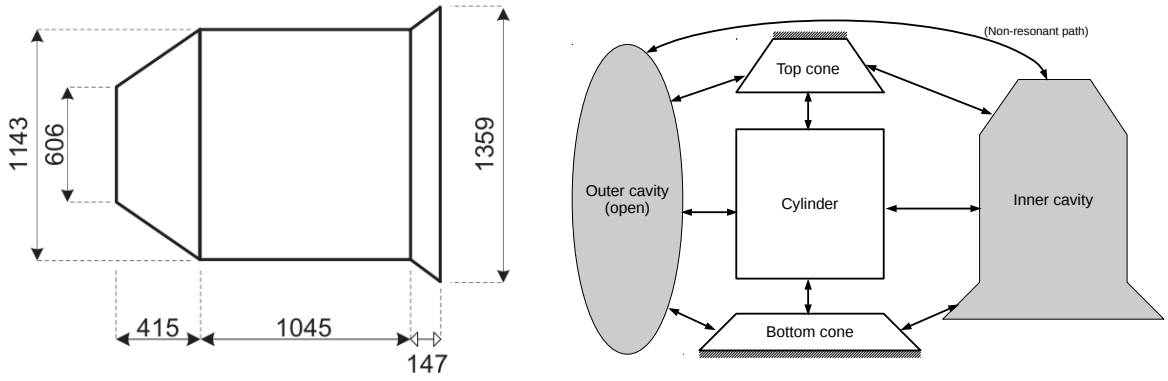

(a) Dimensions in mm.

(b) SEA subsystems and connections

Figure 6.9 – SEA model of the SYLDA-like structure.

average, and one around 8dB, more than one standard deviation away from the average, which pleads in favour of looking for more advanced statistical features of the response distribution than just the mean.

5 Conclusion

The parametric sensitivity analysis method FAST has been employed in this chapter to study the effect of model and parametric uncertainties on the noise reduction and transmission loss through composite structures modelled with SEA. The academic case of a transmission suite allowed us to apply uncertainties on several SEA model features such as coupling loss factors and damping loss factors, showing that the most important parameters are, unsurprisingly, the plate-cavity coupling and, much less, the cavity's absorption coefficient. The effect of the probability law was also tested, comparing a uniform law on the model error parameters to a lognormal law. Both results were found compatible, as the laws were chosen to have the same average and standard deviation, but the unboundedness of the parameter range with the lognormal law leads to interactions between parameters. Concerning uncertainties on design or engineering parameters, the results found on the academic case are consistent with common knowledge, while the more general frame of the SEA method allowed us to validate these results on a more complex industrial-like case. It should be noted that the results in this case are very specific to the chosen set-up, and hence cannot be intuitively extrapolated from the results of the academic case.

The fact that the FAST method uses a sampling of the parameter space makes it possible to derive some informations about the general statistics of the response. For the studied cases,

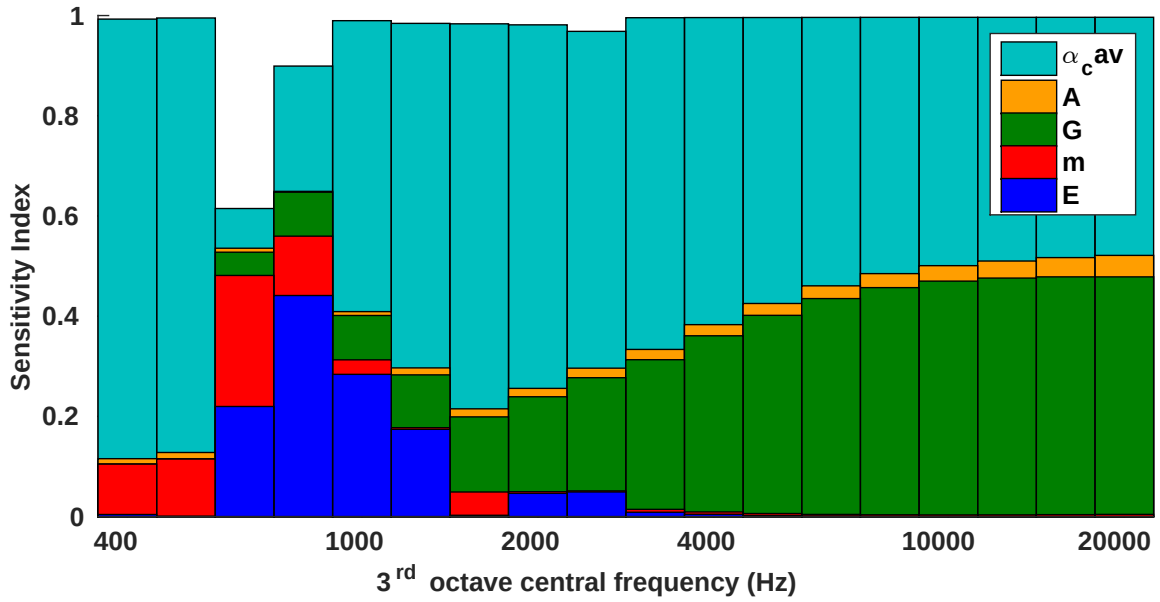

(a)

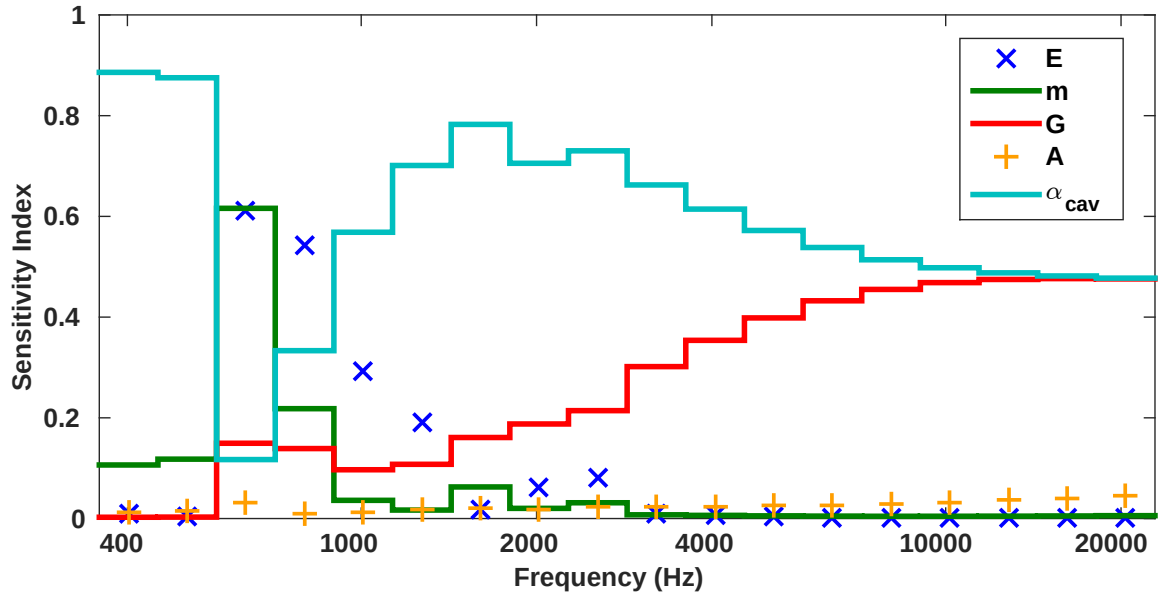

(b)

Figure 6.10 – Main effect (6.10a) and Total Sensitivity indices (6.10b) of the five engineering parameters of the SYLDA-like structure

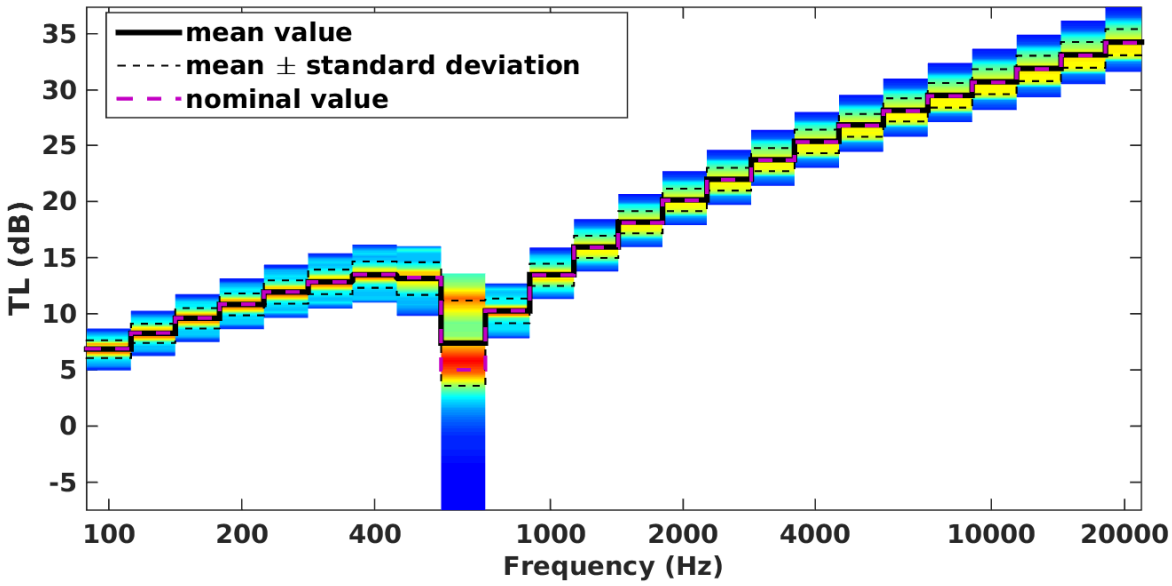

Figure 6.11 – Distribution of the NR around the mean for SYLDA-like test case.

the most probable response is usually close to the nominal and to the average response, but difference may arise especially around the critical frequency, when the interactions between parameters in the sense of ANOVA is high.

Part III

Effect of poroelastic treatment on sound transmission

Chapter 7

Sensitivity of transmission loss through plates with sound package

This chapter is partly a transcript of a paper presented to the international conference on dynamics of composites Dyncomp'2015 in Arles, France.

Abstract

Composite materials are widely used in the aerospace industry, for their low mass and high stiffness, however, these characteristics tend to increase noise transmission. Sound protection must therefore be added, in the form of porous material layers. Uncertainties may affect both the structural and sound package parameters. It is therefore important to assess the influence of these uncertain parameters on the sound transmission properties of the assembly. The sound transmission loss through a composite plate-foam assembly is first computed with the transfer matrix method. The effect of uncertainty of several parameters such as the porosity, flow resistivity and mechanical parameters is then analysed with the FAST (Fourier amplitude sensitivity test) method. The effect of adding a thin screen at the interface between the porous and air is also investigated.

Contents

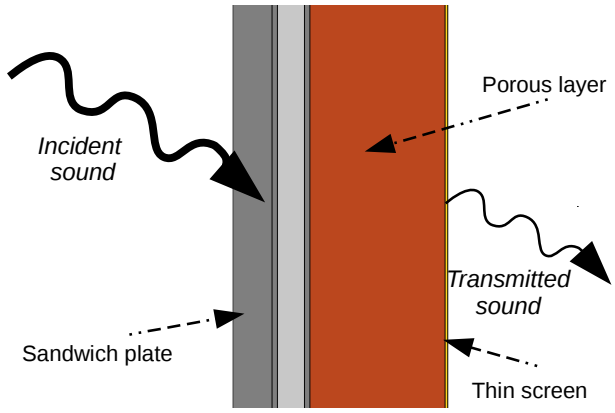

Figure 7.1 – View of the studied configuration. The influence of the presence of a limp screen on the transmission side is studied

1 Introduction

Noise transmission is often a major concern in the industry. Composite structures are known to have lower acoustic performance than their metallic counterparts, but their high stiffness to mass ratio makes them more and more used in aerospace applications. One of the most frequently used construction is the sandwich one, where a rather soft core is constrained between two stiffer skins, so that the main deformation in the core is due to shear. Analytical models of sound transmission have been proposed in the literature [81, 92]. Some kind of acoustic treatment is then needed to enhance the transmission loss. Porous materials such as fibreglass are commonly employed for this purpose, which can be modelled with the Biot model [13, 3]. Sometimes a thin screen can be glued to the porous material to protect it on the transmission side.

Some variability always occur when modelling the transmission loss of structures with noise treatment, due either to uncertainty in the parameter measurement, or to design latitudes allowing for optimisation. It is therefore of utmost importance to assess the effect of this variability on the model output, and estimate the sensitivity of it with respect to each uncertain parameter. Several methods have been proposed for this purpose, one of the most popular being the evaluation of Sobol indices [107]. The Fourier Amplitude Sensitivity Test (FAST) method [26] has been proposed to accelerate the computation of these indices and already used successfully for acoustic and poroelastic applications [87, 34]

2 Sensitivity of a sandwich plate with attached limp poroelastic material

The transmission loss of a system composed of a honeycomb panel and a fibreglass layer has been studied. This was modelled with the analytical model described in section 5, where the global transfer matrix is

$$T_{bare} = T_{sandwich} T_{poro}, \tag{7.1}$$

where $T_{sandwich}$ is given in equation 1.50 and T_{poro} in equation 1.69. A second configuration in which a thin limp screen is glued to the porous layer at the interface with the receiving cavity is studied. In this case, the transfer matrix is

$$T_{screen} = T_{bare} \begin{pmatrix} 1 & \mathrm{i}\omega m_{screen} \\ 0 & 1 \end{pmatrix}. \tag{7.2}$$

In both cases, the diffuse field transmission loss is computed with equation 1.48 between 100Hz and 10kHz. All constant parameters are summarised in Table 7.1. We would like to study the effect of five parameters on the overall transmission loss in the two configurations, namely 2 parameters of the sandwich, core shear modulus and damping coefficient, and 3 parameters of the fibreglass layer, its porosity φ_0, flow resistivity σ and viscous characteristic length Λ_{visc}. The two characteristic lengths Λ_{visc} and Λ_{therm} are usually correlated, which will be taken into account by taking $\Lambda_{therm} = 2\Lambda_{visc}$. The variation ranges of these five parameters are shown in Table 7.2. They are chosen as realistic considering both uncertainty in measurement and some latitude in design.

Results of the FAST analysis are presented in Figure 7.2 for the bare case and 7.3 for the case with a screen. The sensitivity indices of each parameter are presented as proportions of the standard deviation. Some conclusions can be drawn for both cases: none of the considered parameters is important in low frequency, while the dominant parameter in HF is the viscous length, which accounts also for the thermal characteristic length, as they are considered proportional. The parameters of the structure (G and η) have no significant incidence on the transmission loss in their considered variation ranges. This is due to the fact that the considered frequency range is well below the coincidence frequency, which occurs around 19kHz.

The transmission loss variation range is shown for the two cases in Figure 7.4 for the two cases. It can be seen that the addition of a thin screen reduces the loss in low frequency, but improves in much more in high frequency. A mass-fluid-mass resonance phenomenon appears in both cases, where the TL is lower around 500Hz for the screen case, and around 1kHz for

the bare case. In both cases, flow resistivity σ is the dominant parameter between 1000 and 1500Hz. This phenomenon is due to the mechanical resonance of the cavity filled of porous, analogous to what happens in a double-plate system.

The main difference between the two cases in terms of sensitivity is the preponderance of porosity between 400 and 1200 Hz when a screen is placed after the porous material. The overall effect of the screen is globally to increase the transmission loss above 650 Hz, and reduce the variability of the TL with respect to the investigated parameters.

Parameter	description	unit	value
E	Skin Young modulus	GPa	47
ν	Poisson ratio	–	0.1
h_{skin}	Skin thickness	mm	1
h_{core}	Core thickness	mm	12.7
m	Sandwich surface density	kg.m^{-2}	8
α_∞	Tortuosity	–	1.25
ρ_1	Porous *in vacuo* density	kg.m^{-3}	5.5
Λ_{therm}	Thermal characteristic length	μm	$2\Lambda_{visc}$
h_{poro}	Porous thickness	mm	50
m_{screen}	Screen surface density	kg.m^{-2}	0.2

Table 7.1 – Constant parameters considered in this study

Parameter	description	unit	min. value	max. value
G	Shear modulus of the sandwich's core	MPa	20	40
η	Structural damping	–	10^{-3}	10^{-2}
φ_0	Porosity	–	0.85	0.99
σ	Flow resistivity	kN.m^{-4}.s	10	30
Λ_{visc}	Viscous characteristic length	μm	25	75

Table 7.2 – Variable parameters considered in this study

3 Conclusion

The sensitivity of a model of transmission loss through composite sandwich plates with attached limp poroelastic materials to several parameters is studied with the FAST method, which allows to efficiently estimate the sensitivity indices of parameters subjected to uncertainty in a model. However the uncertainty level of the parameters should be known before the analysis, in the form of a variation range or a probability distribution.

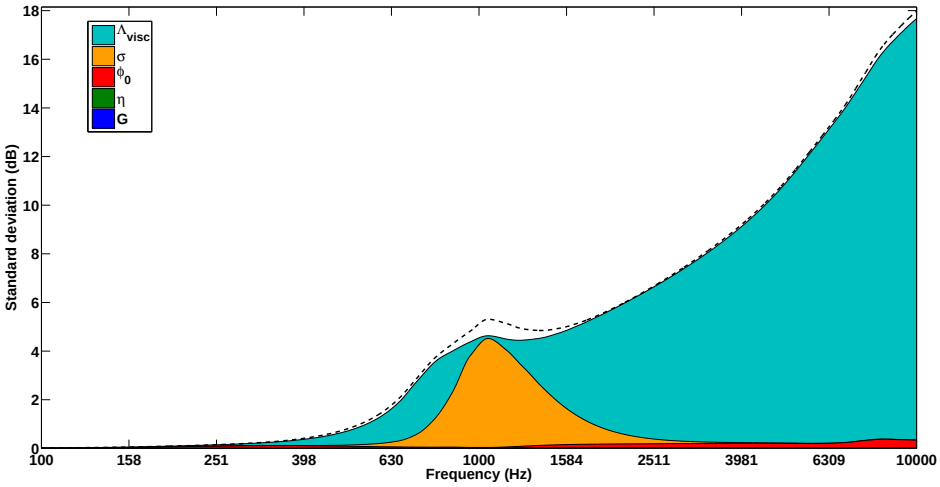

Figure 7.2 – Sensitivity indices in the porous configuration

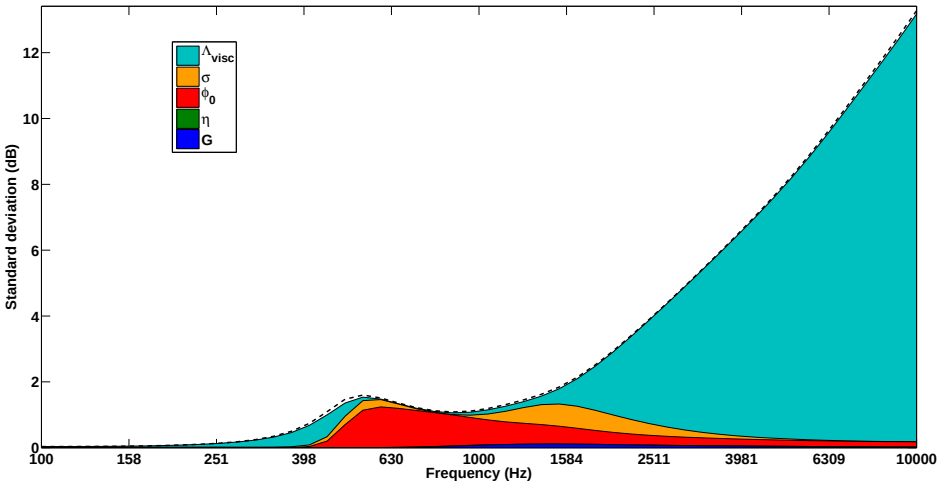

Figure 7.3 – Sensitivity indices in the porous+screen configuration

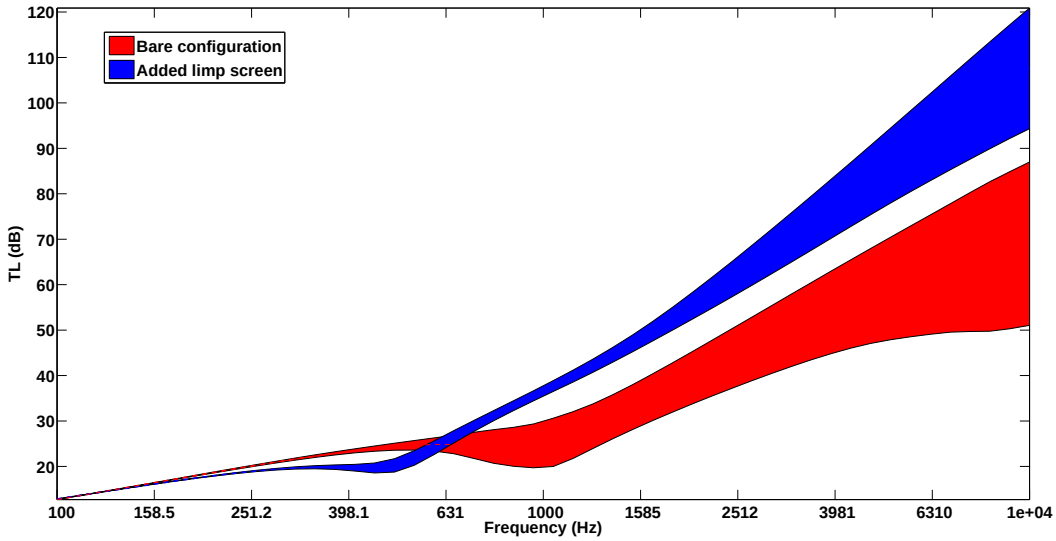

Figure 7.4 – Transmission loss variability in the two configurations (average value ± standard deviation). Red: bare case ; blue: thin screen.

In the considered case, it has been found that the most important parameters in high frequency are the viscous and thermal characteristic lengths, as well as the flow resistivity in an intermediate frequency range around the mass-fluid-mass resonance. The presence of a light thin screen on the transmission side allows to efficiently increase the TL in high frequency, though lowering the mass-air-mass resonance, which leads to slightly reduced performance in low frequency. In low frequency, the overall variability of the parameters stays low, well below 1dB, because none of the investigated parameters have an effect on the mass of the system, and the effect of poroelastic materials is usually rather weak in low frequencies.

Chapter 8

Sensitivity analysis of transmission loss through treated composite panels: experimental and numerical study

Abstract

The previous chapters aimed at numerically estimating the sensitivity of the transmission loss (TL) to material parameters. An experimental study was carried out in collaboration with the Groupe d'Acoustique de l'Université de Sherbrooke (GAUS, Sherbrooke, Canada) in order to compare experimental results and numerical sensitivity analysis. The objective was to assess the transmission loss through a composite sandwich plate with several different noise treatments. The variable parameters were of two kinds: on the one side porous materials, with different fibrous and foam configurations, and viscoelastic treatment on the plate on the other side, allowing to increase damping of the plate without adding much mass. The results of the parametric study are then used to validate a numerical model of the structure using the simplified transfer matrix method (TMM). Finally, a numerical sensitivity analysis using the FAST method is performed on the sTMM model. The most influential parameters can be identified that way, as well as the effect of uncertainties in the experiments can be evaluated. It is shown that although many variables, such as the air gap between the plate and the treatment, are difficult to control accurately, they have little effect on the results.

Contents

1 Introduction

The FAST method has proved useful in the previous chapters to estimate the sensitivity of transmission loss models to uncertain or design parameters. The objective of this study is now to assess experimentally the validity of the approach. Indeed, experiments intrinsically include uncertainties, and the effects observed with a computer code may be too slight to be acknowledged during tests. On the other hand, as it is much more complex to have parameters vary independently during an experiment, a sensitivity analysis on a representative model may help in identifying the phenomena at hand.

The chapter is structured as follows. Section 2 exposes the experimental set-up and material. The numerical model of the structure is presented and validated in section 3. Finally, section 4 presents and compares the results of an experimental parametric analysis and a numerical sensitivity analysis.

2 Experimental set-up

The aim of this work is to measure the transmission loss of a composite panel with several acoustic treatments. The experimental set-up is described in the present section.

2.1 TL measurements

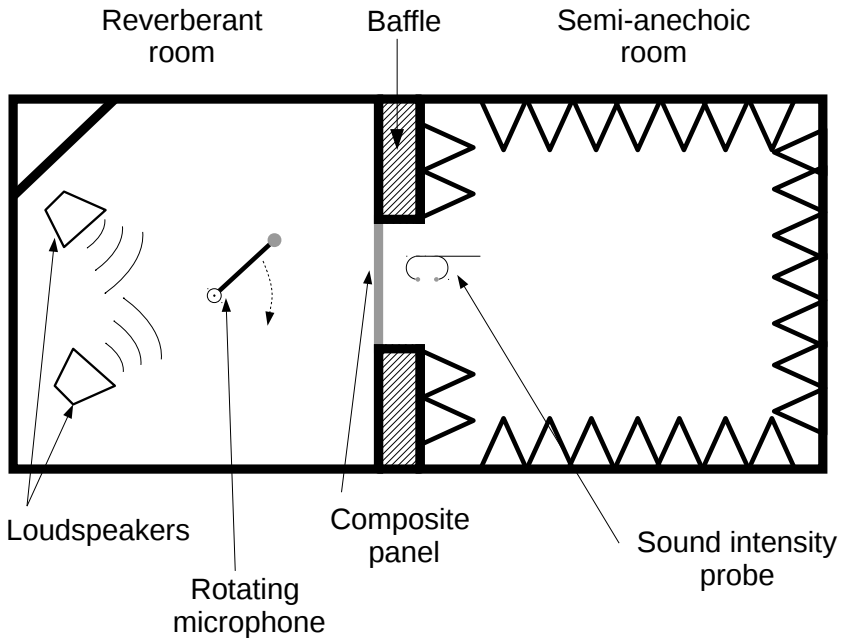

Figure 8.1 – Schematic of the measurement setup

The panel is installed between a reverberant room and a semi-anechoic room, in order to measure the TL with the intensity method [43]. A white noise diffuse field excitation is created in the reverberant room with a sound pressure level of 100dB between 100Hz and 10kHz with the use of four loudspeakers (one for low frequencies up to 2kHz, two for medium frequencies between 1kHz and 8kHz and one for high frequencies above 5kHz. The sound pressure level in the reverberant side L_p^{inc} is measured with a microphone mounted on a rotating stick allowing to take a spatial average in the room. The intensity level on the anechoic side L_i^{trans} is measured with a sound intensity probe. A spatial average is made by manually moving the probe around the whole surface of the panel. Care has to be taken to ensure that the probe is always perpendicular to the plate. The sound transmission loss of the panel defined by the difference of intensity levels on both sides. The sound intensity on

the reverberant room side is [25]:

$$I^{inc} = \frac{< p^2 >}{4\rho_0 c_0}, \tag{8.1}$$

with $< p^2 >$ the mean quadratic pressure in the reverberant room and ρ_0 and c_0 being the density and sound velocity in air. The intensity level on the incident side is then

$$L_i^{inc} = 10 \log_{10} (\rho_0 c_0 I_{inc}) = L_p^{inc} - 6, \tag{8.2}$$

where the approximation $20 \log_{10}(2) \approx 6$ is used. We then obtain the formula for the TL:

$$\text{TL} = L_p^{inc} - L_i^{trans} - 6. \tag{8.3}$$

The TL is then averaged over frequencies to compute the result over 21 third octave frequency bands with central frequencies between 100Hz and 10kHz.

2.2 Sandwich panel

The panel is a made of a thick composite sandwich construction, with carbon-fiber reinforced skins and honeycomb core. The dimensions are 1×1.5m. This panel was used in several past studies [17], so that its material parameters have been fully characterized. They are presented in Table 8.1. With this parameters, the panel's critical frequency is $f_c = 520$Hz.

The panel is mounted in an opening between the two rooms in continuity with the wall on the reverberant room side, so that the niche is fully in the anechoic room, as shown on Figure 8.1. The panel is fixed with silicon glue on the side of the opening and maintained with adhesive aluminium tape on the reverberant room wall to avoid acoustic leaks. This mounting can be approximated by simply supported boundary conditions.

One downside of using this panel was the presence of small massive aluminium mountings glued to the skin on the anechoic side, and which could not be removed for the present study. These were accounted to in the mass of the panel's skins, and are shown in the following to have little incidence on the TL otherwise.

2.3 Viscoelastic treatment

The viscoelastic treatment consists of thin auto-adhesive plates with dimensions 0.610×0.915m (2×3ft), which are glued to the reverberant room side of the composite panel. Three cases are considered: without treatment, with one plate (corresponding to 38% of the panel covered by the treatment) and two plates (77%). The viscoelastic treatment has a surface

Parameter	E_1 (MPa)	E_2 (MPa)	E_3 (MPa)	G_{12} (MPa)	G_{13} (MPa)	G_{23} (MPa)
Skin	46×10^3	46×10^3	46×10^3	17.6×10^3	17.6×10^3	17.6×10^3
Core	1	1	179	1	26	56
Parameter	h (mm)	ν_{12}	ν_{13}	ν_{23}	ρ (kg.m^{-3})	
Skin	0.96	0.3	0.3	0.3	1900	
Core	25.4	0.45	0.01	0.01	64	

Table 8.1 – Material parameters of the bare panel.

mass of 1.68kg.m^{-2}. The loss factor of the panel in the three configurations is measured by the decay rate method (described in chapter 9 of [69]) using an impact hammer. The results are averaged over 4 impact points with 5 impacts each, making a total of 20 measurements. For each impact points 6 accelerometers are placed at random positions around it, at a distance ranging between 5cm and 30cm. The measured loss factors are presented in Figure 8.4, with trend curves following a logarithmic law with the form :

$$\eta = \eta_0 - 3.2 \log_e f. \tag{8.4}$$

For the bare panel case, the results in the mounted configuration are much higher than previous measurements of the same panel made in an anechoic room with free boundary conditions [17], highlighting the importance of boundary conditions on damping of a structure.

2.4 Porous treatments

Two kinds of porous treatments are used in this study: melamine foam and fiberglass (FG). The melamine is rather rigid and very light with a low flow resistivity, while the FG is heavier and has a higher σ. Their material parameters have been characterised and are presented in Table 8.2. The measures were performed directly with a porosity-meter and resistivity-meter for ϕ_0 and σ. The other parameters were obtained from a normal absorption measurement in impedance tube with an inverse characterisation method [7]. The mounting of the porous treatments are presented in Figure 8.5. The FG layers are bonded to the plate with double-sided adhesive tape, and to the sides of the niche with a double layer of neoprene tape and aluminium tape to avoid acoustic leaks. As the fiberglass is wrapped in a loose plastic coating, there is no real mechanical bond between the plate and the fibrous, so that an air gap of 1mm is assumed to lie between them. The mass of the coating is taken into account in the density of the porous.

Due to the fragility of the melamine foam, it was not possible to use the neoprene tape on the sides, so only aluminium tape was employed. Because of the presence of the mountings

(a) Semi-anechoic side (b) Reverberant room side

Figure 8.2 – Bare panel mounting between the two rooms.

(a) 38% coverage (b) 77% coverage

Figure 8.3 – The panel seen from the reverberant room with both viscoelastic treatments

on the panel, it was necessary to leave a wider air gap of about 2cm between the panel and the foam layer.

	h (mm)	ϕ_0 (–)	σ (N.s.m^{-4})	α_∞ (–)	Λ_{visc} (μm)	Λ_{therm} (μm)	ρ (kg.m^{-3})
melamine	25.4	0.99	7300	1	88	160	7.4
FG631	47	0.99	26557	1.07	640	98.5	9.61
FG034	25.4	0.98	28000	1	29.6	312.7	9.57

Table 8.2 – Material parameters of the tested porous materials.

3 Numerical model validation

The experimental set-up of the previous section is modelled with the simplified transfer matrix method (sTMM) presented in subsubsection 5.1.1 of chapter 1. In the following, we consider a panel with $L_x = 1.5$m, $L_y = 1$m, 500 incidence angles θ linearly distributed in $\left[0; \frac{\pi}{2} - 10^{-7}\right]$ and 201 direction angles φ linearly distributed in the interval $[0; 2\pi - 10^{-6}]$. The double integral of equation 1.80 is evaluated with the trapeze rule with 1000 points in each dimension.

The model is validated using the results of the parametric analysis of paragraph 4.2.1. The results are presented on Figure 8.6. Below 300Hz, the model and the measurement never agree, due to the fact that the cut-off frequency of the reverberant room is around 250Hz, and probably partly because of a modal behaviour of the plate. Above this frequency, the agreement between the model and the experiment is far from perfect, with less than 3dB difference for most of the cases, except for the untreated panel in high frequency, where the difference may reach 6dB. The model has the least difference with the measurement in the heavily damped cases. The effect of the damping treatment is also observed sooner in the model than in the measurement, which can be due to measurement errors, as the effect is very small.

However, the trends observed on the measurements are well followed, both qualitatively and quantitatively by the sTMM model, so the model makes a good candidate for a sensitivity analysis, as it runs in a shorter time than the more accurate GLM model [17].

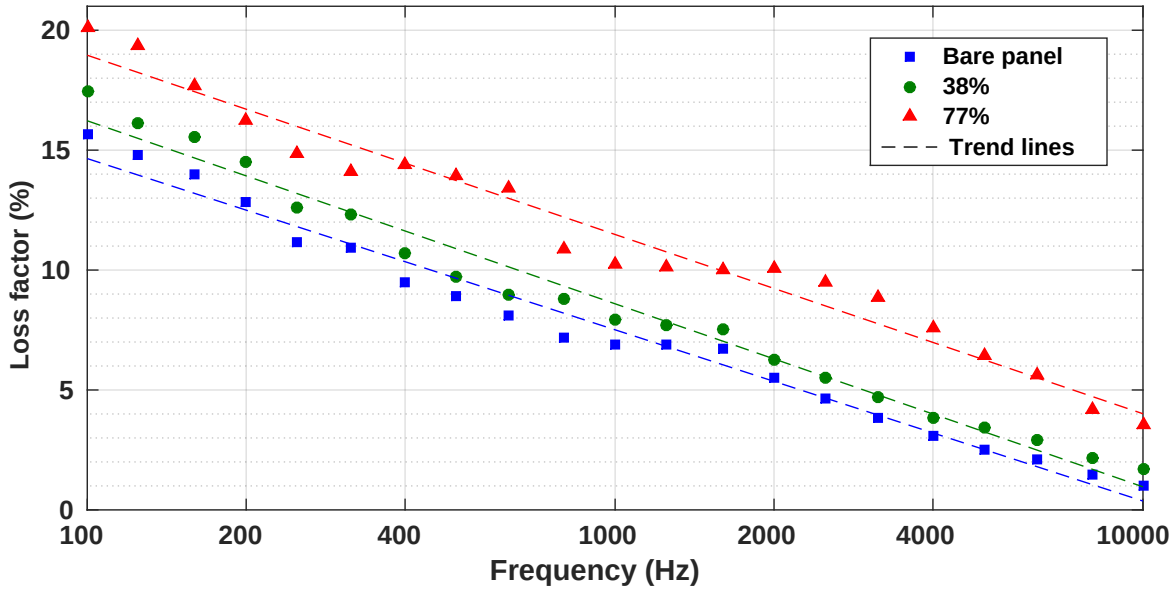

Figure 8.4 – Damping loss factors of the panel in the three cases with respect to frequency.

(a) Fiberglass 631

(b) Melamine foam

Figure 8.5 – The panel seen from the anechoic room with two different porous materials attached.

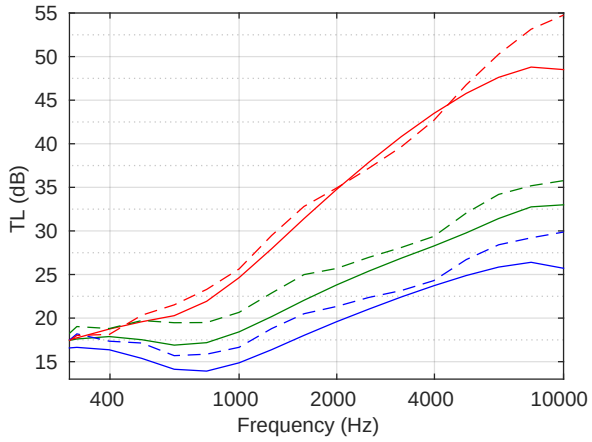

(a) No added damping

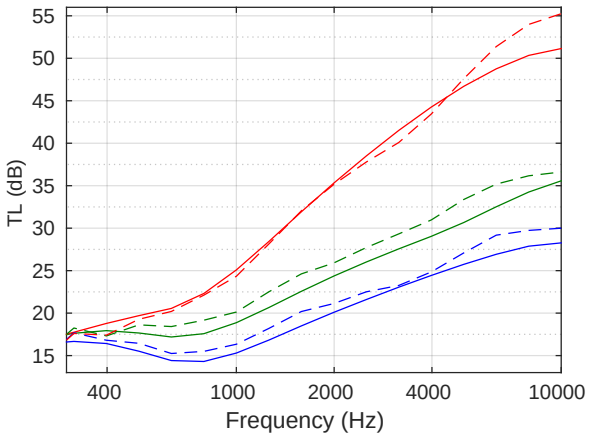

(b) 38% damping

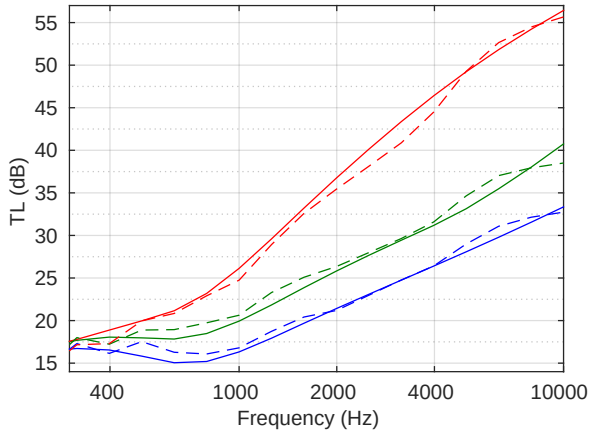

(c) 77% damping

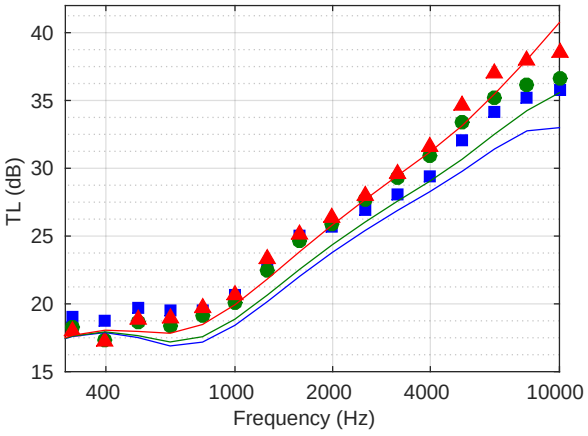

(d) Melamine, all damping treatments

Figure 8.6 – Numerical-experimental comparison. Dashed lines or symbols: measurements, continuous lines: sTMM model. For figures (a),(b),(c): red: FG631, green: melamine, blue: bare panel. For figure (d): red: 77% damping, green 38%, blue: no damping added.

4 Numerical and experimental sensitivity analysis results

4.1 Fiberglass

4.1.1 Parametric analysis

The results of all cases of porous materials without adding damping to the panel are presented in Figure 8.7a. It can be seen that adding a poroelastic treatment does not modify the TL of the panel below 400Hz. Above this frequency, any FG treatment is better than the bare panel, and their ranking never changes. The FG employed here have rather similar parameters, which enables comparisons. The thickest FG631 always exhibits the best TL, which can be explained by the fact that, since all FGs have a similar flow resistivity, their thickness is important.

4.1.2 FAST analysis

The FAST analysis is conducted on an sTMM model consisting of three layers: the plate as defined by Table 8.1, an air gap and a porous material modelled with the limp skeleton model. The first FAST analysis has 6 parameters, of which 4 are characteristics of the fiberglass (σ, Λ_{therm}, Λ_{visc}, ρ) and 2 are geometrical parameters (h, h_{air}). The number of samples is 7000.

The results are presented in figure 8.7b, along with the standard deviation of the TL over the sampling. For low frequencies below 400Hz, the most important parameter is the thermal characteristic length Λ_{therm}, but since the standard deviation is below 0.2dB, the main conclusion is that the TL is insensitive to any FG parameter in this range, since it is mainly governed by the mass law of the panel.

Above 400Hz, the standard deviation increases to reach almost 2dB at 2kHz. The two most important parameters are then the thickness of the foam layer h, and again Λ_{therm}. The viscous length Λ_{visc} comes third between 800Hz and 5000Hz, but the thickness of the air gap h_{air} and the density of the skeleton ρ have practically no incidence. The same is true for the flow resistivity σ, which is bound to vary in a rather narrow region, whereas the characteristic lengths have a broad range of variation. The observed dispersion of the TL is smaller than in the test, due to the narrower variation range of the thickness h.

	σ (N.s.m^{-4})	Λ_{visc} (μm)	Λ_{therm} (μm)	h_{air} (mm)	h (mm)	ρ (kg.m^{-3})
Min. Value	25000	25	90	1	45	9
Max Value	30000	650	320	3	55	10

Table 8.3 – Variation intervals for the 6-parameter FAST analysis of a range of fiberglass.

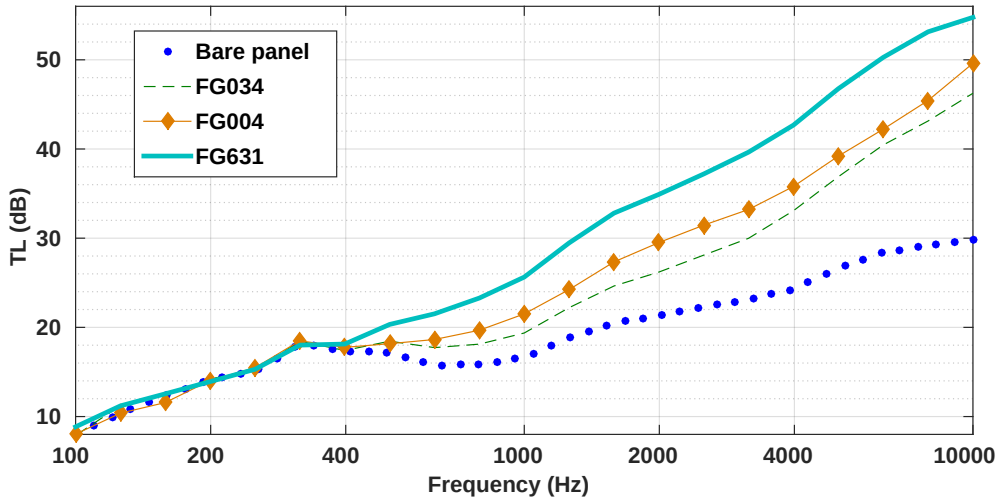

(a) TL of the panel with 3 different fiberglass treatments without added damping. Dotted line: bare panel.

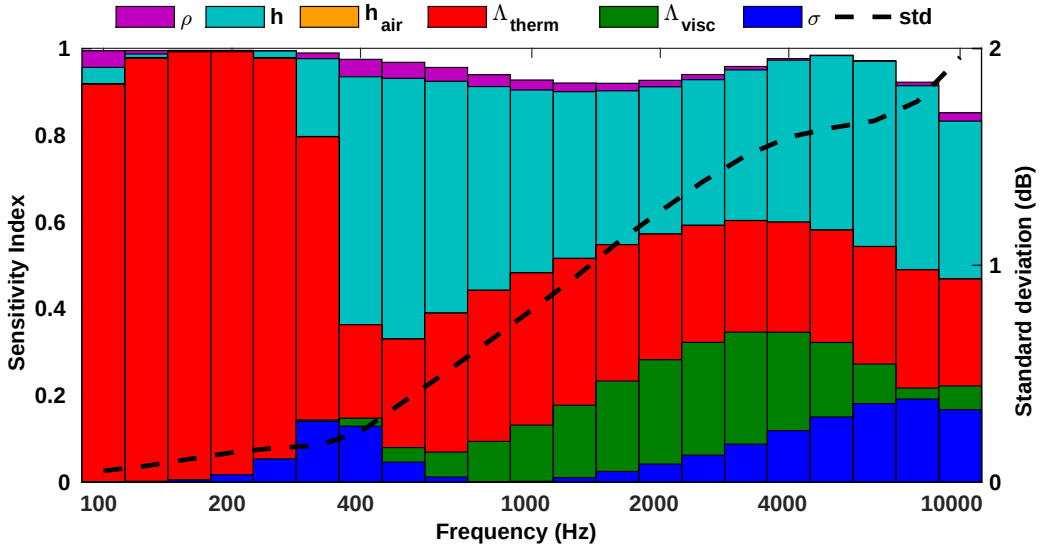

(b) Sensitivity indexes of the 6 parameters for the fiberglass variability analysis.

Figure 8.7 – Experimental TL and FAST results for the fiberglass sensitivity analysis

4.2 Porous material and viscoelastic damping

4.2.1 Parametric analysis

The second part of the experiment aimed at comparing the effects of the added viscoelastic damping and of the porous treatment. The parametric study involved three types of porous treatment (none, melamine foam and FG631) and three types of viscoelastic treatment (0%, 38% and 77% of the plate's surface treated). The test results are presented on Figure 8.8a, where the TL for the 38% and 77% damping cases have been corrected by removing the mass law added by the viscoelastic plate.

It can be seen that on overall the effect of damping, although sensible, is less important than that of the porous treatment. For all three porous cases, a change in damping affects the TL by about 2dB between 400Hz and 1kHz, then again above 3kHz. No matter the damping treatment, the plate with FG631 always as a higher TL than with melamine than with no porous. Since the melamine and the FG631 have very different characteristic lengths and resistivity, it is difficult to separate the contribution of each.

4.2.2 FAST analysis

For this case, the FAST analysis has 7 variables. All are assumed to obey uniform repartition laws within intervals chosen to match those of experimental conditions. They are defined in table 8.4. The number of samples is again 7000.

With the interval given in table 8.4 for η_0, the DLF of the structure spans the interval measured experimentally. The other parameters are characteristics the porous materials σ, Λ_{visc} and Λ_{therm}, their mass density ρ and two geometric parameters, the width of the air gap h_{air} and the thickness of the porous layer h. In the previous parametric study, damping and porous characteristics are controlled parameters, while the width of the air gap and the exact thickness of the porous are uncertain to some extent.

The results are presented in figure 8.8b. As expected, the most important parameters above the critical frequency, which lies in the 500 Hz band, are the porous characteristics σ, the thickness h and the viscoelastic damping η_0. The other parameters, especially the mass of the skeleton, only have influence in the low frequency part, where the variance is small both in the model and the experiment. The effect of damping follows the trend observed in the above parametric analysis, being more important between 400Hz and 1kHz and above 2kHz than between 1 and 2kHz. However, its importance seems much higher than it is in reality, since it is nearly predominant in the 8kHz and 10 kHz bands. This effect was also observed by comparing the model with the results in section 3.

To conclude, with such a wide variation of all parameters, the most influential phenomenon on the TL of a damped composite plate with attached porous material is the resistance of the porous material to the air flow, combination of the material thickness and its intrinsic flow resistivity. Increasing the panel's damping with a viscoelastic treatment also can help much towards improving the TL, though only in higher frequencies.

5 Conclusion

The sensitivity of the transmission loss of a composite plate with attached noise treatment was studied in this chapter, by comparing the results of an experimental parametric analysis to a FAST sensitivity analysis of a representative numerical model. The same effects are qualitatively observed on both models, and the numerical analysis helps in explaining features of the behaviour of the porous treatment.

The well known mass law regime is determined only by the panel's mass, the porous treatment being too light to have a significant effect up to the critical frequency. Beyond it, a hierarchy of effects can be derived from this analysis, where the resistance of the porous material to an air flow, combining porous thickness and resistivity, is predominant for most frequencies. As the panel tested exhibited high damping, which was further enhanced by the use of viscoelastic treatments, this effect comes second as for the influence on TL. Then come the thermal and viscous dissipation effects in the porous, in this order. For fibrous materials with a limp skeleton, the inertial effect of the mass of the skeleton have very little influence on TL above the critical frequency.

Finally the air gap present in the experiment is shown by the FAST analysis to have very little effect on the TL variability, which is an important result in order to compare the performance of noise control treatments, since the size of this air gap is difficult to control due to the limp nature of fibrous materials.

	η_0 (–)	σ (N.s.m^{-4})	Λ_{visc} (μm)	h_{air} (mm)	h (mm)	Λ_{therm} (μm)	ρ (kg.m^{-3})
Min. Value	28	5000	75	10	25	98	7
Max. Value	35	30 000	700	30	40	160	10

Table 8.4 – Variation ranges of the 7-parameter FAST analysis

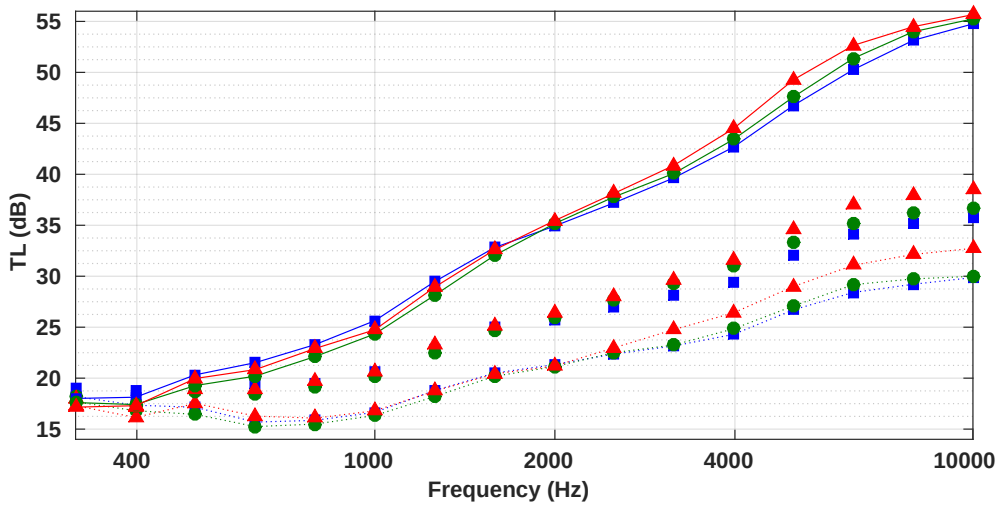

(a) TL of all 9 cases of the parametric study with correction for the added mass of the damping treatment. The shape of the marker indicates the damping treatment, the line style the porous material. Dotted line (···): bare panel. No line: melamine foam. Continuous line (—): fiberglass FG631.

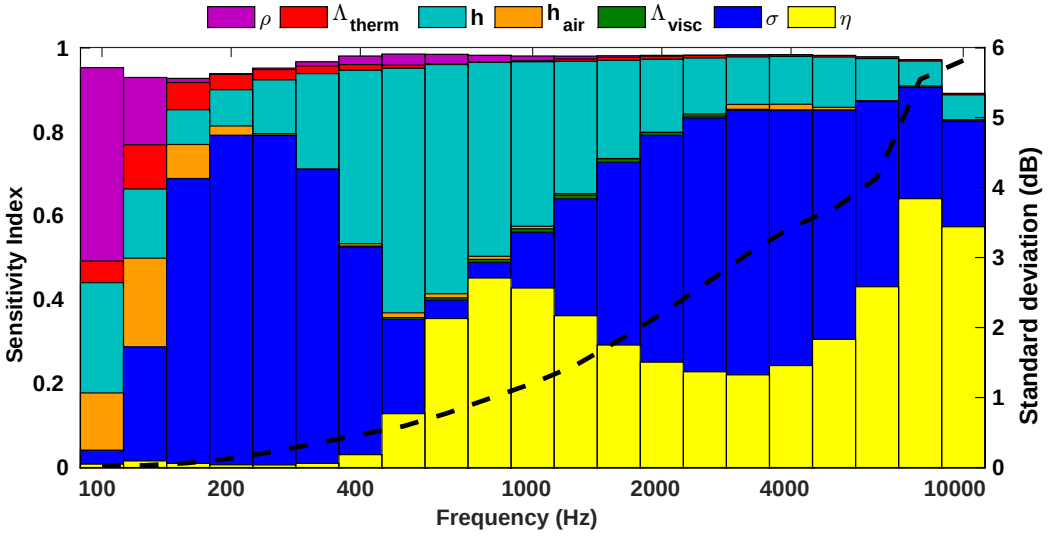

(b) Sensitivity indexes of the 7 parameters of the acoustic treatments.

Figure 8.8 – Experimental TL and FAST results for the *poro vs. visco* sensitivity analysis

Appendix A: Mass correction

According to chapter 5, the effect of mass above coincidence is negligible, the dominant parameter being by far damping. In order to justify the correction for mass law used in this chapter, we conducted a small numerical experiment, allowing to separate the effects of mass and damping on the TL of a plate. We consider an initial 6mm-thick aluminium plate with parameters $E = 70\text{GPa}$, $\nu = 0.33$, $\eta = 5\%$ and $\rho = 2700\text{kg.m}^{-3}$, compared to one with identical parameters, except for a density of $\rho_h = 2900\text{kg.m}^{-3}$. The transmission loss is represented in Figure 8.9 for the original plate, the heavy plate and the heavy plate with mass correction, in each case in narrow and third-octave bands. In this case, it can

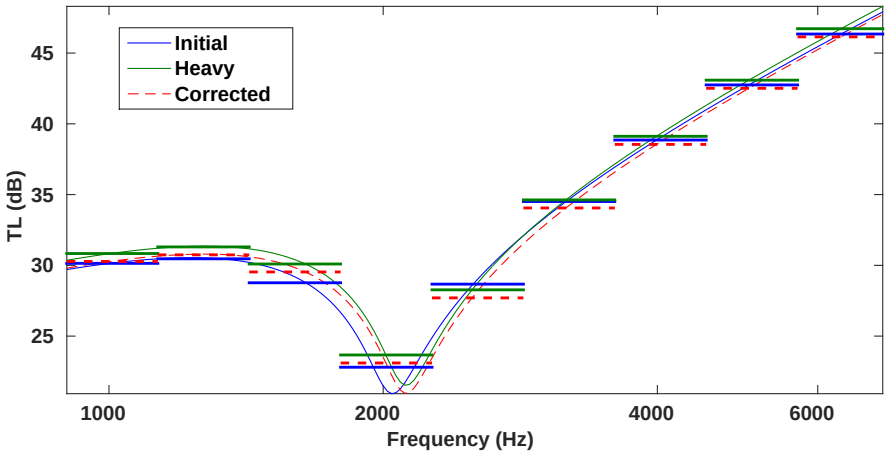

Figure 8.9 – TL for the initial, heavy and corrected plates, narrow and 3$^{\text{rd}}$-octave bands.

be seen that the asymptotic behaviour of the initial and the heavy plate with correction are identical in low and high frequencies, and that only the region around the critical frequency is affected by the mass change. Since the critical frequency varies as the square root of the plate's surface density, the error on the critical frequency is less than the relative change of mass. In the case where the added mass is small compared to the mass of the original panel, the critical frequency stays in the same third-octave band, meaning that the error on frequency can be neglected. On the third-octave band plots, it can still be seen that the non-corrected TL of the heavy plate is closer to that of the initial plate in the octave just above coincidence.

We can conclude that the correction is valid only for low and high frequencies, and not close to the critical frequency. However, for structures exhibiting high damping such as the ones studied in the rest of this chapter, with a shallower dip or no dip at all at coincidence the validity region may be larger.

Appendix B: FAST analysis for the inverse characterisation of porous materials

The inverse method characterisation of porous materials involves a measurement of normal absorption in an impedance tube. For this test, the sample is placed at the end of the tube, potentially backed by an air cavity, and excited with a white noise signal by a loudspeaker located at the other end of the tube. The pressure wave is measured at two locations in the tube using two microphones, in order to separate the incident and reflected sound waves. Applying a Fourier transform to the obtained signals allows to compute the normal absorption coefficient with respect to frequency. An optimisation routine using a TMM model of the system placed in the tube can then be applied to find the porous material parameters that fit best the model to the measurement.

It has been shown [7] that each parameter can be identified using some specific parts of the absorption curve. This curve typically starts with 0 absorption at 0Hz, then increases steeply to reach a maximum, usually close to 1, then decreases and oscillates, as shown on Figure 8.10. The FAST analysis is conducted on the poroelastic parameters ranging in intervals defined in Table 8.5. These ranges correspond roughly to a polyurethane foam. The absorption is calculated with a TMM model with rigid skeleton assumption.

The results are presented on Figure 8.10, along with the absorption of the material with the median values of parameters. The sensitivity indices are here weighted with the standard deviation, to highlight regions of high and low variability. It can be seen that the variability is very low around the peak of absorption, which is expected since absorption cannot be greater than 1. The dominant parameter before it is clearly the resistivity, while all parameters but Λ_{therm} are important when absorption decreases after the peak. The porosity is slightly more important than the others in this region. Finally, it can be noted that Λ_{therm} has significant influence on absorption only around the local minimum between the first two peaks of absorption, making it the most difficult parameter to estimate with this method. The goal of adding a backing cavity in the Kundt tube is to lower the frequency at which these peaks appear into the working range of the tube, making it easier to obtain the thermal length.

	φ_0	σ	α_∞	Λ_{visc}	Λ_{therm}
	(–)	(Nsm^{-4})	(–)	(μm)	(μm)
Min. value	0.90	14400	1.0	90	180
Max.value	0.97	17600	1.1	110	220

Table 8.5 – Values for the FAST analysis of the normal absorption coefficient

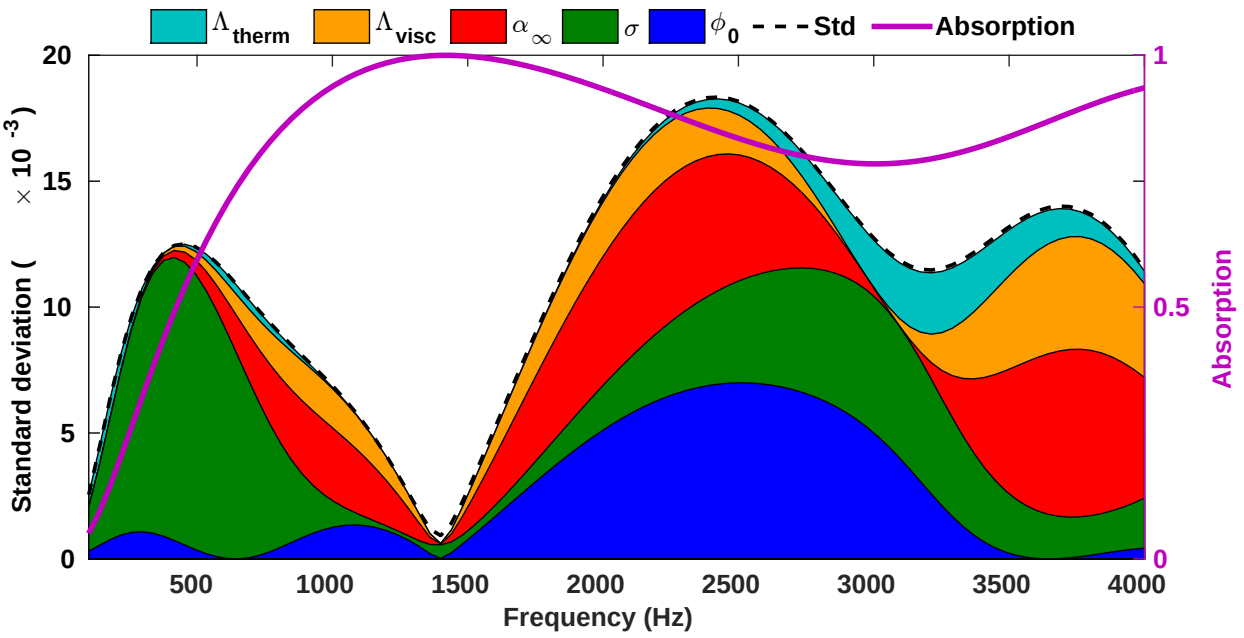

Figure 8.10 – FAST analysis of the normal absorption, main effects as a proportion of standard deviation. Purple thick line: Absorption of the nominal material.

Chapter 9

Experimental investigation of noise reduction through a cylindrical shell with noise treatment

Abstract

The effect of noise treatment on the noise reduction of a composite cylindrical shell is studied in this chapter. An experimental study was carried out at LTDS using a sandwich composite cylinder. The study can be decomposed in two phases, namely mechanical and acoustic tests. The mechanical tests were performed by exciting the cylinder with a shaker in a broadband frequency range, in order to retrieve the bending wave propagation characteristics of the shell. These were then used for fitting a model and obtain the mechanical parameters such as shear and Young's moduli. The foam used as acoustic treatment was also characterised using impedance tube measurements. Noise reduction (NR) measurements were then performed in a reverberant room, in two cases, in presence and absence of the poroelastic layer. The presence of the treatment clearly improves the NR throughout the whole frequency band. The causes of this improvement are then analysed by comparing the results with an SEA model: added mass effect and reduction of the cavity size play a small but significant role, while the remaining is due to absorption of the foam.

Contents

1 Introduction

Noise reduction capability of cylindrical shell have been studied since the 60s, mainly with aerospace applications in mind. Numerical model for the cavity have been developed since the 70s and are reviewed in chapter 3. Most of these models [53, 62, 31] focus on the transmission loss (TL), which assume a perfectly absorbing cavity. However, since the transmission in the case of a shell occurs though the whole surface and into a finite, reverberating cavity, the TL is not the most relevant indicator. Koval [55] introduced a model for the noise reduction index (NR), taking into account the reverberated field inside the cavity. This model was extended by Magniez et al. [72] to more complex layerings including dissipative poroelastic materials. An analytical model for a *finite* cylindrical shell was proposed and validated experimentally by Li and Vipperman [66]. The latter used a modal model of the shell and its interior cavity to compute the response to a plane wave.

Experimental validations of the models are much less commonly published than theoretical papers. One can cite the work of White [115], who first measured the noise reduction of

a steel cylindrical barrel in reverberant room and anechoic room. His results were compared to an SEA model. Lee and Kim [62] validated their TL model with a thin shell cylinder with a very small radius of 10cm. Yuan et al. [119] investigated the noise reduction through a cylindrical shell, using a point source acoustic excitation.

Poroelastic linings, despite being extensively studied for the case of plates, have attracted much less attention in the case of shells. The most used model is the one of Lee et al. [63], for a the TL of a poroelastic layer sandwiched between two shells, where the properties of an equivalent fluid are computed with a plate model using the full Biot model. Magniez et al.[73] developed an analytical model for the TL of assemblies comprising one or two shells and a poroelastic layer, which was validated against FE models.

The chapter is structured as follows. The material used for the experiment is presented in section 2, namely a composite shell and the porous material lining. The characterisation of the porous material parameters is also explained in this section. The characterisation procedure of the cylindrical shell is then presented in section 3. The principles of the acoustic measurements are then detailed in section 4, where the results are also compared to a numerical SEA model.

2 Material

2.1 Composite cylinder

The cylindrical shell is made of a Nomex honeycomb sandwiched between two layers of carbon fibre-epoxy skins. The honeycomb cells are rectangular. The core has a thickness $h_c = 12.7$mm and a density $\rho_c = 48\text{kg.m}^{-3}$, while the skins' thickness is $h_s = 0.5$mm for each skin, with a density $\rho_s = 1400\text{kg.m}^{-3}$. The outer radius is $R = 350$mm. The surface inside the cylinder is smoother than the outer surface, due to the manufacturing process, which also eases the installation of the porous lining. The total mass of the cylinder is 5.30kg.

For the acoustic tests in reverberant room, the cylinder is closed on the top by a heavy lid made of a square chipboard plate[1], weighing 8.65kg, in order to minimise the sound transmission through it. The bottom rests on the ground, a carpet ring on both sides ensuring acoustic isolation.

[1]French: médium (aggloméré)

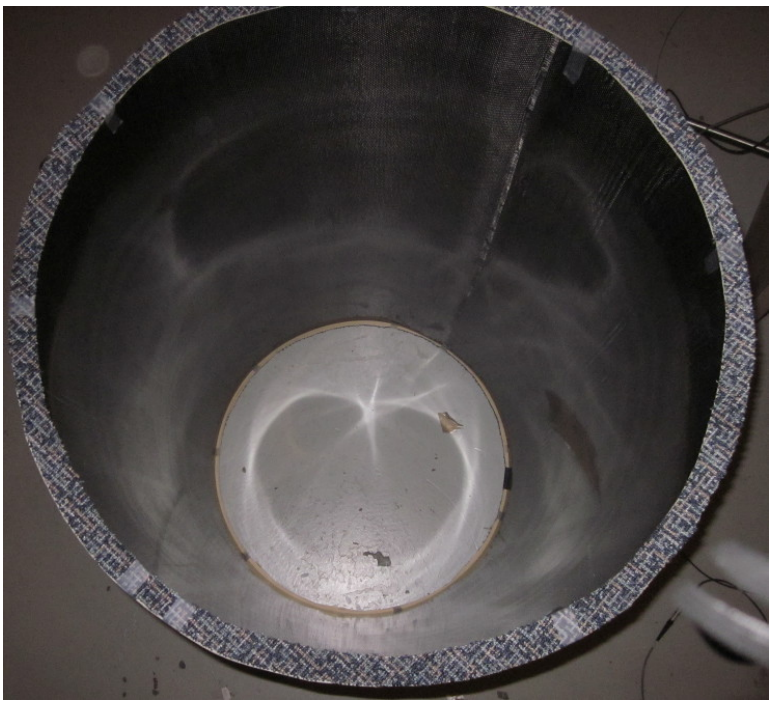

Figure 9.1 – Bare cylinder seen from the top. The isolating carpet ring is visible.

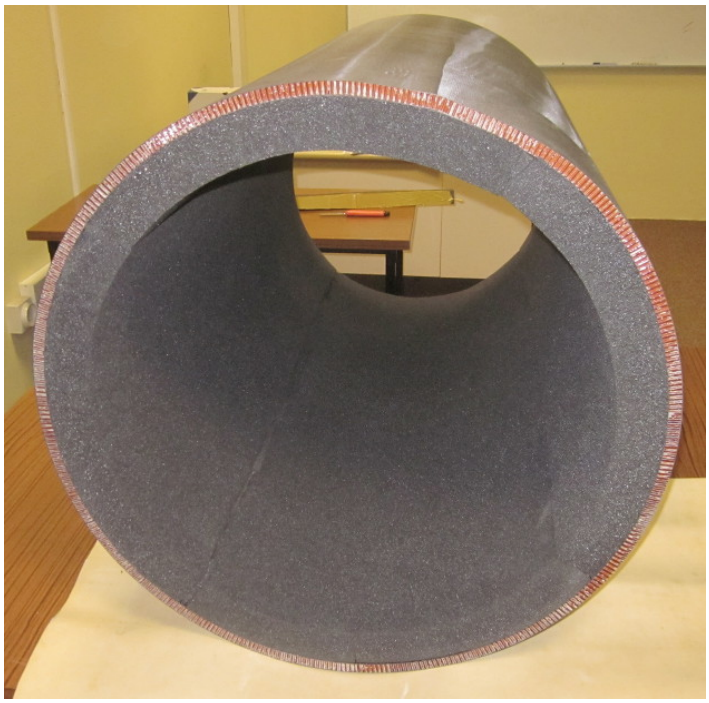

Figure 9.2 – Cylinder with poroelastic treatment.

2.2 Porous lining

The porous material used in this study is a polyurethane (PU) foam in the form of plates with thickness 5cm coated with a thin adhesive layer on one side. The foam was characterised in the GAUS. The porosity ϕ_0 and *in vacuo* skeleton density ρ were obtained from a 100mm diameter circular sample with a porosity-meter using the missing mass method [88]. The resistivity σ was also measured directly with an air flow resistivity-meter [108]. The Young modulus E was measured with a Quasi-static Mechanical Analyzer (QMA) [61]. The tortuosity α_∞ and the viscous and thermal characteristic lengths Λ_{visc} and Λ_{therm} were obtained with an inverse characterisation [7] from a normal absorption measurement in impedance tube with diameter 44mm.

The parameters are summarised in Table 9.1. The total mass of the noise treatment installed inside the cylinder is 4.25kg.

	E (kPa)	ϕ_0 (–)	σ (N.s.m^{-4})	α_∞ (–)	Λ_{visc} (μm)	Λ_{therm} (μm)	ρ (kg.m^{-3})
value	53	0.956	6900	1.85	122	265	32.17
error bounds	±3	±0.006	±150	±0.1	±26	±67	0

Table 9.1 – Material parameters of the foam

3 Mechanical characterisation of the cylinder

The principle of the wave characterisation is to measure the displacement field on the surface of the cylinder using a laser vibrometer, and derive from a spatial Fourier transform the wave propagation characteristics, as proposed in [11, 12]. The dispersion curves can then be used as a basis for identification of material parameters.

3.1 Experimental setup

The cylinder is mounted on a holding structure comprising a metal frame, an axis and two bicycle wheels and tyres, as depicted in Figure 9.3. The inflated tyres hold the shell by friction by effectively decoupling it from the holding structure. The vibrometer's scanning head is located exactly 3m away from the cylinder, and the laser beam is aligned to a radius. The principle is then to take advantage of the scanning laser vibrometer, and to scan along generatrices, while the angular coverage is obtained by manually rotating the cylinder around its axis. Since the laser beam has to be reflected in order to measure anything, and

the cylinder's outer surface have poor light reflection properties, reflective tape is glued to the cylinder at the measurement points, as shown on Figure 9.3b. An electromechanical shaker is mounted inside the cylinder and held by elastic straps to the top wheel's spokes. The excitation point lies about 25cm from the cylinder's edge.

3.2 Wavenumber characterisation

The velocity field is measured by the scanning laser vibrometer on a regular grid covering most of the cylinder's surface. The grid has 44 points in the circumferential direction (θ), and 39 points in the axial direction (z), hence 1716 points in total. The spacing between the points is $d_\theta = 5$cm along the circumference, and $d_z = 2.36$cm along a generatrix. The shaker is fed with a white noise signal between 0.01 Hz and 4 kHz. The measurement is made with a sampling frequency of 10 kHz, and a time-domain discrete Fourier transform (DFT) is computed with a resolution of 10 Hz. Scanning one generatrix took around 70s.

The resulting complex velocity field $v(f, \theta, z)$ in the frequency domain is then integrated to obtain the displacement field $u = \frac{1}{2\mathrm{i}\pi f} v$. A 2D spatial DFT is then applied to the displacement field u. The wavenumber space for several frequencies is represented in Figure 9.4. Although the results are rather noisy, a "figure 8" typical of cylindrical shells in low frequencies can be observed above 1 kHz. The cylindrical shell's behaviour in θ-direction is close to that of a plate with the same material configuration, while below the ring frequency, no 0-order wave in θ (also known as breathing waves) can propagate along the axial direction. The circumferential wavenumbers can therefore be used to identify material parameters from a plate model.

Since the used sandwich is rather stiff, it can be represented with a 4^{th} order sandwich plate model as used in [94] or [42]. The dispersion curve, expressing the wavenumber k as a function of the angular frequency $\omega = 2\pi f$, reads

$$k^2 = \frac{1}{2S}\left(m\omega^2 + \omega\sqrt{m^2\omega^2 + \frac{4mS^2}{D}}\right), \tag{9.1}$$

where $S = Gh_c\left(1 + \frac{h_s}{h_c}\right)$ is the shear parameter and $D = \frac{E}{2}h_s h_c^2\left(1 + \frac{h_s}{h_c}\right)^2$ is the bending stiffness. In these equation G and E are respectively the shear and Young's moduli of the plate, and h_s (resp. h_c) is the skin (resp. core) thickness.

The experimentally obtained frequency-wavenumber space of the cylinder is shown on Figure 9.5 for a normalised displacement amplitude. The normalisation is made by dividing the amplitude by its maximum along k_θ for each frequency. Due to noise in the signal, it was not possible to extract the relevant parameter model automatically, and the points used

(a) Holding structure

(b) Mounted cylinder

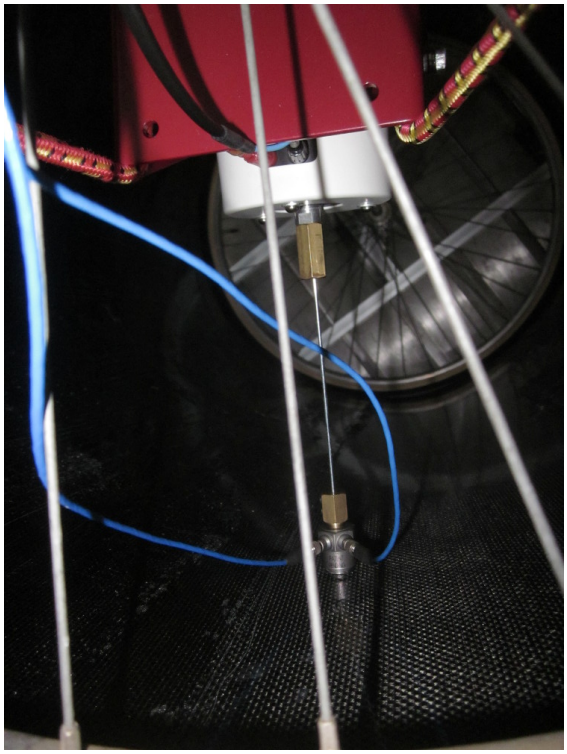

(c) Shaker

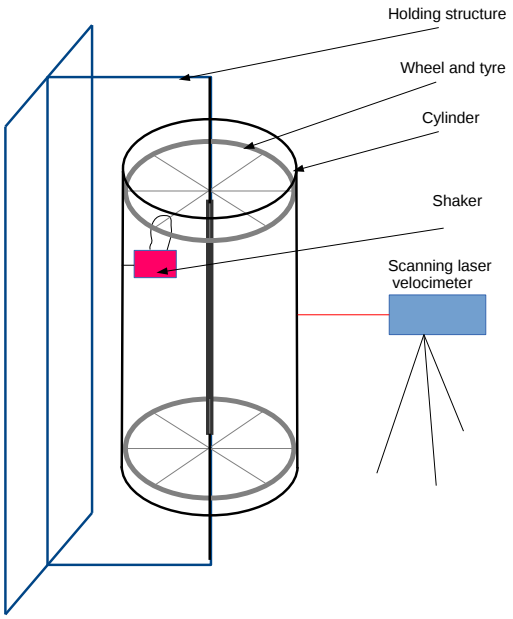

(d) Schematics

Figure 9.3 – Set-up for the mechanical characterisation

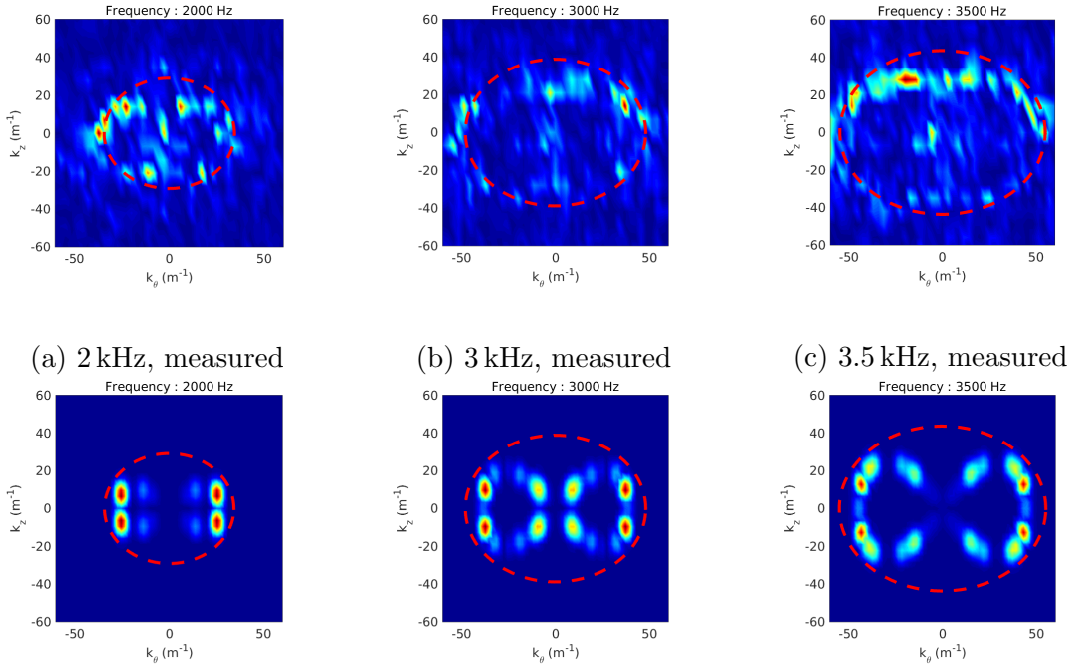

(a) 2 kHz, measured (b) 3 kHz, measured (c) 3.5 kHz, measured

(d) 2 kHz, FEM (e) 3 kHz, FEM (f) 3.5 kHz, FEM

Figure 9.4 – k-space at several frequencies for the finite element model and the measurement. In each figure, the red ellipse is the wavenumber for the equivalent plate.

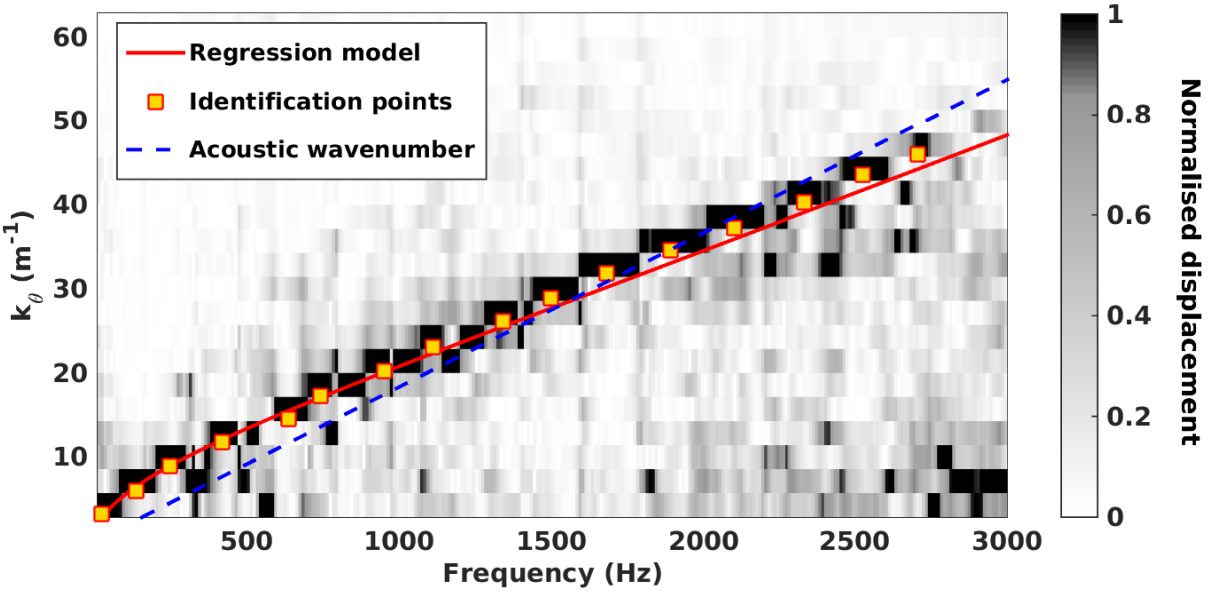

Figure 9.5 – $f - k_\theta$-space for $k_z = 0$ with normalized amplitude of displacement.

for evaluation were picked manually, as seen in the same figure. A non-linear fitting routine was then used to identify E_θ and $G_{r\theta}$ from equation 9.1. The retained parameters for the cylinder are finally $E_\theta = 22000\,\text{MPa}$ and $G_{r\theta} = 23\,\text{MPa}$. Because the pure bending effect is most important in low frequencies, below 500 Hz, this estimation of E_θ is not very accurate, and can reach up to 45 GPa depending on the points chosen for identification. The shear modulus however is estimated with less than 15% error.

Due to the construction of the skins (multiple layers of woven carbon fibres), it can be reasonably assumed that the Young modulus along z is the same as along θ. Since the rectangular honeycomb construction of the core is not invariant by a rotation of $\pi/2$, the same cannot be said of the shear modulus G_{rz}, which usually differs from the other by a factor of 2, which will be assumed here, hence $G_{rz} = 46\,\text{MPa}$.

These value are implemented in a finite element model of the cylinder, which is very finely meshed with 694080 DOFs over the whole surface. The cylinder is represented with shell elements, and an equivalent orthotropic material is considered, with all Poisson's ratios set to 0. The equivalent density of the material is $\rho = 146.6\text{kg.m}^{-3}$. A harmonic point load is applied at the same location, and the resulting radial displacement enables to do the same analysis as for the experimental set-up, with the same discretisation in z and θ directions. The resulting k-spaces are plotted on the bottom line of Figure 9.4, along with the identified wavenumber at these frequencies. While the experimental and numerical results do not match perfectly, they are still close to each other and follow the same trends, which validates the approach.

The results of Figure 9.5 also give an estimate of the critical frequency, which is defined as the frequency where the bending and acoustic wavenumbers of grazing incidence are equal. In this case, the critical frequency lies around 1900 Hz according to the experimental data. The regression model is not accurate enough in this region to give relevant results, as it would yield a value closer to 1500 Hz. The experimental value $f_{crit} = 1900\,\text{Hz}$ is retained in the following.

Once the Young's modulus of the skins is known, the ring frequency can be approximated. It is defined by the frequency where the compression wavelength is equal to the perimeter, and therefore does not depend on flexural motion of the shell. Neglecting Poisson effects, this reads:

$$f_{ring} = \frac{1}{2\pi R}\sqrt{\frac{E_\theta}{\rho}} = 5570\,\text{Hz}, \tag{9.2}$$

For higher values of E_θ, the ring frequency can reach 8 kHz. In any case, this value is above the maximum frequency that could be reached with the shaker we used, so it could not be verified experimentally.

4 Acoustic tests

4.1 Description

The quantity to be assessed in the tests is the noise reduction index (NR) of the cylinder with and without a porous lining. The structure is closed by a thick, heavy wooden plank, and is placed in a reverberant chamber and excited by a diffuse acoustic field thanks to an omnidirectional source. The room has a surface $S = 155\text{m}^2$ and a volume $V = 127\text{m}^3$. A white noise excitation between 100 Hz and 10 kHz is provided by a B&K 4292 dodecahedral source. Despite having a lower intensity above 5 kHz, the sound pressure level (SPL) provided was sufficient to perform measures up to 10 kHz. The SPL are measured by two B&K 4187 microphones, one placed outside the structure, and the other inside. A holder system is used to control the position of the inside microphone. Technical details about the mounting can be found in Appendix A. Measures are taken at several locations, inside and outside the cavity. The inner microphone was placed at 96 different locations corresponding to 8 values of the angle, 3 of the distance to the axis, and 4 heights. The values are then averaged over space and third-octave frequency bands. The NR is then defined as the difference between the outside and inside noise levels:

$$\text{NR} = L_{\text{out}} - L_{\text{in}}. \tag{9.3}$$

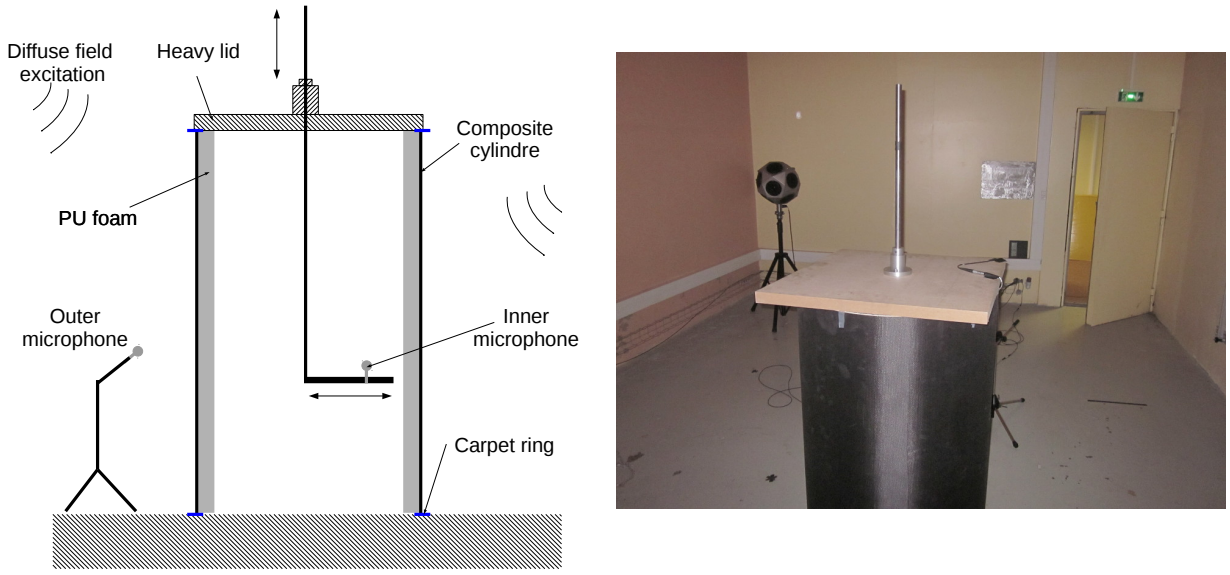

Figure 9.6 – Schematic of the measurement set-up.

4.2 Results

The NR results for the cylinder with and without porous lining are presented on figure 9.7. In both cases, the response is characteristic of a modal behaviour in the low frequency range below 400 Hz, while a high frequency behaviour appears afterwards. The phenomena at hand are reviewed in the following.

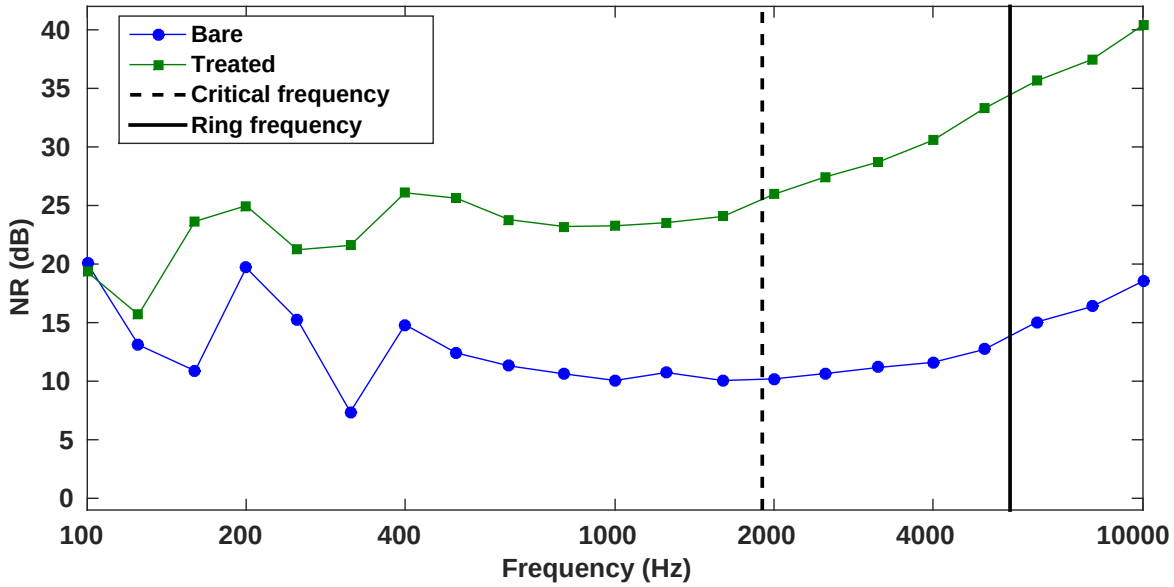

Figure 9.7 – Noise reduction for the shell with and without porous lining

4.2.1 Low frequencies

The first modes of the cavity, assuming rigid walls, have been computed with a finite element code, and the mode count is given in Figure 9.8. Since the porous layer is rather thick, the change in cavity radius cannot be neglected. In either case, there is one double mode in the 160 Hz band, and a local maximum in the 315 Hz band corresponds to a local minimum in the NR. This supports the conclusion that the behaviour is mainly modal in this range. Besides, since the room's Schroeder frequency is around 500 Hz (see Appendix B), even the exciting field cannot reliably be considered diffuse below this frequency.

Above 500 Hz, the mode count in each band is enough to assume high frequency behaviour in the inner cavity [113]. However, the SPL measured at various points inside the cavity spread over more than 3dB up to 2 kHz. Above this frequency, the sound field can be considered perfectly diffuse in the cavity.

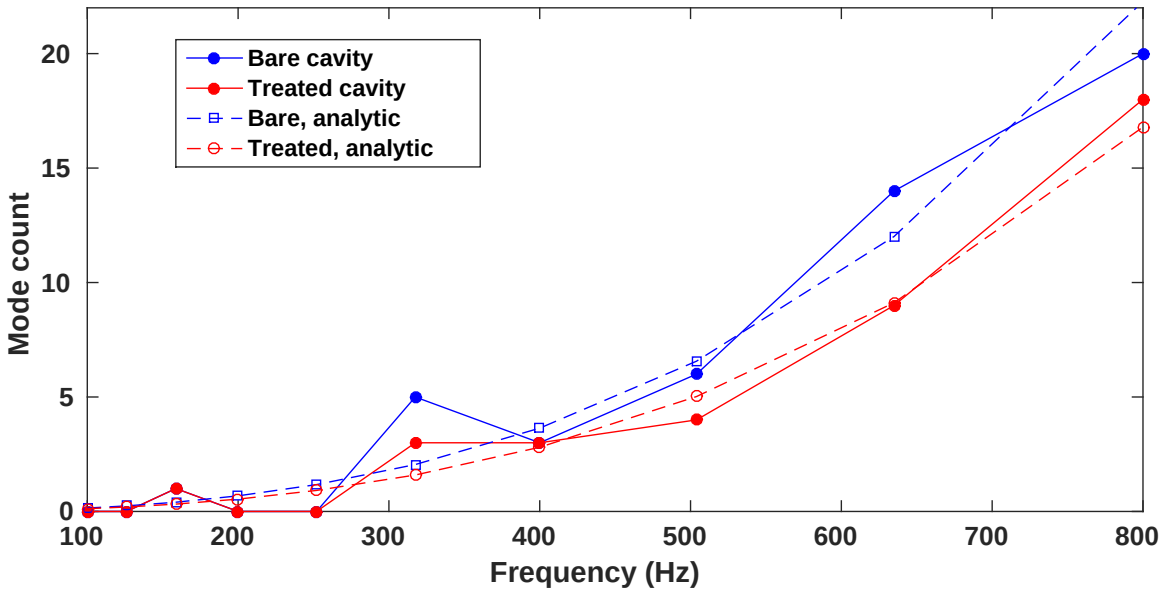

Figure 9.8 – Mode count of the inner cavity with and without the poroelastic layer.

4.2.2 High frequencies

The estimated ring and critical frequencies estimated in subsection 3.2 are also plotted on Figure 9.7. The are not visually related to any change in the NR. A drop in NR would be expected around both ring and critical frequencies, but no such thing appear on the results, maybe masked by the third-octave averaging. Since the ring frequency is located close to the upper limit of the studied frequency spectrum, and due to the third-octave averaging, not much can be said about it. However, it can be observed that the NR starts to increase after the critical frequency, which is consistent with the expectations.

4.2.3 Porous lining

The effect of the porous lining can be seen on the whole frequency range considered here, except for the first third octave centred on 100 Hz. Above 400 Hz, the difference in NR between the treated and untreated cylinder is above 10dB and increases logarithmically with frequency, as seen in Figure 9.9.

The improvement of the NR due to the porous layer can be attributed to three phenomena:

- increase in mass of the structure
- reduction of the size of the inner cavity, and hence of its modal density, and
- increase of sound absorption.

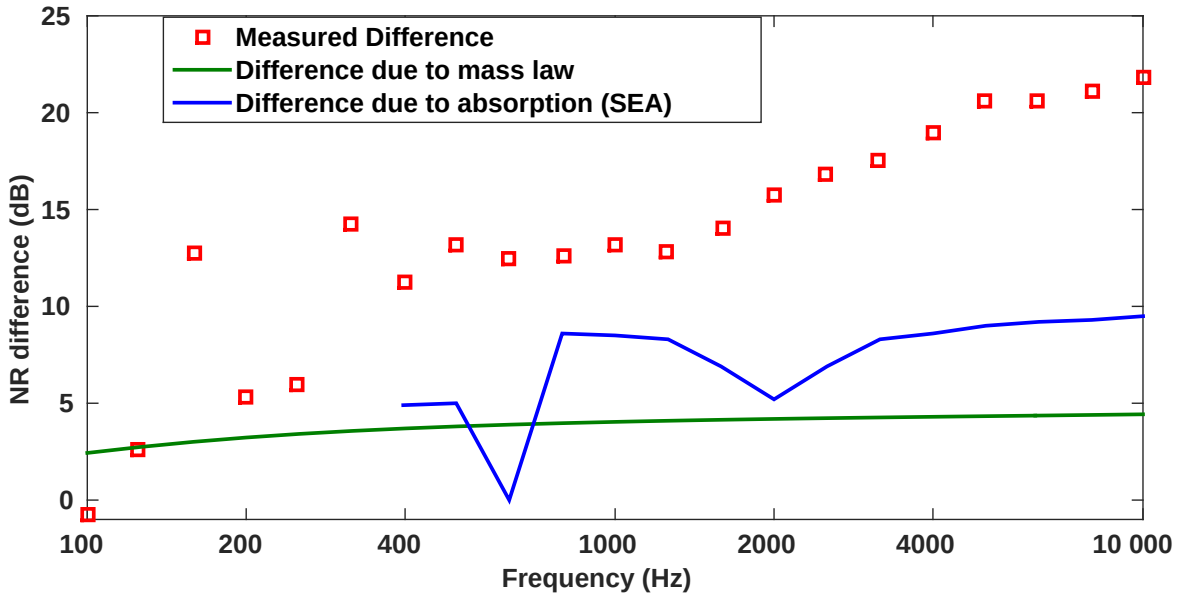

Figure 9.9 – Differences in NR: measurement, difference attributable to mass law and to absorption effects.

Since the NR has been shown to follow the same trends as the TL, among which the mass law between the ring and critical frequencies, the difference attributable only to mass law is rather easy to compute. It is also plotted on Figure 9.9, and is slightly less than 4.5dB. This means that most of the improvement to the TL are due to the other effects.

The effect of the volume change can be assessed using a 3-subsystem SEA model for noise reduction, such as the one found in [121]. The cylindrical structure is modelled on modal basis with the SEALASCAR software. It shows that, all else being equal, the ratio E_{in}/E_{out} of energies in the inner and outer cavities is proportional to the modal density of the inner cavity, which is itself proportional to the cavity volume up to the first order. As $\mathrm{NR} = -10\log_{10}(E_{in}/E_{out})$, decreasing the volume leads to an increase of the NR. With the values used in this study, this leads to an increase of about 1.4dB. However, the difference between the SEA model and the experiment is more than 10dB in most of the range, so it cannot be considered valid.

The remaining difference is therefore due to sound absorption in the foam. It is estimated using an SEA model of the cylindrical shell with a low value of absorption and one using the supplier's data for absorption given in Figure 9.14, since absorption measurement described in Appendix C did not prove conclusive. The added mass of the porous was neglected in this computation to account solely for the effect of absorption. The modal density was not sufficient below 400 Hz to establish the SEA model, therefore the results are given only above

400 Hz in Figure 9.9. The effect of absorption is sensible in this range, and more important than the added mass effect.

5 Conclusion

The noise reduction of a cylindrical shell with a poroelastic treatment was studied in this chapter. An attempt at the mechanical characterisation of the cylinder was made using displacement field measurements transferred to the wavenumber space through a discrete Fourier transform. This enabled us to identify the dispersion curves. These wave propagation characteristics were then used to identify the values of the cylinder's mechanical parameters, such as Young's modulus and shear modulus, leading to estimations of the ring and critical frequencies of the structure. However, due to the low precision of the identification procedure, these estimates are provided with high uncertainty. This may be the reason why the SEA model derived from these parameters failed to represent correctly the experimental results.

In the second part of the study, acoustic measurements were performed in a reverberant room in order to measure the NR with and without a polyurethane foam layer. The inclusion of the foam layer leads naturally to an increase of the NR inside the cavity, due to 3 effects, namely reduction of the cavity size, absorption and added mass. A comparison to several simple SEA model using the mechanical parameters identified in the first step enables to estimate the contribution of each of these effects. The improvement of the NR is finally shown to be due mainly to absorption secondly to added mass effects, and marginally to the reduction of the inner cavity volume.

Appendix A: Technical details for acoustic measurements

Microphone holding system

The microphone placed inside the shell is supported by a structure specifically designed for this purpose. It consists of a vertical cylindrical rod hanging from the lid through a metal guiding hole. This system ensure the vertical sliding and the rotation of the microphone around the axis. A horizontal bar with a square section is attached at the end of the rod. The microphone is fixed to this bar with a bracket, which can slide on a rail to ensure radial positioning. The centring of the rod is manually ensured by the fact that the side length of the lid is equal to the outer cylinder's radius (70cm).

The design of this mounting structure means that the lid need not be removed for height and angular positioning, but that it has for radial positioning. Besides, the centring of the part is difficult to achieve perfectly. Care has to be taken so that the microphone cable does not interfere with the rotation, especially at low positions. Since the noise level within the room is very high, the operator cannot stay inside during the measurement, and the process of changing the microphone position is rather noisy due to the tight play between parts, which is necessary to avoid leaks. All of this makes that the measurements have to be averaged over discrete locations, as opposed to the continuous path followed by the intensity probe in chapter 8.

Boundary conditions of the cylinder

The vibroacoustic response of the experimental set-up may prove rather sensitive to boundary conditions. The isolation of the cylinder from the ground and the lid was ensured by two rings of carpet held in place by adhesive tape. This is made in order to reduce acoustic leaks due to imperfect flatness of the ground, the cylinder's edges and the lid at the same time.

The condition can be further enhanced by adding tape at the two interfaces, as shown on figure 9.10. The difference in NR is noticeable between the two mounting with and without tape as shown in Figure 9.11, where the difference in NR between the two conditions is plotted: the difference is low in mid frequency, but around 2dB above 2 kHz. The very high difference observed below 200 Hz can be explained by the fact that the first modes of the cylinder are affected by the change in boundary conditions.

Figure 9.10 – Interface between the ground and the shell: tape and carpet ring for isolation.

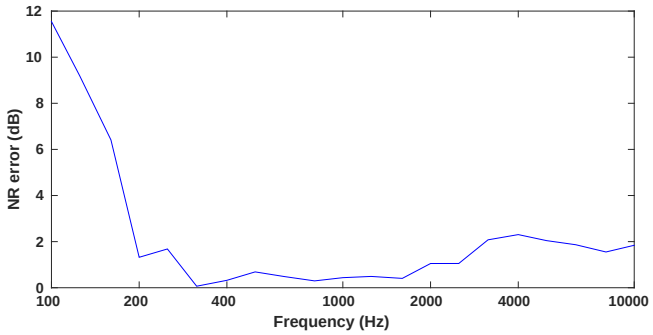

Figure 9.11 – Difference in NR between the taped and simply supported boundary conditions.

Assembling and disassembling the foam layer

The porous treatment consists of autoadhesive foam panels (ref. AA2050 from the company Spectra) with dimensions 1×1.5m. As the width is greater than the diameter of the cylinder, they had to be cut in half to be installed. Two panels were first cut to form 4 panels with dimensions 0.5×1.5m, which were installed in the cylinder. The excess part was removed with a box cutter blade [2]. It was not possible to fit the parts very tightly, so some of the excess material was used to fill the gaps between parts. It is recommended that the cylinder be installed between two tables during the process to avoid rotation.

Two people are necessary to install and remove the foam panels. The assembly took about 2h, while the removal lasted 40 minutes. The removal proved harder than expected. Indeed, contrarily to what happened when tested with small quantities, the adhesive could not be removed completely from the carbon fibre skin, and the foam was damaged during the removal operation.

[2] it is important to use a new blade in order to obtain a clean cut

Appendix B: Reverberant room characterisation

The reverberation time of the reverberant room of the École Centrale de Lyon was measured during this test campaign. Two methods were employed, namely the decay rate method and the impulse response method.

Decay rate

The decay rate method implies generating a white noise in the room during several seconds, then cut the excitation and measure the time for the sound pressure level to decrease by 60dB (the actual measure is made for 30 dB and multiplied by 3 or 2 to achieve 60dB). The generator was set to deliver a 90dB white noise signal with frequencies ranging from 22.7 Hz to 12.8 kHz during 10 seconds, then stop. The reverberation time at 60 dB (RT60) of the empty room was known to lie around 10s for low frequencies, so measurements were taken every 10ms during 10s, starting 1s before the sound source was cut off. Two microphones were used for this task, and the measurement were taken for four different positions of both of them, hence at eight points in total. The Fourier transform of each signal is taken in order to extract the contributions for each third octave band between 100 Hz and 5 kHz. The average decay slope is extracted by a built-in routine.

Impulse response

Another method is to measure the impulse response of the room. As this cannot be done with a loudspeaker, the solution is to excite the room with a white noise during a relatively long time, monitoring both the generator signal (x) and the microphone signal (y). The frequency domain transfer function $H(\omega)$ of the room can then be computed by Fourier analysis with the formula

$$H(\omega) = \frac{\mathrm{E}(\bar{X}Y)}{\mathrm{E}(\bar{X}X)}, \tag{9.4}$$

where X and Y are the Fourier transforms of respectively x and y, and $\bar{X}$ is the complex conjugate of X. This function can be used to compute the impulse response of the room, and after an appropriate filtering (a 6th order Butterworth filter is used here) the decay curve can be extracted for each frequency band. The reverberation times per third octaves obtained with the two methods are presented in Figure 9.12. It can be seen that both methods give close results above 400 Hz.

Sound field diffuseness

Taking a reverberation time of RT60 = 8s around 400 Hz and a volume of $V = 127\text{m}^3$, the Schroeder frequency [103, 104] of the room is $f_s = 2000\sqrt{\frac{\text{RT60}}{V}} \approx 500\,Hz$. This means that the modal overlap above f_s is enough to consider the sound field inside the room to be diffuse. The Schroeder frequency should be considered as a "safe" lower limit for high frequency (HF) behaviour of the room, but does not mean that the room's behaviour is modal below it.

The sound field around the cylinder was measured at several points and averaged. Measurements for 12 microphone locations around the cylinder and their average are displayed on Figure 9.13. The dispersion of the SPL is less than 3dB only from the 630 Hz third-octave band, which confirms that the Schroeder frequency is a correct indicator in our case: measurements below 500 Hz are polluted by some modal behaviour of the reverberant room.

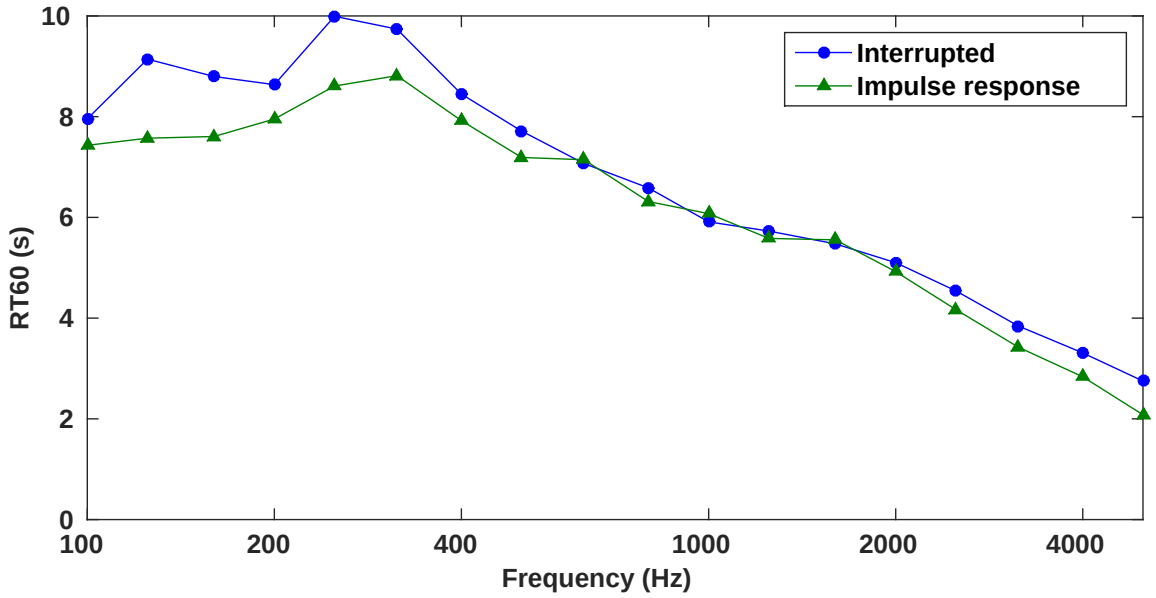

Figure 9.12 – Reverberation time of the room at 100 Hz obtained with the decay rate and impulse response methods.

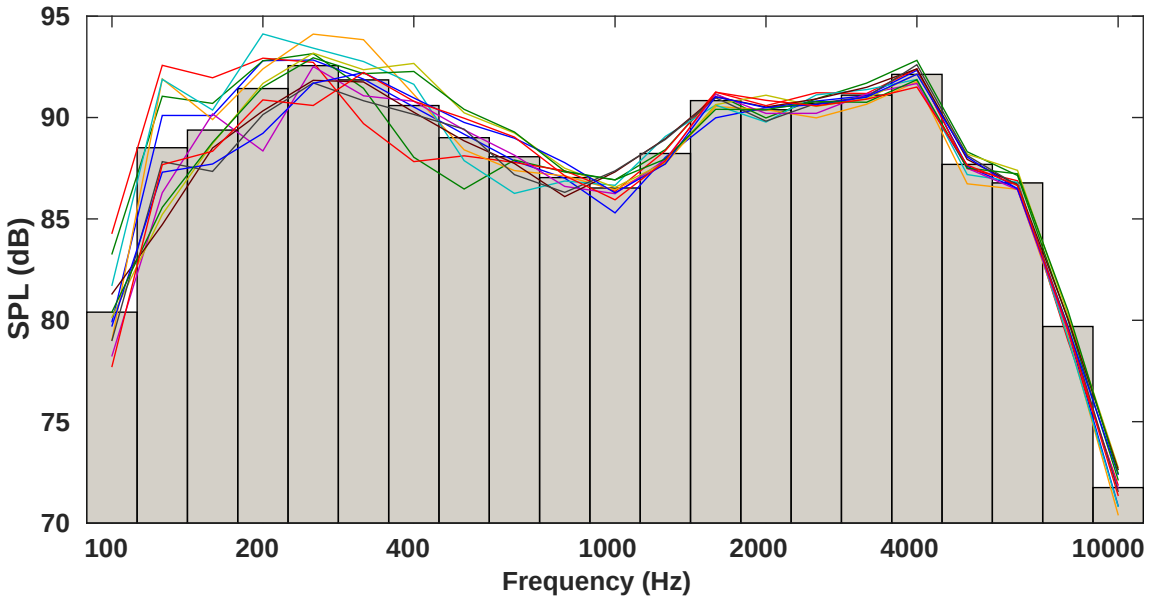

Figure 9.13 – Sound pressure level in the reverberant room at various points around the cylinder, and average.

Appendix C: Sabine absorption

In addition to the normal absorption measurements in impedance tube described in 2.2, the diffuse field absorption (alpha Sabine) was also measured in the ECL reverberant room. The Sabine equation [10] links the reverberation time (in seconds) and the equivalent absorption of a reverberant room as:

$$\mathrm{TR}_{60} = \frac{0.16V}{A}, \tag{9.5}$$

where V is the volume of the room in m^3 and A the specific absorption of the room in m^2. For the empty room, the diffuse field absorption α is defined as

$$\alpha_{empty} = \frac{A_{empty}}{S}, \tag{9.6}$$

where S is the surface of the room. For a room with n different surface materials, the global absorption is

$$A = \sum_{i=1}^{n} \alpha_i S_i, \tag{9.7}$$

where α_i is the absorption coefficient of material i and S_i the surface it covers. In particular, for the room in which a layer with surface S_{foam} of foam has been introduced, the overall absorption is

$$A_{foam} = \alpha_{empty}(S - S_{foam}) + \alpha_{foam} S_{foam}. \tag{9.8}$$

The knowledge of α_{foam} can then be obtained from two reverberation time measurements, one of the empty room and one in presence of foam. Assuming $S_{foam} << S$, we get

$$\alpha_{foam} = \frac{0.16V}{S_{foam}} \left(\frac{1}{\mathrm{TR}_{foam}} - \frac{1}{\mathrm{TR}_{empty}} \right). \tag{9.9}$$

The values of absorption are give in Figure 9.14. The results differ widely from the data given by the supplier, which appears closer to the impedance tube normal absorption. Reverberation times obtained by the impulse response and decay rate method presented in Appendix B are compared. The impulse response results were averaged over octave and third octave bands. The obtained results are completely different, despite originating in the same data. However, the two methods (impulse response and interrupted source) give similar third-octave absorption coefficients. The measurement can therefore be considered robust enough, but the room may not be suited to Sabine's theory.

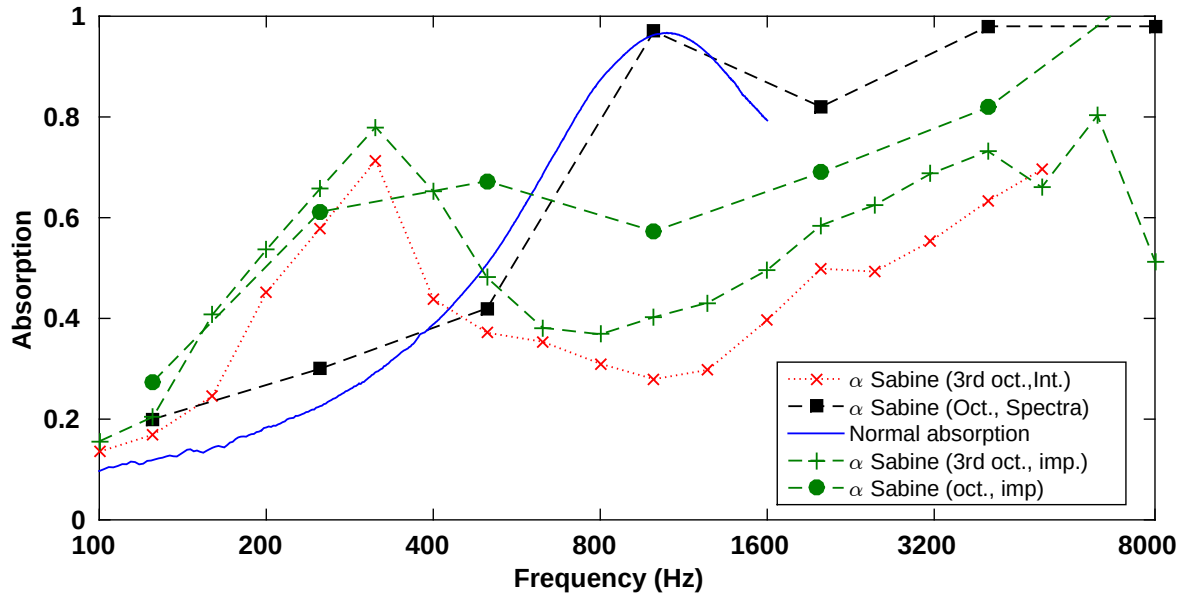

Figure 9.14 – Values of absorption coefficients of the foam per octave and 1/3rd octave band with various methods. Int. stands for interrupted source, and Imp. for impulse response.

Conclusions and perspectives

This doctoral work has been an opportunity to address different topics in the field of vibroacoustics, which is reflected in the three parts of the present dissertation. In the first part a contribution was made to vibroacoustic modelling through the development of a WFE-based method for computing the transmission loss of infinite plates and cylinders. The proposed methods have the same basics: the fluid is modelled analytically while the structural part is taken into account with a finite element model of a unit cell, expanded with the periodic structure theory. This approach was validated against results from the literature and found to agree well with existing models, while proposing a unifying framework for all laminated structures. The proposed formulation could relatively easily be extended to more exotic material models, like poroelastic or piezoelectric. In the case of the cylinder model, the calculation of the NR can also be implemented to complete the proposed TL formulation.

The sensitivity of vibroacoustic systems modelled analytically and with the SEA method is studied in the second part. The FAST method is used for the computation of sensitivity indices of uncertain parameters. The results presented in chapters 5 and 6 were mostly already found during a nearly century-long experience and literature in vibroacoustics, but serve as a justification to the use of the FAST sensitivity analysis method in this context. It was especially shown that the dominant parameter on acoustic transmission in low frequency is the mass of the system (mass law), while above the coincidence region damping is predominant for diffuse field excitation and stiffness is dominant for plane wave excitation. The effect of core shear in sandwich constructions is also investigated, and found to be very important if a large variability of this parameter is allowed. The whole idea behind sensitivity analysis is to assess the effects of both aleatory (non-repeatable phenomenon) and epistemic (lack of knowledge) uncertainties at the same time. In other words, as long as the uncertainty on a parameter can be represented by bounds or a probability density function, the FAST method can be applied. This enables to make decisions about whether some parameters are sensitive enough to be optimised, and in which frequency range a change in a parameter value will take effect.

Finally, the third part groups studies on the effect of a porous material on the transmission

loss of plates and on the noise reduction of cylinders, enabling to identify the most influential parameters and phenomena occurring in the considered set-ups. A theoretical study using again the FAST method compares the effect of porous treatment and that of uncertain core shear modulus on the transmission loss of a sandwich panel. It is found that there is a narrow frequency region, around coincidence, where uncertain core shear is very influential on the TL, while dissipation in the porous is the dominant phenomenon in the remaining of the frequency range observed. The other important result in this part lies in the study of chapter 8, which compares an experimental parametric analysis to FAST studies of the transmission loss through a plate lined with fiberglass and foam layers. In this case, the theoretical and experimental results agree well with each other, while the FAST analysis enables to give finer conclusions over the role played by the different phenomena at hand in acoustic transmission by porous media, especially viscous and thermal dissipation and flow resistivity.

To summarise, the main contributions of this work are

- first, the development of the hybrid WFE-analytic method for plates and cylinders, which can be used as validation tools complex analytical models, and,

- secondly, the application of the FAST method to vibroacoustic context, along with the experimental validation of chapter 8 on composite plate with porous treatment.

The experiments on the cylindrical shell presented in the last chapter did not prove conclusive, mainly due to lack of time at the end of the thesis, but can be used as a basis for the same kind of experimental analysis as for the plate in the future.

Perspectives

TL of periodic plates and cylinders

The methods developed in chapters 2 and 3 can be further enhanced to calculate the response of periodic structures to plane waves. This has been proposed by Parrinello and Ghiringhelli [89]. However, the field radiated in both directions is strictly speaking not a plane wave, but can be described as a superposition of propagating plane waves and evanescent waves [67]. The definition of the TL in this case could be further refined, which could find applications for large stiffened panels or honeycomb panels with large cores and at high frequencies.

Correlated FAST

One rather strong hypothesis in the ANOVA framework of sensitivity analysis is the independence of parameters, which is rarely ensured when considering physical materials: there is often some degree of correlation between design parameters. For example in porous material modelling, the viscous and thermal characteristic lengths are usually separated by a factor around 2, but this relation is not deterministic. Several methods have been proposed to tackle parameter correlation in global sensitivity analysis, especially by Xu and Gertner [117], who proposed an extension of the FAST method to this case.

Experimental analysis of a cylindrical shell

The cylinder used for the last chapter was tested only with a single poroelastic material lining. An experimental study in the same fashion as the one conducted in chapter 8, with different porous materials could yield interesting results. The effect of boundary conditions should also be assessed. The PU foam used was indeed chosen for its adhesive back side, allowing bonded condition and a facilitating installation. However, since an air gap tends to increase the NR [63], this mounting condition should be tried in the future. The mechanical characterisation of the cylinder presented in the same chapter could also be enhanced by a more in-depth theoretical analysis, in order to try and match the experimental k-spaces with numerical dispersion curves not only along the circumference, but in all directions.

Bibliography

[1] M. Abramowitz and I. Stegun. *Handbook of mathematical functions*. Dover publications, Inc., 1964.

[2] L. Alimonti, N. Atalla, A. Berry, and F. Sgard. A hybrid finite element–transfer matrix model for vibroacoustic systems with flat and homogeneous acoustic treatments. *The Journal of the Acoustical Society of America*, 137(2):976–988, 2015.

[3] J. F. Allard and N. Atalla. *Propagation of sound in porous media*. John Wiley & Sons, Ltd., 2009.

[4] Angels Aragonès and Oriol Guasch. Ranking paths in statistical energy analysis models with non-deterministic loss factors. *Mechanical Systems and Signal Processing*, 52–53:741 – 753, 2015.

[5] N. Atalla, R. Panneton, and P. Debergue. Mixed displacement-pressure formulation for poroelastic materials. *Journal of the Acoustical Society of America*, 104(3):1444–1452, 1998.

[6] N. Atalla, M. A. Hamdi, and R. Panneton. Enhanced weak integral formulation for the mixed (u,p) poroelastic equations. *The Journal of the Acoustical Society of America*, 109(6): 3065–3068, 2001.

[7] Y. Atalla and R. Panneton. Inverse acoustical characterization of open cell porous media using impedance tube measurements. *Canadian Acoustics*, 33(1):11–24, 2005.

[8] I. Bartoli, A. Marzani, F. Lanza di Scalea, and E. Viola. Modeling wave propagation in damped waveguides of arbitrary cross-section. *Journal of Sound and Vibration*, 295:685–707, 2006.

[9] W. Batko and P. Pawlik. New method of uncertainty evaluation of the sound insuation of partitions. *Acta Physica Polonica A*, 123(6), 2013.

[10] L. L. Beranek. Analysis of Sabine and Eyring equations and their application to concert hall audience and chair absorption. *The Journal of the Acoustical Society of America*, 120(3): 1399–1410, 2006.

[11] J. Berthaut. *Contribution à l'identification large bande des structures anisotropes. Application aux tables d'harmonie de pianos.* PhD thesis, École Centrale de Lyon, 2004.

[12] J. Berthaut, M.N. Ichchou, and L. Jezequel. K-space identification of apparent structural behaviour. *Journal of Sound and Vibration*, 280(3–5):1125–1131, 2005.

[13] M. A. Biot. Theory of propagation of elastic waves in a fluid saturated porous solid. I. low frequency range. II. higher frequency range. *The Journal of the Acoustical Society of America*, 28(2), 1956.

[14] B. Brouard, D. Lafarge, and J.-F. Allard. A general method of modelling sound propagation in layered media. *Journal of Sound and Vibration*, 183(1):129–142, 1995.

[15] R. Büssow and B. A. T. Petersson. Path sensitivity and uncertainty propagation in sea. *Journal of Sound and Virbation*, 300:479–489, 2007.

[16] E. Carrera. An assessment of mixed and classical theories on global and local responses of multilayered orthotropic plates. *Composite structures*, 50:183–198, 2000.

[17] R. Cherif and N. Atalla. Experimental investigation of the accuracy of a vibroacoustic model for sandwich-composite panels. *The Journal of the Acoustical Society of America*, 137(3): 1541–1550, 2015.

[18] J.-L. Christen, M. Ichchou, B. Troclet, and M. Ouisse. Global sensitivity analysis of acoustic transmission models through infinite plates. In *Proceedings of ISMA 2014 - International Conference on Noise and Vibration Engineering and USD 2014 - International Conference on Uncertainty in Structural Dynamics*, pages 4177–4188, 2014.

[19] J.-L. Christen, M. Ichchou, B. Troclet, O. Bareille, and M. Ouisse. Global sensitivity analysis of analytical vibroacoustic transmission models. *Journal of Sound and Vibration*, 368:121 – 134, 2016.

[20] D. Chronopoulos, B. Troclet, M. Ichchou, and J.-P. Lainé. A unified approach for the broad-band vibroacoustic response of composite shells. *Composites: Part B*, 43:1837–1846, 2012.

[21] A. Cicirello and R. S. Langley. The vibro-acoustic analysis of built-up systems using a hybrid method with parametric and non-parametric uncertainties. *Journal of Sound and Vibration*, 332(9):2165–2178, 2013.

[22] V. Cotoni, R.S. Langley, and M.R.F. Kidner. Numerical and experimental validation of variance prediction in the statistical energy analysis of built-up systems. *Journal of Sound and Vibration*, 288(3):701 – 728, 2005.

[23] V. Cotoni, R. S. Langley, and P. J. Shorter. A statistical energy analysis subsystem formulation using finite element and periodic structure theory. *Journal of Sound and Vibration*, 318: 1077–1108, 2008.

[24] M. J. Crocker and A. J. Price. Sound transmission using statistical energy analysis. *Journal of Sound and Vibration*, 9:469–486, 1969.

[25] M. J. Crocker, P. K. Raju, and B. Forssen. Measurement of transmission loss of panels by the direct determination of transmitted acoustic intensity. *Noise Control Engineering*, 17(1): 6–11, 1981.

[26] R. I. Cukier, C. M. Fortuin, K. E. Shuler, A. G. Petschek, and J. H. Schaibly. Study of the sensitivity of coupled reaction systems to uncertainties on rate coefficients. I. Theory. *Journal of Chemical Physics*, 59(8), 1973.

[27] A. Culla, W. D'Ambrogio, and A. Fregolent. Parametric approaches for uncertinty propagation in SEA. *Mechanical Systems and Signal Processing*, 25:193–204, 2011.

[28] R. D'Amico, A. Pratellesi, M. Pierini, and N. Baldanzini. Stochastic BEM for the vibroacoustic analysis of three-dimensional structures. *Advances in Acoustics and Vibration*, 2011, 2011.

[29] R. D'Amico, A. Pratellesi, N. Baldanzini, and M. Pierini. Reformulation of the stochastic BEM to improve the computational efficiency in the prediction of the vibro-acoustic behaviour of structures with uncertainties. *Journal of Sound and Vibration*, 332(9):2132 – 2148, 2013.

[30] V. Damljanovic and R. L. Weaver. Propagating and evanescent elastic waves in cylindrical waveguides of arbitrary cross-section. *The Journal of the Acoustical Society of America*, 115: 1572–1581, 2004.

[31] K. Daneshjou, and A. Nouri, and R. Talebitooti. Sound transmission through laminated composite shells using analytical model. *Archive of Applied Mechanics*, 77:363–379, 2007.

[32] W. Desmet, B. van Hal, P. Sas, and D. Vandepitte. A computationally efficient prediction technique for the steady-state dynamic analysis of coupled vibro-acoustic systems. *Advances in Engineering Software*, 33(7–10):527–540, 2002.

[33] R. D'Ippolito, B. Newill, and B. Van der Heggen. Uncertainty modeling for aircraft interior noise - composites transmission loss optimization. *SAE Technical Paper*, 2013-01-2216, 2013.

[34] O. Doutres, M. Ouisse, N. Atalla, and M. Ichchou. Impact of the irregular microgeometry of polyurethane foam on the macroscopic acoustic behavior predicted by a unit-cell model. *The Journal of the Acoustical Society of America*, 136:1666–1681, 2014.

[35] C. Droz, C. Zhou, M.N. Ichchou, and J.-P. Lainé. A hybrid wave-mode formulation for the vibro-acoustic analysis of 2D periodic structures. *Journal of Sound and Vibration*, 363: 285–302, 2016.

[36] F. J. Fahy and P. Gardonio. *Sound and structural vibration.* Academic Press, 2007.

[37] F.J. Fahy and A.D. Mohammed. A study of uncertainty in applications of SEA to coupled beam and plate systems, part I: Computational experiments. *Journal of Sound and Vibration*, 158(1):45 – 67, 1992.

[38] C. Fredö. A SEA-like approach for the derivation of energy flow coefficients with a finite element model. *Journal of Sound and Vibration*, 199(4):645–666, 1997.

[39] S. Ghinet and N. Atalla. Sound transmission loss of insulating complex structures. *Canadian acoustics*, 29(3):26–27, 2001.

[40] S. Ghinet, N. Atalla, and H. Osman. On the transmission loss of curved laminates and sandwich composite panels. *The Journal of the Acoustical Society of America*, 18(2):774–790, 2005.

[41] S. Ghinet, N. Atalla, and H. Osman. Diffuse field transmission into infinite sandwich composite and laminate composite cylinders. *Journal of Sound and Vibration*, 289:745–778, 2006.

[42] Laurent Guillaumie. Vibroacoustic flexural properties of symmetric honeycomb sandwich panels with composite faces. *Journal of Sound and Vibration*, 343:71–103, 2015.

[43] R. W. Guy and A. De Mey. Measurement of sound transmission loss by sound intensity. *Canadian Acoustics*, 13(2):25–44, 1985.

[44] J.-L. Guyader and C. Lesueur. Transmission of reverberant sound through orthotropic viscoelastic multilayered plates. *Journal of Sound and Vibration*, 70(3):319–332, 1980.

[45] J.-L. Guyader, C. Boisson, and C. Lesueur. Energy transmission in finite coupled plates, part I: Theory. *Journal of Sound and Vibration*, 81(1):81–92, 1982.

[46] D. M. Hamby. A review of techniques for parameter sensitivity analysis of environmental models. *Environmental monitoring and assessment*, 32:134–154, 1994.

[47] B. Hiverniau. *Transmissions solidiennes : méthodologie de prévision vibroacoustique moyennes et hautes fréquences sous excitations aéroacoustiques.* PhD thesis, École Centrale de Lyon, 2007.

[48] L. Houillon. *Modélisation vibratoire des carrosseries automobiles en moyennes et hautes fréquences.* PhD thesis, École Centrale de Lyon, 1999.

[49] Y. Hu. *Développement de panneaux hybrides passifs/actifs pour l'acoustique*. PhD thesis, École Centrale de Lyon, 2010.

[50] G. Inquiété. *Simulation numérique de la propagation des ondes dans les structures composites stratifiées*. PhD thesis, École Centrale de Lyon, 2008.

[51] B. Iooss, F. Van Dorpe, and N. Devictor. Response surfaces and sensitivity analyses for an environmental model of dose calculations. *Reliability Engineering and System Safety*, 91(10–11):1241–1251, 2006. The Fourth International Conference on Sensitivity Analysis of Model Output (SAMO 2004).

[52] J. P. C. Kleijnen. Kriging metamodeling in simulation: A review. *European Journal of Operational Research*, 192(3):707–716, 2009.

[53] L. R. Koval. On the sound transmission into a thin cylindrical shell under "flight conditions". *Journal of Sound and Vibration*, 48(2):265–275, 1976.

[54] L. R. Koval. On sound transmission into an orthotropic shell. *Journal of Sound and Vibration*, 63(1):51–59, 1979.

[55] L.R. Koval. Effects of cavity resonances on sound transmission into a thin cylindrical shell. *Journal of Sound and Vibration*, 59(1):23–33, 1978.

[56] S. Kumar, L. Feng, and U. Orrenius. Predicting the sound transmission loss of honeycomb panels using the wave propagation approach. *Acta Acustica unite with Acustica*, 97:869–876, 2011.

[57] G. Kurtze and B. G. Watters. New wall design for high transmission loss or high damping. *The Journal of the Acoustical Society of America*, 31:739–748, 1959.

[58] P. Ladevèze. A new computational approach for structure vibrations in the medium frequency range. *Comptes rendus de l'Académie des Sciences de Paris*, 322(II b):849–856, 1996.

[59] R. S. Langley and A. W. M. Brown. The ensemble statistics of the band-averaged energy of a random system. *Journal of Sound and Vibration*, 275:847–857, 2004.

[60] R. S. Langley and A. W. M. Brown. The ensemble statistics of the energy of a random system subjected to harmonic excitation. *Journal of Sound and Vibration*, 275:823–846, 2004.

[61] C. Langlois, R. Panneton, and N. Atalla. Polynomial relations for quasi-static mechanical characterization of isotropic poroelastic materials. *The Journal of the Acoustical Society of America*, 110(6):3032–3040, 2001.

[62] J.-H. Lee and J. Kim. Study on sound transmission characteristics of a cylindrical shell using analytical and experimental models. *Applied Acoustics*, 64:611–632, 2003.

[63] J.-H. Lee, J. Kim, and H.-J. Kim. Simplified method to solve sound transmission through structures lined with elastic porous material. *The Journal of the Acoustical Society of America*, 110(5):2282–2294, 2001.

[64] F. G. Leppington, K. H. Heron, and E. G. Broadbent. Resonant and nonresonant transmission of random noise through complex plates. *Proceedings of the Royal Society of London A*, 458, 2002.

[65] C. Lesueur, M. Heckl, and J. Delcambre. *Rayonnement acoustique des structures*. Eyrolles, 1988.

[66] D. Li and J. S. Vipperman. Mathematical model for characterizing noise transmission into finite cylindrical structures. *The Journal of the Acoustical Society of America*, 117(2):679–689, 2005.

[67] Gau-Feng Lin and Joel M. Garrelick. Sound transmission through periodically framed parallel plates. *The Journal of the Acoustical Society of America*, 61(4):1014–1018, 1977.

[68] S. N. Lophaven, H. B. Nielsen, and J. Sondergaard. DACE – a matlab kriging toolbox, version 2.0. Technical report, Informatics and Mathematical Modelling, Technical University of Denmark, 2002. URL `http://www.imm.dtu.dk/~hbni/dace`.

[69] R. H. Lyon and R. G. DeJong. *Theory and application of Statistical Energy Analysis*. Butterworth-Heinemann, 1995.

[70] B. R. Mace. Statistical energy analysis, energy distribution models and system modes. *Journal of Sound and Vibration*, 279(1-2):141–170, 2005.

[71] Brian R. Mace and Elisabetta Manconi. Modelling wave propagation in two-dimensional structures using finite element analysis. *Journal of Sound and Vibration*, 318(4–5):884–902, 2008.

[72] J. Magniez, J.-D. Chazot, M. A. Hamdi, and B. Troclet. A mixed 3d-shell analytical model for the prediction of sound transmission through sandwich cylinders. *Journal of Sound and Vibration*, 333(19):4750–4770, 2014.

[73] J. Magniez, M. A. Hamdi, J.-D. Chazot, and B. Troclet. A mixed "Biot–shell" analytical model for the prediction of sound transmission through a sandwich cylinder with a poroelastic core. *Journal of Sound and Vibration*, 360:203–223, 2016.

[74] G. Maidanik. Response of ribbed panels to reverberant acoustic fields. *The Journal of the Acoustical Society of America*, 34:809–826, 1962.

[75] E. Manconi. *Modelling wave propagation in two-dimensional structures using a wave/finite element technique*. PhD thesis, University of Parma, 2008.

[76] E. Manconi and B. R. Mace. Wave characterization of cylindrical and curved panels using a finite element method. *The Journal of the Acoustical Society of America*, 2009.

[77] A. Marrel, B. Iooss, F. Van Dorpe, and E. Volkova. An efficient methodology for modeling complex computer codes with Gaussian processes. *Computational Statistics and Data Analysis*, 52:4731–4744, 2008.

[78] A. Marzani, E. Viola, I. Bartoli, and F. Lanza di Scalea. A semi-analytical finite element formulation for modeling stress wave propagation in axisymmetric damped waveguides. *Journal of Sound and Vibration*, 318:488–505, 2008.

[79] G. J. McRae, J. W. Riden, and J. H. Seinfeld. Global sensitivity analysis – a computational implementation of the Fourier amplitude sensitivity test (FAST). *Computers and Chemical engineering*, 6(1):15–25, 1981.

[80] D. J. Mead. A general theory of harmonic wave propagation in linear periodic systems with multiple coupling. *Journal of Sound and Vibration*, 27(2):235–260, 1973.

[81] D. J. Mead and S. Markus. The forced vibration of a three-layer damped sandwich beam with arbitrary boundary conditions. *Journal of Sound and Vibration*, 10:163–175, 1969.

[82] R. G. Mindlin. Influence of rotatory inertia and shear on flexural vibrations of isotropic, elastic plates. *Journal of Applied Mechanics*, 18, 1951.

[83] S. Narayanan and R. L. Shanbhag. Sound transmission through a damped sandwich panel. *Journal of Sound and Vibration*, 80(3):315–327, 1982.

[84] R. B. Nelson, S. B. Dong, and R. D. Kalra. Vibrations and waves in laminated orthotropic circular cylinders. *Journal of Sound and Vibration*, 18:429–444, 1971.

[85] Roger Ohayon and Christian Soize. *Advanced Computational Vibroacoustics – Reduced-Order Models and Uncertainty Quantification*. Cambridge University Press, 2014.

[86] Ulf Orrenius, Hao Liu, Andrew Wareing, Svante Finnveden, and Vincent Cotoni. Wave modelling in predictive vibro-acoustics: Applications to rail vehicles and aircraft. *Wave Motion*, 51(4):635–649, 2014.

[87] M. Ouisse, M. Ichchou, S. Chedly, and M. Collet. On the sensitivity analysis of porous material models. *Journal of Sound and Vibration*, 331:5292–5308, 2012.

[88] R. Panneton and E. Gros. A missing mass method to measure the open porosity of porous solids. *Acta Acustica united with Acustica*, 91(2):342–348, 2005.

[89] A. Parrinello and G.L. Ghiringhelli. Transfer matrix representation for periodic planar media. *Journal of Sound and Vibration*, 371:196–209, 2016.

[90] E. Perrey-Debain, J. Trevelyan, and P. Bettess. Plane wave interpolation in direct collocation boundary element method for radiation and wave scattering : numerical aspects and applications. *Journal of Sound and Vibration*, 261(5):839–858, 2003.

[91] J. N. Reddy. *Mechanics of Laminated Composite Plates and Shells: Theory and Analysis*. CRC Press, 2004.

[92] K. Renji. Sound transmission loss of unbounded panels in bending vibration considering transverse shear deformation. *Journal of Sound and Vibration*, 283:478–486, 2005.

[93] K. Renji, P. S. Nair, and S. Narayanan. Modal density of composite honeycomb sandwich panels. *Journal of Sound and Vibration*, 195(5):687–699, 1996.

[94] K. Renji, P. S. Nair, and S. Narayanan. Critical and coincidence frequencies of flat panels. *Journal of Sound and Vibration*, 205(1):19–32, 1997.

[95] J. M. Renno and B. R. Mace. Calculating the forced response of two-dimensional homogeneous media using the wave and finite element method. *Journal of Sound and Vibration*, 330:5913—5927, 2011.

[96] J. M. Renno and B. R. Mace. Calculating the forced response of cylinders and cylindrical shells using the wave and finite element method. *Journal of Sound and Vibration*, 333(21): 5340–5355, 2014.

[97] E. Reynders. Parametric uncertainty quantification of sound insulation values. *The Journal of the Acoustical Society of America*, 135, 2014.

[98] D. Rhazi and N. Atalla. A simple method to account for size effects in the transfer matrix method. *The Journal of the Acoustical Society of America*, 127(2):EL30–EL36, 2010.

[99] A. Saltelli, S. Tarantola, and K. P.-S. Chan. A quantitative model-independent method for global sensitivity analysis of model output. *Technometrics*, 41(1):39–56, 1999.

[100] A. Saltelli, M. Ratto, T. Andres, F. Campolongo, J. Cariboni, D. Gatelli, M. Saisana, and Stefano Tarantola. *Global Sensitivity Analysis: The Primer*. John Wiley & Sons, 2008.

[101] H. Sathyanarayanamurthy and R. B. Chinnam. Metamodels for variable importance decomposition with applications to probabilistic engineering design. *Computers and Industrial Engineering*, 57:996–1007, 2009.

[102] J. H. Schaibly and K. E. Shuler. Study of the sensitivity of coupled reaction systems to uncertainties in rate coefficients. II Applications. *Journal of Chemical Physics*, 59(8):3879–3888, 1973.

[103] M. R. Schroeder. Die statistischen Parameter der Frequenzkurven von grossen Räumen. *Acustica*, 4:594–600, 1954.

[104] M. R. Schroeder. The "Schroeder frequency" revisited. *The Journal of the Acoustical Society of America*, 99(5):3240–3241, 1996.

[105] Q. Serra. *Modèles réduits d'interface dissipatives par approche* k-space. PhD thesis, École Centrale de Lyon, 2014.

[106] Q. Serra, M. N. Ichchou, and J.-F. Deü. On the use of transfer approaches to predict the vibroacoustic response of poroelastic media. *Journal of Computational Acoustics*, 23:1550020, 2015.

[107] I. M. Sobol. Sensitivity analysis for nonlinear mathematical models. *Mathematical modeling and computational experiment*, 1:407–414, 1993.

[108] M. R. Stinson and G. A. Daigle. Electronic system for the measurement of flow resistance. *The Journal of the Acoustical Society of America*, 83(6):2422–2428, 1988.

[109] A.N. Thite and B.R. Mace. Robust estimation of coupling loss factors from finite element analysis. *Journal of Sound and Vibration*, 303(3–5):814 – 831, 2007.

[110] N. Totaro, C. Dodard, and J. L. Guyader. SEA coupling loss factors of complex vibro-acoustic systems. *ASME Journal of Vibration and Acoustics*, 131(4):8 pages, 2009.

[111] E. Trefftz. Ein Gegenstück zum Ritzschen Verfahren. In *Proceedings of the 2nd International Congress on Applied Mechanics, Zurich*, 1926.

[112] B. Troclet. Prediction of the vibroacoustic response of Ariane 4 fairing and the equipment bay. In *Proceedings of Internoise 89: Engineering environmental noise control*, pages 263–266, 1989.

[113] B. Troclet, B. Hiverniau, M. Ichchou, L. Jézéquel, K. Kayvantash, T. Bekkour, J. B. Mouillet, and A. Gallet. FEM/SEA hybrid method for predicting mid and high frequency structure-borne transmission. *The Open Acoustics Journal*, 2:45–60, 2009.

[114] M. Villot, C. Guigou, and L. Gagliardini. Predicting the acoustical radiation of finite size multi-layered structures by applying spatial windowing on infinite structures. *Journal of Sound and Vibration*, 245(3):433–455, 2001.

[115] P. H. White. Sound transmission through a finite, closed, cylindrical shell. *The Journal of the Acoustical Society of America*, 40(5):1124–1130, 1966.

[116] J. Whitney and N. Pagano. Shear deformation in heterogeneous anisotropic plates. *Applied mechanics transactions of the ASME*, 37, 1970.

[117] C. Xu and G. Gertner. Extending a global sensitivity analysis technique to models with correlated parameters. *Computational statistics and data analysis*, 51:5579–5590, 2008.

[118] M. Xu, Z. Qiu, and X. Wang. Uncertainty propagation in SEA for structural–acoustic coupled systems with non-deterministic parameters. *Journal of Sound and Vibration*, 333:3949–3965, 2014.

[119] C. Yuan, N. B. Roozen, O. Bergsma, and A. Beukers. Experimental-numerical study and optimization of sound insulation of a finite composite cylinder. *Engineering Analysis with Boundary Elements*, 37(2):250–259, 2013.

[120] C.W. Zhou, J.P. Lainé, M.N. Ichchou, and A.M. Zine. Multi-scale modelling for two-dimensional periodic structures using a combined mode/wave based approach. *Computers and Structures*, 154(0):145–162, 2015.

[121] R. Zhou and M. J. Crocker. Sound transmission loss of foam-filled honeycomb sandwich panels using statistical energy analysis and theoretical and measured dynamic properties. *Journal of Sound and Vibration*, 329:673–686, 2010.

dernière page de la thèse

AUTORISATION DE SOUTENANCE

Vu les dispositions de l'arrêté du 7 août 2006,

Vu la demande du Directeur de Thèse

Monsieur M. ICHCHOU

et les rapports de

M. M. BEN TAHAR
Professeur - Université de Technologie de Comiîègne - Rue du docteur Schweitzer - CS 60319
60203 COMPIEGNE cedex

et de

M. N. ATALLA
Professeur - Université de Sherbrooke - 2500 bd de l'Université - Sherbrooke (Québec)
CANADA J1K 2R1

Monsieur CHRISTEN Jean-Loup

est autorisé à soutenir une thèse pour l'obtention du grade de **DOCTEUR**

Ecole doctorale MECANIQUE, ENERGETIQUE, GENIE CIVIL ET ACOUSTIQUE

Fait à Ecully, le 22 septembre 2016

P/Le directeur de l'E.C.L.
La directrice des Etudes

M-A. GALLAND